4-17-2020

Theoretical Investigation of Fundamental Cathode Processes in Metal-02 Batteries

Saurin Hiren Rawal

THEORETICAL INVESTIGATION OF FUNDAMENTAL CATHODE PROCESSES IN METAL-O_2 BATTERIES

A Dissertation

Submitted to the Graduate Faculty of the
Louisiana State University and
Agricultural and Mechanical College
in partial fulfillment of the
requirements for the degree of
Doctor of Philosophy

in

The Gordon A. and Mary Cain Department of Chemical Engineering

by
Saurin Hiren Rawal
B.S., University of Mumbai, 2012
M.S., Rutgers, The State University of New Jersey, 2015
August 2020

Dedicated to my parents and my wife

Acknowledgements

I would like to thank Prof. Ye Xu, who has been a great advisor and a mentor. I greatly admire his ability to take difficult concepts to make them presentable in a simple, cogent manner. He accorded me with a lot of intellectual freedom to pursue a wide range of problems during my graduate work. I am grateful for his constant encouragement and passing on his knowledge. He has been instrumental in directing my energy and many ideas into fruitful projects. I would like to thank my research colleagues especially Dr. W. Chad Mckee who got me started in the field of computational catalysis and batteries in specific. He played a tremendous in shaping my graduate work and has been a great intellectual comrade.

Next, I'd to thank the many professors in LSU with their stimulating discussions which helped shaped my many projects. Particularly I would like to thank Prof. Bill Shelton and Prof. Chris Arges who made me understand many theoretical and experimental complexities involved in the many research topics that I tackled. I would also like to thank my dissertation committee, Prof. Revati Kumar, Prof. Ying Wang, Prof. Krishnaswamy Nandakumar and Prof. Jian Xu for their valuable time and inputs. I am grateful to the computational resources provided by LSU HPC and LONI.

I am grateful to my close group of friends at LSU who have kept me motivated through the duration of my Ph.D. From conversations of different research aspects to exploring different opportunities helped transform my professional outlook. The many social events and sports events helped me unwind and stay focused on what's important.

I am deeply grateful to my parents who had faith in my throughout my academic life and supported every decision of my mine with love and kindness. Lastly I would like to mention my wife Siddhi Hate who was the reason I began my Ph.D, who convinced me to follow my scientific

intrigue and pursue a degree in engineering. My parents and my wife have been my emotional pillar for the last 5 years. It is hard to express in words the role they have had in shaping me and I am greatly indebted to them for everything I have done.

Table of Contents

Abstract

In this dissertation we theoretically explore the different fundamental phenomena associated with metal-air batteries (where the metal can be Li, Na or K) using first principles density functional theory. We start by investigating the adsorption of the starting reactants/primary intermediates i.e. metal superoxides and superoxide anion on Au(111) and Au(211). We elucidate the influence of electric fields and the importance of including explicit solvents on the adsorption energy of these intermediates. We show that these effects are considerable and should be included for future reaction modeling of these batteries. Following this we investigate the reaction of M^+ and O_2^- in solution phase where the solvents considered are dimethyl sulfoxide (DMSO) and Acetonitrile (ACN), which are commonly used electrolytes in these batteries. We show the for Li-O_2 pair the peroxide species is the most stable final product while for Na-O_2 and K-O_2 pairs the metal superoxide is the most stable species. We explore the possibility of dimerization and trimerization of the metal superoxide and peroxide in solvent and show that only Li_2O_2 tends form clusters in solution. Next we proceed to investigate the discharge product formed as a result of the metal assited oxygen reduction reaction (M-ORR). We only consider the discharge product for Li-O_2 batteries where the primary discharge product is Li_2O_2. We show that doping the discharge product during the electrochemical growth phase with solvated dopant/metal cations could lead to microdomains of discharge product. We use evolutionary algorithm as implemented in the USPEX package in conjunction with DFT to probe the potential energy surface for novel configurations of composition $Li_{15}DO_{16}$ (stoichiometric composition) and $Li_{14}DO_{16}$ (composition representing a structure with vacancy). Where D is the dopant atom. We consider Ba, Co, Mg Na and Ni ions as dopants which are commonly found as solvated ions in batteries. We show thermodynamically that these structures can viably form as compared to the $P6_3/mmc$ Föppl structure of Li_2O_2.

Additionally, we show that novel doped structures improve on the electron mobility through the bulk aiding in reduction of overpotential.

Chapter 1. Introduction

The main focus of this dissertation is the understanding the fundamental phenomena associated with the electrochemistry of oxygen at the cathode of metal-O_2 batteries which are at the forefront of sustainable energy storage technologies for the 21st century.[1] The exploitation of the electrochemistry of oxygen has technological importance in metal air batteries.[2-3] However, oxygen electrochemistry has a deeper scientific importance as it has served to build the foundational understanding of surface electrocatalysis. In this dissertation we try to address some engineering challenges using fundamental first principles approach. The challenges are related to the metal assisted oxygen electrochemistry commonly found in metal-O_2 batteries. The goal of the dissertation is to identify some of the fundamental limits associated with the physical phenomena and reactions occurring at the cathode of these batteries.

The approach to identifying the fundamental limits is based on computational modeling of the underlying physicochemical processes. The rapid increase in computing capabilities has enabled computational modeling as a means to carry out "experiments" on the computer to gain a deeper understanding of the experimental data and in some select cases inspire new experiments. The dissertation will discuss the use of computational modeling to develop a theoretical understanding of the underlying processes associated with oxygen electrochemistry (reduction and oxidation) with Lithium, Sodium and Potassium. The developed concepts and models can be more generally applied to a broad range of electrochemical systems.

1.1. Dissertation Overview and Contributions

The goal of this dissertation is to develop an understanding of the various fundamental processes occurring at the cathode of metal-O_2 batteries based on computational modeling of the underlying

processes. This understanding is used to identify fundamental insights associated with these processes. We briefly summarize below the contributions of the dissertation work.

1.1.1. Effect of Electric Fields and Explicit Solvents on the Adsorption of Molecular Superoxide Species

Superoxide species are key intermediates in the oxygen reduction reactions (ORR) that occur at the cathodes of aprotic metal–air batteries. Herein we report a DFT study of the effects of an externally applied electric field (e) on the stability of various molecular superoxide species, including MO_2 (M = Li, Na, K) and O_2, on gold surfaces, which shows that the stability of such species on Au electrodes can be materially affected by the presence of an electric field and solvent molecules, suggesting that such effects should be included in the first-principles modeling of cathode reactions in metal-O_2 cells. In the ε range of ±0.4 V Å1, the stability of MO_2 species is found to vary by up to |0.4| eV on Au(111) and |0.2| eV on Au(211) *in vacuo*, which is larger than the field effects on the stability of O and OH, key intermediates in the ORR by hydrogen. An aprotic solvent such as dimethyl sulfoxide (DMSO), considered here via the inclusion of explicit DMSO molecules above the Au surfaces, stabilizes all three MO_2 species at zero fields and amplifies the field effects on the stability of MO_2, on both Au surfaces. The variations in the stability of the molecular MO_2 species with ε, which have small polarizabilities, are closely approximated by the first-order Stark effect ($\mu_0 \cdot \varepsilon$, where μ_0 is the static surface dipole moment induced by adsorption at $\varepsilon = 0$ V/Å). The superoxide anion (O_2) that has been identified on an under-coordinated Au site has a larger polarizability than the MO_x species and a μ_0 that is opposite in sign to those of the metal MO_2 species, which results in larger errors by the first-order approximation, although its stability varies only moderately under positive electric fields of up to 0.4 V/Å.

1.1.2. Solution Mediated Reaction Mechanisms for Metal Air Batteries

Spectroscopic identification of the ORR products and intermediates on an Au electrode in a Li^+ DMSO electrolyte coupled with detailed DFT calculations concluded that the generation of O_2^- and LiO_2 intermediates depends critically on the electrode potentials and determines the final peroxide formation mechanism.[4] At high potentials (low overpotentials) O_2^- has been identified as the first intermediate while at low potentials (high overpotentials) molecular LiO_2^* forms. The O_2^- formed tend to diffuse into the electrolyte and react chemically with solvated Li^+ cations to form Li_2O_2 through a solution mediated reaction mechanism.[5] The molecular LiO_2^* electrochemically leads to the formation of Li_2O_2 on the electrode through a surface mediated reaction mechanism.[6-7] The schematic for solution and surface reaction mechanisms are shown in Fig. 1. The solution mediated reaction mechanism leads to the precipitation of nanoparticles of the discharge product on the surface of the electrode. Surface mediated reaction mechanisms lead to uniform coverage of the electrode with the discharge product. Similar behavior is also shown for Na-O_2 pair and the reaction mechanistic can also be extended to the K-O_2 pair.

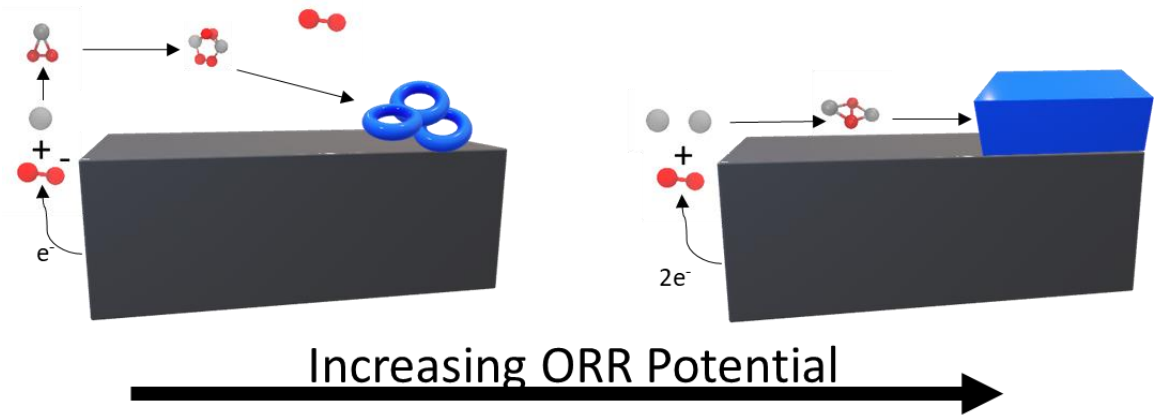

Figure 1.1: Schematic of solution mediated reaction mechanism at high operation potential and surface mediated reaction mechanism at low potentials.

In all cases the discharge product tends to be insulating in nature[8-9] which leads to multiple engineering issues. Solution mediated reaction mechanism leads to formation of discharge product in the form of precipitated nanoparticles on the surface of the electrode which occupies less surface area as compared to uniform growth of discharge product thus leading to improved discharge capacity.[10-11] Herein we present a solution mediated reaction mechanism between metal cation and oxygen superoxide anion and the associated thermodynamic analysis. As part of the study we developed a novel stochastic approach to probe the potential energy surface for nanoclusters that could form through dimerization and trimerization of metal superoxides and metal peroxides. The method has two variations termed as RASS and R-Kick respectively.[12] The solvent selected are dimethyl sulfoxide (DMSO) and acetyl cyanide (ACN). The solvents in this case is modeled implicitly using polarizable continuum model (PCM) and fitted atomic radii for M (Li, Na and K) and O atom by a method described previously. We propose the mechanism to proceed through a dimerization of metal superoxide step and the dimer configuration is found by probing the potential energy surface using the R-Kick method that we proposed earlier. Based on our calculations, we

found that Li_2O_2 is the most stable discharge product while for the other metal candidates, based on the precipitation energy calculated, both metal superoxide and peroxide can form in case of Na and only superoxide is favorable for K. For Na and K based mechanism, an endergonic process needs to be overcome for the disproportionation of the dimer to form solvated metal peroxide.

1.1.3. Effect of Dopant on the Crystalline and Electronic Structures of Li_2O_2

One of the major engineering issue plaguing Li-O_2 batteries is the decomposition of the dominant discharge product i.e. Lithium Peroxide (*c*-Li_2O_2). *c*-Li_2O_2 is a wide bandgap insulator which causes large overpotential during oxygen evolution reaction (OER).[13] Thermodynamically Li_2O_2 forms a $P6_3/mmc$ Föppl structure.[14] The growth mode and morphology of Li_2O_2 depend on a number of factors including rates of nucleation and precipitation, which in turn depend on local electronic and ionic conductivity, in the electrolyte and to/from the electrolyte/electrode interface, while the entire micro-environment is under an applied voltage.[15] There have been studies that theoretically explore different phases of *c*-Li_2O_2, defective *c*-Li_2O_2, or amorphous Li_2O_2 (*a*-Li_2O_2),[8, 16-18] or the Föppl structure with a substitutional or interstitial dopant atom.[8, 19-20] None so far have considered the possibility of a dopant fundamentally altering the structure of Li_2O_2 as shown schematically in Fig. 2. Herein we theoretically explore the potential energy surface (PES) for Li_2O_2 doped with Na, Mg, Co, Ni, and Ba, cations that are commonly found either as ingredients of Li-based electrodes or as solvated components of the electrolyte, using global optimization techniques based on evolutionary algorithms and density functional theory (DFT) calculations, and we investigate the potential effect that these dopants have on the geometric and electronic structure of solid Li_2O_2. We found that the incorporation of foreign cations leads to structures that differ significantly from the Föppl structure and reflect instead the preferred oxidation states of the dopants. Some of the doped microstructures have free energies of formation

that are lower (i.e. more favorable) than that of Li in the Föppl structure and possess electronic structures that may help reduce overpotentials associated with electric conductivity.

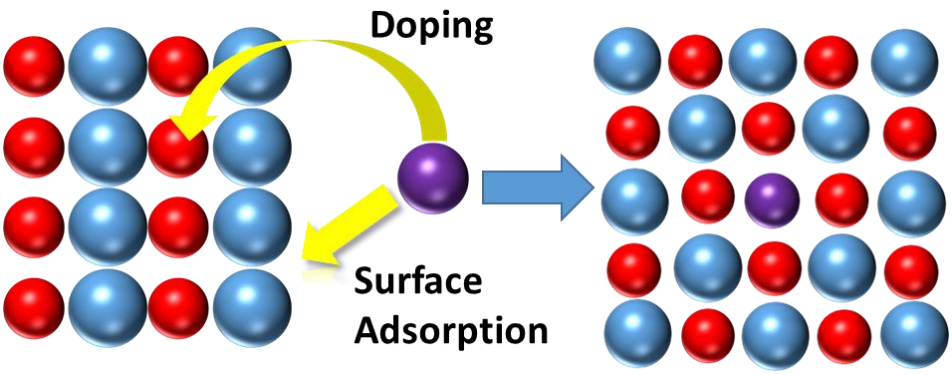

Figure 1.2: schematic representation of doping altering the crystal structure of *c*-Li_2O_2

1.2. Organization of the Dissertation

In we introduce the methods to be employed in this dissertation. This chapter covers the basis for density functional theory and illustrates how density functional theory calculations can be used to calculate free energy changes for an electrochemical reaction as well as calculate formation energies/ free energies for determining the stability of different molecules and bulk structures. We proceed to describe the methodology of evolutionary algorithm as implemented in USPEX[21-22] used to search for different doped Li_2O_2 structures. We also describe the stochastic search algorithm RASS and R-Kick which is used to search for different nanocluster configurations. Additionally we provide details for the thermodynamic cycles utilized to calculate the free energy of solvation using DFT.

In Chapter 3 we describe the stability of different metal superoxides and superoxide anion on different Au surfaces. We describe the effect of electric fields on the adsorption energy of these species (i) *in vacuo* and (ii) in the presence of explicit solvent.

In Chapter 4 we describe the solution mediated reaction mechanism between solvated metal cation and superoxide anion in DMSO and ACN. We also explore the possibility of precipitation phenomena as well as dimerization and trimerization of the metal superoxide and peroxide species.

In Chapter 5 we discuss the possibility of doping Li_2O_2 with commonly found solvated metal cations and its effect on the overall bulk structure. We provide extensive thermodynamic evidence for the formation of these structures. We investigate the electronic structure of these doped microstructures and empirically provide the positive benefits on electron mobility of doping Li_2O_2.

In Chapter 6, we offer some concluding remarks on the accomplishments of this dissertation and proceed to provide recommendations for future work.

Chapter 2. Methods

This chapter discusses the methods and techniques employed in the dissertation. With the rapidly rising computing power, it has become possible to describe chemical bonds in molecules and solid surfaces. The description of these bonding properties has become computationally tractable through the development of an efficient scheme to solve the electronic structure of these systems. This efficient scheme is based on the approximations invoked through density functional theory (DFT), which this dissertation relies on extensively.

We begin by briefly introducing density functional theory followed by a discussion of the exchange correlation functionals employed in this dissertation. This is followed by a discussion of using planewave DFT to calculate the thermodynamics of surface processes in an electrochemical environment. This treatment can be used to calculate the free energy of reaction intermediates, which is helpful to understand the reaction landscape surfaces. Following which we describe the application of an electric field and how it is treated within the confines of DFT. Further we gaussian wave DFT to calculate reactions in a solvated phase. Following this we describe the different thermodynamic cycles employed to calculate the solvation energies of metal cations.

Finally, the chapter discusses stochastic approaches for discovery of nanoclusters on the potential energy surface and evolutionary algorithms to discover doped structures. These are methods of global optimization that is used extensively in this dissertation for the purpose of studying dimerization, trimerization and doping of solids in an electrochemical environment.

2.1. Density Functional Theory

In quantum mechanics, a system is completely defined by its wave function which is a function of time t, electron coordinates $\{r_1, \dots r_N\}$ and nuclear coordinates $\{R_1, \dots R_K\}$. Thus, the overall wavefunction is $\Psi = \Psi(r_1, \dots r_N, R_1, \dots R_K; t)$ [23] which satisfies the time dependent Schrodinger equation

$$\widehat{H}\Psi = i\frac{\partial \Psi}{\partial t} \tag{2.1}$$

Where $\widehat{H}$ is the Hamiltonian operator. In coordinate representation, the Hamiltonian is given by

$$\widehat{H} = -\frac{1}{2}\sum_{i=1}^{N}\nabla_{\mathrm{i}}^2 - \sum_{k=1}^{K}\frac{1}{2M_k}\nabla_{\mathrm{i}}^2 - \sum_{i=1}^{N}\sum_{k=1}^{K}\frac{Z_k}{|r_i - R_k|} + \frac{1}{2}\sum_{i\neq j}^{N}\frac{1}{|r_i - r_j|} + \frac{1}{2}\sum_{k\neq l}^{K}\frac{Z_k Z_l}{|R_k - R_l|} \tag{2.3}$$

The first term is the kinetic energy of the electrons, the second term is the kinetic energy of the nuclei, the third term is the interaction between the electrons and the nuclei, the fourth term is the electron-electron interaction and the fifth term is the interaction between the nuclei. As the nuclei are 3 to 4 orders of magnitude heavier than the electrons, we can apply the Born-Oppenheimer (BO) approximation, where it is assumed that the electrons respond instantaneously to the movements of the nuclei. This allows a separation of the problem into the electronic structure problem and the nuclear motion. Focusing on stationary solutions to the electronic structure problem, the time independent electronic wave function $\Phi = \Phi(r_1, \dots r_N)$ satisfies the Schrodinger equation.

$$E\Phi = \{\widehat{T_e} + \widehat{V_{en}} + \widehat{V_{ee}}\}\Phi \tag{2.4}$$

where $\widehat{T_e}$ is the kinetic energy operator for the electrons, $\widehat{V_{en}}$ is the electron nucleus interaction and $\widehat{V_{ee}}$is the electron electron interaction.

In Density Functional Theory, the search for the *N*-particle wavefunction is replaced by a search for the electron density $n(\mathbf{r})$. This transformation reduces the problem from a 3*N* to a 3-dimensional problem. From a physical point of view, it is clear that the ground state is uniquely defined by the external potential and the number of electrons in the potential, since the external potential specifies the Hamiltonian.

In 1964, Hohenberg and Kohn proved that the external potential is also uniquely determined by the ground state density $n(\mathbf{r})$.[24] As the external potential determines the Hamiltonian, the ground-state *N*-particle wavefunction and all observables of the ground state are functionals of the density $n(\mathbf{r})$. In particular, the ground state energy is a functional of the density $E[n(\mathbf{r})]$.

Using the variational principle, it can be shown,[25] that the ground state density $n(\mathbf{r})$ minimizes the energy, $E[n(\mathbf{r})]$. Following the constrained search approach proposed by Lieb and Levy,[26-27] the ground state energy may be obtained by minimizing the energy over all possible wavefunctions with the density $n(\mathbf{r})$, and then minimizing over all densities. The ground state energy may then be written formally as

$$E_0 = \min_{n(r)}\{F[n(r)] + \int v_{ext}(r)n(r)dr\} \tag{2.5}$$

where v_{ext} is the external potential and $F[n(\mathbf{r})]$ is a universal but unknown functional obtained by minimizing over all wavefunctions with density $n(\mathbf{r})$

$$F[n(r)] = \min_{\Psi \to n(r)} \langle \Psi | \widehat{T_e} + \widehat{V_{ee}} | \Psi \rangle \quad (2.6)$$

The energy functional may thus be expressed as

$$E[n(r)] = F[n(r)] + V_{ext}[n(r)] \quad (2.7)$$

Where $V_{ext}[n(r)] = \int v_{ext}(r) n(r) dr$. The first term is independent of the external potential and thus the same for all systems of electrons interacting through the Coulomb potential. The second term is easily evaluated and depends on the system. The Hohenberg-Kohn theorem only proves that the energy is a functional of the density. However, it does not prescribe a scheme for obtaining this functional. A year later, Kohn and Sham developed an approximate scheme for obtaining the functional[28] and this will be discussed in the next section.

2.1.1. The Kohn Sham Equations

The Kohn-Sham scheme is based on the observation that we can construct a fictitious system based on non-interacting electrons in an effective potential, v_{eff}, that can match the density of the true system consisting of interacting electrons. Then, by invoking the Hohenberg-Kohn theorem, given the densities of the two systems are the same, then the energy and other ground state properties are the same. Through the construction of the effective potential, we need to ensure that the electrons in the Kohn-Sham scheme have the exact same density as the (real) interacting electrons

The total energy, in the Kohn-Sham scheme, is given by[28]

$$E[n(r)] = T_s[n(r)] + V_H[n(r)] + E_{xc}[n(r)] + V_{ext}[n(r)] \quad (2.8)$$

Where $T_s[n(r)]$ is the kinetic energy of the non-interacting electron gas with density $n(r)$ and $V_H[n(r)]$ is the Hartree energy, given by

$$V_H[n(r)] = \frac{1}{2}\int\int \frac{n(r')n(r)}{|r-r'|}dr'dr \tag{2.9}$$

There is an additional ingredient required in the Kohn-Sham scheme to match the densities of the non-interacting system to that of the interacting system. This term is called the exchange correlation energy functional, $E_{xc}[n]$, which is introduced as a correction that contains electron exchange and correlation. The exchange correlation functional is not known exactly, and the strength of density functional theory relies on the accuracy of the approximations to the exchange correlation functional, E_{xc}.

Using the variational principle invoking the constraint that the number of electrons needs to be conserved, we can derive the Kohn-Sham (KS) equations. The KS equations are given by[28]

$$\left[-\frac{1}{2}\nabla^2 + v_{eff}\right]\phi_j(r) = \epsilon\phi_j(r) \tag{2.10}$$

Where $\phi_j(r)$ represents the Kohn-Sham orbital and the effective potential is

$$v_{eff}(r) = v_{ext}(r) + \int \frac{n(r')}{|r-r'|}dr' + v_{xc}(r) \tag{2.11}$$

and the exchange correlation potential is the functional derivative of E_{xc}

$$v_{xc}(r) = \frac{\delta E_{xc}}{\delta n(r)} \tag{2.12}$$

$$[-\frac{1}{2}\nabla^2 + v_{ext}(r) + \int \frac{n(r')}{|r-r'|}dr' + v_{xc}(r)]\phi_j(r) = \epsilon_j\phi_j(r) \tag{2.13}$$

$$n(r) = \sum_{j\in occupied}\left|\phi_j(r)\right|^2 \tag{2.14}$$

The KS equations describe non-interacting electrons in a fictitious potential that gives the same density as the interacting electrons. Since the effective potential v_{eff} depends on $n(\mathbf{r})$, the Kohn-Sham equations (2.10) and (2.11) must be solved iteratively until a self-consistent density is obtained.

2.1.2. Exchange Correlation Functionals

In their original scheme, Kohn and Sham proposed a simple approximation to the exchange correlation functional (xc-functional).[28] They assumed that the exchange correlation energy at density $n(\mathbf{r})$ is the same as that of a homogeneous electron gas with the same density. This later became known as the local-density approximation (LDA).

The exchange correlation energy, within the LDA, is given by

$$E_{xc}^{LDA} = \int \epsilon_{xc}^{hom}\big(n(r)\big)n(r)dr \tag{2.15}$$

Where $\epsilon_{xc}^{hom}\big(n(r)\big)$ is the energy of the exchange correlation hole in the homogeneous electron gas of density n. The local density approximation is, in principle, unique. However, different parametrizations of ϵ_{xc}^{hom} have been proposed.[29-31]Despite its simplicity, LDA has had remarkable success in describing properties such as lattice constants, vibrational frequencies and equilibrium geometries of physical systems. Dissociation energies of molecules and cohesive energies of solids are predicted within 10-20% and bond geometries are often predicted within 1%. The success of LDA is partly rationalized by the fact that the exchange correlation hole is normalized as in real systems. It is exact in the limit of high density and the slowly varying limit.

Although LDA was often sufficiently accurate to describe properties of solids, the wide-spread application of density functional theory did not become commonplace until the

development of the Generalized Gradient Approximations (GGA). In a Generalized Gradient Approximation, the exchange correlation energy depends on the gradient of the density as well as the density. The exchange correlation energy is given by

$$E_{xc}^{GGA}[n(r)] = \int \epsilon_{xc}^{GGA}\big(n(r), \nabla n(r)\big)dr \quad (2.16)$$

However, unlike ϵ_{xc}^{hom}, which is uniquely defined, ϵ_{xc}^{GGA} is not unique. Several GGA's have been suggested, for example PW91,[32] PBE[33-34] and RPBE.[35] The choice of the functional depends on the system and properties of interest.

However, both LDA and GGA have serious shortcomings and we present a brief review of its failures to motivate the search for improvements. A brief catalog of typical failures include:[36]

1. Band structure predictions of metallic materials that are experimentally known to be insulating (*e.g.*, CoO and FeO),
2. Absence of magnetism for materials that are magnetic (e.g., for many undoped high-temperature superconducting oxides) and vice versa (such as Pu),
3. Band gaps that are much too small compared with experiment (*e.g.*, for many semiconductors),

More examples can be found elsewhere,[36] but this list suffices for our purposes. When examining this list, it becomes clear that most of the problems listed are associated with the spectral properties of the electronic structure of a material. However, as explained carefully in the original papers on LDA,[24, 28] this type of theory is designed to minimize the total ground-state energy of the electrons in a material as a functional of the spatial distribution

of the number density of electrons. Thus, the eigenvalues of the Kohn-Sham equations[28] were never supposed to represent the actual quasiparticle spectrum of electrons.

Nonetheless, because the eigenvalues often, in fact, are a reasonably good representation of the spectral properties measured in experiments, this identification is commonly made in practice. Hence, although this has no justification, most attempts to improvements to density functional theory beyond the GGA level are actually attempts to make corrections to the eigenvalue spectra to bring it into better agreement with various spectroscopic measurements that probe the quasi-particle properties of the materials, such as optical and photoemission spectra. Even the metal versus insulator problem involves this issue, since this distinction depends upon knowing the quasi-particle spectral distribution as a function of energy.

In the next section, we will discuss a general formalism that uses density functional theory calculations to determine the free energy of surface adsorbates on solid surfaces.

2.1.3. Ab Initio Molecular Dynamics

Ab initio molecular dynamics (AIMD) uses quantum mechanical equations in order to calculate the electronic structure of a molecular/solid surface syste,. The internal forces are then calculated from the electronic structure and used to calculate velocities and new positions of the atoms.

MD simulations are classically done within the microcanonical ensemble where the number of particles, volume and energy are considered as constants. However, in real experiments one usually controls the temperature instead of the energy. This means that a more effective way of simulating the real world is to instead use the canonical ensemble i.e. constant number of particles, volume and temperature. There exists many different methods of achieving constant

temperature simulations within the canonical as well as the microcanonical ensemble, the most commonly used for its accuracy and efficiency is the Nose´-Hoover thermostat

Nose´ developed a thermostat algorithm that is based on the use of an extended Lagrangian (Eq 2.17)[37-38] where Nose´ introduced an additional degree of freedom coordinates to represent an external heat bath. This was then later improved upon by Hoover [39-40]. The extended lagrangian for the Nose´-Hoover algorithm is given as

$$\mathcal{L}_{Nose} = \frac{1}{2}\sum_{i=1}^{N} m_i(s\dot{r}_i)^2 - U(r^N) + \frac{Q\dot{s}^2}{2} - gk_bTln\ s \tag{2.17}$$

Where the first two terms are the kinetic and potential energy for a system of N particles. The last two terms represent the kinetic and potential energy respectively of the external heat bath. *Q* is an effective mass associated to *s* and *g* is the number of independent momentum degrees of freedom of the system.[41] For the canonical ensemble $g = 3N + 1$. The momentum for the extended system is then given by

$$\mathrm{p_i} \equiv \frac{\partial \mathcal{L}_{Nose}}{\partial \dot{r}_i} = m_i s^2 \dot{r}_i \tag{2.18}$$

$$p_s \equiv \frac{\partial \mathcal{L}_{Nose}}{\partial \dot{s}} = Q\dot{s} \tag{2.19}$$

From the extended Lagrangian we get the Hamiltonian as

$$H_{Nose} = \sum_{i=1}^{N} \dot{r}_i \mathrm{p_i} - \mathcal{L}_{Nose} = \sum_{i=1}^{N} \frac{\mathrm{p_i^2}}{2m_i s^2} + U(r^N) + \frac{p_s^2}{2Q} + gk_b \ln s \tag{2.20}$$

The equations of motion can then be derived from the Hamiltonian.

$$\dot{r}_i = \frac{\partial H_{Nose}}{\partial \mathrm{p_i}} = \frac{\mathrm{p_i}}{m_i s^2} \tag{2.21}$$

$$\dot{\mathrm{p}}_i = -\frac{\partial H_{Nose}}{\partial r_i} = -\frac{\partial U(r^N)}{\partial r_i} \tag{2.22}$$

$$\dot{s} = \frac{\partial H_{Nose}}{\partial p_s} = \frac{p_s}{Q} \tag{2.23}$$

$$\dot{p_s} = -\frac{\partial H_{Nose}}{\partial s} = \frac{1}{s}\left[\sum_{i=1}^{N} \frac{\mathrm{p_i^2}}{m_i s^2} - g k_b T\right] \tag{2.24}$$

The coordinates *r*, *p*, Δt and *s* of the virtual particle-heat bath system is related to the real variables *r'*, *p'*, $\Delta t'$ and *s'*

$$r' = r \tag{2.25}$$

$$p' = \frac{p}{s} \tag{2.26}$$

$$s' = s \tag{2.27}$$

$$\Delta t' = \frac{\Delta t}{s} \tag{2.28}$$

The temperature is constant within the virtual system however because energy will be transferred between the particle system and the heat bath the real system will experience oscillatory temperature changes.

2.2. Thermodynamics of surface and solution processes

In this section, we discuss a thermodynamic formalism to treat surface processes on solid surfaces. We first develop the thermodynamics for surface adsorption and then extend the treatment to an electrochemical environment. This formalism can be used, along with density functional theory calculations, to calculate free energies of reaction intermediates along a reaction coordinate. The resulting free energy diagrams can be used to determine the efficacy of that catalyst in catalyzing the reaction under study.

2.2.1. Surface Adsorption

Adsorption occurs when atoms or molecules from a vapor or liquid phase becomes bound to solid surfaces. Consider the surface adsorption associated with the process below:

$$A + * \leftrightarrow A^* \tag{2.29}$$

where * is a surface site on a solid surface. The case considered here is the localized adsorption of A on a lattice site. The free energy change associated with this process is given by

In the discussion below, we assume A is a gas and discuss the free energy change associated with the surface adsorption process of (2.29) is given by

$$\Delta G = G_{A^*} - G_* - G_{A(g)} \tag{2.30}$$

We briefly review standard thermodynamic relations to calculate the free energy change associated with surface adsorption. The Gibbs Free Energy is given by

$$G = H - TS = U + pV - TS \tag{2.31}$$

The internal energy, *U*, for adsorbed A^*, at a temperature T_s , is given by

$$U = E_0 + ZPE + \int_{T=0}^{T=T_s} C_p(T')dT' \ \ and \ ZPE = \sum_{i=1}^{N_m} \frac{1}{2} h\nu_i \tag{2.32}$$

Using the harmonic approximation, Zero Point energy (ZPE) is a summation over the energy associated with the different vibrational modes, N_m. Typically, in the case of adsorption, changes associated with the pressure volume energy are small compared to the internal energy. Thus, the enthalpy is given by

$$\Delta H = \Delta(E_0 + ZPE) + \Delta(\int_{T=0}^{T=T_s} C_p(T')dT') \tag{2.33}$$

Neglecting changes in the pressure volume energy, the change is enthalpy is given by the change in the electronic energy between the reactant gas A and the adsorbed state, A*. The electronic and zero point energy, E_0 and ZPE, can be calculated using density functional theory calculations.

The entropic contribution to the surface adsorption process is given by

$$\Delta S = S_{A*} - S_{*} - S_{A_{(g)}} \tag{2.34}$$

The entropy of A* has two components (i) entropy associated with the vibration between the adsorbed atom or molecule and the surface, and (ii) the configurational entropy associated with the adsorbates. The vibrational and configurational entropy of adsorbed A* is given by

$$S_{A*}^{vib} = \sum_{i=1}^{N_m} S_{v_i}, with\ S_{v_i} = -k_B \ln\left(1 - \exp\left(-\frac{h\nu_i}{k_B T}\right)\right), \text{ and} \tag{2.35}$$

$$S_{A*}^{conf} = -k_B[\theta_{A*} \ln(\theta_{A*}) + (1 - \theta_{A*}) \ln(1 - \theta_{A*})] \tag{2.36}$$

Where θ_{A*} is the coverage of adsorbate A. We have invoked the harmonic approximation for the vibrational part of the entropy. The entropy of a gas has several components.

$$S_{A_{(g)}} = S_{A_{(g),trans}} + S_{A_{(g)},rot} + S_{A_{(g)},vib} + S_{A_{(g)},el} \tag{2.37}$$

Typically, the entropy of the gas phase species is much larger than the entropy of adsorbed species. Thus, the entropy change can be approximated by

$$\Delta S \approx -S_{A_{(g)}} \tag{2.38}$$

A similar treatment can be carried out for adsorption from a liquid. The free energy of species in the liquid phase is computed by using the vapor pressure at the temperature of interest and adding this to free energy of the gas phase. For instance, the free energy of liquid water can be calculated

by using the vapor pressure, p_{298K} = 0.035 bar. This yields the thermodynamic relation at standard conditions,

$$G^{\ominus}_{H_2O(l)} = G^{\ominus}_{H_2O(g)} + k_B T ln[0.035] \quad (2.39)$$

2.2.2. Modeling Electric Fields and Electrochemical Double Layer

The methods of Neugabauer et al. and Makov et al.[42-43] were employed to generate an external electric field. No extra electron was added to any of the systems considered. While directly modeling the entire electrical double layer formed at the electrode | electrolyte interface would in principle provide a more realistic description of the electric field effects,[44-45] such an approach is still too computationally demanding to be routinely applicable. Here a positive (negative) ε value corresponds to the buildup of a positive (negative) charge on the side of the slab where adsorption occurs; i.e., a positive field points in the positive *z* direction. The stability of adsorbed molecular species under an electric field was calculated as

$$\Delta G(\varepsilon)_{ads} = G(\varepsilon)_{adsorbate/slab} - G(\varepsilon)_{slab} - E_{adsorbate} \quad (2.40)$$

where $G(\varepsilon)_{adsorbate/slab}$, $G(\varepsilon)_{slab}$, and $E_{adsorbate}$ are the total energies of the metal slab with a with a molecular species adsorbed thereon, the metal slab without any adsorbate, and the neutral adsorbate species in the gas phase, and where ε is the applied electric field. In chapter 3, where this equation is used extensively, the molecular species that is adsorbed is either a metal superoxide or neutral molecular O_2. More negative $\Delta G(\varepsilon)_{ads}$ values indicate stronger adsorption. At zero field (ε = 0 V/Å) the stability corresponds to the DFT total energy adsorption energy ($\Delta G(0)_{ads} = \Delta E_{ads}$). Both the slab and the adsorbate-slab system were optimized at a given ε value. The preferred solvent used in all the study is dimethyl sulfoxide (DMSO). DMSO molecules were taken to be part of the slab when modeling the electrode | solvent interface explicitly. The

minimum total energy geometry at a given electric field for an adsorbed species was verified by using *ab initio* molecular dynamics simulations to generate additional candidate structures for optimization and comparison. We focused on the effects of an electric field on the *associative molecular* adsorption of superoxide species to Au (preferred metal slab) and on the electrostatic interaction between these species and DMSO molecules. Previous theoretical work suggests that the RPBE functional is a good choice for describing both,[46-47] while van der Waals (vdW) contributions in DMSO adsorption on Au, even though it might be appreciable, are not expected to affect either and so a vdW functional or method was not used.

It is not possible to calculate $\Delta G(\varepsilon)_{ads}$ at a constant surface work function as would be demanded by a given electrode potential. However, adsorption energies based on the total energies are expected to be only slightly affected by this.[48] The field-induced change in stability ($\Delta\Delta G(\varepsilon)_{ads}$) is generally interpreted in terms of a basic electrostatic model (sometimes referred to as an electrostatic Stark effect) as:[49,50]

$$\Delta\Delta G(\varepsilon)_{ads} = \Delta G(\varepsilon)_{ads} - \Delta G(0)_{ads} = \mu_0 \varepsilon - \frac{1}{2}\alpha\varepsilon^2 \tag{2.41}$$

where μ_0 is the static surface dipole moment in eÅ, induced by the adsorbate at $\varepsilon = 0$ V/Å, and α is the polarizability of the adsorbate in eÅ^2/V. An external electric field not only interacts with the surface dipole but affects the bond between an adsorbate and the surface as well, by polarizing the electron distribution at the surface. For adsorbates with small polarizabilities, or in cases of small ε, the second term on the right-hand side of Eq. 2.41 would become negligible resulting in a "first-order" field effect where ΔG_{ads} varies linearly with ε. The dipole moment of an adsorbate was calculated as the dipole moment of the adsorbate-slab system minus that of the slab without any adsorbate. This approach produced μ_0 values that were in close agreement with the

coefficients of the first-order terms derived from fitting DFT-calculated $\Delta\Delta G(\varepsilon)_{ads}$ values to Eq. 2.41. The convergence of surface dipole moments with the vacuum thickness was verified by further increasing the vacuum thickness by up to 25%. In our sign convention, a positive adsorbate dipole moment is one that points away from the surface in the positive *z* direction, the same sign convention as adopted for the electric field.

2.2.3. Solvation energy, solubility and solution phase reaction mechanism calculations

Two schemes are used to calculate the solvation energy of different species. The first section describes the first scheme i.e. the calculation of solvation energy using an implicit solvation treatment for DMSO and acetonitrile (ACN) which are the solvents considered in chapter 4. We also describe the relevant reaction mechanism involved in the solution mediated reaction mechanism between solvated metal cations and superoxide anion. In the second section we describe the second scheme i.e. use of mixed cluster-continuum thermodynamic cycle to calculate the solvation energy of metal cations in DMSO used in chapter 5.

2.2.3.1. Solvation Energy and Solubility using Solvent Corrected Atomic Radius method

Electronic structure calculations are carried out using Gaussian09 package.[51] Calculations were done at multiple level of theories, the B3LYP flavor of density functional [52] is used with 6-311++G(d,p) basis set [52-54] to optimize geometries of all species. The dimers and trimers configurations of the different MO_2 and M_2O_2 species were scanned through the configurational space using the RASS method [12] at B3LYP/LANL2DZ level of theory followed by further geometry optimization at B3LYP/6-311++G(d,p) level of theory. Quasi harmonic thermochemical data from Gaussian frequency calculations at 298.15 K is used to calculate the thermal correction to the free energy. The G4 method [55], which is based on CCSD(T) theory, is used to obtain accurate electronic energies using B3LYP optimized geometries for all the molecular species. The

synchronous transit guided quasi newton method as implemented in Gaussian09 is used to find the transition state of the metal superoxide dimers $(MO_2)_2$. The PCM continuum solvation model,[56] as implemented in Gaussian09, is used to implicitly calculate the free energy of solvation (ΔG_{solv}) of the molecular species in DMSO and ACN with a dielectric constants of 46.82 and 35.69 respectively. The experimental thermochemical heats of formation are taken from the NIST-JANAF database.[57] For calculating reaction energies in solution, the free energy of the various molecular species is converted from 1 atm (the standard output of Gaussian 09) to 1M by using the conversion factor of 1.89 kcal/mol [58-59] (($\Delta G_{solv}^{0\rightarrow *}$ or $\Delta G_{solv}^{1\ atm\rightarrow 1M}$=RT*ln(24.46)=1.89 kcal/mol, T=298.15K). The default UFF radii for the different atomic species, M(Li, Na & K) and O atoms, are replaced by values that are fitted to reproduce experimental solvation free energies of the ionic M^+ and O_2^- using the method of solvation corrected atomic radius (SCAR) method as described earlier.[60] This method helps accurately describe the solvation thermodynamics of M-O species (M_xO_y) using pure continuum solvent model like PCM with fitted radii. The fitted atomic radii for the different atoms are shown in Table 2.1. The solute-solvent dispersion and repulsion interaction energy and the solute cavitation energy is included in the total energy calculated in the PCM model. The solvation free energy is of the molecular species ($\Delta G_{solv}(species)$) solvated in either DMSO or ACN is calculated as

$$\Delta G_{solv}^{0}(species) = E_{sol}(species) - E_{gas}(species) \quad (2.42)$$

Where $E_{sol}(species)$ is the internal energy of the molecular species solvated in either DMSO or ACN implicitly modeled through PCM and with fitted solute radii, $E_{gas}(species)$ is the gas phase internal energy of the respective molecular species. Accurate solvation energies for Li^+, Na^+ and K^+ in organic solvent isn't reported so instead the solvation energy in water were taken from values reported by Kelly et al. [61-62] These values were then corrected for the organic solvents like DMSO

and ACN by applying the gibbs free energy of transfer of ions to organics solvents as reported by Marcus et al. [63-64] In DMSO the free energy of transfer of ions for Li^+, Na^+ , K^+ is 6.8 kcal/mol, 2.84 kcal/mol, 1.55 kcal/mol respectively and in ACN the free energy of transfer of ions is -4.13 kcal/mol, -303 kcal/mol, -2.92 kcal/mol respectively. The free energy of solvation for the superoxide ion O_2^- in DMSO and ACN is reported by Kwabi et al.[65] In case of O_2^-, the solvation free energy is calculated by Eq. (2.43)[58],

$$\Delta G^*_{solv}(O_2^-) = -\Delta_f G^0_{298}(Li^+) - \Delta_f G^0_{298}(O_2^-) - FE^* - \Delta G^*_{solv}(Li^+) - 2\Delta G^{0\rightarrow *} \quad (2.43)$$

Where F is the faradays constant and E^* is the reduction potential of O_2/O_2^- . The value of E^* is a strong function of the organic solvent and can vary significantly. Thus, an error of ~ 1.85 kcal/mol shown in Table 2.2 between calculated and reported solvation energies is within acceptable bounds. The comparison of reported free energy of solvation and the best fit for free energy of solvation by solute radii adjustment is shown in Table 2.1.

Table 2.1: Fitted solute radii R_s in Å using mixed cluster continuum solvent model where the subscript 's' denotes either DMSO or ACN for different solute atoms (Li, Na, K or O)

Atom	R_{DMSO} (Å)	R_{ACN} (Å)
Li	1.074	1.174
Na	1.342	1.426
K	1.626	1.709
O	1.798	1.773

Table 2.2: Solvation free energies of M^+ and O_2^- ions calculated using solute radii shown in table 1a and fitted to reported values in kcal/mol

Ions	DMSO		ACN	
	Calculated	Reported	Calculated	Reported
Li+	-133.43	-132.53	-120.79	-121.60
Na+	-107.03	-106.23	-99.23	-100.36
K+	-90.31	-88.92	-83.61	-84.45
O_2^-	-64.95	-66.80	-64.85	-66.70

The formation of superoxide anion on the electrode surface is not considered in this work and is assumed to form on the electrode and dissociate into the solvent. Hence, the solvent reaction mechanism between solvated M^+ atom and O_2^- atom to ultimately form metal superoxide or peroxide is broadly described below in Eq. (2.44-2.51),

$$2M^+_{(sol)} + 2O^-_{2\,(sol)} \rightarrow MO_{2\,(sol)} + M^+_{(sol)} + O^-_{2\,(sol)} \tag{2.44}$$

$$MO_{2\,(sol)} + M^+_{(sol)} + O^-_{2\,(sol)} \rightarrow 2MO_{2\,(sol)} \tag{2.45}$$

$$2MO_{2\,(sol)} \rightarrow \{MO_2\}_{2\,(sol)}(global\ minimum) \tag{2.46}$$

$$\{MO_2\}_{2\,(sol)}(global\ minimum) \rightarrow \{MO_2\}^{\ddagger}{}_{2\,(sol)}(transition\ state) \tag{2.47}$$

$$\{MO_2\}^{\ddagger}{}_{2\,(sol)}(transition\ state) \rightarrow \{MO_2\}_{2\,(sol)}(high\ energy) \tag{2.48}$$

$$\{MO_2\}_{2\,(sol)}(high\ energy) \rightarrow M_2O_{2\,(sol)} + O_{2\,(sol)} \tag{2.49}$$

$$M_2O_{2\,(sol)} + O_{2\,(sol)} \rightarrow M_2O_{2\,(s)} + O_{2\,(sol)} \tag{2.50}$$

$$M_2O_{2\,(s)} + O_{2\,(sol)} \rightarrow M_2O_{2\,(s)} + O_{2\,(g)} \tag{2.51}$$

Where $\{MO_2\}_{2\,(sol)}(global\ minimum)$ is the stable superoxide dimer in solution found through RASS method. $\{MO_2\}_{2\,(sol)}(high\ energy)$ is the stable high energy complex dimer formed before disproportionation to $M_2O_{2\,(sol)}$. While Eq. (2.44-2.51) represents the main reaction pathways, additional side steps for the precipitation of the metal superoxide from Eq. (2.45) is considered as shown in Eq. (2.40).

$$MO_{2\,(sol)} \rightarrow MO_{2\,(s)} \tag{2.51}$$

The precipitation energy (P.E) for the above reaction (Eq. 2.51) is calculated as

$$P.E = \Delta G^{f}_{(s)}(M_xO_2) - \Delta G^{f}_{(sol)}(M_xO_2) \tag{2.53}$$

$$\Delta G^{f}_{(sol)}(M_xO_2) = \Delta G^{f}_{(g)}(M_xO_2) + \Delta G^{0}_{(solv)}(M_xO_2) \tag{2.54}$$

Where $\Delta G^{f}_{(sol)}(M_xO_2)$ is the computed heat of formation of either superoxide (x=1) or peroxide (x=2) in solvent, $\Delta G^{f}_{(s)}(M_xO_2)$ is the experimental heat of formation of solid superoxide or peroxide obtained from NIST-JANAF, $\Delta G^{f}_{(g)}(M_xO_2)$ is the computed heat of formation of either superoxide or peroxide in gas phase.

The solubility of MO_2 and M_2O_2 is calculated by the method established by Cheng et al. [66] [67] [59] where the solubility ($S_{species}$) is calculated as a function of the dissolution free energy ($\Delta G^{*}_{(diss)}(species)$) which is in turn a function of the free energy of solvation of the species ($\Delta G^{*}_{(solv)}(species)$) and the free energy of sublimation of the crystal of the respective species to gas phase ($\Delta G^{*}_{(sub)}(species)$) as shown in Eq. (2.56)

$$\Delta G^{*}_{(diss)}(species) = \Delta G^{*}_{(sub)}(species) + \Delta G^{*}_{(solv)}(species) = -RTln(S_{species}V_{species}) \tag{2.56}$$

Where $V_{species}$ is the molar volume (L/mol) of the respective M_xO_2 species. The standard sublimation free energy $\Delta G^0_{(sub)}$ must be corrected for isothermal expansion of an ideal gas[59]

$$\Delta G^*_{(sub)}(species) = \Delta G^0_{(sub)}(species) - RTln\left(\frac{V_{species}P_0}{RT}\right) \quad (2.57)$$

Where P_0 is the standard condition pressure. The $\Delta G^0_{(sub)}(species)$ of bulk is the summation of $\Delta H^0_{(sub)}(species)$ and $\Delta S^0_{(sub)}(species)$. The $\Delta H^0_{(sub)}(species)$ can be calculated according to

$$\Delta H^0_{(sub)}(species) = -(U_{latt} + 2RT) \quad (2.58)$$

Where U_{latt} is the lattice energy calculated from crystal structure defined as

$$U_{latt} = \frac{E_{crystal}(species) - nE_{mol}(species)}{n} \quad (2.59)$$

With $E_{crystal}(species)$ and $E_{mol}(species)$ are the total energy of the respective M_xO_2 crystal that consists of n basic molecular units in a crystal cell, and $E_{mol}(species)$ being the corresponding total energy of a basic molecular unit from a DFT calculation. The 2RT term arises by including lattice vibrational energy and energy of the vapor.[67] The $\Delta S^0_{(sub)}(species)$ is approximated by the difference between the rotation and translation contributions to the entropy of the gas phase at 298 K and the intermolecular vibrational contribution to the entropy of the crystal at 298 K.

2.2.3.2. Solvation energy using cluster-continuum thermodynamic cycle and formation of doped products

In chapter 5 we investigate the doping of Li_2O_2 with different dopant atoms *D* and the resultant bulk solid formed can be described with the thermodynamics described below.

The doping process considered in chapter 5 involved replacing a Li atom in *c*-Li_2O_2 (without or with a Li vacancy) with a dopant atom while charge neutrality was maintained, without

introducing or removing any oxygen atom. This is because we are considering doping by positively charged metal cations. Effect of oxygen vacancies and negatively charged solvated anions will be investigated in future studies. The difference in the free energy of formation between such a doped solid and the corresponding undoped Li_2O_2 was calculated as:

$$\Delta\Delta G_f = \Delta G_f' - \Delta G_f = (E' - E) - (G_D - G_{Li}) = (E^{'} - E) - \left((G_{D^{m+}} - mG_{e^-}) - (G_{Li^+} - G_{e^-})\right)$$

$$= (E^{'} - E) - (G_{D^{m+}} - G_{Li^+}) + (m-1)eU \quad (2.60)$$

where E is total energy and G is free energy, $'$ or no $'$ indicates a doped or corresponding undoped structure, D refers to the dopant, and m is the number of electrons needed to fully reduce the dopant cation. m = 1 for Na and 2 for Mg and Ba. m is set to 2 for Co and Ni as well because +2 is the most common oxidation state for these metal ions. The (m−1) excess electrons introduced by the dopant vs. Li thus make $\Delta\Delta G_f$ of the process dependent on the electrode potential U if $m \neq 1$. We first calculate the $\Delta\Delta G_f$ when the cell is short circuit i.e. U = 0 V and the shift the $\Delta\Delta G_f$ by the potential of $U=U^{eqm}$= 2.96 V i.e. the equilibrium potential for the overall Li-O_2 cell whenever an additional electron appears in Eq. (2.60) i.e. when m=2.

The free energy of a cation ($G_{D^{m+}}$, including G_{Li^+}) is given as the sum of the total energy of the cation in gas phase ($E_{D^{m+}}$) and the respective single ion solvation energy in a particular solvent (DMSO as an example in this study):

$$G_{D^{m+}} = E_{D^{m+}} + \Delta G^*_{solv}(D^{m+}) + G^{0\rightarrow *} \quad (2.61)$$

where $G^{0\rightarrow *}$ represents the conversion of an ideal gas at standard state of 1 atm to an ideal solution standard state of 1 M. The single ion solvation energy was calculated using the thermodynamic cycle using the cluster cycle variant established earlier [58, 61, 65] and shown in Scheme 1.

Scheme 1:

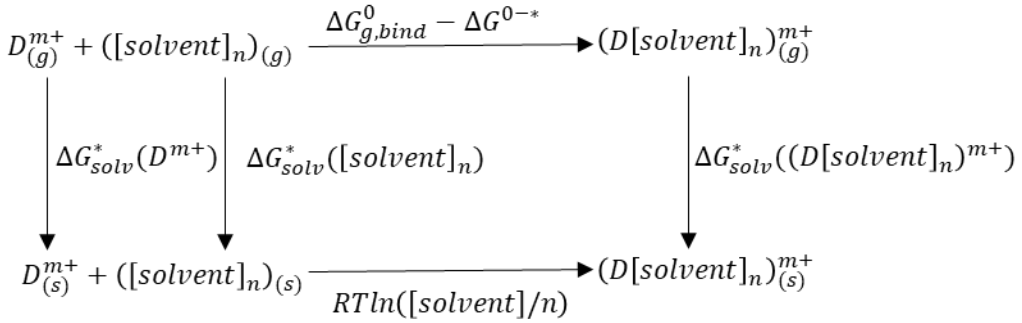

Thus $\Delta G^*_{solv}(D^{m+})$ was calculated as

$$\Delta G^*_{solv}(D^{m+}) = \Delta G^0_{g,bind} - \Delta G^{0-*} + \Delta G^*_{solv}((D[solvent]_n)^{m+} - RTln\left(\frac{[solvent]}{n}\right) - \Delta G^*_{solv}([solvent]_n) \quad (2.62)$$

Here $\Delta G^0_{g,bind}$ is the gas phase complexation free energy of the ion D^{m+} and n solvents (DMSO in this case); n is the number of solvent molecules present the first solvation shell of D^{m+}; $RTln\left(\frac{[solvent]}{n}\right)$ represents the free energy change of 1 mol of $(solvent)_n$ gas from [solvent]/n M liquid state to 1 M. Both $G^{0\rightarrow*}$ and $RTln\left(\frac{[solvent]}{n}\right)$ are standard state corrections terms that must be applied to bring each reactant and product in the thermodynamic cycle to the same standard state (1 M).[59] Electronic structure calculation for the metal ion and solvent cluster structures necessary for the thermodynamic cycle shown in scheme 1 were carried out using Gaussian09 package. Configurational sampling of solute-solvent and pure solvent clusters was performed using born oppenheimer molecular dynamics (BOMD) as implemented with the Gaussian09 package.[51] Full geometry optimization in gas phase and implicit solution phase of the different solute-solvent and pure solvent cluster configuration was done using B3LYP/6-31G(d,p) followed by single point energy using M06-L/6-311++G(d,p) level.[52, 68-70] Vibrational frequencies were computed analytically at the B3LYP/6-31G(d,p) level. To correct for the well-known breakdown

of the harmonic approximation for the free energies of low-frequency vibrational modes,[71-72] vibrational frequencies below 50 cm^{-1} were raised to 50 cm^{-1}.

Absolute single-ion solvation free energies in Eq. 2.62 were calculated using the thermodynamic cycle (cluster cycle) shown in Scheme 1.[58, 61] Solute-solvent interactions in the first solvation shell were computed explicitly while solvent effects beyond the first solvation shell were approximated using a dielectric, Poisson-Boltzmann continuum model (PCM model). Previous studies indicated that due to a favorable compensation of errors the cluster cycle with (solvent)n cluster as a reagent provides more accurate solvation free energies than the monomer cycle with n distinct solvent molecules as reagents.[61] From Scheme 1, $\Delta G^{*}_{solv}(D^{m+})$ can be expressed as the algebraic sum of the gas-phase complexation free energy ($\Delta G^{0}_{g,bind}$), the difference in the solvation free energy for $(D[solvent]_n)^{m+}$ and $[solvent]_n$ clusters calculated using a dielectric continuum model, and the standard state/concentration correction terms[59, 61]

ΔG^{0-*} represents the conversion of an ideal gas at standard state of 1 atm (24.46 L mol^{-1}) to an ideal solution standard state of 1 M (1 mol L^{-1}):[59]

$$\Delta G^{0-*} = RT * \ln(24.46) = 1.89 \frac{kcal}{mol} = 0.082\ eV \qquad (2.63)$$

According to Eq. 2.48, the accuracy of single-ion solvation free energies depends on (i) the accuracy of DFT methods for predicting complexation free energies in the gas phase, (ii) the accuracy of dielectric continuum models for predicting solvation free energies of solvent molecules and (iii) adequate sampling of solvent and solute-solvent clusters. We utilize the experimental coordination numbers for the different cations instead of doing a convergence of results with cluster size n. The Li^{+} ion tetrahedrally coordinated in bulk solution with DMSO while Na^{+} coordinates with 5 DMSO molecules.[65, 73] Co^{+2}, Mg^{+2} and Ni^{+2} all tend to coordinate

with 6 DMSO molecules within the first solvation shell.[74-76] It was earlier shown that M06-L density functionals give the best performance against the experimental data for Li^+ and Na^+ cation in DMSO.[65] We utilize the same procedure and extend it to Co^{2+}, Mg^{+2}, Ni^{+2}. Since Ba^{+2} is located well down the periodic table relative to the other ions considered, the level of applicable theory and basis set are different from that of the other ions. Instead we utilize the gibbs free energy of transfer of Ba^{+2} ion from water to DMSO given by Marcus *et. al.*[63-64] These data are based on the reference electrolyte assumption that the solvation free energy of the tetraphenylarsonium tetraphenylborate (TATB) salt is split evenly between its cation and anion. The value for transfer of Ba^{+2} from water to DMSO recommended by Marcus[63] is −0.275 eV and the experimental free energy of solvation Ba^{+2} ion in water is -13.51 eV.[77] The density of DMSO is 1100 g/L and molecular weight of 78.13 g/mol. Thus, the concentration of pure DMSO is taken as 14.08 M. The coordination geometries for Li^+, Na^+, Co^{+2}, Mg^{+2} and Ni^{+2} with DMSO molecules are shown in Fig. S11. The corresponding gas phase complexation energy $\Delta G^0_{g,bind}$ and the ion solvation energy $\Delta G^*_{solv}(D^{m+})$ is shown in table a1.

2.3. General Methodology and Calculation Parameters

The stochastic algorithm RASS and R-Kick [12] used for determining the global minimum structures of the metal superoxide and peroxide dimer and trimer are given in appendix A. The description of the evolutionary algorithm USPEX and the configurations of different doped structures obtained from the algorithm are given in appendix B.

In chapter 3 and 5 the periodic DFT calculations were performed within the generalized gradient approximation (GGA-RPBE[78]) and hybrid exchange correlation functional HSE06[79-80] as implemented in the Vienna Ab initio Simulation Package (VASP).[42, 81] The incorporation of exact exchange in HSE06 serves to compensate for self-interaction errors in DFT and gives a better

description of semi-local effects, particularly in terms of electronic structure. In chapter 3 the Kohn-Sham valence states [Li(1s2s2p), Na(3s4p), K(3s3p4s), Au(5d6s), O(2s2p), C(2s2p), H(1s), S(3s3p)] were expanded in a plane-wave basis with a cutoff energy of 700 eV in keeping with our previous work on metal-ORR,[4,82] which allows surface adsorption and electronic properties to be sufficiently converged and in chapter 5 the Kohn-Sham valence states [Li(1s2s2p), O(2s2p), Mg(3s4p), Na(3s4p), Ni(3d4s), Co(3d4s), Ba(5s5p6s)] were expanded in a plane wave basis with a cutoff energy of 520 eV. The core electrons were described using the projected-augmented wave (PAW) method.[83] In chapter 3 a first-order Methfessel-Paxton scheme was used to smear the electronic states with a width of 0.1 eV and chapter 5 a tetrahedron method with Blöchl corrections was used to sample the electronic states with a width of 0.05 eV. All total energies were extrapolated to 0 K. The RPBE-optimized lattice constant of Au is 4.198 Å, which agrees closely with experiment (4.08 Å).[84] The Au(111) surface was modeled either by a four-layer thick Au(111) slab with a $2\sqrt{3}\times2\sqrt{3}$ surface unit cell (in the *xy* plane) and ~19 Å of vacuum between adjacent periodic slabs in the *z* direction (for MO_2), or a $4\sqrt{3}\times4\sqrt{3}$ surface unit cell with ~27 Å of vacuum between adjacent slabs (for O_2^-). Au(211) was modeled by a Au(211) slab that has a four atom wide step edge and a three atomic row deep terrace, for a total of 9 atomic rows of Au, with ~21 Å of vacuum space. The reciprocal space of the Au(211) and the $2\sqrt{3}\times2\sqrt{3}$ Au(111) slabs was sampled on a 7×7×1 Monkhorst-Pack k point grid; that of the $4\sqrt{3}\times4\sqrt{3}$ Au(111) slab was sampled on a 3×3×1 Monkhorst-Pack k point grid. During geometry optimization, the top two Au layers in Au(111), the top four rows of Au in Au(211), and all adsorbate and solvent molecules deposited thereon were fully relaxed until the maximum force in each relaxed degree of freedom fell below 0.03 eV/Å. The lattice constants of Li_2O_2 (*c*-Li_2O_2) in the *P6₃/mmc* Föppl structure were *a*=3.21 Å and *c*=7.81 Å (RPBE) and *a*=3.12 Å and *c*=7.61 Å (HSE06). These values agree well with the

lattice parameters reported by Föppl[85] (a=3.14 Å and c=7.65 Å) and later by Cota et al.[14] (a=3.15 Å and c=7.71 Å).

The structures that we modeled in chapter 5 included (A) 16 O and 16 Li ($Li_{16}O_{16}$); (B) 16 O, 15 Li, and one dopant atom ($Li_{15}DO_{16}$); and (C) 16 O, 14 Li, and one dopant atom ($Li_{14}DO_{16}$), which were globally optimized using VASP coupled to USPEX, as well as directly (locally) optimized using VASP only for comparison. (A) corresponds to a supercell of 4 unit cells of *c*-Li_2O_2, each unit cell containing 2 units of Li_2O_2 (i.e., $Li_{16}O_{16}$). (B) corresponds to the preceding $Li_{16}O_{16}$ with one Li replaced with a dopant atom, which is at an atomic concentration of 1/16 of the Li in Li_2O_2. (C) corresponds to $Li_{16}O_{16}$ with one Li removed (a Li vacancy, denoted V_{Li}) and one Li replaced with a dopant atom.

The PES for a given composition was probed for minimum energy structures using VASP in combination with USPEX,[21, 86] a global optimization code based on evolutionary algorithms. For each composition, a maximum of 20 generations, each with a population of 20 structures, were generated, optimized, and assessed.

The first generation of structures was generated randomly. If a seed structure was specified, then it was included in the first generation. In each subsequent generation, the candidate structures were generated through a combination of default operators: 50 % of the candidate structure were generated through heredity from the previous generation, 20 % were randomly generated, 10% were generated by applying the lattice mutation and permutation operators on the most stable structure from the previous generation, and 20 % by applying the soft mutation operator that connects the global optimization to lattice dynamics.[22, 87] The candidate structures were then subject to 5 levels of optimization using VASP at the GGA-RPBE level. Structures that did not converge within specified VASP parameters at any level of optimization were rejected.

The reciprocal space resolution for k-points generation was varied as 0.13, 0.11, 0.1, 0.08, and 0.06 (in units of 2π $Å^{-1}$), with 0.13 being the lowest grid density for the first level of optimization. For the first level of optimization, the convergence criteria for force and total energy were set to 0.2 eV/Å and 0.03 eV, respectively. The ionic positions and the shape and volume of the unit cell were all allowed to change while the volume of the unit cell was fixed. In the second level of optimization, the convergence criteria for force and total energy were reduced to 0.01 eV/Å and 0.001 eV. Like the first level of optimization, the ionic positions and the shape of the unit cell were both allowed to change while the volume of the cell was fixed. For the third level of optimization, the convergence criteria for force and total energy were reduced to 0.02 eV/Å and 0.001 eV. For the third, fourth and fifth levels, the ionic positions and shape and volume of the unit cell were all allowed to change. For the fourth and fifth levels of optimization, the convergence criteria for total energy was further reduced to 0.0003 and 0.0001 eV, respectively.

This process was continued until the most stable configuration remained unchanged (based on total energy, with a threshold of 0.0001 eV) for 8 generations, at which point the global optimization was considered done. Such a structure was designated as the global minimum energy structure for a given composition. In a case where no structure remained unchanged for 8 generations after a total of 20 generations, then the structure with the lowest total energy amongst the entire generated pool of structures generated in all 20 generations was designated as the global minimum energy structure. 3 sets of USPEX calculations were done for each composition, one without any seed structure, one biased with a directly substitutionally doped (DSD) structure that was energy-minimized using VASP as a seed and anti-seed calculations (explained below). While probing the PES, USPEX sometimes repeatedly generates structures (with default USPEX parameters mentioned above) near a local minimum that are very close to each other in geometrical

structure and energy. This phenomenon is known as “trapping”. To make sure that USPEX was not trapped in such a manner, a separate calculation was carried out where the anti-seed technique was enabled. In this method, local minimum structures found in earlier USPEX calculations were provided for the anti-seed calculations. Thus, in the anti-seed calculations, these local minima structures were penalized such that USPEX consciously avoids generating structure in the vicinity (geometrically) of the local minimum structures provided. Energy minimization of DSD structures was done using the same set of parameters. The projected density of states (DOS) for GGA-RPBE optimized structures was calculated with a 15×15×15 Monkhorst-Pack k-point grid.

The globally optimized structure thus identified by USPEX (and optimized at the GGA-RPBE level) for a given composition was then re-optimized using the HSE06 functional (the DSD structures were not re-optimized). The reciprocal space integration was performed on a 2×2×2 Monkhorst-Pack k-point grid. Both the ionic positions and the unit cell were fully relaxed until the maximum force in each relaxed degree of freedom fell below -0.03 eV/Å. The projected DOS was calculated on the same k-point grid. The total DOS of different defective or doped Li_2O_2 structures was compared by having the top of their oxygen σ_p* bands aligned.

Chapter 3. Estimation of Electric Field Effects on the Adsorption of Molecular Superoxide Species on Au based on Density Functional Theory[1]

3.1. Introduction

Aprotic metal-air ($M-O_2$) batteries are highly promising candidates for next generation electrochemical energy storage technologies because of their significantly higher theoretic energy densities than Li-ion batteries,[88] but the development of a practical and reversible $M-O_2$ battery is hindered by many obstacles, including poor reversibility of the air cathode.[2, 88-93] Developing a more reversible air cathode requires a precise knowledge of the molecular level processes that occur during the cycling of $M-O_2$ batteries. However, at present many fundamental aspects of $M-O_2$ cell chemistries, and in some cases, the very identities of the discharge products, remain debated.

Theoretical efforts to model basic $M-O_2$ cell chemistries have generally focused on evaluating potential-dependent electrode reaction energetics.[7, 13, 94-95] Here an applied potential on proton/electron transfer reactions is commonly accounted for using the thermodynamic computational electrode approach popularized by Nørskov and coworkers.[96] A subtle but potentially important effect on the stability of reaction intermediates that are adsorbed on the electrode may be introduced by the presence of an electric field, which is created by the formation of the electric double layer at the electrode | electrolyte interface. Since the magnitude of such a field effect depends on the specific electrochemical species under consideration, and can range from negligible in some cases[48, 97] to substantial in others, even with both types of species present

[1]This chapter is adapted from Rawal, Saurin H., William C. McKee, and Ye Xu. "Estimation of electric field effects on the adsorption of molecular superoxide species on Au based on density functional theory." Physical Chemistry Chemical Physics 19.48 (2017): 32626-32635 with permission from the PCCP Owner Societies

in the same reaction system,[49, 98] it is not clear *a priori* whether neglecting field effects in the context of M-O_2 cell reaction modeling is an acceptable approximation.

The discharge of a M-O_2 battery relies critically on the efficiency of the oxygen reduction reaction (ORR) at the positive electrode. Our previous studies of the Li-ORR[4] and Na-ORR[82] in model cells consisting of polycrystalline Au electrodes and DMSO-based electrolytes have suggested the molecular superoxide anion (O_2^-) and metal-superoxide (i.e., LiO_2 and NaO_2) species to be key intermediates that control the onset of the overall ORR and *on-surface* formation of the bulk discharge products (i.e. Li_2O_2 and NaO_2), respectively. The mechanistic significance of these species has also been suggested by other researchers in both experimental and theoretical studies.[95, 99-101] Herein we systematically investigate how the stability of molecular MO_2 (M = Li, Na, K) and O_2^- species on Au vary as a function of an applied interfacial electric field, in order to gauge the importance of including electric field effects in the theoretical modeling of M-O_2 electrode chemistries. Analogous results for O and OH are presented for comparison. We find that in an electric field (ε) range of ±0.4 V/Å, the stability of molecular MO_2 species can vary by up to |0.4| eV on the close-packed Au(111) surface and by up to |0.2| eV on the stepped Au(211) surface, *in vacuo*. The field effect is amplified in the presence of explicit DMSO molecules, an aprotic solvent widely used in metal-air battery research, in all cases except KO_2 on Au(111). The variations in the stability of the MO_2 species is traced primarily to the product of the static surface dipole moment induced by adsorption at zero field (μ_0) and the interfacial electric field (ε), $\mu_0 \cdot \varepsilon$, which provides an easy way to estimate the field-induced changes in stability. Molecular O_2^-, which has been previously identified on a Au corner site,[82] has on the other hand a much larger polarizability

(α) than the MO_2 species and a μ_0 that is opposite in sign to those of the metal MO_2 species, although the field-induced variation in stability mainly occurs under negative fields.

3.2. Results and Discussion

3.2.1. MO_2 Adsorption at Au | Vacuum

The structure of adsorbed molecular MO_2 (M = Li, Na, K) on Au(111) and Au(211) *in vacuo* at ε = 0 V/Å are presented in Figure 1. In contrast to O_2,[102] all three MO_2 species adsorb exothermically (i.e., are stabilized) on Au(111). For LiO_2, NaO_2, and KO_2, ΔE_{ads} is −0.26, −0.68, and −0.57 eV, respectively. On Au(211), which features under-coordinated Au atoms at the step edge, ΔE_{ads} is lowered to −0.98, −1.26, and −1.16 eV for LiO_2, NaO_2, and KO_2 respectively, i.e., ca. 0.6 eV more stable than on Au(111).

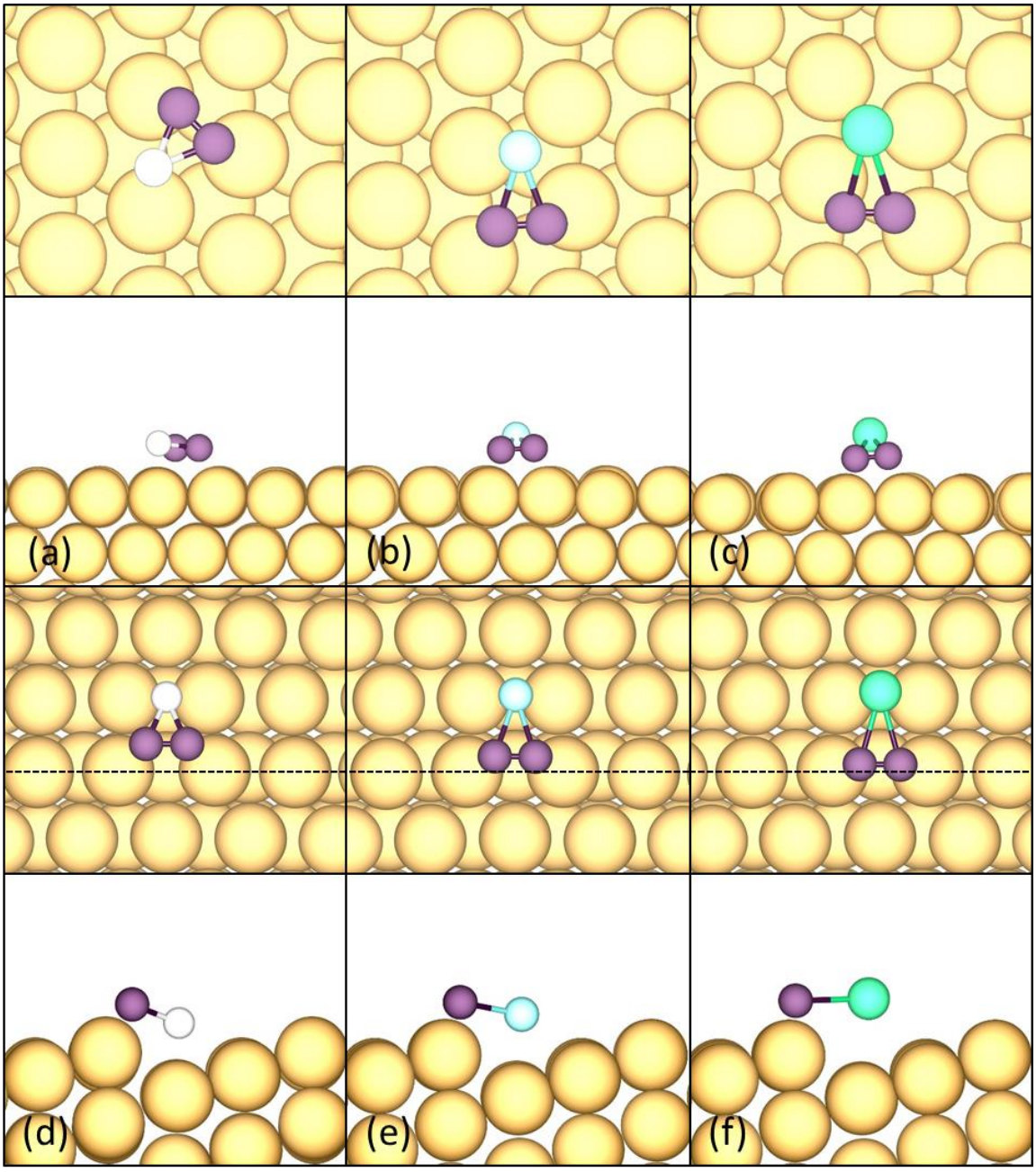

Figure 3.1: Top (top panels) and side (bottom panels) views of minimum total energy geometries for molecular (a) LiO_2, (b) NaO_2, and (c) KO_2 adsorbed on Au(111), and molecular (d) LiO_2, (e) NaO_2, and (f) KO_2 adsorbed on Au(211) *in vacuo* at $\varepsilon = 0$ V/Å. Color code: Au = yellow, Li = white, Na = cyan, K = light green, and O_2 = purple. Length of O-O bond (in Å) in each panel: (a) 1.447, (b) 1.419, (c) 1.412, (d) 1.450, (e) 1.433, (f) 1.433.

Since the electrolyte is conducting, most of the potential drop across the electrolyte occurs within the electric double layer close to the electrode. However, the nature and dimension of the electric double layer in the aprotic Li-, Na-, and K-ORR systems are poorly understood. We estimate the relevant range of the electric field strength at the electrode surface in the following two ways. First, we take the screening of the surface charge to occur largely within the outer Helmholtz plane (OHP) of the electric double layer. Consistent with the Gouy-Chapman-Stern model, the distance between the Au surface to the OHP can be approximated as the sum of the adsorbate adlayer thickness, the effective anion radius, and the diameter of a DMSO molecule.[103-104] The thickness of the MO_2 adlayer is taken to be the average distance of the O_2 moiety from the metal surface, which is ca. 2.0 Å (based on the optimized configurations for all cases *in vacuo* and with explicit DMSO molecules over both Au(111) and Au(211)) and the vdW radius of O which is ca. 1.5 Å. Thus the adlayer thickness is ca. 3.5 Å. Furthermore the ionic radius of an anion commonly used in Li-Air cells like ClO_4^- is ca. 2.4 Å,[105] and the calculated hard sphere diameter of a DMSO molecule is 5.0 Å.[106] Thus the distance to the OHP is ca. 10.9 Å. The estimated maximum potential drop for the respective systems is 2.96 V for Li-ORR (based on solid Li_2O_2), 2.27 V for Na-ORR (based on solid NaO_2), and 2.48 V for K-ORR (based on solid KO_2). The maximum electric field inclusive of all three systems is therefore 2.96 V / 10.9 Å = 0.27 eV/Å. Alternatively, we may assume an exponential decay in the electric potential between the electrode and the OHP, in which case the electric field at the electrode surface is approximately equal to:

$$\varepsilon = \left.\frac{d\phi}{dx}\right|_{x=0} = \left.\frac{d}{dx}\right|_{x=0} \phi_s e^{-\frac{x}{\lambda_D}} = \frac{\phi_s}{\lambda_D} \tag{3.1}$$

where λ_D is the Debye length ($\lambda_D = \left(\frac{2c_0 z^2 q^2}{\varepsilon \varepsilon_0 k_B T} \right)^{-\frac{1}{2}}$). With equal anion/cation concentrations (c_0) of 0.1 M, a charge (z) of ±1, and a relative permittivity (ε) of 46.7 for DMSO, λ_D is calculated to be 2.96 V / 7.42 Å = 0.40 V/Å at room temperature. We take the larger of the two field values (|0.40| V/Å) and explore the effects of electric field in the ±0.40 V/Å range on the stability of the molecular MO_2 species. The main drawback of the current applied electric field approach is that the field strength cannot be directly related to the electrode potential. Therefore, we cannot determine, e.g., at what potential vs. Li/Li^+ ε = 0 V/Å occurs, but it is reasonable to expect the field strength at electrode surfaces to fall somewhere within ±0.40 V/Å at typical discharge potentials.

The variations in ΔG_{ads} for LiO_2, NaO_2, and KO_2 adsorbed on Au(111) *in vacuo* over ±0.4 V/Å are presented in Figure 2a, and those on Au(211) in Figure 3.2b. On Au(111), the total variation in stability over ±0.4 V/Å is 0.14 eV for LiO_2, 0.40 eV for NaO_2, and 0.67 eV for KO_2. The total variation in stability for LiO_2 is essentially the same as for O and OH on Au (see below) and on Pt(111)[48] but it becomes pronounced as the size of the alkali atom increases from Li to K. The electric field effects on the stability of MO_2 species on Au(211) are less pronounced than on Au(111). On Au(211), the total variation in stability due to the electric field is reduced for all three species: 0.11 eV for LiO_2, 0.09 eV for NaO_2, and 0.34 eV for KO_2 over ±0.4 V/Å.

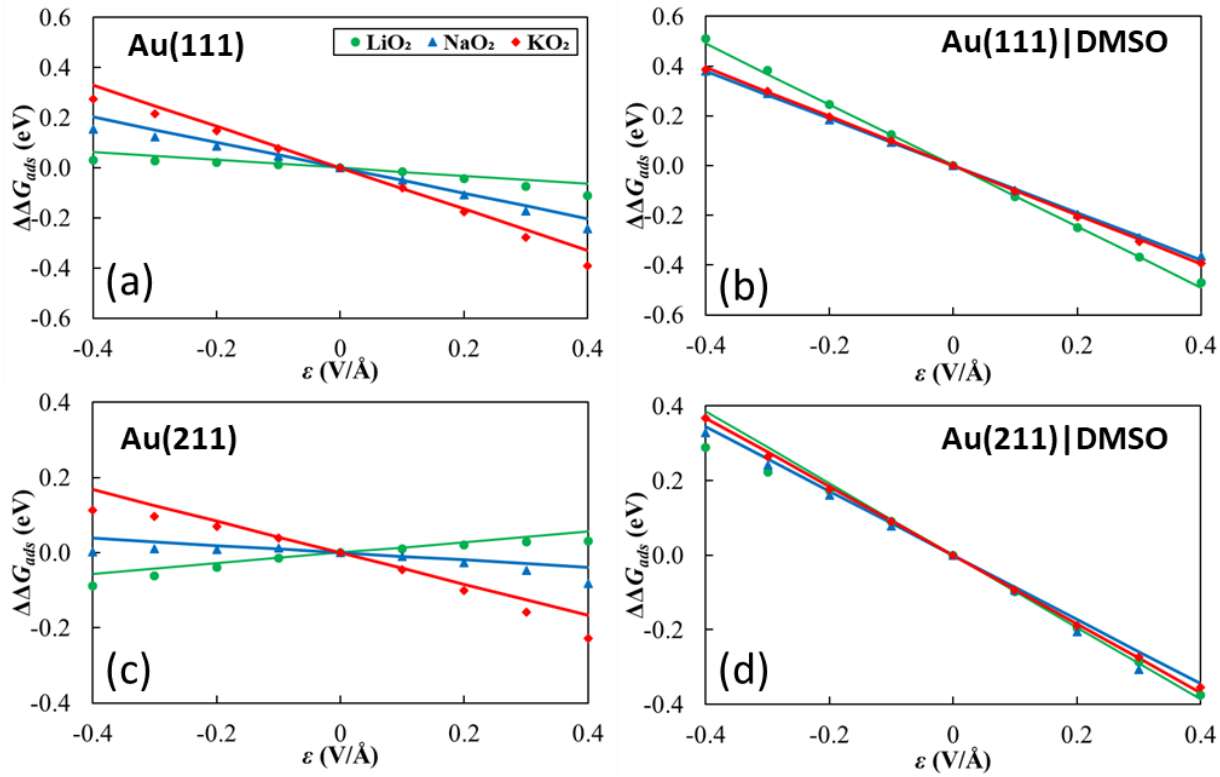

Figure 3.2: Electric field induced variations in stability ($\Delta\Delta G_{ads}$, relative to ε = 0 V/Å) for molecular MO_2 (M = Li, Na, K) species adsorbed at: (a) Au(111) | vacuum; (b) Au(111) | DMSO; (c) Au(211) | vacuum; (d) Au(211) | DMSO. The solid straight lines give the predicted changes in stability based on the first-order approximation ($\mu_0 \cdot \varepsilon$). The Au | DMSO results are based on minimum total energy configurations with each alkali atom coordinated to two sulfinyl oxygen atoms ($(S{=}O)_2$-M) except for LiO_2 on Au(111).

The results of fitting the calculated $\Delta\Delta G(\varepsilon)_{ads}$ to Eq. 2 are shown in Table 3.1. As can be seen, all of the adsorbed molecular MO_2 species exhibit small polarizabilities. A non-zero polarizability causes $\Delta\Delta G(\varepsilon)_{ads}$ to exhibit some curvature when plotted against ε, but over ±0.4 V/Å the maximum second-order contribution amounts to only 0.06 eV (for KO_2 on Au(111)) and are therefore negligible. Thus, a simple first-order approximation ($\mu_0 \cdot \varepsilon$) is useful and advantageous because it can be obtained rapidly and without the need to perform any DFT calculation with an applied field. The closeness of the first-order approximation can be seen in Figure 2 (plotted as solid straight lines; same below). The weaker field effects on the stability of

MO_2 on Au(211) than on Au(111) are reflected in the smaller absolute values of μ_0 and α as on Au(211).

Table 3.1: Fitting results of the variations in the stability ($\Delta\Delta G(\varepsilon)_{ads}$, in eV) as a function of electric field (ε, in V/Å) for MO_2 (M = Li, Na, K) and O_2^- species on various Au surface models, the corresponding static surface dipole moment at zero field (μ_0, in eÅ) calculated using the approach described in Methods, and the maximum absolute error between DFT-calculated and estimated (by $\mu_0 \cdot \varepsilon$) stability over ±0.4 V/Å.

Species/surface	Fitting results	μ_0	| max. error |
Au(111) | vacuum			
LiO_2	$\Delta\Delta G(\varepsilon)_{ads} = -0.2552 \cdot \varepsilon^2 - 0.1731 \cdot \varepsilon + 0.0003$	−0.16	0.05
NaO_2	$\Delta\Delta G(\varepsilon)_{ads} = -0.2869 \cdot \varepsilon^2 - 0.4934 \cdot \varepsilon + 0.0003$	−0.51	0.05
KO_2	$\Delta\Delta G(\varepsilon)_{ads} = -0.3700 \cdot \varepsilon^2 - 0.8248 \cdot \varepsilon + 0.0010$	−0.83	0.06
Au(211) | vacuum			
LiO_2	$\Delta\Delta G(\varepsilon)_{ads} = -0.1784 \cdot \varepsilon^2 + 0.1491 \cdot \varepsilon + 0.0010$	+0.14	0.03
NaO_2	$\Delta\Delta G(\varepsilon)_{ads} = -0.2552 \cdot \varepsilon^2 - 0.1008 \cdot \varepsilon + 0.0019$	–0.10	0.04
KO_2	$\Delta\Delta G(\varepsilon)_{ads} = -0.3586 \cdot \varepsilon^2 - 0.4265 \cdot \varepsilon + 0.0000$	–0.42	0.06
Au(111) | DMSO†			
LiO_2	$\Delta\Delta G(\varepsilon)_{ads} = +0.1372 \cdot \varepsilon^2 - 1.2361 \cdot \varepsilon - 0.0036$	−1.22	0.02
NaO_2	$\Delta\Delta G(\varepsilon)_{ads} = +0.0818 \cdot \varepsilon^2 - 0.9422 \cdot \varepsilon - 0.0003$	−0.93	0.02
KO_2	$\Delta\Delta G(\varepsilon)_{ads} = -0.0051 \cdot \varepsilon^2 - 0.9885 \cdot \varepsilon - 0.0025$	−0.99	0.01
Au(211) | DMSO†			
LiO_2	$\Delta\Delta G(\varepsilon)_{ads} = -0.2732 \cdot \varepsilon^2 - 0.8519 \cdot \varepsilon - 0.0013$	–0.97	0.10
NaO_2	$\Delta\Delta G(\varepsilon)_{ads} = -0.2829 \cdot \varepsilon^2 - 0.9282 \cdot \varepsilon - 0.0058$	–0.86	0.08
KO_2	$\Delta\Delta G(\varepsilon)_{ads} = +0.0522 \cdot \varepsilon^2 - 0.9036 \cdot \varepsilon - 0.0046$	–0.92	0.01
Au_1/Au(111) | DMSO			
O_2^-	$\Delta\Delta G(\varepsilon)_{ads} = -1.9393 \cdot \varepsilon^2 + 0.8253 \cdot \varepsilon - 0.0058$	+1.05	–

† Based on minimum total energy configurations with each alkali atom coordinated to two sulfinyl oxygen atoms ($(S{=}O)_2$-M) except for LiO_2 on Au(111).

In addition to the impact of ε on the stability of the molecular MO_2 species on Au, there is also a noticeable influence on their geometries. In particular, the distance between the metal atom in MO_2 and the Au surface varies as a function of field strength. As summarized in Figure 3, positive ε values (which lead to positive charging of the surface) shift the cationic Li, Na, and K atoms away from the surface. Conversely, a negative electric field draws them closer to the surface. For example, at +0.4 V/Å the z coordinates of the Li, Na, and K atom increase by 0.23, 0.19, and 0.26 Å respectively relative to their ε = 0 V/Å values, while at −0.4 V/Å, the z coordinates decrease by 0.10, 0.18, and 0.15 Å respectively. Similar behavior is also evident for the MO_2 species adsorbed on Au(211) (Figure 3.3).

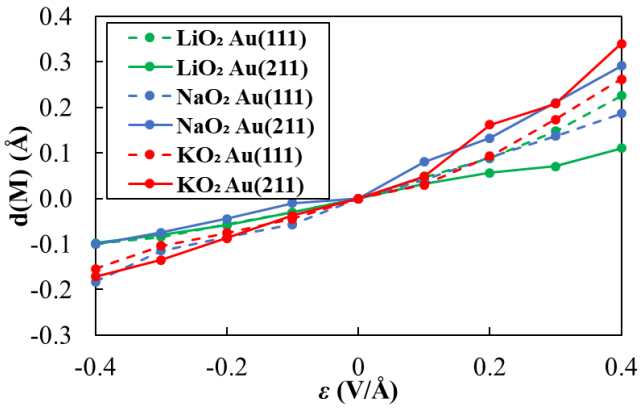

Figure 3.3: Relative variation (d(M), relative to ε = 0 V/Å) in the z coordinate of the alkali atom in molecular MO_2 species (M = Li, Na, K) adsorbed on Au(111) and Au(211) as a function of ε.

3.2.2. Au | DMSO

Next, we consider how the presence of explicit DMSO molecules modifies the electric field effect on MO_2 stability. In an STM study of DMSO adsorption on Au single crystal surfaces, Ikemiya et al.[107] observed that DMSO molecules formed ordered stripes on clean Au(111) under ambient conditions. We have approximated this interfacial structure with two DMSO molecules per $2\sqrt{3}\times2\sqrt{3}$ Au(111) surface unit cell forming a chain at a surface density of 1/6 ML.[108] The purpose

here is not to accurately model the observed structure in STM but to create a unit cell in which molecular superoxide species can be studied as adsorbed in the Au | DMSO interface. The DMSO solvent shell by itself has a total static dipole moment of −0.08 eÅ on the Au(111) surface unit cell and +0.14 eÅ on the Au(211) surface unit cell with ε = 0 V/Å and no adsorbate. The polarizable nature of a solvent is characterized by α, the polarizability. The polarizability of *individual* DMSO molecules can be estimated using the Clausius-Mossotti relation:[109]

$$\frac{\ni-1}{\ni+2}=\frac{N\alpha}{3\ni_0} \tag{3.2}$$

Here the dielectric constant of DMSO, ∋, is 47.24, the permittivity of free space, $\ni_0$, is 8.854×10^{-12} F/m, and the number density of DMSO, *N*, is 8.482×10^{27} molecules/m^3 at ambient conditions. Using these values we obtain α = 1.836 eÅ^2/V from Eq. 3.2. By fitting the $\Delta\Delta G(\varepsilon)_{ads}$ of the DMSO molecules on Au(211) (with no superoxide) to Eq. 2 we obtain $\Delta\Delta G(\varepsilon)_{ads} = -0.7738\cdot\varepsilon^2 + 0.1208\cdot\varepsilon + 0.0046$, for α = 1.548 eÅ^2/V. The same approach based on our Au(111) results yields a similar value of α = 1.624 eÅ^2/V. The results are shown in Figure 3.4.

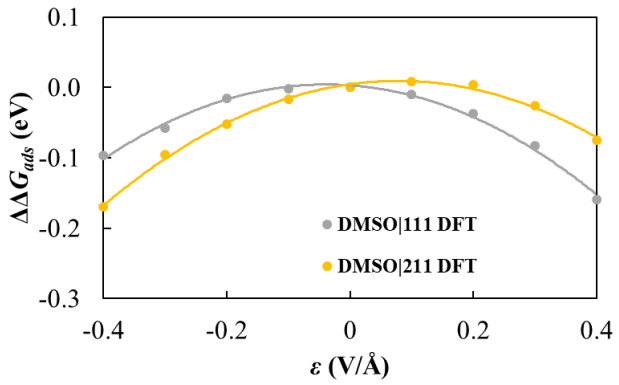

Figure 3.4: Electric field induced variations in stability ($\Delta\Delta G_{ads}$, relative to ε = 0 V/Å) for molecular DMSO adsorbed on Au(111) and Au(211). The solid lines are quadratic fits of the data.

While our current DMSO solvent model is simple and not dynamic, the close agreement with the value obtained using the Clausius-Mossotti relation suggests that the electrostatic properties of the DMSO solvent is captured by the RPBE functional. This is desirable because for each MO_2 species, there is a tendency for DMSO molecules to interact electrostatically with the alkaline atom via the sulfinyl oxygen atom (see below). As a result, the MO_2 species are more stable in the presence of DMSO molecules, even at zero field.

3.2.3. MO_2 Adsorption Au | DMSO under Positive Electric Fields

The minimum-free energy configurations under positive electric fields, which are more relevant to the discharge of metal-air batteries, for molecular LiO_2, NaO_2, and KO_2 adsorbed on Au(111) and Au(211) with a single shell of explicit DMSO molecules each involve the alkali atom being coordinated to two sulfinyl oxygen atoms (denoted $(S{=}O)_2$-M). The minimum total energy geometries for such $(S{=}O)_2$-M configurations at zero field are shown in Figure 3.5. This is consistent with the fact that under more positive electric fields, the alkali atoms are farther away from the Au surfaces (see Figure 3.3) and therefore interact more with the solvent than with the O_2 group. At zero field, ΔE_{ads} for LiO_2, NaO_2, and KO_2 shown in Figure 5 are −1.16, −1.33, and −1.11 eV at Au(111) | DMSO, and −1.64, −1.71, and −1.47 eV at Au(211) | DMSO, respectively. Overall the superoxide species are 0.3~0.8 eV more stable than the corresponding values *in vacuo*, at zero field.

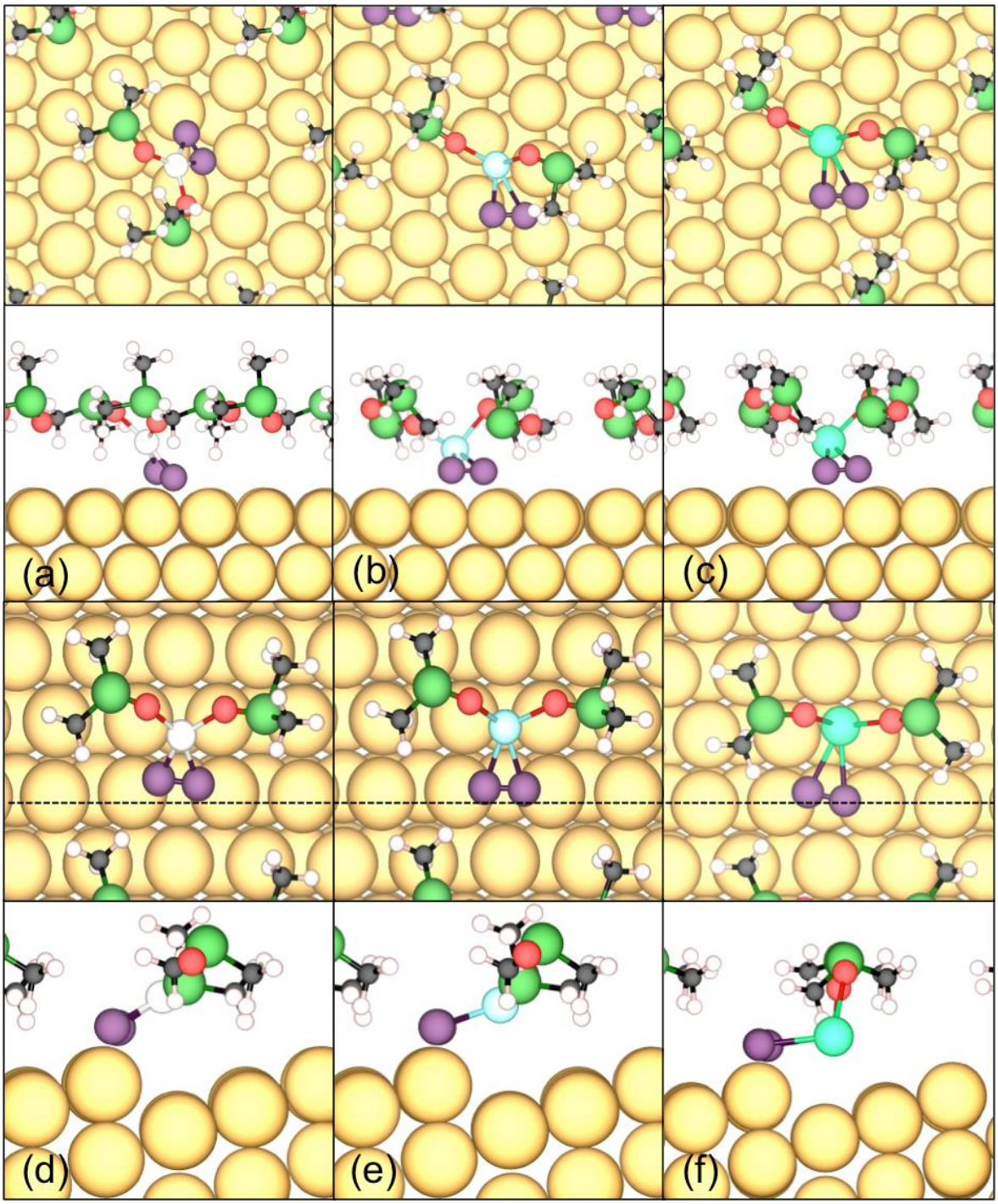

Figure 3.5: Top (top panels) and side (bottom panels) views of minimum total energy $(S{=}O)_2$-M configurations for molecular (a) LiO_2, (b) NaO_2, and KO_2 (c) adsorbed on Au(111), and molecular (d) LiO_2, (e) NaO_2, and (f) KO_2 adsorbed on Au(211), with explicit DMSO molecules at $\varepsilon = 0$ V/Å. Color code: Au = yellow, S = dark green, C = black, H = white (small), O = red, Li = white (large), Na = cyan, K = light green, and O_2 = purple. Length of O-O bond (in Å) in each panel: (a) 1.457, (b) 1.407, (c) 1.404, (d) 1.454, (e) 1.442, (f) 1.418.

The field-induced changes in the stability of molecular MO_2 species in the presence of DMSO on Au(111) and Au(211) are compared with the corresponding changes at the Au | vacuum interface over the ε range of 0 ~ +0.4 V/Å in Figure 3.2. The presence of DMSO amplifies the field effect on the stability (vs. zero field) of the MO_2 species on both Au surfaces, as can be seen from the larger μ_0 values in the presence of DMSO vs. those *in vacuo* (Table 3.1). For instance, at +0.4 V/Å on Au(111), the dipole-field interaction stabilizes LiO_2 by ca. −0.1 eV and NaO_2 by ca. −0.2 eV *in vacuo*, but stabilizes LiO_2 and NaO_2 by ca. −0.5 and −0.4 eV in the presence of DMSO. Overall, the inclusion of explicit solvent molecules appears to be necessary for accurately predicting the stability of molecular MO_2 species on Au, both in terms of chemical/electrostatic interactions at zero field and in terms of the additional field-dipole interaction. For both surfaces the product $\mu_0 \cdot \varepsilon$ continues to provide a good estimate of the predicted variations in stability due to an electric field in the range of 0 ~ +0.4 V/Å for all three MO_2 species based on field-included DFT calculations.

3.2.4. MO_2 Adsorption Au | DMSO over ±0.4 V/Å

It is instructive to compare the adsorption of molecular MO_2 species at Au | DMSO under negative fields even though they are less relevant to the cathode side of metal-air batteries during discharge. Contrary to positive electric fields, here the minimum-free energy configurations for MO_2 involve the alkali atoms coordinated to only one sulfinyl oxygen atom. For every species, the minimum total energy geometry with the alkali atom coordinated to one sulfinyl oxygen atom (denoted as (S=O)-M) and that of the minimum total energy geometry with the alkali atom coordinated to two sulfinyl oxygen atoms (denoted $(S=O)_2$-M) are nearly energetically identical at zero field. Below we use NaO_2 at Au(111) | DMSO and KO_2 at Au(211) | DMSO as examples (see Figure 3.6). For NaO_2 at Au(111) | DMSO, the (S=O)-M configuration has a μ_0 of −0.38 eÅ, whereas the $(S=O)_2$-

M configuration has a μ_0 of −0.93 eÅ. The difference in μ_0 causes the former to be increasingly preferred under increasingly negative fields, whereas the latter to be increasingly preferred under increasingly positive fields (Figure 3.6a). The same holds true for KO_2 at Au(211) | DMSO, for which the μ_0 for the (S=O)-M and $(S=O)_2$-M configurations are −0.47 and −0.92 eÅ, respectively (Figure 3.6b). If taken together, the minimum-free energy hull as a function of ε exhibits a more appreciable curvature (α) and a μ_0 that is intermediate between those of the (S=O)-M and $(S=O)_2$-M configurations.

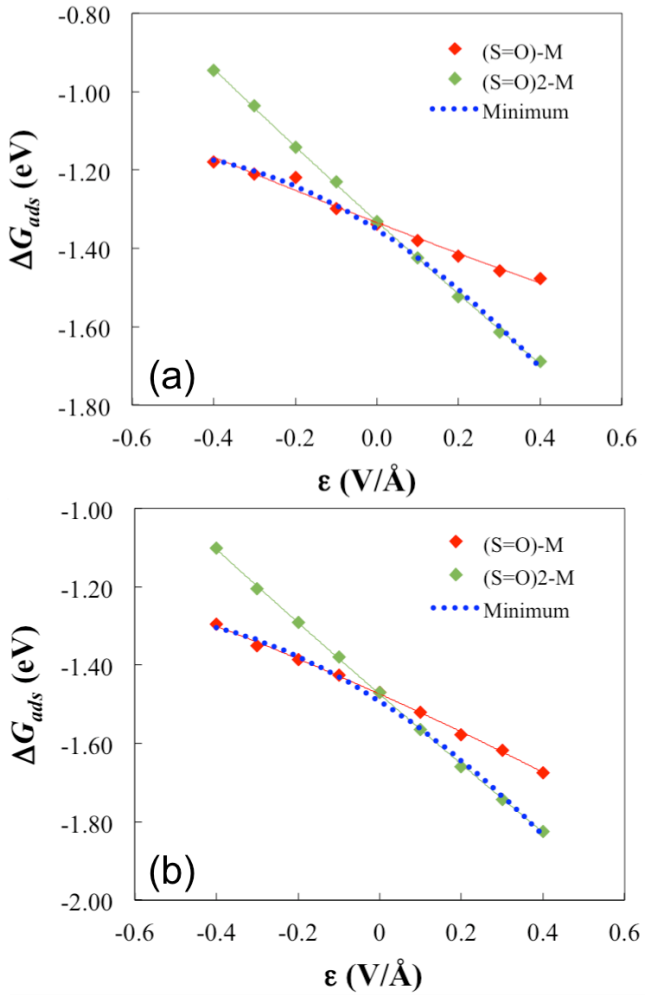

Figure 3.6: Minimum free energies for (a) NaO_2 at Au(111) | DMSO and (b) KO_2 at Au(211) |

fig. caption cont'd

DMSO when the alkali atom is coordinated to one ((S=O)-M) and two ((S=O)$_2$-M) sulfinyl oxygen atoms of DMSO. The solid lines are best fits according to Eq. 2. For NaO_2, the fitting of adsorption free energy ($\Delta G(\varepsilon)_{ads}$) as a function of electric field (ε) yields: $\Delta G(\varepsilon)_{ads} = +0.0385\cdot\varepsilon^2 - 0.4024\cdot\varepsilon - 1.334$ for (S=O)-M; $\Delta G(\varepsilon)_{ads} = +0.0818\cdot\varepsilon^2 - 0.9422\cdot\varepsilon - 1.3318$ for (S=O)$_2$-M; and $\Delta G(\varepsilon)_{ads} = -0.5498\cdot\varepsilon^2 - 0.6627\cdot\varepsilon - 1.3518$ for the overall minimum free energy. For KO_2, the results are: $\Delta G(\varepsilon)_{ads} = -0.0831\cdot\varepsilon^2 - 0.4664\cdot\varepsilon - 1.474$ for (S=O)-M; $\Delta G(\varepsilon)_{ads} = +0.0522\cdot\varepsilon^2 - 0.9036\cdot\varepsilon - 1.4744$ for (S=O)$_2$-M; and $\Delta G(\varepsilon)_{ads} = -0.478\cdot\varepsilon^2 - 0.663\cdot\varepsilon - 1.4921$ for the overall minimum free energy.

3.2.5. O_2^- Adsorption on Au Corner Site at Au | DMSO

Previously we identified an O_2 species adsorbed on a Au adatom at Au(111) | DMSO as a model for a Au corner site (Figure 7a), whose properties (including O-O bond length (1.300 Å) and vibrational frequency (1,175 cm^{-1}), and Bader charge (-0.39 *e*))[18] are in line with the superoxide anion state (O_2^-) identified by surface enhanced Raman spectroscopy (SERS) in electrochemical ORR experiments.[4, 82, 108, 110] Here we explore electric field effects on the chemisorption of this O_2^- species. To be consistent with our previous work the calculations here are carried out on the larger $4\sqrt{3}\times4\sqrt{3}$ surface unit cell, which is four times the size of the $2\sqrt{3}\times2\sqrt{3}$ surface unit cell used elsewhere in this study.

The results are plotted in Figure 3.7b. Unlike the metal superoxide MO_2 species, the superoxide anion has a large polarizability (similar to what Hyman et al. reported for adsorbed O_2 on Pt(111)[97]), so the plot of $\Delta\Delta G_{ads}$ vs. ε exhibits a pronounced curvature. The best fit of the calculated stability to Eq. 2 yields $\Delta\Delta G(\varepsilon)_{ads} = -1.9393\cdot\varepsilon^2 + 0.8253\cdot\varepsilon - 0.005862$. The ΔG_{ads} varies by a total of 0.62 eV in the range of ±0.4 V/Å, which is more pronounced than the field effects on the stability of the MO_2 species due to both a large μ_0 and a large α, particularly when the field is negative. The O-O bond length (d(O-O)) varies consistently with the field strength, from 1.316 Å at −0.4 V/Å to 1.296 Å at +0.4 V/Å. This trend is consistent with a more negative field

corresponding to a more negatively charged surface, which induces a greater degree of charge transfer into the O_2 molecule (confirmed by Bader analysis) thereby lengthening the O-O bond. There is no direct coordination of the DMSO to the O_2^- (the distances between the upper O atom of the O_2^- and the nearest H, sulfinyl O, and S atoms at zero field are: At ε = +0.4 V/Å, 2.893, 3.189, and 2.955 Å; at ε = 0 V/Å, 2.735, 4.045, and 3.185 Å; at ε = −0.4 V/Å, 2.514, 4.264, and 3.583 Å).

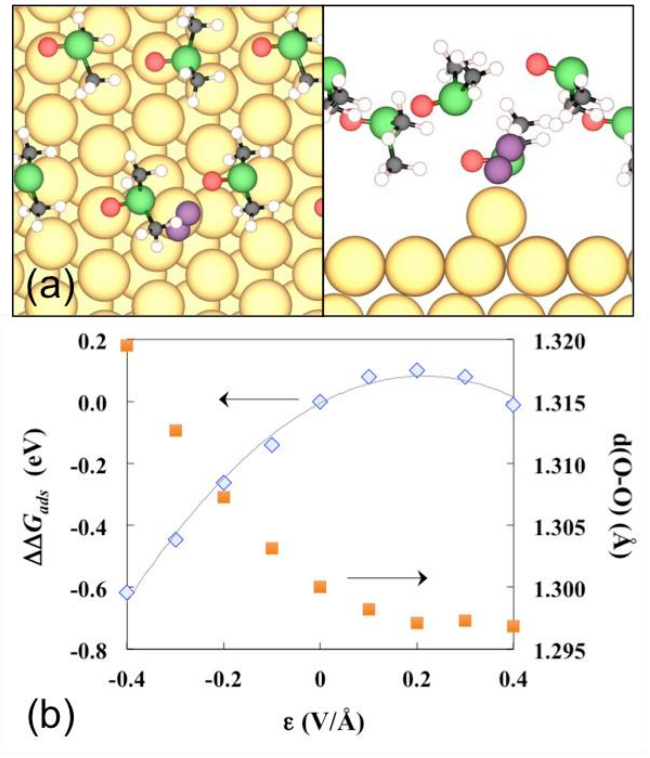

Figure 3.7: (a) Top (left panel) and side (right panel) view of the superoxide anion O_2^- species on Au_1/Au(111) | DMSO at ε = 0 V/Å. Color code: Au = yellow, C = black, O = red, S = green, H = white, and O_2 = purple. (b) Electric field induced changes in stability ($\Delta\Delta G_{ads}$, relative to ε = 0 V/Å) and O-O bond length (d(O-O)) for O_2^-. The solid line is the best fit according to Eq. 2. Calculation for the O_2^- at ε = −0.4 V/Å could only be converged to 0.10 eV/Å.

It is evident in Figure 3.7 that significant variations in $\Delta G(\varepsilon)_{ads}$ and d(O-O) occur between 0 and −0.4 V/Å. Negative potentials are less relevant to the discharge of metal-air batteries, and

under a very negative potential O_2^- may be further reduced to a peroxide (O_2^{2-}) or even dissociate into O^{2-}. On the other hand, between 0 and +0.4 V/Å the stability of O_2^- varies by a much more moderate 0.10 eV and d(O-O) varies by only 0.004 Å. Since the discharge voltages of metal-air batteries correspond to positive interfacial electric fields, our results suggest that the properties of O_2^- should not change appreciably with potential in metal-air cells, which is inline with the fact that experimentally observed O-O vibrational frequency for O_2^- is nearly invariant over a range of ca. 1 V below the equilibrium potentials for Li-ORR and Na-ORR.[4, 82]

For individual molecules, higher polarizabilities are usually associated with larger, more diffuse electron clouds or less tightly bound electrons. Polar molecules (e.g. the MO_2 species) would therefore be expected to have small α, compared to e.g. O_2^-. Note that a large α indicates a stronger *dependence* of stability on field. Whether it means stabilization or destabilization, and what the magnitude of the effect is, depend on the specific molecule and field strength in question. In the case of the O_2^-, its stability varies only moderately between 0 and +0.4 V/Å because the maximum of $\Delta\Delta G_{ads}$ with respect to ε occurs in the middle of this field range.

3.2.6. O and OH Adsorption at Au | Vacuum

O and OH are the key intermediates in the hydrogen ORR. Their adsorption on Au has been studied in detail previously,[111-115] and is revisited here in part to validate our DFT setups. On Au(111), DFT predicts atomic O to prefer the fcc threefold hollow site, which is supported by experiment. Depending on the O coverage and the exchange correlation functional used, ΔE_{ads} for O ranges from −2.19 to −3.38 eV (relative to a gas-phase O atom),[102, 114, 116-120] with which our result is consistent (−2.93 eV). For OH, Santiago-Rodriguez et al.[120] reported a tilted configuration on the twofold bridge site to be preferred for adsorption at 1/4 ML with ΔE_{ads} = -1.70 eV, while Phatak et al.[119] found an upright configuration at the fcc site to be preferred at a lower coverage of

1/9 ML, with $\Delta E_{ads} = -2.10$ eV (GGA-PW91). At 1/12 ML we also find OH preferentially adsorbs in an upright geometry at the fcc site with $\Delta E_{ads} = -1.89$ eV.

On Au(211) both O and OH preferentially adsorb at the step edge. Xu and Mavrikakis[102] and Daigle and BelBruno[114] found the preferred adsorption site for O to be the "hanging fcc site" at the step edge (Figure 8), which yielded ΔE_{ads} of −2.77 eV (GGA-PW91) and −3.24 eV (GGA-PBE) respectively. We find the same site preference for O adsorption, with $\Delta E_{ads} = -2.89$ eV. Liu et al.[121] reported that OH prefers adsorption at the bridge site on the step edge (Figure 3.8) of Au(211) with a binding energy of −2.39 eV (GGA-PW91). We find the same site preference and a similar ΔE_{ads} of −2.30 eV on Au(211).

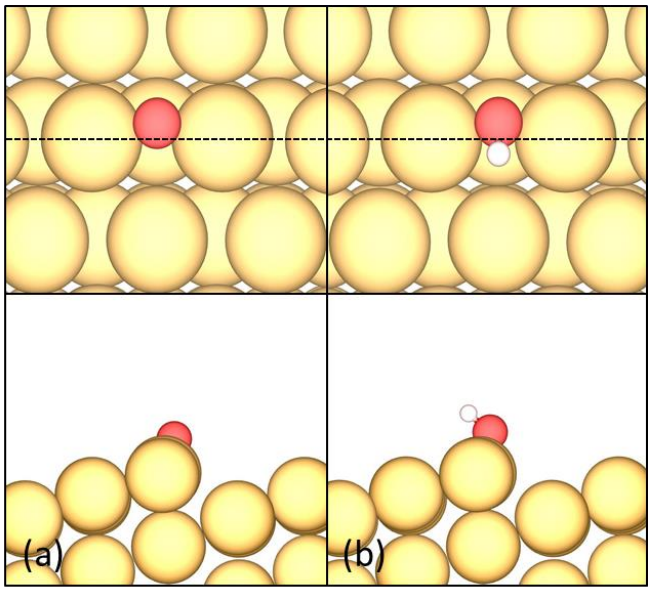

Figure 3.8: Top (top) and side (bottom) views of minimum total energy adsorption sites for O (a) and OH (b) on Au(211). Color code: Au = yellow, O = red, and H = white.

The variations in stability for O and OH on Au(111) and Au(211) over an ε range of ±0.4 V/Å are presented in Figure 9. For both adsorbates on both surfaces, ΔG_{ads} varies by a total of 0.25 eV or less over ±0.4 V/Å. In particular, ΔG_{ads} for O on Au(111) varies by less than 0.15 eV,

and is nearly field-independent for OH on Au(211). The $\Delta\Delta G_{ads}$ vs. ε behavior and the small magnitude of the field effect on stability of O and OH are consistent with what Karlberg et al.[48] (who included explicit water molecules in their models) and Hyman et al.[97] previously reported for O and OH on Pt(111), which helps validate our computational approach to study the field effects on superoxide adsorption on Au surfaces here. The similarity in field effects on O and OH on Au compared to Pt suggests that the dependence and magnitude of the field effects as indicated by our calculations for the molecular superoxide species adsorbed on Au may be qualitatively similar on other late transition metals.[94]

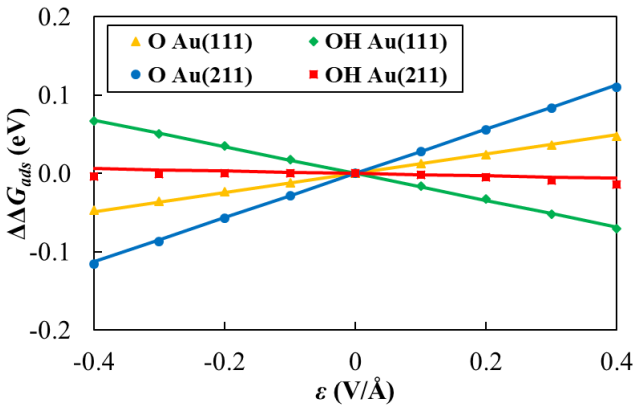

Figure 3.9: Electric field induced variations in stability ($\Delta\Delta G_{ads}$, referenced to ε = 0 V/Å) for O and OH adsorbed on Au(111) | vacuum and Au(211) | vacuum. The solid lines give the predicted changes in stability based on the first-order approximation (μ0·ε).

3.3. Conclusions

Periodic DFT calculations have been performed to investigate the effect of an interfacial electric field (such as is present in the electric double layer) on the chemisorption of key intermediates in the metal-ORR in metal-air batteries, i.e. the superoxide anion (O_2^-) and molecular metal superoxide (LiO_2, NaO_2, and KO_2), on the (111) and (211) facets of gold. In the absence of an electric field (ε = 0 eV/Å), the metal superoxides adsorb with an ΔG_{ads} of −0.26 eV or more stable on Au(111), each of which is ca. 0.6 eV more stable on Au(211). The presence of a shell of explicit

DMSO molecules electrostatically stabilizes MO_2 species by 0.3~0.8 eV on each surface compared to *in vacuo*.

While the inclusion of an external electric field in our DFT calculations does not permit a one-to-one relationship to be established between field strength and electrode potential, we estimate that over the entire range of discharge potential range for Li-, Na-, and K-air batteries the absolute value of the interfacial field strength does exceed |0.4| V/Å. On each surface we then applied fields between ±0.4 V/Å to each of the molecular metal superoxide species *in vacuo* and in the presence of explicit DMSO molecules. In this range of ε, the stability of the metal superoxides are calculated to vary by up to |0.4| eV vs. the zero-field values, which is larger than that for O and OH, two key intermediates in ORR by hydrogen, on Au and Pt (ca. |0.1| eV). The presence of DMSO molecules serves to amplify the field effect on the stability of the adsorbed MO_2 species vs. *in vacuo*. We have furthermore shown that the electric field effect on the stability of the molecular MO_2 species can be closely estimated by the product of the electric field ε and the zero-field dipole moment μ_0 over ±0.4 V/Å. That is, $\Delta G(\varepsilon)_{ads}$ at any field strength in the given range can be reasonably estimated by the sum of zero-field adsorption energy ΔE_{ads} and $\mu_0 \cdot \varepsilon$, thereby avoiding the need for DFT calculations with electric fields that are computationally intensive and occasionally difficult to converge. The error of the first-order approximation is, however, large for the adsorbed superoxide anion (O_2^-) because of its large polarizability compared to the MO_2 species. The stability of this O_2^- state is predicted to vary by up to |0.7| eV over ±0.4 V/Å, although it varies by a more moderate amount of 0.10 eV between 0 and +0.4 V/Å. In short, the effect of the interfacial electric field on the stability of key metal-ORR intermediates may be appreciable and yet different for different species (O_2^-, MO_2) at typical discharge potentials of Li-, Na-, and K-air batteries (2.2~2.8 V).

Not including the electric field effect may therefore have a material impact on the DFT-based theoretical analyses of the mechanism and limiting potentials of metal-ORR. The first-order approximation represents an easy-to-apply and low-cost way to include this important correction. However, as our results for O_2^- have shown, one needs to verify whether the first-order approximation is valid for an adsorbed species by checking its polarizability. An easy way to do so would be to calculate the stability of the adsorbed species in question at both the largest and the smallest field strength of interest and also at zero field (if it lies inside the range of ε of interest), to estimate how far $\Delta\Delta G_{ads}$ vs. ε deviates from linearity. We recommend that this set of procedures be adopted by those researchers who use the thermodynamic approach to model electrochemical interfacial reactions.

Chapter 4. Solution Mediated Reaction Mechanisms for Metal Air Batteries: A First Principles Approach

4.1. Introduction

The world's largest economies are slowly transitioning to renewable energy and sustainable technologies like electric vehicles. There is a need for efficient and large capacity energy storage to enable these technologies. Currently Li-ion battery technology is majorly used for these applications and they are inherently limited by their specific energy. The demand for energy storage is only touted to increase in the future thus making the need for better energy storage technologies vital. Aprotic metal air batteries (M-O_2) (where M=Li, Na & K), with large theoretical capacities, stand to be the most promising candidate to replace the current Li-ion battery technology. But prototype M-O_2 battery development is hindered with many obstacles like solvent degradation, poor cycling efficiency, parasitic reactions.[2, 88-93] Successful development of M-O_2 prototypes requires detailed understanding at the molecular level of the many chemistries occurring in parallel in these batteries.

The discharge products formed in all M-O_2 batteries are some form of an alkali oxide (either superoxide, peroxide or oxide) and all of them have been shown to be insulating in nature.[122-124] The cell discharge reaction can occur through two major routes for the growth of the discharge product. The first is a surface mediated electrochemical mechanism that produces conformal growth of the discharge product on the cathode. The growth through this mechanism is limited as the insulating nature of the discharge product limits charge transport through the oxide layer and thus further discharge product formation is hindered.[125-126] The second path involves a solution mediated mechanism for the formation of the main discharge product mainly limited by the solubility of the metal superoxide, where the superoxide anion O_2^- acts as a redox mediator.[10-11, 127] The proposed second path of solution mediated mechanism is postulated to be triggered

through multiple routes. Aetukuri et al. proposed the formation of LiO_2^* on the surface followed by desorption and dissociation brought about in electrolytes with varying amounts of water.[10] They proposed that the dissolved LiO_2 reacts on an already formed surface Li_2O_2. This leads to the discharge product with toroid shaped morphology. On the other hand Zhang et al. showed the formation of O_2^{-*} on the electrode surface in anhydrous aprotic electrolyte.[4] At high potentials (or low overpotentials), the O_2^{-*} desorbs and reacts with Li^+ in solution to form Li_2O_2 which later precipitates onto the electrode. The toroidal morphology of Li_2O_2 has been observed in many studies of Li-O_2 systems.[15, 128-132] A similar formation of cuboid morphology for Na-O_2 batteries have also been observed.[11, 133-138] Similar solution based behavior for K-O_2 batteries is yet to be explored. This solution mediated morphology helps improve the discharge capacity and reduce overpotential as these morphologies occupy less surface area relative to a uniformly grown film of discharge product. As the discharge product is dissolved in the electrolyte solution, the nature of the solvent has a profound effect in the electrochemical discharge mechanism.

It has been demonstrated that the dissolution of the superoxide anion or the surface formed metal superoxide is a strong function of the electrolyte's donating and accepting properties.[127, 135, 139-142] These properties are characterized by the Gutmann donor number (DN) and acceptor number (AN). In case of Li-O_2 batteries, solvents with high DN can induce solubility of discharge product by stabilizing the intermediates in solution.[65, 99, 143-144] For Na-O_2 batteries, high DN and AN is preferable to initiate solution phase reaction mechanism but other solvated components can also have an influence as well like solvated conducting salts.[135, 145] Higher DN has the effect of better solvating the cation while a higher AN has the effect of better solvating the anion

Herein, we investigate through density functional theory, the solution phase reaction mechanism for formation of discharge products of M-O_2 battery. We probe related molecular

species and the resultant cluster formation in dimer and trimer configuration. These species are modeled in the presence of two solvents. The two solvents considered are DMSO(DN= 29.8 Kcal/mol ,AN=19.3 Kcal/mol)[146-148] which has a high value for DN as well as AN and contrastingly we consider ACN (DN=14.1 Kcal/mol ,AN=18.9 Kcal/mol)[147, 149] which has a relatively low DN and high AN. While DN and AN are properties that cannot be directly modeled, we instead opt for an implicit solvent method to factor in the properties through a solvent specific polarizable continuum. We consider the possibility of precipitation of metal superoxide and peroxide, reporting the concurrent precipitation energy. We find that for the case of Li-O_2 precipitation of superoxide is unfavorable while for Na-O_2 and K-O_2 the precipitation of the superoxide represents a downhill trend in the free energy space. The barriers for the transition state and overall free energy profile for the reaction mechanism are dependent on the choice of the solvent. We currently focus purely on the mechanistic study of the solution mediated electrochemical mechanism of different M^+ ions (Li^+, Na^+ and K^+) with O_2^- ion in solution. The effect of added anions and the resulting complexes, different coupling effects, solvent decomposition etc. is left for future studies.

4.2. Results and Discussions

4.2.1. Solvation of Molecular Species

The solvation free energy in DMSO and ACN of the M^+, MO_2, the minimum energy metal superoxide dimer formed before the transition state $(MO_2)_{2(min)}$ and M_2O_2 is shown in Table 4.1 & 4.2. Recently the standard redox potentials of O_2/Li^+-O_2^- in different aprotic solvents was quantified and was correlated with the O_2/O_2^- and Li^+-O_2^- solubility. [65] In our calculation, the solvation energy of O_2 is ca. 4.48 kcal/mol (4.78 kcal/mol) while that of O_2^- is ca. -64.95 kcal/mol (-65.85 kcal/mol) for DMSO (ACN). These values indicate O_2 being sparingly soluble in the

considered solvents and thus the necessity of superoxide ion in the solvent to initiate the solvent based mechanism. Contrastingly, the solvation energy of the cations in both solvents indicate that if we start with an equimolar basis of metal atoms and O_2 then all of the O_2^- should find a solvated cation to react with. Interestingly, all the possible solution mediated reaction intermediates and products (the reaction mechanism is elaborated in the later section) have a lower solvation energy as compared to their respective M^+ cation and O_2^- anion.

Table 4.1: $\Delta G^0_{(solv)}$ (kcal/mol) for different species in DMSO

Species	Li	Na	K
M^+	-133.43	-107.03	-90.31
MO_2	-35.26	-37.96	-33.27
M_2O_2	-47.98	-52.64	-45.03
$\{MO_2\}$ (min)	-39.79	-39.74	-35.33

Table 4.2: $\Delta G^0_{(solv)}$ (kcal/mol) for different species in ACN

Species	Li	Na	K
M^+	-120.79	-99.23	-83.61
MO_2	-28.33	-33.00	-28.93
M_2O_2	-38.31	-45.84	-38.91
$\{MO_2\}_2$ (min)	-30.29	-39.74	-28.98

Solubility of metal superoxides and peroxides vary by huge order of magnitudes in different solutions. Molecules like LiO_2 do not have direct measurements for solubility. [150-155] The

calculation for solubility is especially cumbersome as the $S_{species}$ is an exponential function of the free energy of dissolution which is in turn a summation free energy of sublimation and solvation. Thus, $S_{species}$ value varies by huge orders of magnitude with small errors in the free energy values making it extremely sensitive to the choice of level of theory. Thus, the solubility values in Table 4.3 are meant to depict a qualitative comparative trend between the MO_2 and M_2O_2 of the same species as LiO_2 and Li_2O_2.

For LiO_2 and Li_2O_2, the overall favorability of Li_2O_2 stems from the relevant thermodynamic instability of LiO_2 to precipitate out as a solid which is further propounded by the fact that LiO_2 is soluble in organic solvents (Table 4.3). The presence of LiO_2 in solvent as a solvated species enables it to react with itself to undergo disproportionation reaction, the further driving force of which is governed by the relevant energy barriers in the organic solvent. In case of Na and K, the peroxide of each species appears to be relatively less soluble as compared to its superoxide counterpart. The conclusion for which species is more favorable requires the consideration of the reaction barriers during the formation mechanism and the viability of forming higher order clusters in the relevant organic solvent. The huge relative difference in solubilities requires further inspection for the formation of metal peroxide for both Na and K.

Table 4.3: Solubilities (mol/L) of M_xO_2 molecular species in DMSO and ACN using B3LYP/6-311++G(d,p) , PCM model and fitted atomic radii.

Species	**DMSO**	**ACN**

LiO_2	1.96E-01	1.78E-06
Li_2O_2	6.70E-17	6.06E-24
NaO_2	3.73E-13	4.56E-17
Na_2O_2	4.40E-63	4.89E-68
KO_2	1.07E-01	7.39E-05
K_2O_2	7.09E-24	2.47E-28

We initially consider the gas phase reaction mechanism for the formation of metal peroxide M_2O_2. The primary intermediate in this case is the metal superoxide dimer which disproportionates to form metal peroxide. Various isomers of the superoxide exist and are shown in Fig. 4.1. The relative stability of these isomers is shown in Table 4.4.

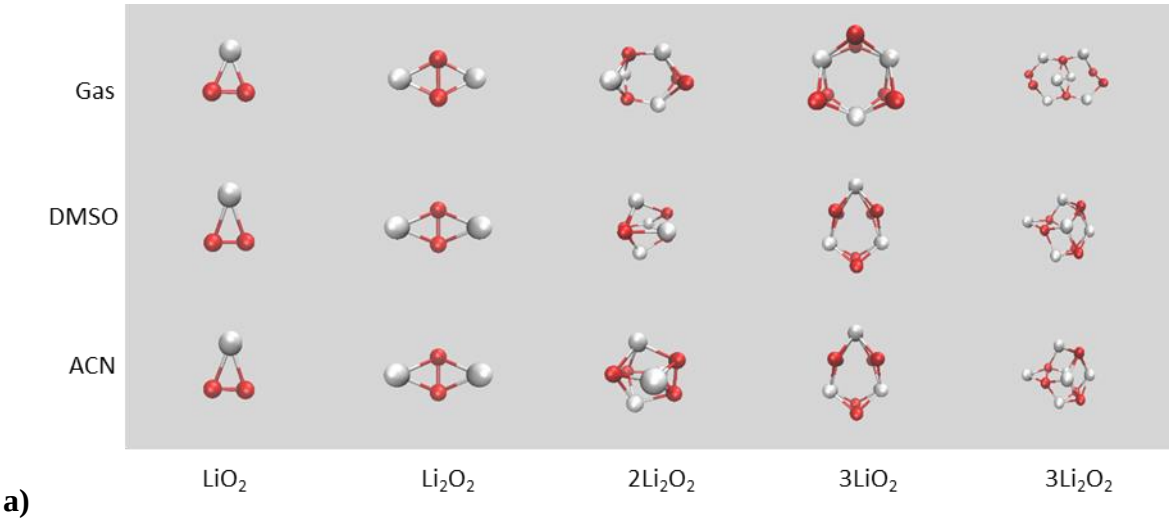

a)

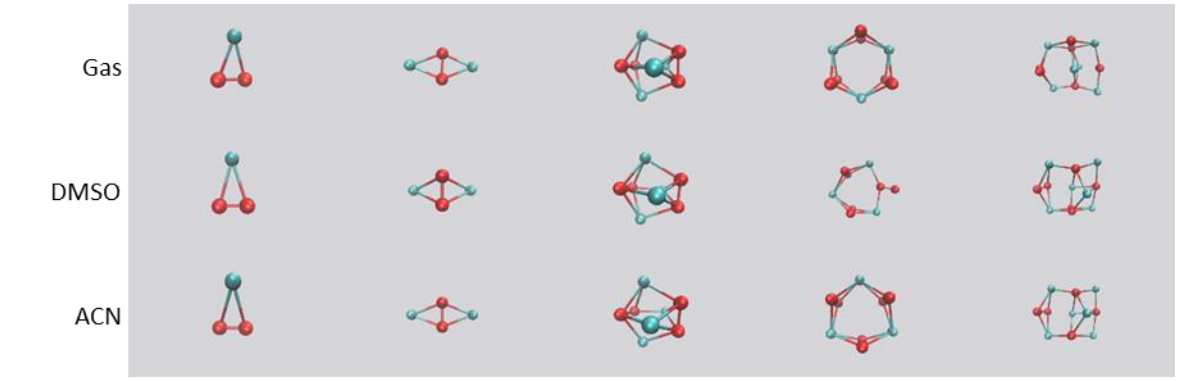

b)

Figure 4.1: Stable structures in gas phase, DMSO and ACN for MO_2, M_2O_2, $2M_2O_2$, $3MO_2$ and $3M_2O_2$ shown in a) for Li, b) for Na and c) for K based species. The different possible dimer isomers including low energy $(MO_2)_2$ and high energy MO_2MO_2 dimers in gas phase, DMSO and ACN are shown d) for Li, e) for Na and f) for K. The transition state for different M^+ atoms between low and high energy dimers in different phases is shown in (g)

fig. cont'd

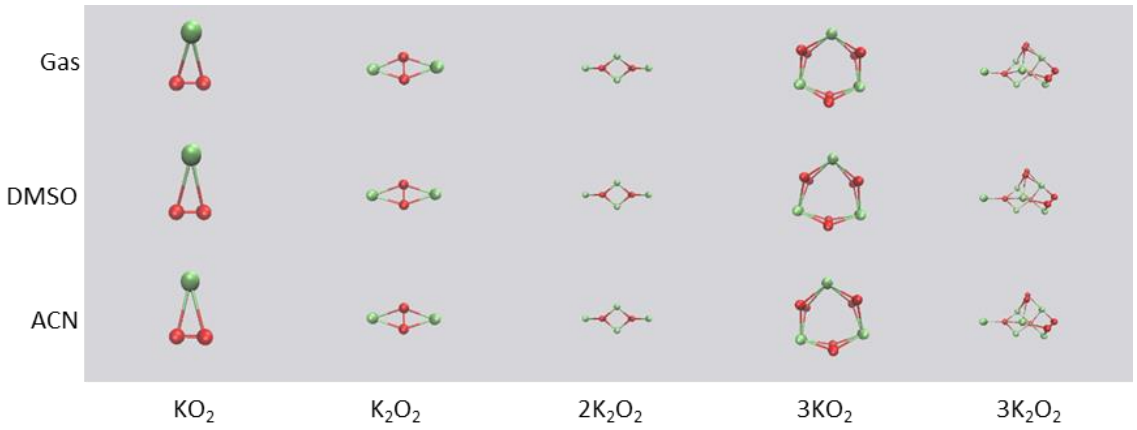

c)

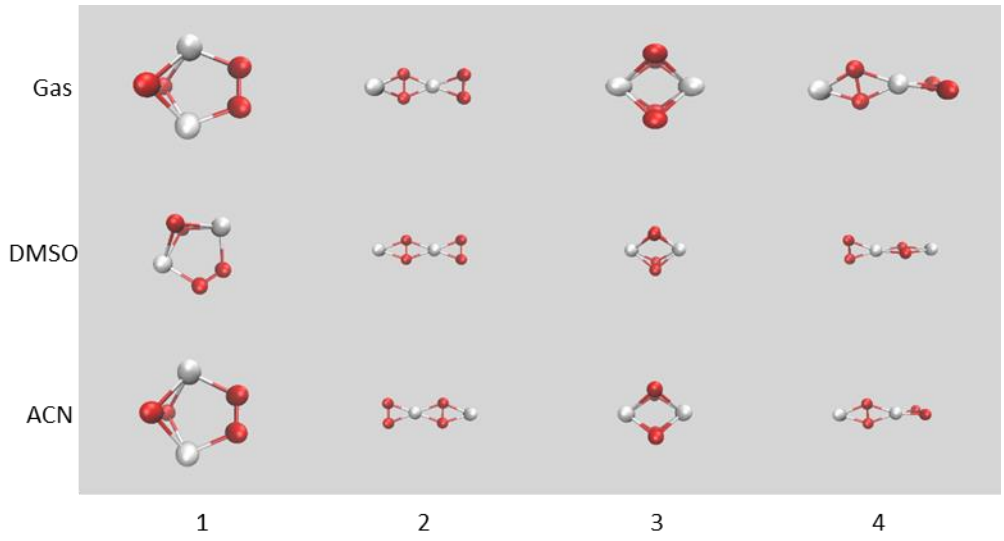

d)

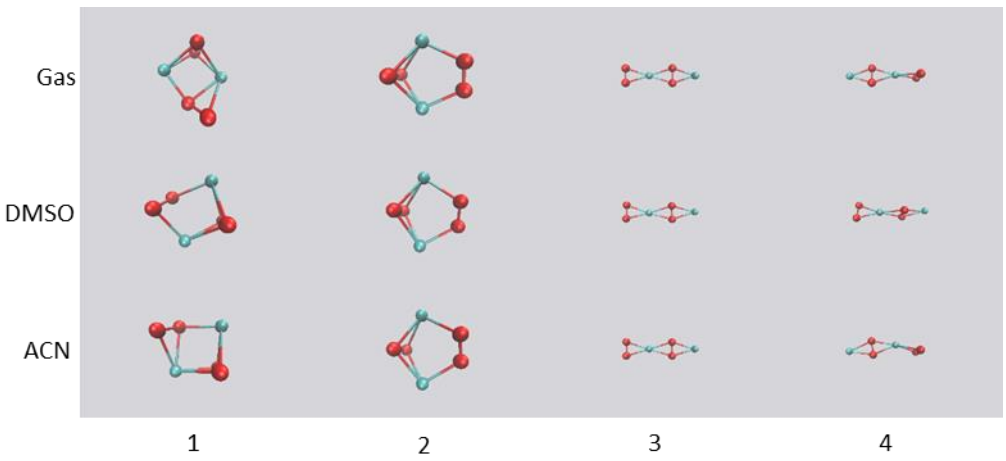

e)

fig. cont'd

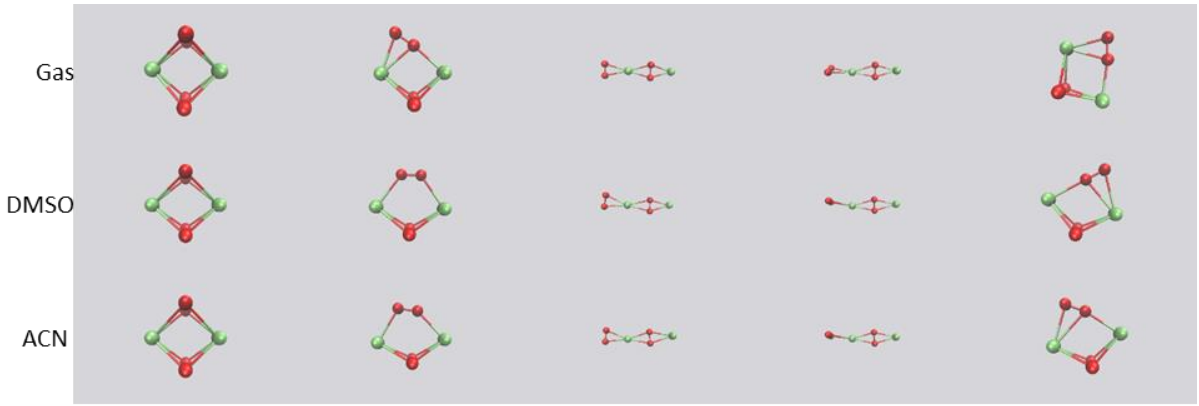

f)

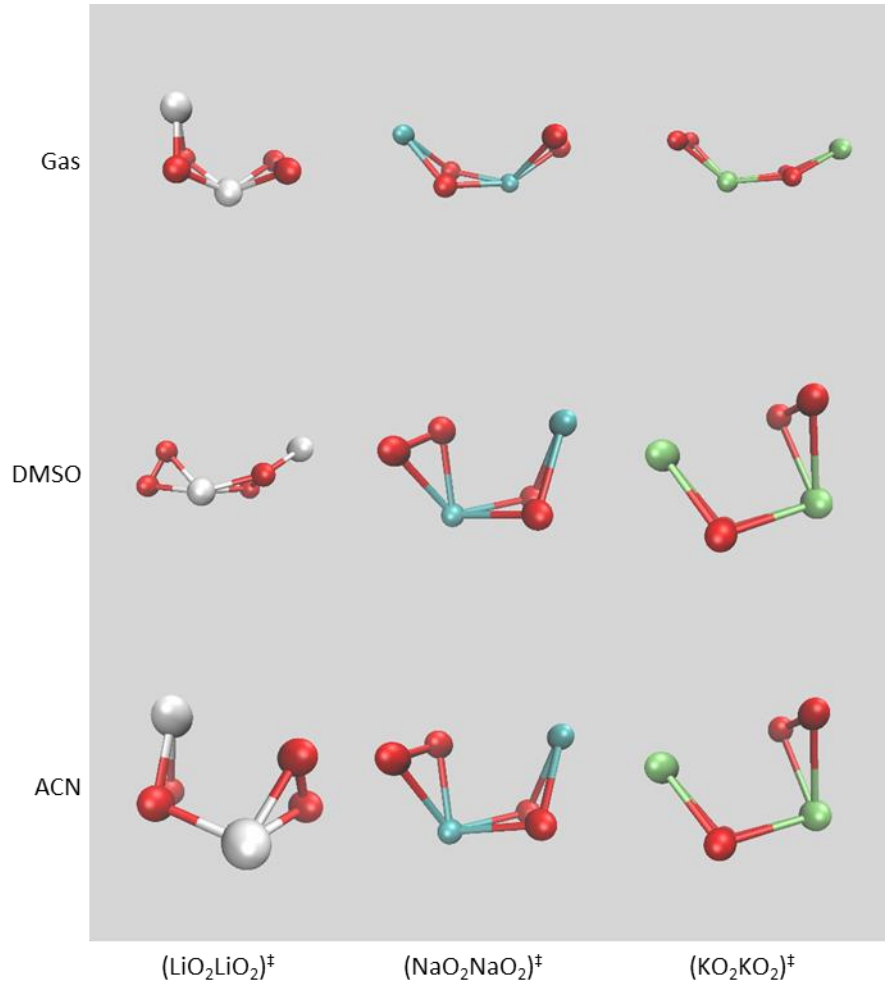

g)

Table 4.4: Relative Electronic Energies (with and without zero-point-energy (ZPE) corrections) and Standard Gibbs Free Energies (kcal/mol) for $(MO_2)_2$ calculated with B3LYP and G4 Methods for the dimers shown in Figure 4.1

			B3LYP			G4		
Species	**Dimer**	**spin**	**G(gas)**	**G(DMSO)**	**G(ACN)**	**G(gas)**	**G(DMSO)**	**G(ACN)**
LiO_2	1	3	0.00	0.00	0.00	0.00	0.00	0.00
	2	3	8.72	-1.16	-1.04	18.19	8.21	8.97
	3	3	10.94	12.47	14.46	11.88	13.83	13.74
	4	3	8.99	-2.85	-1.43	15.59	5.35	5.76
NaO_2	1	3	0.00	0.00	0.00	0.00	0.00	0.00
	2	3	0.25	0.99	0.39	1.99	0.78	0.86
	3	3	13.08	-0.80	-1.96	21.05	6.14	6.64
	4	3	12.89	-0.46	-1.24	17.47	3.16	3.61
KO_2	1	3	0.00	0.00	0.00	0.00	0.00	0.00
	2	3	2.46	-1.34	-0.22	5.43	3.20	3.21
	3	3	13.53	-3.08	-3.26	16.83	1.58	2.29
	4	3	13.38	-2.78	-2.49	16.17	0.95	1.73
	5	3	-0.80	-0.43	0.26	4.58	6.38	6.69

The most stable isomer is different at different levels of theory. The dimer 1 for all cases of M atoms, which is the most stable in gas as well as in solution at 298 K as predicted by G4 is not the most stable isomer in solution according to B3LYP. For LiO_2, the gas phase symmetry indicates a C_{2V} molecule (using G4) as shown earlier by Bryantsev et al.[5] The C_{2v} molecular symmetry is lowest energy structure for NaO_2 and KO_2 as well, in agreement with past studies.[156-157] The gas phase reaction mechanism of these alkali superoxides with itself to give alkali peroxide

is described in Eq. (4.1-4.4) below. The only difference between Eq. (4.1-4.4) and Eq. (2.46-2.49) is that the species here are in gas phase instead of solution phase.

$2MO_{2(g)} \rightarrow \{MO_2\}_{2(g)}$ (global minimum) (4.1)

$\{MO_2\}_2$ (g) (global minimum) $\rightarrow \{MO_2\}_2^{\ddagger}$ (g) (transition state) (4.2)

$\{MO_2\}_2^{\ddagger}$ (g) (transition state) $\rightarrow \{MO_2\}_2$ (g) (high energy) (4.3)

$\{MO_2\}_2$ (g) (high energy) $\rightarrow M_2O_{2(g)} + O_{2(g)}$ (4.4)

This mechanism is based on the mechanism described by Bryantsev et. al.[5] for the reaction LiO_2 with itself. The reference state is two MO_2 molecules in gas phase which is treated as 0 kcal/mol. The overall energetics of the reaction for the different alkali metals is shown in Fig. 4.2. First a stable MO_2 ring shaped dimer is formed (step 1) which is followed by the formation of a stable high energy intermediate MO_2MO_2 form dimer (step 3) by a mechanism involving the abstraction of a M^+ ion from one of the superoxides in the initial dimer. This rate-determining step proceeds through the transition state (step 2) with a barrier of 16.63 (16.99) kcal/mol, 17.53 (17.49) kcal/mol and 15.89 (16.24) kcal/mol in the forward direction for Li, Na and K respectively at 298 K (0 K). For Li, the following formation of high energy dimer and disproportionation to form peroxide (step 4) is energetically downhill both enthapically (0 K) and in free energy (298 K). For Na and K, there is an additional endergonic process for disproportionation for Na_2O_2 and K_2O_2 (unlike Li_2O_2) which amounts to 11.09 (16.72) kcal/mol and 15.57 (21.25) kcal/mol respectively at 298 K(0 K). In the backward direction there exist a barrier of 7.51 (1.14) kcal/mol for Li while for Na and K the reverse process is energetically downhill.

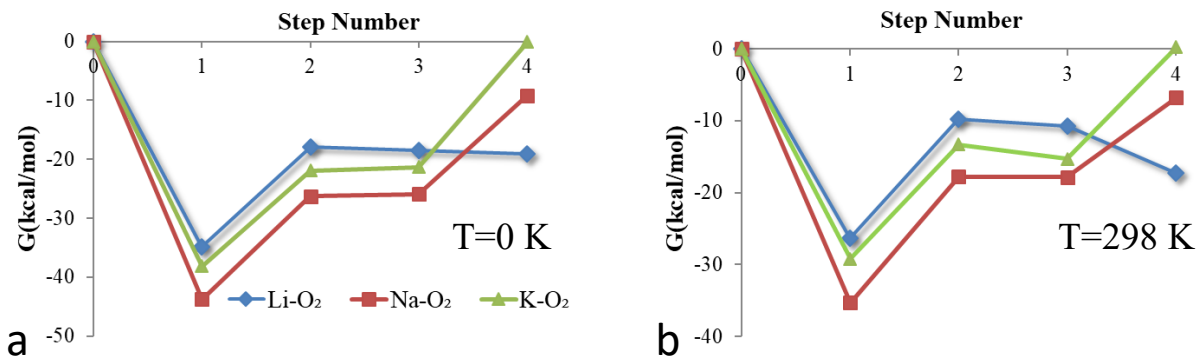

Figure 4.2: Gas phase reaction free energy profile at (a) T=0 K and (b) T=298 K for the disproportionation of the MO_2 molecule to M_2O_2 and O_2 (kcal/mol) obtained at G4 level of theory.

Based on the gas phase reaction mechanism proposed here, all of the MO_2 dimer species are more stable than the M_2O_2+O_2 species at both 0 K and 298 K. However, the thermodynamic stability of the M_2O_2 will increase if the molecules can aggregate. In the limit of infinite crystal size, the thermodynamic stability of MO_2(solid) compared to M_2O_2(solid) at an oxygen pressure of 1 atm can be estimated from the recent DFT calculations. For Li, based of the work by Seriani[158], the Li_2O_2 structure is more stable as compared to $2LiO_2$ stoichiometry by 8.3 kcal/mol at 0 K (after considering the underestimation error of GGA). The estimated standard reaction free energy of LiO_2=Li_2O_2 + O_2 is -22.9 kcal/mol [5] (after considering the entropy of molecular oxygen at T= 298 K and p_{O2}=1 atm (49.03 cal mol^{-1} K^{-1})[159]), which is a strong thermodynamic driving force to form Li_2O_2. For Na, at 0 K $2NaO_2$ stoichiometry is more stable than Na_2O_2 by 6.918 kcal/mol while at 298 K, Na_2O_2 is more stable than $2NaO_2$ by 1.38 kcal/mol [160] before considering the entropy of O_2. This relatively low thermodynamic difference coupled with the kinetic energy released and local oxygen concentration variation could be a contributing factor to the observation of both NaO_2 and Na_2O_2 in different batteries. For K, at T=0 K the KO_2 crystal is more stable by 18.09 kcal/mol

and at T=298 K KO_2 is more stable by 12.7 kcal /mol (before considering the entropy of O_2).[91] When we factor the entropic change due to O_2 at 298 K (14.6 kcal/mol), K_2O_2 becomes more stable of a discharge product by 1.9 kcal / mol. The relatively small thermodynamic stability difference between the superoxide and peroxide of K warrants a future study of the kinetic and thermodynamic effects on the final discharge product.

4.2.2. Solution Based Reaction Mechanism

The solution based mechanism for different M-O_2 batteries in DMSO and ACN are shown in Fig. 4.3 a-f. In each case, the initiating step or starting point is the solvated M^+ and O_2^- ions (labeled as step 0) which we showed earlier are favorably solvated in DMSO and ACN. It is shown experimentally that solvated O_2^- is present in Li^+/DMSO solution at high potentials, thereby justifying the initial step for the mechanism.[4, 108, 110] The solvation energy of the reference state i.e. $2M^+$ and O_2^- is fitted to the experimental values thereby making the comparison of the solvated metal superoxide and peroxide apt. The reaction mechanisms for all three metal candidates proceed through the formation of a metal superoxide (labeled as step 1). The formation energy for LiO_2, NaO_2 and KO_2 are -5.74 kcal/mol (-11.56 kcal/mol), -6.66 kcal/mol (-9.60 kcal/mol) and -3.08 kcal/mol (-5.55 kcal/mol) in DMSO (ACN) respectively.

The next step in the reaction plot in Fig. 4.3 a-f represents the formation of two metal superoxide, at which point the phenomena of precipitation is considered. For LiO_2, $\Delta G^f_{(s)}(LiO_2)$ (the experimental free energy of formation) isn't currently reported thus making the calculation of P.E. improbable. For NaO_2 and KO_2 the P.E. is -1.68 kcal/mol (-6.64 kcal/mol) and -3.55 kcal/mol (-7.89 kcal/mol) in DMSO (ACN) respectively. The net effect of these favorable precipitation energies is the overall downhill free energy slope from solvated ions to final solid discharge

product in the form of metal superoxide. This step is more favorable than the subsequent step i.e. formation of MO_2 dimer for Na based and K based reactions as shown in Fig. 4.3 c-f.

In case of Na-O_2 batteries, the formation of NaO_2,[136, 161-163] Na_2O_2 [164-166] and a mixture of both[167-169] are observed. While NaO_2 offer a lower gravimetric energy (1108 Wh/kg) than Na_2O_2 (1605 Wh/kg), it is associated with a much lower overpotential (~ 100 mV).[138] For K-O_2 batteries, KO_2 (935 Wh/kg)[91] is the only observed discharge product. The formation of discharge product is a complex function of the solvent, electrode potential, solvated anions and many more parameters. So, we consider the formation of metal peroxide for Na and K. For Li, Li_2O_2 is currently the most stable desirable oxide (barring Li_2O). The next step is the formation of metal superoxide dimer. Based on our RASS method, we exhaustively probe the potential energy surface and the dimer presented is the closest structure to a global minima we achieve. Yet, like any other global search algorithm, there is a probability of other more stable isomers to exist. After the formation of the minimum structure metal dimer (step 3 or Eq. 4), the molecule undergoes isomerization to form a high energy dimer (step 5 or Eq. 2.47) which readily disproportionates to form metal peroxide and solvated O_2 molecule (step 6 or Eq. 2.48). Transition state theory is used to find the transition state structure (step 4 or Eq. 2.46) between the minimum and high energy dimer structure and the corresponding activation barrier. For $(LiO_2)_2$, $(NaO_2)_2$ and $(KO_2)_2$ the activation barrier is 7.22 kcal/mol (11.23 kcal/mol), 5.06 kcal/mol (5.64 kcal/mol) and 2.97 kcal/mol (3.40 kcal/mol) in DMSO (ACN) respectively. Following the formation of a high energy metal dimer, the structure undergoes disproportionation to give solvated metal peroxide. Out of the three metal candidates, only Li has a net exothermic energy for the disproportion reaction step of -1.83 kcal/mol (-1.77 kcal/mol) in DMSO (ACN). This is mainly attributed to the instability of the LiO_2 species and its dimer. Thus, consequently the mechanism is more favorable towards the formation of Li_2O_2 as

compared to Na and K based mechanism. While for Na and K, the disproportionation reaction energy is 15.09 kcal/mol (14.54 kcal/mol) and 23.68 kcal/mol (22.97 kcal/mol) in DMSO (ACN) respectively which represents an energetically uphill process. Following this, the metal peroxide precipitates (step 7-8 or Eq. 2.49-2.50) from solvated species to solid while the dissolved $O_{2(sol)}$ goes back into the gas phase. The reaction energy for the combination of these two steps for Li, Na and K are -27.92 kcal/mol (-37.89 kcal/mol), -26.91 kcal/mol (-34.01 kcal/mol) and -22.58 kcal/mol (-29.01 kcal/mol) in DMSO (ACN) respectively. From Fig. 4.3 c and d, our calculations portray similar overall stability for solid NaO_2 and Na_2O_2. While for K, from Fig. 4.3 e and f, overall stability of solid KO_2 precipitate is far greater than K_2O_2. For the case of Li, there is a strong thermodynamic driving force to form Li_2O_2 crystals at all temperature which is coupled with small activation barrier for the disproportionation reaction both in solution (Fig. 4.3 a and b) and gas phase.[5] This is consistent with the fact that there are no experimental reports on crystal structure of LiO_2 at room temperature.[158]

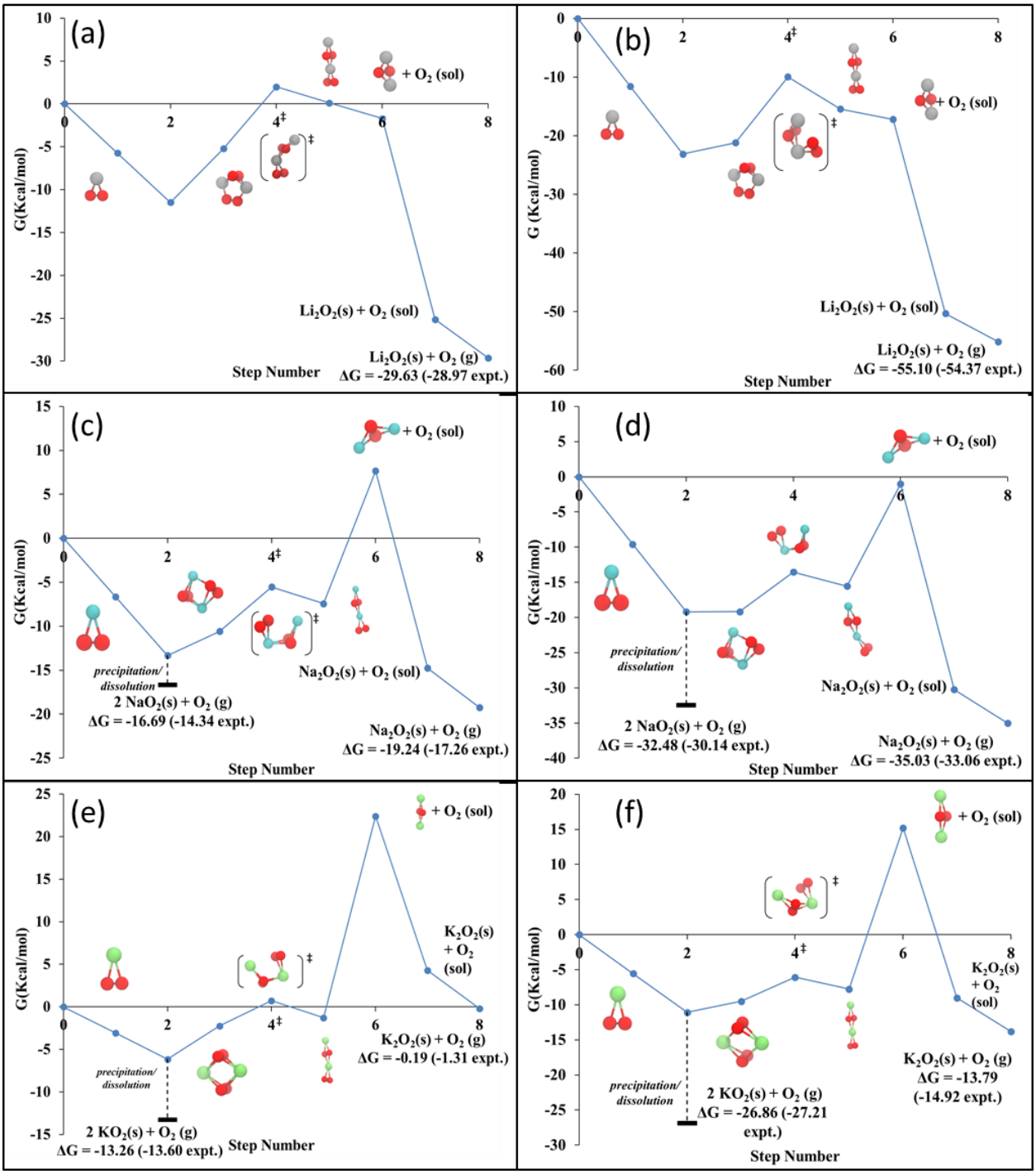

Figure 4.3: Solution mediated reaction free energy profile (T=298.15 K) for the formation of metal superoxide and peroxide for Li (a[b]), Na (c[d]) and K (e[f]) in DMSO [ACN]. The dimer structures are found using R-RASS method and the transition state is found using synchronous transit guided quasi newton method. All structures are optimized using B3LYP/6-311++G** and single point energies were calculated using the G4 method.

The overall free energy changes in solution ΔG^{o}_{solv} at 298 K based on either MO_2 or M_2O_2 formation is shown in Table 4.5. For a metal like Li, where Li_2O_2 is the major product, we observe a high exothermic overall reaction with small barriers to overcome. In case of Na, based on the right condition we could either have NaO_2 or Na_2O_2, where Na_2O_2 formation requires the overcoming of a significant reaction barrier. In case of K, only KO_2 is found experimentally to be the major discharge product. The peroxide doesn't form mainly due to the large reaction barrier and relatively similar stability on the free energy landscape as compared to solvated K^+ and O_2^- ions.

Table 4.5: Overall free energy change in solution ΔG^{o}_{solv} at 298 K for M-O_2 solution mediated reaction mechanism for different discharge products

Metal	DMSO		ACN		Discharge
Species	Exp.	Calc.	Exp.	Calc.	product
Li	-28.97	-29.63	-54.37	-55.11	Li_2O_2
Na	-7.17	-8.34	-15.07	-16.24	NaO_2
	-17.26	-19.24	-33.06	-35.03	Na_2O_2
K	-6.80	-6.63	-13.60	-13.43	KO_2
	-1.31	-0.19	-14.92	-13.79	K_2O_2

4.2.3. Formation of Dimers and Trimers

The cluster formation of LiO_2,[170] Li_2O_2[124] and NaO_2[122] have been studied extensively in gas phase while Na_2O_2, KO_2 and K_2O_2 cluster formation in gas phase and solution are not yet studied. Here we present the formation of dimers and trimers of metal superoxide and peroxide in gas, DMSO and ACN at the B3LYP/6-311**G++ level of theory. As the molecules get larger in size, the G4 level of theory treatment becomes increasingly expensive, thus the results from the B3LYP/6-

311++G** serve as a quantitative measure for the favorability of different clusters. The dimer and trimer formation in gas and solution phase are described as

$MO_2 + MO_2 \rightarrow (MO_2)_2$ (4.5)

$(MO_2)_2 + MO_2 \rightarrow (MO_2)_3$ (4.6)

$M_2O_2 + M_2O_2 \rightarrow (M_2O_2)_2$ (4.7)

$(M_2O_2)_2 + M_2O_2 \rightarrow (M_2O_2)_3$ (4.8)

The free energy of formation of the different clusters in gas and solution phase is given in Table 4.6. In gas phase, the formation energies of the LiO_2 dimer and trimer match very closely with the values of Bryanstev et. al.[5] and Das et. al.[170], which show a general exergonic trend for the formation of the dimer and trimer. But as we move to DMSO and ACN, we see this trend reverse and the process becomes endergonic with increasing unfavorability as the cluster size increases. As we move to Li_2O_2, we see an increasingly favorable trend for the formation of clusters and is in agreement with experiments.[152] As we go to the other clusters (Na and K), there is a general trend suggesting that the formation reaction is exergonic in gas phase and become endergonic in solution for all cases, with larger clusters being unfavorable in solution. For Na, this conclusion is counter intuitive to the experimental observations [11, 135, 138, 144-145] where solution mediated growth of NaO_2 growth is preferred. Lutz et. al. [145] showed experimentally that the electrolyte has a minor effect on the solution mediated mechanism and other factors like added anions play a greater role, thus warranting a future study on the effect of other parameters in solution to the solution mediated mechanism. The current understanding for K-O_2 experimental systems is limited making current conclusions as a first fundamental attempt to explain the current observation in these batteries.

Table 4.6: The free energy of formation for different dimers and trimers in kcal / mol at the B3LYP/6-311++G** level of theory

Species	Gas	DMSO	ACN
$(LiO_2)_2$	-23.66	10.12	4.51
$(LiO_2)_3$	-30.52	24.07	17.88
$(Li_2O_2)_2$	-39.57	-0.94	-6.06
$(Li_2O_2)_3$	-53.43	-8.04	-16.70
$(NaO_2)_2$	-30.94	5.90	4.14
$(NaO_2)_3$	-33.58	7.40	30.69
$(Na_2O_2)_2$	-29.88	1.08	-0.99
$(Na_2O_2)_3$	-71.10	1.23	3.20
$(KO_2)_2$	-23.30	9.77	7.30
$(KO_2)_3$	-30.41	22.36	30.99
$(K_2O_2)_2$	-30.53	2.86	-1.44
$(K_2O_2)_3$	-15.82	15.80	14.79

4.3. Conclusion

Thus, we elaborate the gas phase reaction and the solution mediated reaction mechanism for M(Li, Na & K) O_2 systems in DMSO and ACN for the formation of either metal superoxide and peroxide via formation and disproportionation of metal superoxide dimer. For Li, the only reported discharge product is Li_2O_2 and in our calculations this process is associated with a free energy change of -29.63 kcal/mol (-55.11 kcal/mol) in DMSO (ACN). For Na, within the single mechanism proposed earlier, we explored the precipitation of NaO_2 and Na_2O_2. The P.E. of $NaO_{2(s)}$ makes the entire precipitation process a downhill task. The formation of Na_2O_2 requires the overcoming of a reaction barrier of 15.09 kcal/mol (14.54 kcal/mol) in DMSO (ACN). In the case of K, where KO_2 is the only experimentally reported species, the P.E. of $KO_{2(s)}$ also makes the entire precipitation process favorable. While formation of K_2O_2 is associated with a larger barrier of 23.68 kcal/mol (22.97 kcal/mol). Formation of metal superoxide and peroxide cluster formation is highly exergonic in gas phase. In solution phase the only species to be shown to

grow favorably in solution is Lithium peroxide, while the growth of all other species considered is endergonic. The process described above is subject to change with inclusion of different parameters like solvated anions, inclusion of explicit solvent molecules etc. These parameters will be systematically included in future studies to propound on the current fundamental studies and further gain understanding of current physical systems.

Chapter 5. Effect of Dopant on the Crystalline and Electronic Structures of Li_2O_2

5.1. Introduction

With the increasing world energy demands and significant relevance of renewable energy,[3] the need for efficient and large energy storage has become tantamount. Aprotic Li-O_2 batteries are highly promising candidates for viable energy storage. However, the development of this technology is hindered by a range of scientific problems especially on the reversible cathode side of the battery,[3, 171] which stands to be a major hurdle in commercializing these batteries. Developing a reversible air cathode requires a detailed knowledge of the molecular level processes that occur during the cycling of M-O_2 batteries and detailed understanding of the various reaction mechanism and discharge products forming. However, there are still many fundamental debates on the essential chemistry occurring during charge and discharge as well as the product forming on the cathode surface.

The thermodynamically most stable discharge product for aprotic Li-O_2 battery at ambient conditions is typically solid lithium peroxide (Li_2O_2). The most stable structure of crystalline Li_2O_2 is the *P6*$_3$*/mmc* Föppl structure,[14] which is a wide band gap insulator.[13] During discharge, the lack of electronic conductivity results in a limiting thickness for the layer of discharge product beyond which electron transport to the discharge product-electrolyte interface is insufficient to allow the oxygen reduction reaction (ORR) to take place further.[10, 172-173] During the charging process, a high overpotential is typically needed to drive the reverse reaction i.e. oxygen evolution reaction (OER) at the interface between discharge product and electrolytes, which unfortunately also opens up side reaction channels.[3, 171-172] Thus the overall reversibility of the cathode is severely affected. Early on considerable effort was directed at developing electrocatalysts to improve the efficiency of the ORR and OER, but the role of the electrocatalysts was questionable

due to passivation by solid products.[19, 174-175] A major current research focus is on devising ways to shift the formation of and decomposition of Li_2O_2 away from the electrode surface via redox shuttles and other solution-phase additives.[176-178]

There have been reports that metal ions such as Co and Ni are incorporated into the discharge products when materials such as Co_3O_4 were used as cathodes.[179-180] In such a case the cathode catalyst dissolves into the adjoining electrolyte to form the respective solvated metal ion.[181] Other studies have shown that dissolved anions/cations or side products can be incorporated into the discharge products that are identified as amorphous or defective Li_2O_2.[175, 182-183] These impurities are broadly referred to as additives, promoters, or dopants.[15, 179, 184-185] In this study we refer to a foreign atom incorporated into bulk Li_2O_2 as a dopant. Experimentally, the doping approach has sometimes been shown to have a positive effect in reducing overpotential during recharge[175] and in some cases to increase the discharge capacity.[183, 186]

The growth mode and morphology of Li_2O_2 depend on a number of factors including rates of nucleation and precipitation, which in turn depend on local electronic and ionic conductivity, in the electrolyte and to/from the electrolyte/electrode interface, while the entire micro-environment is under an applied voltage.[15] There have been several studies that theoretically investigated different phases of Li_2O_2, defective Li_2O_2, or amorphous Li_2O_2,[8, 16-18] or the Föppl structure with a substitutional or interstitial dopant atom.[8, 19-20] None so far have considered the possibility of a dopant fundamentally altering the structure of Li_2O_2. Herein, we theoretically explore the potential energy surfaces (PES) for Li_2O_2 doped with Na, Mg, Co, Ni, and Ba, which are commonly found either as ingredients of Li-based electrodes or as solvated components of the electrolyte, using global optimization techniques based on evolutionary algorithms and density functional theory (DFT) calculations, and we investigate the effects that these dopants have on the geometric and

electronic structure of Li_2O_2. We find that the incorporation of these dopants leads to local structures that differ significantly from the Föppl structure and reflect instead the preferred oxygen coordination of the dopants. Some of the doped local structures have free energies of formation that are lower (i.e. more favorable) than that of Li in the Föppl structure, but no transition to metallicity is observed that may be associated with enhanced electric conductivity.

5.2. Results and Discussions

5.2.1. Bulk Li_2O_2

The properties of Li_2O_2 has been theoretically studied both with[16, 123, 172, 187-188] and without[8, 19] defects. The predicted band gap is 1.88 eV (GGA-RPBE) and 4.5 eV (HSE06), respectively (see Figure 5.1a), which agrees with the literature results of 1.9 eV (GGA),[13,189] 4.5 eV (HSE06),[190-192] and 4.91 eV (G_0W_0).[13] Radin et al. reported a band gap of 6.63 eV using a modified HSE calculation (mixing parameter of exact exchange α=0.48 instead of 0.25).[8] In Li_2O_2 there are two symmetry-inequivalent Li sites, trigonal prismatic (TP) and octahedral (Oct) (Figure 5.1c and 5.1d), which a dopant atom can substitutionally occupy. The formation energy of a neutral Li vacancy (V_{Li}) in the TP site is 0.06 eV lower than in the Oct site, which agrees with what was found earlier.[8] The difference in formation energy for V_{Li} increases to 0.33 eV using HSE06 (the TP site still being more favorable than the Oct site), which is in close agreement with the difference of 0.34 eV (HSE06) reported by Radin et al.[8] The fully relaxed $Li_{15}O_{16}$ unit cell with a V_{Li} in the TP site has the lattice constant along the *c* axis contracted by 2.23 % (from *c*=7.61 Å to 7.44 Å).

The total projected DOS for Li_2O_2 with a neutral V_{Li} in the TP site is shown in Figure 5.1b. The V_{Li} has a negligible effect on the RPBE electronic structure, but according to HSE06 a split develops between the spin-up and spin-down states at the top of the oxygen $\pi*$ band with the Fermi level crosses the top of the spin-down states of the oxygen $\pi*$ band, in agreement with prior studies

based on HSE06.[190-191] New states appear in the band gap (Figure 5.1b), which was also reported by Varley et al.[192] but not by Lyu et al.[191] We surmise that in the latter study the projected DOS on only a subset of the atoms in the unit cell was reported. These gap states are localized on O_2 moieties adjacent to the V_{Li} and also have O_2 π^* characters (Figure 5.1d and 5.1e). In contrast, the spin-down states at the Fermi level are spatially delocalized (Figure 5.1c), consistent with the presence of a state that crosses the Fermi level in the band structure (Figure B13). This characteristic is in line with the assertion by the handful of studies in the literature that examined the electronic structure of Li_2O_2 with V_{Li},[13, 191-192] that neutral V_{Li} enhances electronic conductivity in Li_2O_2, thereby reducing the overpotential for charging. This is in addition to other mechanisms that enhance the bulk conductivity of Li_2O_2, such as polaron formation and defect mobility.[8, 13, 193]

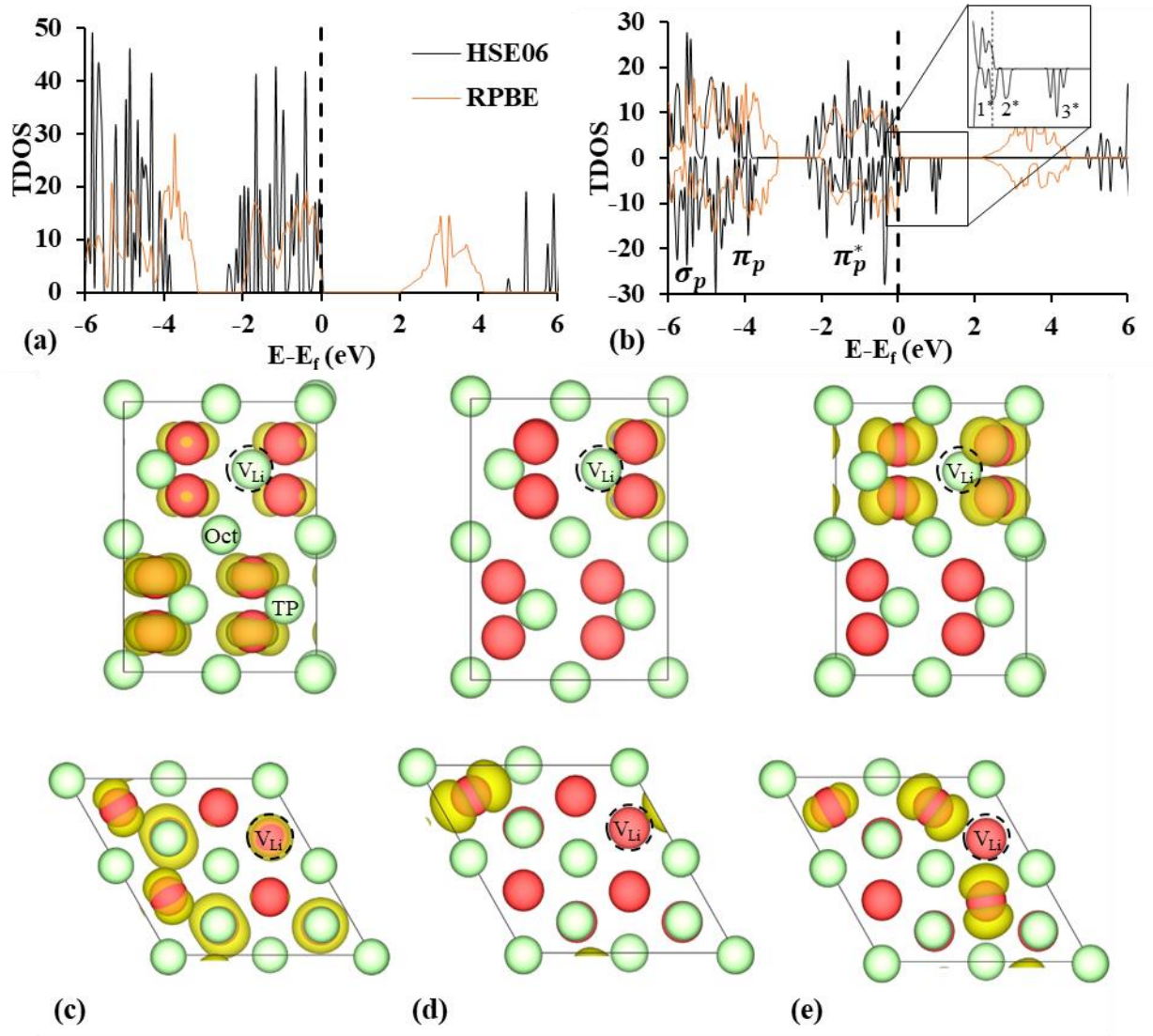

Figure 5.1: Total density of states of (a) Li_2O_2 and (b) Li_2O_2 with a V_{Li}. The HSE06 charge density of the states labeled 1^*, 2^* and 3^* in (b) are shown in (c), (d), and (e) respectively, with the top panel in the *yz* view and bottom panel in the *xy* view. The iso-surface corresponds to an electron density of 0.0025 e/Å^3. Color code: Li = green, O = red.

5.2.2. Doped Li_2O_2

In Figure 5.2, we compare the difference in free energies of formation ($\Delta\Delta G_f$, relative to Li) of doped microstructures optimized by USPEX and their counterparts that were obtained by energy-minimizing directly substitutionally doped (DSD) Li_2O_2 or Li_2O_2 with a V_{Li}. In the latter case

non-equivalent locations of V_{Li} with respect to the dopant atoms were checked. The $\Delta\Delta G_f$ accounts for the solvation energy of individual ions (the values shown in Figure 5.2 are specific for DMSO), which would be affected by different solvents with different donor and acceptor numbers. All the USPEX-optimized structures are more stable than their DSD counterparts except $Li_{15}NaO_{16}$, for which the USPEX-optimized structure is slightly less stable than its DSD counterpart (by 0.13 eV in RPBE). The Ba doped structures have the largest difference between the USPEX-optimized and DSD structures (ca. 4 eV in RPBE). Below we refer solely to the USPEX-optimized structures. All doped structures have larger volumes than their Li counterparts (Figure 5.3), and especially so with Ba, Co, and Ni as dopants. With Mg and Na both the change in structure and the increase in volume are minor compared to the lattice of Li_2O_2 (USPEX Mg and Na doped structures shown in SI). This reflects the large ionic size of Ba compared to the other dopant atoms, and the significant changes caused by Co and Ni on the local structure in Li_2O_2 (see below).

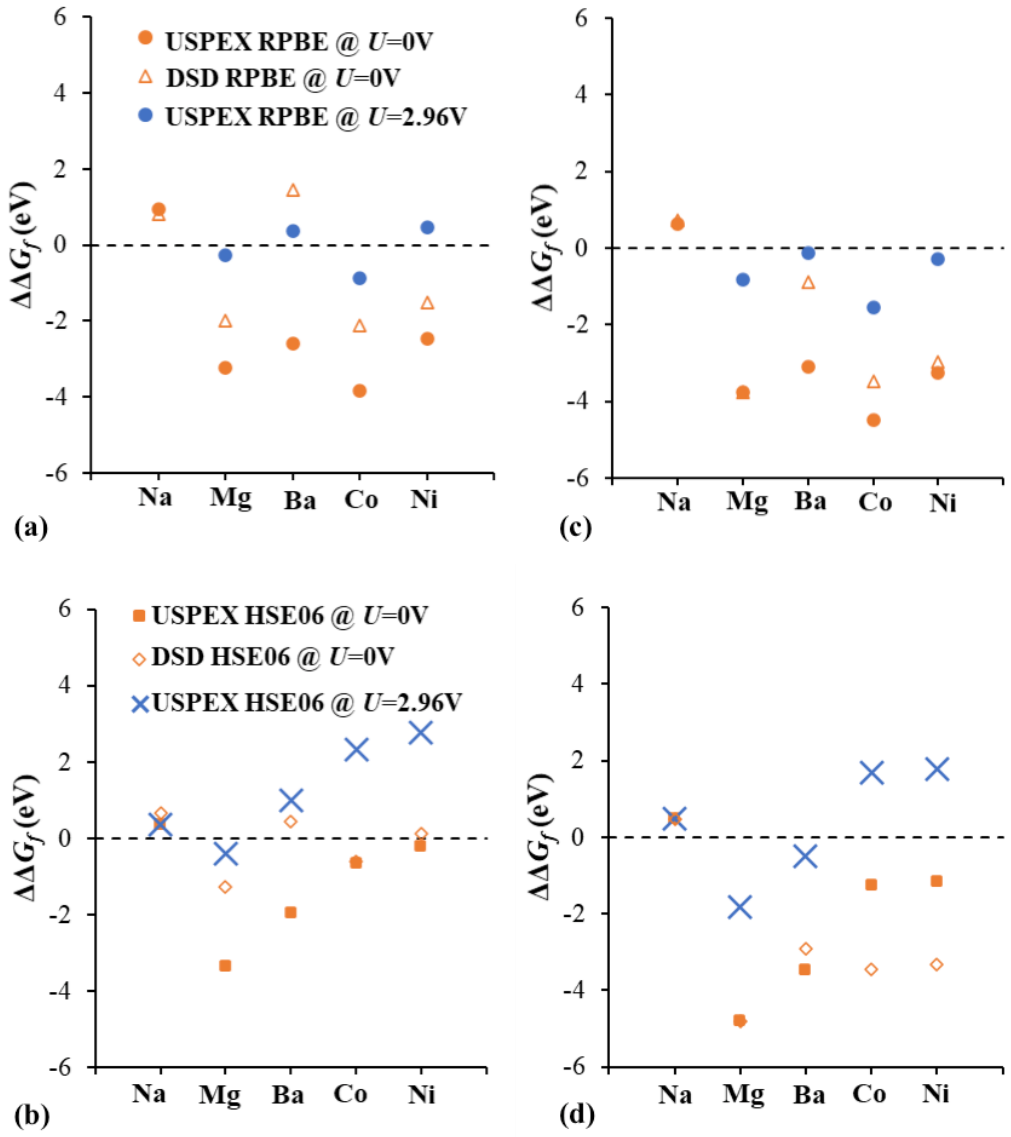

Figure 5.2: Difference in free energy of formation ($\Delta\Delta G_f$) for USPEX optimized $Li_{15}DO_{16}$ (a, RPBE; b, HSE06) and $Li_{14}DO_{16}$ (c, RPBE; d, HSE06) compared to Li_2O_2 and Li_2O_2 with a V_{Li}, respectively. Directly substitutionally doped structures ("DSD") are included in (a, c) for comparison. Two different electrode potentials are considered: U = 0 V and U = 2.96 V. Na is a monovalent cation like Li, so its $\Delta\Delta G_f$ with respect to Li does not change with U.

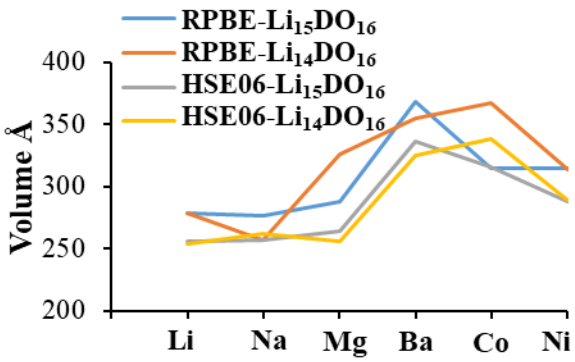

Figure 5.3: Volumes (in $Å^3$) of USPEX-optimized $Li_{15}DO_{16}$ and $Li_{14}DO_{16}$ unit cells, in comparison to Li_2O_2 without and with a V_{Li}.

RPBE and HSE06 predict different most stable dopants. At U = 0 V, all structures doped with divalent atoms are more stable than Li_2O_2 regardless of composition, while doping with Na, which is a monovalent atom, is less stable. This broadly parallels the formation potentials of the corresponding bulk peroxides/oxides as compared to that of Li_2O_2 (Table 1). Co is the most stable dopant according to RPBE, yielding $Li_{15}CoO_{16}$ ($\Delta\Delta G_f$ = -3.83 eV) and $Li_{14}CoO_{16}$ ($\Delta\Delta G_f$ = -4.50 eV), whereas HSE06 predicts Mg to be the most stable dopant, with $Li_{15}MgO_{16}$ and $Li_{14}MgO_{16}$ having $\Delta\Delta G_f$ of -3.35 eV and -4.79 eV, respectively. At U = 2.96 V, RPBE predicts the Co and Mg doped $Li_{15}DO_{16}$ structures to be more stable than Li_2O_2, and the Co, Mg, Ba and Ni doped $Li_{14}DO_{16}$ structures to be more stable than Li_2O_2 with a V_{Li}. On the other hand, HSE06 predicts only the Mg doped $Li_{15}DO_{16}$ structure to be more stable than Li_2O_2, and the Mg and Ba doped $Li_{14}DO_{16}$ structures to be more stable than Li_2O_2 with a V_{Li}. Additionally, Table 5.1 compares the accuracy of RPBE and HSE06 functional in reproducing experimental formation potential. For Li_2O_2, MgO_2, BaO_2 and NiO HSE06 tends to perform better than RPBE. For CoO and Na_2O_2 RPBE tends to perform much better. For CoO, HSE06 tends to overestimate by 2 V which is

indicative that HSE06 tends to significantly overestimate the Co-O bond. This is also evident when comparing DSD-$Li_{14}CoO_{16}$ with HSE06 and RPBE. For the HSE06 DSD-$Li_{14}CoO_{16}$ the Co is coordinated by 6 O atoms which is higher than u-$Li_{14}CoO_{16}$ where the Co is coordinated by 4 O atoms thus showing increased stability with HSE06. A similar phenomena occurs with DSD-$Li_{14}NiO_{16}$ where the Ni-O bond tends to be much more stable as compared to RPBE. As the entire search of the potential energy surface was done using RPBE functional in USPEX, the parity of the Co-O bond between HSE06 and RPBE functional cannot be directly factored. For the case of Li_xCoO_{16} composition, RPBE can more accurately account for bonding nature and is thus used to define its electronic structure.

Table 5.1: Formation potentials (E^o, in V vs. Li/Li^+) of the bulk peroxides or oxides of Li and the dopants.[57, 194] All formation potentials are reference to respective bulk solid and molecular oxygen as calculated by either RPBE or HSE06 functional.

	RPBE	**HSE06**	**Experimental**
Li_2O_2	2.62	2.94	2.96
Na_2O_2	2.23	2.06	2.66
MgO_2	3.13	3.58	3.62
BaO_2	2.67	2.99	3.19
CoO	3.94	5.91	3.91
NiO	2.98	3.51	3.89

Replacing Li with Mg or Ba, both of which are strictly divalent, injects an extra electron into Li_2O_2, forming a small polaron on a nearby O_2 moiety and cleaving a single O-O bond (Figure 5.4a). As Kang et al. have shown,[190] this local arrangement to accommodate an extra electron in Li_2O_2 is not stable. Instead, removing a Li accommodates the extra electron so that all O_2 moieties remain in the peroxo state. Co and Ni, on the other hand, are inherently multivalent, which results in the breaking of multiple O-O bonds and formation of oxo groups. Introducing a V_{Li} does not prevent this from occurring (Figure 5.4b).

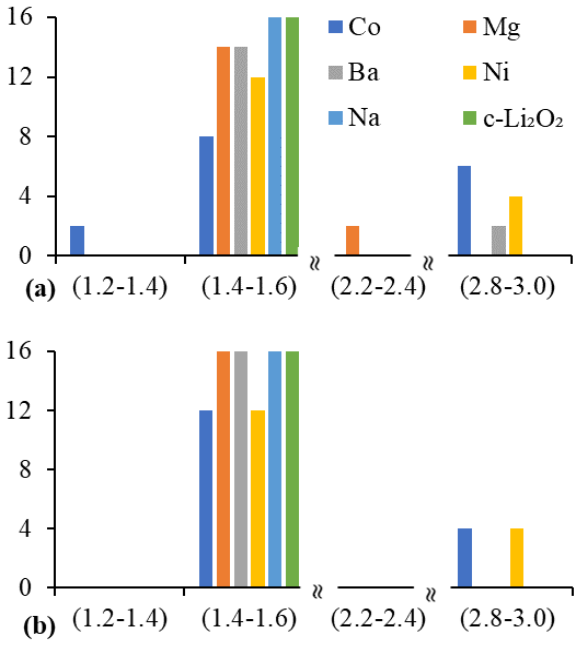

Figure 5.4: Nearest O-O distances ($d^{min}_{O\text{-}O}$ in Å) for all O atoms in USPEX-optimized (a) $Li_{15}DO_{16}$ and (b) $Li_{14}DO_{16}$ structures using HSE06 functional. $d^{min}_{O\text{-}O}$ between 1.4 and 1.6 Å represents oxygen in the peroxo state while values of 2.2 Å and above indicates oxygen in the oxo state.

Based on the results presented in Figure 5.2 we can predict, with greater confidence than for the other dopants, that it is thermodynamically favorable for Mg and Ba to be incorporated into Li_2O_2. The recent work by Matsuda et al. has confirmed the significant incorporation of Mg and Ba into discharge products of non-aqueous Li-O_2 cells.[175] They reported that doped products had low crystallinity. The presence of the alkaline earth metal dopants improved both the coulombic efficiency and the charging performance, although a large *decrease* in the discharge potential was seen with Mg. What was not directly addressed in that study is whether the discharge product was a mixture of Li-O_x and e.g. Mg-O_x, or a single Li-Mg-O_x phase. The formation potentials of the bulk alkaline earth metal peroxides (Table 5.1) suggest that Mg is much more likely than Ba to form a separate phase. However, the $\Delta\Delta G_f$ for incorporation of Mg into Li_2O_2 (with a V_{Li}; Figure

5.2d) is significantly higher than the difference in E^o of MgO_2 and Li_2O_2, which suggests that incorporation into Li_2O_2 (provided that Li_2O_2 is formed simultaneously) is favored over formation of a separate phase. The relative concentration of a dopant vs. Li and kinetic factors can also influence the doping process but they are beyond the scope of the current study.

Most experimental Li-O_2 cathodes discharge at a 0.2~0.4 V overpotential,[139-140, 195] thus making some of the doped structures possible despite being slightly less stable than Li_2O_2, such as Na. Lyu et al.[191] performed HSE06 calculations and reported directly substituted $Li_{15}NaO_{16}$ and $Li_{14}NaO_{16}$ to be 1.3 eV and 0.9 eV less stable respectively than $Li_{16}O_{16}$ (i.e. $(Li_2O_2)_8$) and $Li_{15}O_{16}$. These values are somewhat larger than our values shown in Figure 5.2b and 5.2d, but it should be kept in mind that different reference states were used. Lyu et al. used a reference state relative to bulk Li and Na metals. Their experiments show that discharge overpotential increased by ca 0.1 V, but reduced charge overpotentials by just adding a very low Na+ amount of 10% and increased energy efficiency. This necessarily comes at the expense of capacity, as more Na tends toward the capacity of a corresponding Na-O_2 cell. Detailed characterization work demonstrates that Na is incorporated into Li_2O_2 forming amorphous products with Li coordination number between Li_2O_2 and LiO_2, which the authors interpreted as defective Li_2O_2 with V_{Li}.

In our case $\Delta\Delta G_f$ ($Li_{15}NaO_{16}$) = 0.37 eV and $\Delta\Delta G_f$ ($Li_{14}NaO_{16}$) = 0.48 eV using HSE06 functional where in our case $\Delta\Delta G_f$ is defined by Eq. 1. The larger difference in formation energy can be attributed due to the different reference state, where the solvated ion reference state would let us account for de-solvation of ions from solution to bulk. The $Li_{14}DO_{16}$ structures are calculated to be more stable than their $Li_{15}DO_{16}$ counterparts for all the dopants except Na, which suggests that the incorporation of these dopants into Li_2O_2 will likely induce Li vacancy formation. Replacing Li with Mg or Ba, both of which are strictly divalent, injects an extra electron into *c*-

Li_2O_2, forming a small polaron on a nearby O_2 moiety and cleaving a single O-O bond (Fig. 3a). As Kang et al. have shown,[190] this local arrangement to accommodate an extra electron in *c*-Li_2O_2 is not stable. Instead, removing a Li accommodates the extra electron so that all O_2 moieties remain the peroxo state. Co and Ni, on the other hand, are inherently multivalent, which results in the breaking of multiple O-O bonds and formation of oxo groups both in the USPEX and DSD structures. Introducing a V_{Li} as a site defect in DSD structure or as a compositional variation in USPEX does not prevent the breaking of O-O bonds (Fig. 5.3b). In Li_2O_2 with V_{Li} the O-O bonds in the one of the layers are contracted to 1.434 Å which is contracted from that in bulk Li_2O_2 of 1.505 Å. In the case of DSD-$Li_{14}CoO_{16}$ all the O-O bonds in the top layer remain in the bulk value.

The structures calculated with RPBE functional have their charge density calculated at a higher kpoint mesh for accurate description of DOS and associated bandstructure(shown in SI). Thus, all the study below for electron tunneling through these structures are done using RPBE functional. Below we will discuss in detail the Co-doped structures, $Li_{15}CoO_{16}$ and $Li_{14}CoO_{16}$ as they are the most stable doped structures predicted by RPBE and has states crossing the fermi level at both compositions that could lead to electron tunneling. The Mg, Ni, Ba, and Na doped structures are shown in the Supplemental Information. For both compositions considered, the configurations have all 3 oxidation states of O atom i.e. oxide, superoxide and peroxide as will be shown in the latter half of the paper. Thus, these structures don't represent a complete peroxide discharge product, though all the structures obtained has most of the O atoms in the peroxide state. This representation is in empirical agreement with experimental findings[191, 196] that during discharge due to various reasons like current localization,[197] presence of dopants,[175, 182-183] or local variation in of oxygen gas across the electrode[16] can cause a variation in the oxidation states of O atom in the discharge products. Soluble electrocatalyst[176, 186, 198] which can be incorporated into

the bulk discharge product could cause a local change in oxidation state of O atom immediately adjacent to the electrocatalyst.

In Figure 5.6, we show the USPEX-optimized $Li_{14}CoO_{16}$ and $Li_{15}CoO_{16}$ doped structures. For $Li_{15}CoO_{16}$, out of the 16 O atoms, 10 atoms form dimers 8 of which are in peroxide state while the remaining 2 are in superoxide state. 6 O atoms are in the oxide phase in which 4 O atoms are tetragonally coordinated with the Co atom and 2 O atoms octahedrally coordinated with Li atoms forming bonds in the range of 1.9-2.01 Å. While for $Li_{14}CoO_{16}$, 12 O atoms form dimers and 4 O atoms are in the oxide phase directly coordinated to Co as shown in Figure 5.5. The state of the oxygen atom is based on 2 parameters, first, the bond length of the O-O distances $d_{\text{O-O}}^{\text{min}}$, for the peroxide state O atoms is ~1.49 Å to 1.58 Å while for the superoxide state O atom is ~1.22 Å to 1.39 Å. The oxide state of the O atom is initially confirmed visually from the schematic followed by bader charge analysis, all the peroxide O atoms in the USPEX structures were compared to the O atoms in Li_2O_2 depicted in Figure 5.1 in terms of charge and $d_{\text{O-O}}^{\text{min}}$. For $Li_{14}CoO_{16}$, the oxide O within the bulk form a sub-structure that is akin to an LiO_2 dimer.[5] A general summary of the states of the O atom for the remaining USPEX structures is shown in the histogram in Figure 5.3. All the bulk structures with O atoms in the oxide state tend to display DOS that cross the Fermi level with RPBE functional as shown in Figure 5.5 and Figure B5 and B9. This crossing gets withdrawn and none of the occupied states crosses the fermi level while using HSE06 functional. Using the HSE06 functional, new states appear in the bandgap as seen in Figure 5.5a and 5.5b, where a new state appears in the spin-down channel for $Li_{14}CoO_{16}$. Similar phenomena occur for the other USPEX generated doped structures like $Li_{15}BaO_{16}$, $Li_{15}MgO_{16}$, $Li_{14}NaO_{16}$, and $Li_{14}NiO_{16}$ effectively reducing the band gap in half in the spin down channel. This reduction in band gap would have a direct impact on the reduction of overpotential which is already seen experimentally for Ba.[175] In

an ideal direct substitution case as seen in DSD, whenever an extra electron is injected into a Li_2O_2 (in this case through Co^{+2} dopant), it results in elongation and cleavage of the O-O bonds as $d_{min\ O\text{-}O}$ goes beyond 2.2 Å as mentioned earlier[190] and form small polaron on the isolated O atom. This self-trapping of electrons was further shown by Kang et. al. to limit electron mobility. Instead in our case the extra electron imbalance due to replacing neutral Li by neutral Co would result in cleaved bonds and isolated O atoms. As the cobalt oxide formation potential is higher than molecular Li_2O_2 (see table 5.1), we see that 4 O atoms coordinate while the 2 O atoms in the oxide phase in the system due to the extra electron would be coordinated by ionic Li atoms (for $Li_{15}CoO_{16}$). For a high concentration of dopants and the resultant strain due to ionic size of Co, the overall solid would no longer maintain its original $P6_3/mmc$ Föppl structure as evidenced from Figure 5.6.

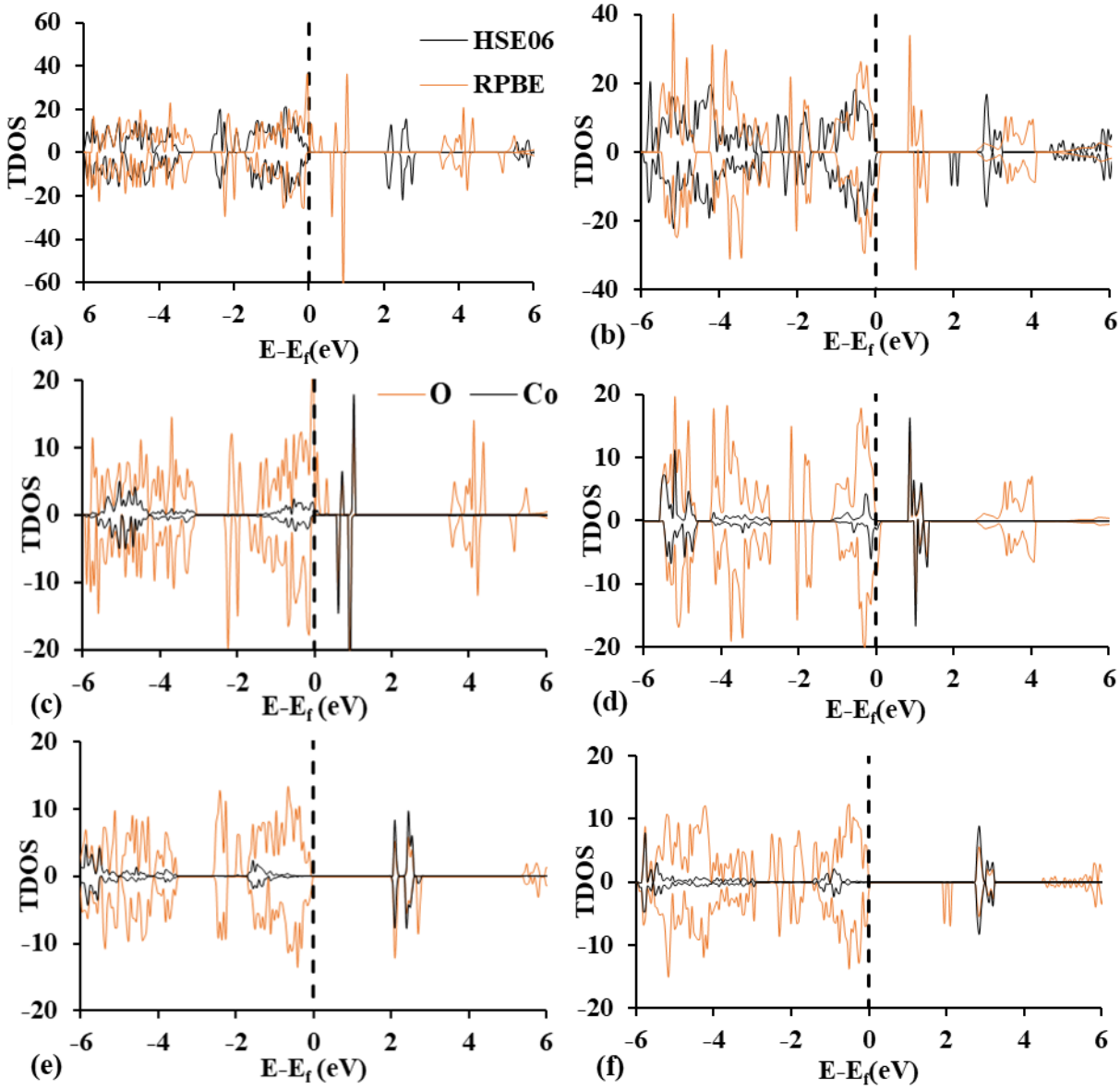

Figure 5.5: The total density of state (TDOS) for the USPEX-optimized structures using RPBE and HSE06 functional for (a) $Li_{15}CoO_{16}$ and (b) $Li_{14}CoO_{16}$. Contribution to the density of state for Co and all O atoms in $Li_{15}CoO_{16}$ using (c) RPBE and (e) HSE06. While the Co and all O atoms spatial charge contributions in $Li_{14}CoO_{16}$ is shown in (d) using RPBE and in (f) using HSE06.

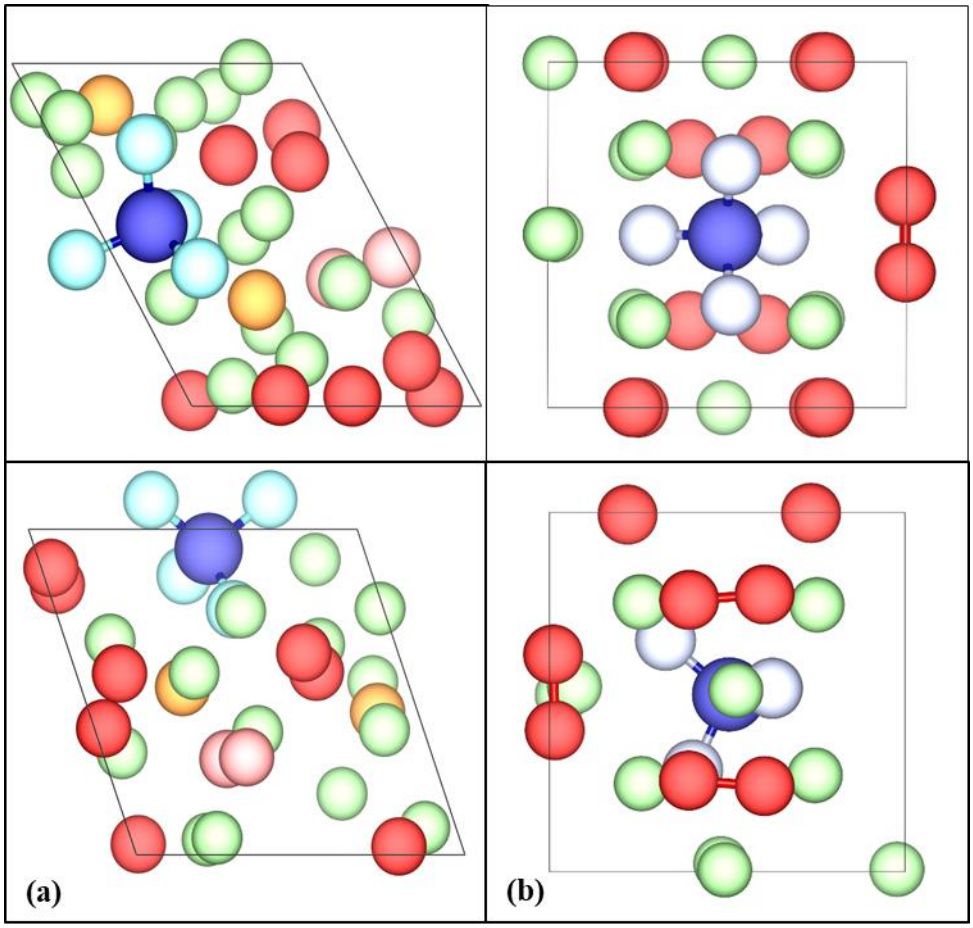

Figure 5.6: xy view (top panels) and yz view (bottom panels) of USPEX generated (a) $Li_{15}CoO_{16}$ and (b) $Li_{14}CoO_{16}$ structures. Oxygen atoms are colored differently based on oxidation and bonding nature. Color code: Li = green, Co = dark blue, O in peroxide state = red, O bonded in oxide state and bonded to Co in $Li_{15}CoO_{16}$ = light blue, O bonded in oxide state and bonded to Co in $Li_{14}CoO_{16}$ = silver, O in superoxide state = pink, O in oxide phase coordinated with surrounding Li atoms = orange

The individual contribution by Co and O at the Fermi level in $Li_{15}CoO_{16}$ and $Li_{14}CoO_{16}$ are shown in Figure 5.5, with the spatial charge distribution over energy range of -1 eV to 1 eV near the Fermi level. We followed the procedure established by Timoshevskii et al.[20] to estimate electron mobility through tunneling. For the case of *u*-$Li_{15}CoO_{16,}$ the entirety of the charge is concentrated on Co and the octahedrally coordinated O atoms, the spin up energy band of Co crosses the Fermi level by 0.108 eV. For $Li_{14}CoO_{16}$, the spatial charge distribution is centered on

the Co and peroxide O atoms. The energy band of Co in the spin down state crosses the Fermi level by 0.17 eV. Conductivity or electron mobility is not a fixed quantity but can vary during discharge and charge because the cell potential can affect the defect and doping concentration through variations in the chemical potential of all the metal cations. Conductivity can be due to migration of charge (ionic conductivity) or tunneling of electron/polaron transport (electronic conductivity). Previously, Viswanathan et. al.[188] under specific conditions showed that electrons can tunnel through 5nm thick Li_2O_2 layers. The thickness of our microdomains are less than 5 nm for all compositions and dopants. Assuming that the electrons can tunnel through our USPEX generated solids, we can empirically estimate the electron mobility in x, y and z direction using Einstein's relation $\mu_e = eD/k_bT$ and $D = L^2/\tau$ where L is the distance between neighboring dopant atoms (assuming charge travels through dopant and not O atoms) and τ is the inverse lifetime of electrons in a given valence orbital and can be estimated as $1/\tau=\gamma/\bar{h}$ where γ is the valence orbital width crossing the Fermi level.[20] Using this the electron mobility in x, y and z direction are $\mu_x = 39.66$ cm^2/[Vs], $\mu_y = 58.10$ cm^2/[Vs] and $\mu_z = 55.56$ cm^2/[Vs] for $Li_{15}CoO_{16}$. The electron mobility values are $\mu_x = 36.81$ cm^2/[Vs], $\mu_y = 37.51$ cm^2/[Vs] and $\mu_z = 34.87$ cm^2/[Vs] for $Li_{14}CoO_{16}$. The improvement to mobility due to the other dopants is shown in table S2. In all cases, the electron is assumed to transfer through the dopant atoms. These values are significantly higher than the polaronic hopping estimates calculated for Li_2O_2 (10^{-9}-10^{-10} cm^2/[Vs]).[190] While these values are considerably higher than polaronic hopping they are still very low as compared to a semiconductor like pure undoped crystalline silicon which has an electron mobility of 1400 cm^2/[Vs].[199] These studies are carried out using the RPBE functional. A more accurate treatment could be employed in the future after more experimental evidence of the dominant charge transport through such amorphous-like structure with dopants is available. Using

RPBE functional we observe electron mobility improvement for the USPEX-optimized $Li_{14}NaO_{16}$, $Li_{14}MgO_{16}$, $Li_{15}NiO_{16}$, $Li_{14}NiO_{16}$, $Li_{14}BaO_{16}$ along with *c*-$Li_{15}O_{16}Ni$ and *c*-$Li_{15}BaO_{16}$ which are DSD structures. The *u*-$Li_{15}NiO_{16}$ structure shows the highest improvement to electron mobility with $\mu_x = 188.6$ cm^2/[Vs]. When we use the above equation to calculate the electron mobility through V_{Li} assuming a tunneling mechanism than the mobility is $\mu_x = 31.74$ cm^2/[Vs], $\mu_y = 31.74$ cm^2/[Vs] and $\mu_z = 46.93$ cm^2/[Vs] for RPBE functional. When a polaron hopping mechanism for a charged V^{-}_{Li} is considered, Radin et. al. got $\mu = 2 \times 10^{-7}$ cm^2/[Vs] along all three directions.[8] Thus, it is necessary to determine the exact mechanism (polaron hopping or electron tunneling) for transport of electron to determine the overall benefit of doping. Determination of different transport models is beyond the scope of the current study.

5.3. Conclusions

Periodic DFT calculations coupled with evolutionary algorithm have been performed to study the possibility of doped microstructures of Li_2O_2 of 2 compositions i.e. $Li_{15}DO_{16}$ and $Li_{14}DO_{16}$. The dopants considered were Mg, Na, Ni, Co and Ba. We found that there exists a series of structures that are lower than substitutionally doped Li_2O_2 structures of the same composition and pure bulk Li_2O_2 itself. The difference between the substitutionally doped structure and USPEX generated structures is that the USPEX-optimized structures might not necessarily be crystalline in nature and the O atoms are found to be in multiple oxidation states i.e. peroxide or superoxide or oxide states. We showed that the USPEX-optimized structures can form more stable bulk structures than Li_2O_2 using both RPBE and HSE06 functional for both compositions. We further showed that through an empirical electron mobility model that the several dopants boast the mobility of electrons, which can have an overall positive effect on the recharge process. As this is a global

optimization technique, we reiterate that there is a possibility of other more stable structures to exist. The above results also warrant future studies for more detailed electron transport studies on said structures.

Chapter 6. Summary and Recommendations for Future Work

6.1. Summary

The main conclusion of this dissertation have been to identify the fundamental understanding the many atomic scale phenomena associated with the electrochemistry of oxygen with lithium, sodium and potassium. These have important implications for metal-O_2 batteries and by extension technologies associated with oxygen reduction reactions and oxygen evolution reactions. We have explored surface adsorption phenomena of metal superoxide and superoxide anion on a model surface like Au(111) and Au(211), a basal plane and step edge. We show that the MO_2 species and O_2^- are materially affected by the presence of an electric field that is set up the electrode-electrolyte interface also known as the electrochemical double layer. The positive electric field effect independently on the above mentioned species is minor but when solvent effect is included in the form of explicit solvent molecules of DMSO then the coupled influence of the electric field and solvation is substantial on the free energy of adsorption on the order of ~|0.4| eV. Thus making it essential to include the above mentioned effects. We further showed that for the MO_2 species, the electric field effect can be included through a first order fit of the electrostatic stark effect where the effect is estimated by the product of the electric field ε and zero field dipole moment μ_0. For the O_2^- intermediate, it becomes necessary to check the overall polarizability of the species in the specific environment of the species under an electric field.

Our findings related to the surface phenomena of metal O_2 batteries and related influence of solvation leads us to investigate solvent only phenomena and the reaction mechanism between solvated metal cation and superoxide anion in solution phase. While there is existing literature for Li-O_2 chemistry, there is no study that elucidates the reaction between solvated Na^+ /K^+ with O_2^-. Given that alternative technologies like the Na-O_2 and K-O_2 chemistries are becoming more

relevant as a technologies due to the inherent safety associated with the handling of Na and K as compared to Li. Na and K metals are also significantly more cost effective in terms of fabricating pure metal electrodes. Thus, it is imperative to have a fundamental perspective into how the solution phase reaction mechanism and the associated dimerization phenomena. We investigated the reaction mechanism between the metal cations and superoxide anion implicitly solvated using a SCAR scheme. We used DMSO and ACN as solvents. We show that the key difference of Li^+-O_2^- solution phase reaction mechanism to that of Na^+-O_2^- and K-O_2^- is the associated high barriers for disproportionation of the high energy superoxide dimer to peroxide molecule for the latter two metals. In all three cases dimerization occurs through the formation of a ring shaped structure and then undergoes a ring opening step to form a high energy dimer. We considered precipitation phenomena for all three metals and showed that the NaO_2 and KO_2 tends to have precipitation energies that are net downhill from the given reference state and would most likely form. For LiO_2, this would not occur as the bulk solid is not stable at room temperature. We also considered dimerization and trimerization of metal superoxide and peroxide in solution for all three metals. In solution only Li_2O_2 tends to form dimers and trimers showing that for all other superoxide and peroxide the nucleation phenomena would occur on the surface of the electrode. We also developed two novel stochastic approaches to probe the potential energy surface for the dimers and trimers called RASS and R-Kick outlined in appendix A.

Lastly, we turned our attention to the final discharge product for the ORR discharge process for Li-O_2 batteries. We were limited to only the Li-O_2 chemistry due to the extremely costly computations involved. We saw recently that in many experimental studies, solvated metal ions other than Li^+ can get incorporated into the discharge product. This led to a favorable reduction in the charging overpotential of the battery. Using evolutionary algorithm as implemented in USPEX

we probed the PES to show that if the Li_2O_2 discharge product is doped with a sufficiently large enough percentage of dopants like Ba,Co, Na, Mg and Ni, then a bulk phase separate (amorphous or crystalline) from *P6₃/mmc* Föppl structure of Li_2O_2 would form. The dopants considered were selected arbitrarily and are commonly found solvated electrolyte ions in batteries. We considered two composition i.e. (a) $Li_{15}DO_{16}$ and (b) $Li_{14}DO_{16}$. We showed that these doped solids could form thermodynamically through an analysis of the USPEX and DSD structures where the USPEX structure is preferred over the DSD and the $Li_{14}DO_{16}$ which reflects a composition with a vacancy V_{Li} is preferred over a stochiometric composition. We further investigate the electronic structure to empirically estimate the electron mobility. We show that the USPEX generated doped solids have μ_x, μ_y and μ_z value that are many order of magnitudes higher than *P6₃/mmc* structure of *c*-Li_2O_2.

6.2. Recommendation for future work

Our current work focused on electrode surface, solution and bulk phenomena. A natural extension would be to study the bulk properties of the discharge product of Na-O_2 and K-O_2 batteries. Both, Na-O_2 and K-O_2 batteries have similar problems of insulating discharge product and high overpotential as Li-O_2 batteries. An in-depth investigation to see if the doping strategy with solvated metal cations would have a net beneficial effect on the discharge product of Na- O_2 and K-O_2 batteries would be warranted.

The next logical direction of the current doping studies would be to suggest the mechanism for the formation of these discharge product. With our current understanding, there are two routes for the formation of the doped discharge product as a microdomain. The first would be the reaction of the dopant metal cation and the Li^+/O_2^- pair. The one current caveat is that for solvents like DMSO the divalent dopant metal cation would have a higher solvation energy than O_2^- and Li^+.

Thus, the ions would be solvent separated in a high donor number and acceptor number solvent. The other route, which is through adsorption of metal cations on the surface of already formed Li_2O_2 surface, would be a more plausible mechanism for formation of microdomains of doped solids. Earlier it was shown theoretical that a wulff construction that the (0001) surface would be the dominating surface by about 79.3% to 95%[200-201] followed by small amounts of the $(11\bar{2}0)$ surface. We conducted preliminary studies for the adsorption of the dopant cations on the surface of (0001) surface using the following equation

$$\Delta E_{ads} = E_{Li_2O_2+D} - E_{Li_2O_2} - G_{D^{m+}} + mU \quad (6.1)$$

Where the ΔE_{ads} is the adsorption energy of the dopant on (0001) Li_2O_2 surface, $E_{Li_2O_2+D}$ is the total energy of the dopant adsorbed on the surface, $E_{Li_2O_2}$ is the total energy of the slab, $G_{D^{m+}}$ is the free energy of the solvated dopant ion in DMSO and U is the potential of the surface. The surface in consideration is a 4 x 4 x 2 (0001)Li_2O_2 surface as shown in Figure 6.1

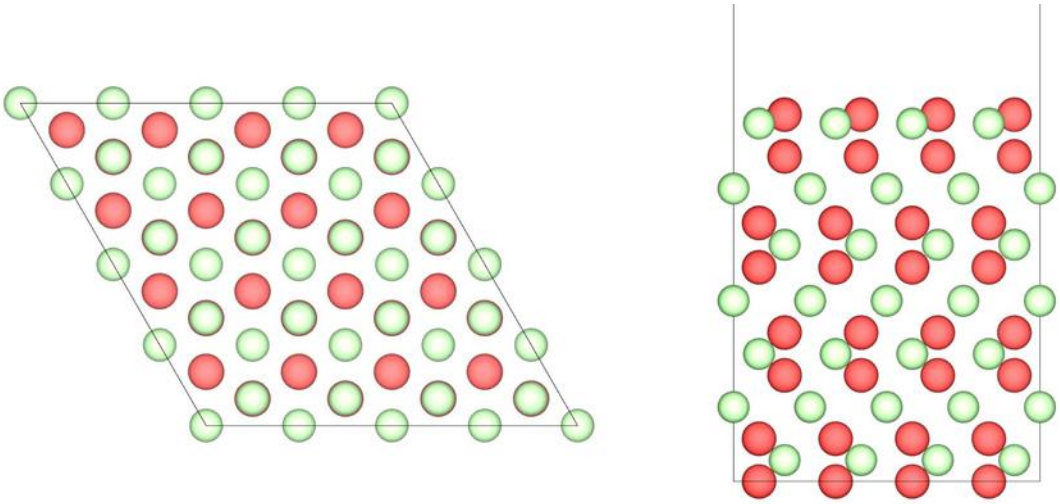

Figure 6.1: 4x4x2 layers of relaxed (0001) Li_2O_2 surface as optimized by RPBE functional. The green spheres represent Lithium and red spheres represent Oxygen. The solid line represents the cell boundaries.

The adsorption energy for the respective dopant ions is higher than that of Li^+ as shown in Figure 6.2. Thus presenting a viable route for growth of microdomains. The next step would be to investigate if the adsorption would be favored on defective sites like Li, O and O_2 vacancies. Following that we would check the co-adsorption of O_2 i.e. simultaneous adsorption of D^{m+} and O_2^- would occur.

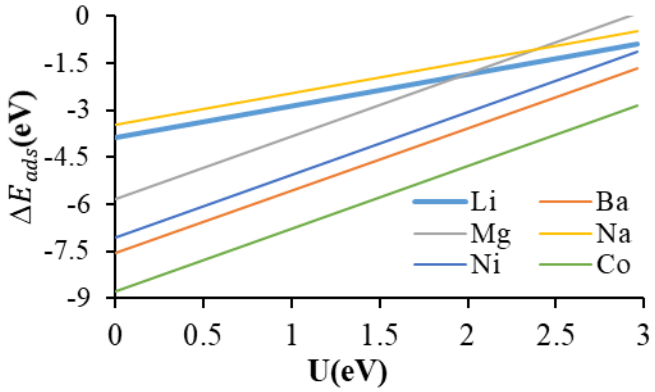

Figure 6.2: Adsorption energy of different dopant ions on the surface of (0001)Li_2O_2 as a function of the applied potential.

Overall, in this dissertation we have shown the successful application of first principles density functional theory to elucidate the fundamental mechanism associated with surface adsorption, solution phase reaction and bulk solid of discharge product for metal-O_2 batteries. Our conclusions help build on existing literature and enable insights in many fundamental processes that would enable future scientist to tackle the various engineering issues associated with metal-O_2 batteries and enable the successful commercialization of these batteries into the mainstream energy storage market.

Appendix A. Efficiency Enhancements of a Restricted Stochastic Search Algorithm for Locating Local and Global Minima[2]

A.1. Introduction

With the rise of new chemistries in the fields of energy storage, heterogeneous catalysis, semiconductors and pharmaceuticals, the ability to accurately identify low-energy configurations of nanoclusters of atoms [202-211] has become critical for future development. One cannot solely rely on chemical intuition [205, 212-214] due to the possibility of low symmetry isomers, counterintuitive bonding mechanisms, and exponential increase in the number of minima on the potential energy surface (PES) with increasing cluster size. The experimental detection of these species is limited by available analytical techniques to identify these clusters. As a result, a large number of methods for identifying local (or global) minima for systems with arbitrary atomic compositions have been devised. Popular examples include genetic algorithm [203, 215], simulated annealing [216], basin hopping [217], and minima hopping [218]. Other methods have also been reported [219-222].

Of all these methods arguably the simplest in both concept and implementation is the stochastic search, sometimes referred to as the Kick method, which was first described within an *ab initio* framework by Saunders [223]. In this technique, a search for minimum-energy structures of a molecule or cluster with a given composition is carried out by placing every atom at the center of a box (or sphere), and then assigning each atom a randomly generated displacement vector whose magnitude is constrained to ensure atoms are displaced inside the box. Following this operation, which is termed a kick, geometry optimization at a low level of theory is performed on the candidate structure.

This appendix is adapted from McKee, William C., Saurin H. Rawal, and Ye Xu. "Efficiency enhancements of a restricted stochastic search algorithm for locating local and global minima." Chemical Physics Letters 725 (2019): 1-7

If a new local minimum is obtained, its structure is then refined at a higher level of theory. Successive kick–geometry optimization cycles are performed until no new structures are found. A significant advantage of the Kick method over other search methods is that it requires no initial structure(s) from the user, eliminating an element of bias in the search. Moreover, for small systems (up to ~15 atoms) the efficiency of the Kick method in terms of structures located vs. computational cost is comparable to genetic algorithm [224]. No complex mathematical formulation is used, and the method is in principle capable of identifying all local minima on a given potential energy surface, something explicit global optimization methods are not designed to do. It is therefore not surprising that the Kick method has been successfully applied to locate minima for a number of interesting systems, and furthermore has come to be used in conjunction with global optimization methods for the purpose of algorithmically generating initial structures [222, 225-232].

As the system size increases or when the heterogeneity of the system becomes more prominent, the convergence rate of the original implementation of the Kick method becomes low as compared to methods like genetic algorithm or basin hopping. This happens because the Kick method samples large parts of the PES that are not chemically relevant, or do not possess low-lying local minima. Some efforts have been made to improve the performance of the Kick method by improving the convergence rate (defined in Methods). This refinement is achieved by introducing predefined *filters* to the original Kick method. The most notable of these filters have been in the form of the Symmetry Adapted Stochastic Search method introduced by Wheeler et al. [233], which limits randomly generated structures to specific point group symmetries. The method of Addicoat and Metha [234] allows pre-defined molecular fragments to be kicked in addition to atoms. Both methods mentioned above has been shown to perform significantly better than the original Kick method, although they introduce certain bias to the procedure. In optimizing Si

nanoclusters Avaltroni and Corminboeuf modified the Kick method to eliminate structures with Si-Si bonds less than 2.04 Å (the shortest known Si-Si bond) and those structures with nearest neighbors distances greater than three time the shortest Si-Si bond [235]. While studying Ge clusters Tai and Nguyen rejected structures with Ge-Ge bonds of less than 2.0 Å (slightly shorter than the bond length of Ge_2) as well as those for which the largest Ge-Ge distance exceeded a value in the range of 5 – 8 Å depending on the size of the cluster [236].

Herein, we propose two filters to the original Kick method that improve the convergence rate significantly (we term this approach R-Kick). The first is based on identifying the minimum limits for distances between all atomic pairs, which are approximated by the sum of their shortest covalent radii (*r*). The second filter is to ensure that every atom is connected (directly or indirectly) to every other atom through a network of bonds that do not exceed the maximum limits for distances between all atomic pairs. This ensures that stationary points on a PES that are in fact two or more separate molecules are rejected. The *r* values have been defined by Pyykkö et al. for every atom in the periodic table, and for most atoms both double and triple bond covalent radii have also been derived [237-239].

The generation of candidate structures in Kick and R-Kick occurs within a pre-defined geometric search volume that limits how far apart atoms can be "kicked". In certain cases, e.g., where a cluster has a linear configuration as the global minimum, the search volume could unduly bias the kick procedure away from producing candidate structures near the global minimum if the search volume is too small or is highly symmetric. At the same time, as the search volume grows larger to accommodate larger system size, the probability of generating candidate structures that lead to high-lying local minima on a potential energy surface (e.g. fragmented species) rapidly increases, resulting in significantly worse convergence rate for Kick or much higher up-front

computational cost for structure generation for R-Kick. Thus, we furthermore propose a stochastic search method in which candidate structures are generated with the above two filters pre-imposed irrespective of any pre-defined search volume. The method involves building up a candidate structure atom by atom according to a distinct set of rules (see Methods Section). We term this method the restricted Random Assembly Stochastic Search (RASS) method. We demonstrate below the benefit of these enhanced forms of stochastic search compared to the original Kick method using several well-known molecules and clusters.

A.2. Methods

A.2.1. R-Kick

To put the two filters outlined in the Introduction into a definite form, we use the covalent radii of Pyykkö [240] and adopt the following conventions. The distance of closest approach between two atoms A and B is set to:

$$d_{min}(A,B) = 0.9(r_{A,min} + r_{B,min}) \quad \text{(A.1)}$$

where $r_{A,min}$ and $r_{B,min}$ are the smallest covalent radii of atoms A and B respectively. As an example, the smallest covalent radii for carbon and nitrogen correspond to their triple bond radii, 0.60 and 0.54 Å, respectively. Therefore d_{min}(C, N) is 1.026 Å, which is slightly smaller than the equilibrium C-N bond length of 1.16 Å in HCN. The 0.9 scale factor is introduced as an attempt to allow for the possibility of ionic bonding. For example, the bond length in LiF is 1.59 Å, whereas the sum of covalent radii of Li and F is 1.77 Å, which would cause a candidate structure with a reasonable Li-F bond length of, e.g. 1.6 Å, to be rejected. The scale factor can be adjusted if strongly ionic systems are anticipated. d_{min} is used only as an initial condition. Once a candidate structure is submitted to an electronic structure code for optimization, the distance between any pair of atoms is free to deviate from d_{min}.

To ensure that all atoms in a candidate structure are connected via a network of bonds, it is necessary to derive a purely geometric definition of bonding. We regard two atoms A and B as bonded if the following inequality is satisfied:

$$d_{max}(A,B) < 1.1(r_{A,max} + r_{B,max}) \quad \text{(A.2)}$$

where $r_{A,max}$ and $r_{B,max}$ are the largest covalent radii of atoms A and B respectively. For the carbon and nitrogen example above, the appropriate radii are now their single bond radii, 0.75 and 0.71 Å respectively, and the cutoff distance for considering C and N to be bonded is 1.606 Å. This can be compared to, e.g., the C-N bond length in methylamine, 1.47 Å. The 1.1 scale factor attempts to account for the possibility of unusually long bonds and can also be adjusted if desired. This criterion is implemented by populating a list of bonding partners for each atom, and then using a backtracking algorithm to determine whether any path connecting two atoms exists.

In the R-Kick method, each initial candidate structure generated is subject to filtering to ensure that no pair-wise interatomic distance is less than d_{min}, and that each atom is connected to every other atom via a network of bonds none of which exceeds d_{max}. Only when both criteria are satisfied is the initial candidate structure is accepted for further optimization. Unless otherwise specified, the longest box diagonal is set to the sum of the single bond covalent radii of the constituent atoms in both methods, as in the original Kick method.

Initial candidate structures for a given composition are optimized using Gaussian09 [241] for a maximum of 50 geometry optimization steps per structure. The maximum number of SCF steps is set at the default value of 128. In the examples given below, B3LYP/LANL2DZ is used for initial optimization and detection of stationary point (except for Au_7 where PBE is used instead of B3LYP for improved accuracy and reduced computational cost [242]). A double zeta basis set is used for structural optimization rather than the faster but less accurate minimal basis sets [223, 243] in

order to more accurately identify proper stationary points. The optimized structures are then resubmitted for either frequency calculations or further optimization at a higher level of theory.

Following the optimization of both sets of candidate structures, a post-processing script is employed to determine the convergence rate (i.e., the percentage of candidate structures that successfully converged to a stationary point) and the number of unique stationary points obtained, and to sort all unique structures according to their energy. Here redundant structures are defined as having energies within 0.00001 a.u. or 0.00027 eV [243] of a structure already located and accepted, and an additional visual inspection is performed in cases where the energy difference between two structures is less than 0.01 eV. The number of times the global minimum is located in each batch of candidate structures is also tabulated.

A.2.2. RASS

The R-Kick method for filtering randomly generated candidate structures to enforce the d_{min} and the connectivity criteria are inherently biased by the box size. The bias due to box size can affect the convergence rate when the symmetry of the structures in question deviate significantly from that of the search box (e.g. linear or quasi-linear structures in a cubic box) or when the system size approaches that of the box. The box size effectively limits the distances between all pairs of atoms in candidate structures to equal to or less than the box diagonal. Since small values are known to favor the location of more compact isomers [236] while large values adversely affect the candidate structure convergence rate [235], the efficacy of Kick and R-Kick searches often hinges on a balancing act in which box sizes are chosen in an attempt to simultaneously minimize convergence bias toward compact structures while maximizing the overall convergence rate. These shortcomings are overcome by replacing the *kick-and-filter* operation of the Kick and R-Kick methods with an approach that *assembles* candidate structures that *automatically* satisfy the d_{min}

and connectivity criteria. To achieve this, it is useful to define a random bond vector between two atoms A and B, $\mathbf{b}_{AB}$, which is constructed by scaling the magnitude of a randomly oriented unit vector ($\mathbf{u}$) by a randomly generated scale factor, *s*, such that:

$$0.9\left(r_{A,min} + r_{B,min}\right) < s < 1.1\left(r_{A,max} + r_{B,max}\right) \quad \text{(A.3)}$$

$$\mathbf{b}_{AB} = s\mathbf{u} \quad \text{(A.4)}$$

The RASS method for generating candidate structures satisfying both restrictions is then defined as follows (a flowchart for the method is shown in Fig. A.1 below):

Step 1: Create a list of atoms with the desired elemental composition (the "atoms list", which contains atomic species only and not coordinates). Create also a blank "candidate list", which will be populated with atom species and coordinates.

Step 2: If the candidate list is empty, select an atom at random from the atoms list. Add it to the candidate list and delete it from the atoms list. Set its coordinates as the origin.

Step 3: Select an atom at random from the atoms list and assign it to variable atom A. Select an atom at random from those that are already on the candidate list and assign it to variable atom B. Generate a random bond vector $\mathbf{b}_{AB}$ subject to Eq. (3) and (4). Set the coordinates of atom A as the sum of the coordinates of atom B and $\mathbf{b}_{AB}$. Check if the coordinates of atom A adhere to the d_{min} criterion with respect to all the remaining atoms on the candidate list besides atom B. If they do, go to Step 4. If they do not, repeat Step 3.

Step 4: Add atom A to the candidate list with the coordinates calculated in Step 3. Delete atom A from the atoms list as it has been successfully added to the candidate list.

Step 5: Check if the atoms list is empty. If it is not empty, go back to Step 3. If the atom list is empty, save the candidate list as a new structure with the desired composition.

The R-Kick method applies the minimum pair-wise interatomic distance (d_{min}) and connectivity filters after a structure is randomly generated to decide whether it should be accepted for further quantum chemical optimization or be rejected. In RASS, on the other hand, candidate structures are built atom by atom with the two criteria implemented in the generation process, so all structures thus generated can pass the two filters. Thus, the RASS method drastically reduces the computational expense associated with candidate structure generation compared to the R-Kick method. Again, it is possible that a candidate structure could fragment in the quantum chemical optimization process. Such an example is considered in C_2H_4 molecule search in the latter section.

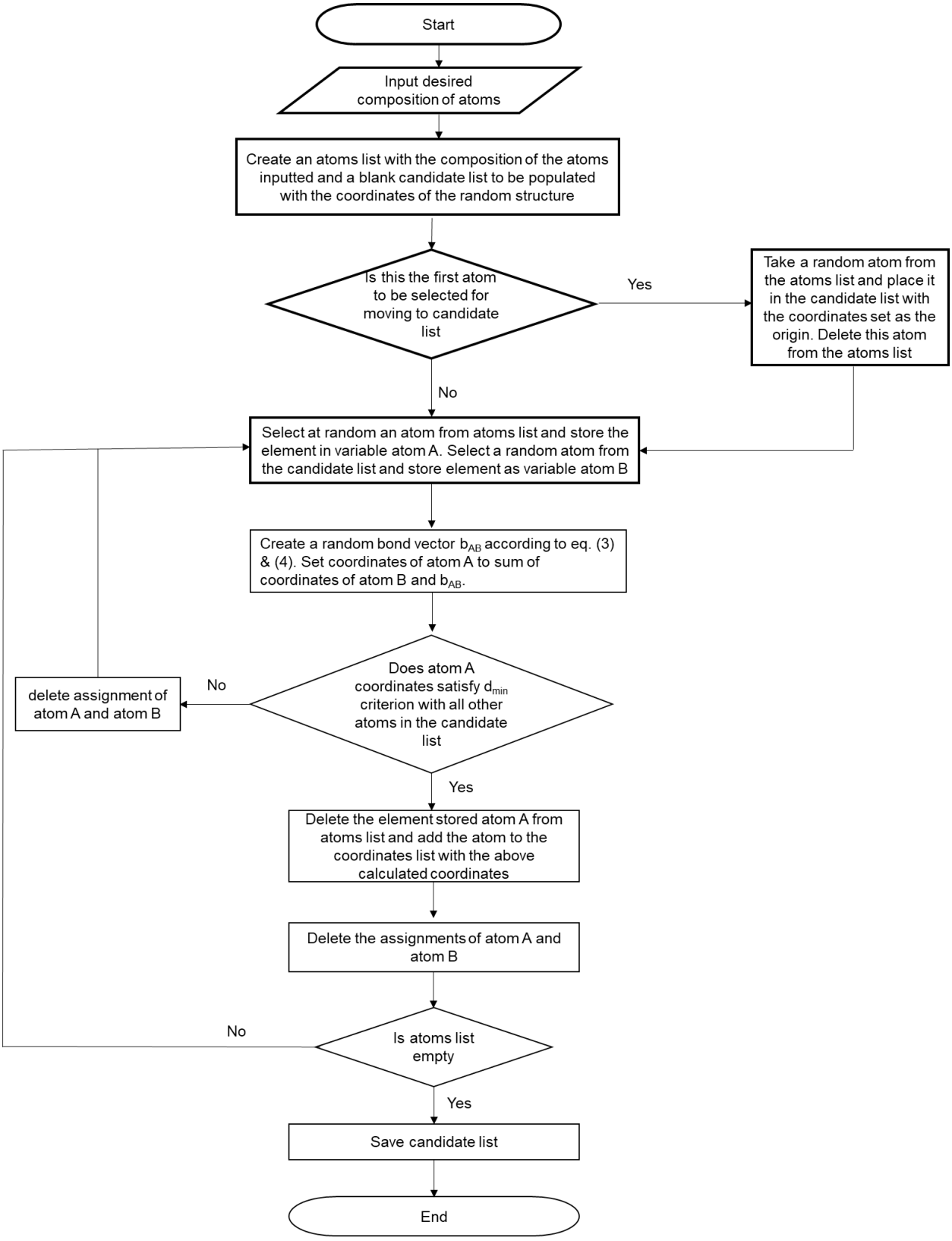

Figure A.1: Flow chart for the RASS algorithm

A.3. Results and Discussion

A.3.1. Comparison to Kick

The primary aim of this study is to evaluate the yield of stationary points obtained from candidate structures when applying the Kick method with and without the proposed filters (i.e. with the R-Kick and RASS methods). As such we use species for which the global minima are well documented, including a) C_6, b) Au_7, c) Si_8, d) BCNOS, and e) C_2H_4. For each species, 250 initial candidate structures are generated using Kick, R-Kick, and RASS methods each to scan the PES and gauge the performance of each method. The stationary points are then refined further at a higher level of theory along with frequency calculations to identify if any of the found configurations are saddle points or local minima. While the PES can change with different levels of theory, the original Kick method is proven to be effective in finding true global minimum-energy structures [124, 244] despite scanning the PES initially at a low level of theory. In the results below our proposed R-Kick and RASS methods are seen as clearly improving on the performance of the original method. As the spin state of the examples are already known, we performed the searches with spin state of each example restricted to the literature value. For unknown structures, the search of PES would be done along all possible spin states.

C_6, Si_8 and Au_7 are chosen as examples as they represent homogeneous organic, inorganic, and metallic clusters with well-established global minima. C_6 was the organic species used by Saunders' investigation of the original Kick method to find its stable forms in the singlet state [223]. The six-membered ring (D_{3h}) and linear ($D_{\infty h}$) structures were found by Saunders to be the competing low-energy minimum configurations with similar energies (1.90 eV in favor of the linear structure) at RHF/6-311G (Fig. A.1a and A.1b). High-level electron-correlated calculations showed that the D_{3h} ring structure is the global minimum [245-247]. For our calculations, the box

dimensions are set to 4.5×4.5×4.5 $Å^3$ with the longest diagonal being 7.79 Å (which is longer than the linear chain configuration of C_6, 6.55 Å, according to B3LYP/6-311++G**). The Kick, R-Kick and RASS methods located the same 10 of the 13 C_6 isomers originally reported by Saunders, including all isomers within 3 eV of the global minimum. Two previously unreported high-energy minima are found with all three methods. The convergence rate for R-Kick and RASS is 57.6% and 58.8% respectively, which is double that achieved by the Kick method (Table A.1)**.** Using Kick method 13 unique structures were found but visual inspection reveals one of the 13 C_6 isomers originally reported by Saunders to be a fragmented T-shaped C_3 dimer, where the closest inter-fragment C···C distance (3.87 Å) exceeds twice the carbon vdW radius (3.40 Å) [248]. Thus 12 unique structures were found using all the methods (structures found using R-Kick and RASS method are listed in Sections S3 and S4 of SI, respectively). At the B3LYP/LANL2DZ level, a linear $D_{\infty h}$ structure is predicted to be the lowest energy structure, lying at 0.5 eV below the next lowest energy D_{3h} ring structure. However, re-optimization of both species at the B3LYP/6-311++G** level switches the energetic ordering in favor of the ring species by 0.28 eV, while further refinement at the CCSD(T)/cc-pVTZ//B3LYP/6-311++G** level yields an energy difference of 0.69 eV in favor of the ring structure. Therefore, the present results are consistent with previous assignments of the D_{3h} ring structure as the global minimum of C_6.

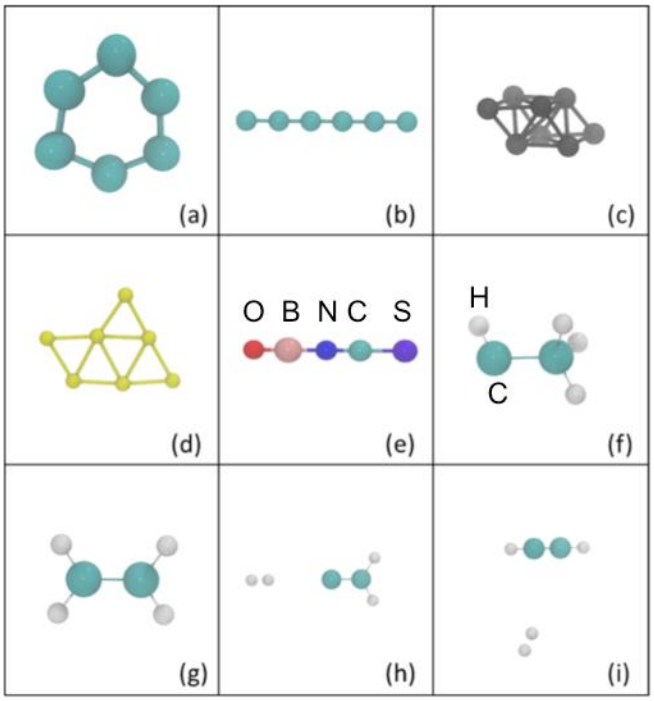

Figure A.1: DFT-optimized (a) D_{3h} ring structure of C_6, (b) $D_{\infty h}$ linear structures of C_6, (c) C_{2h} bicapped octahedron of Si_8, (d) C_s structure of Au_7, (e) $C_{\infty v}$ linear structure of BCNOS, (f) ethylidene, (g) ethylene, (h) fragmented vinylidene+H_2, and (i) fragmented acetylene+H_2. These structures were found by both the R-Kick and the RASS methods. Candidate structures were initially optimized using B3LYP/LANL2DZ and further optimized using B3LYP/6-311++G**, except for Au_7 for which candidate structures were optimized using PBE/LANL2DZ. Color code (online version): C = cyan, Si = dark gray, Au = yellow, H = white, N = dark Blue, O = red, B = pink, S= violet.

Table A.1: Comparison of original Kick method with R-Kick and RASS.

	C_6	Au_7	Si_8	BCNOS	C_2H_4
Number of candidate structures converged					
Kick	62	31	24 (52[a])	40 (36[b])	70
R-Kick	144	121	112	84 (155[b])	161 (195[c])
RASS	147	112	109	101	110
Convergence rate (in %)					
Kick	24.8	12.4	9.6 (20.8[a])	16.0 (14.4[b])	28.0
R-Kick	57.6	48.4	44.8	33.6 (62.0[b])	64.4 (78.0[c])
RASS	58.8	44.8	43.6	40.6	44.0
Number of unique structures					
Kick	13	8	15 (29[a])	26 (28[b])	4
R-Kick	12	16	46	46 (67.0[b])	4 (2.0[c])
RASS	12	19	46	49	4
Number of times global minimum located					
Kick	7	18	0 (0[a])	0 (0[b])	30
R-Kick	13	39	2	2 (5[b])	66 (54[c])
RASS	7	34	1	4	44

[a] Kick method with the filters from Ref. 34.
[b] Kick and R-Kick method using a box with a large aspect ratio of $7.94 \times 1.5 \times 1.5$ Å^3.
[c] R-Kick method with additional filters to reject H-H bonds and restrict H valency to 1.

The inorganic Si_x (x = 2-20) nanoclusters have attracted particular interest from the semiconductor industry, [203, 249] and Avaltroni and Cormindoeuf have previously applied filters on the original Kick method to affect significant improvement in convergence rates for finding minimum-energy structures for these species [235]. The filters involved the rejection of candidate structures with nearest Si-Si distance below 2.04 Å (double the triple bond radius of Si [240]) or above 6.12 Å, the second criterion being less restrictive than requiring all atoms be connected via a network of bonds. The results of a search for Si_8 clusters in a box of 10×10×10 $Å^3$ using the original Kick method, the Kick method with the filters of Ref. 34, and R-Kick and RASS are presented in Table A.1. For Si_8, the established global minimum is the C_{2h} bicapped octahedron structure (Fig. A.1c) [216, 250-252], which has indeed been identified in experiments [253]. The original Kick method gives 24 stationary points, 15 of which are unique structures, which translates to a convergence rate of 9.6% from 250 generated structures. Applying the filters of Ref. 30 produces a substantial improvement in the convergence rate at 20.8% by finding 52 stationary points. The R-Kick and RASS methods yield convergence rates of 44.8% and 43.6% by generating 112 and 109 stationary points, respectively, of which 46 each are unique structures (see Sections S3 and S4 of SI). Within our 250-structure subset, the actual global minimum structure is located twice. While at the B3LYP/LANL2DZ level several other isomers are found to be lower in energy than the C_{2h} bicapped octahedron, the re-optimization of all isomers within 1 eV of the lowest energy structure at the B3LYP/LANL2DZ, now using B3LYP/6-311++G**, confirms the C_{2h} bicapped octahedron to be the lowest in energy. Compared to the original Kick method, the R-Kick and RASS methods increased the convergence rate by a factor of ~4.5. Furthermore, the more stringent connectivity criterion enforced here (R-Kick and RASS) evidently improves upon filters based on nearest neighbor distances only, as the gains in the number of converged and unique structures are

significant. On the other hand, it should be noted that these gains come at the cost of a significantly longer filtering time for R-Kick than the original Kick (discussed in the next section).

Following Haruta's discovery of the surprising catalytic properties of supported gold nanoparticles [254], research interest in the size-dependent reactivities of Au has exploded worldwide [255-258]. As a result, a number of investigations of the lowest energy structures of Au_n species have been reported [259-261]. For Au_7, the global minimum is a planar edge-capped triangle species with C_s symmetry (see Fig. A.1d), which is also observed experimentally [262]. The results of a search for Au_7 isomers in an 8.68×8.68×8.68 $Å^3$ box based on the Kick, R-Kick and RASS methods are given in Table A.1. Of the structures generated using original Kick method, 31 converged to stationary points, of which the global minimum is located 18 times. Of the 31 stationary points 8 are unique structures. Two of the four lowest energy structures reported by Kim and coworkers are recovered [259], and five Au_7 isomers are found to lie within 0.434 eV of the global minimum at the PBE/LANL2DZ level. In total 8 unique species are obtained, with the highest lying isomer located at +1.17 eV in energy over the global minimum. Implementation of the restricted stochastic procedure leads to a substantial increase in the search efficiency, which leads to 121 and 112 converged stationary points for R-Kick and RASS respectively. This is a four times improvement in convergence rate over the original Kick method. Out of the stationary points found for R-Kick and RASS, 16 and 19 are unique structures with relative energies that spans over 1.0 eV from the lowest energy structure. Three of the four low energy species reported by Kim et al. are obtained, and nine species are found to lie within 0.434 eV of the global minimum. The global minimum itself is found 39 and 34 times respectively, which is more than double the corresponding number of times it is found using the Kick method.

The BCNOS molecule is a good species for evaluating the performance of the Kick method [243] because its composition of five different atoms can potentially lead to a large number of distinct minima. This molecule has previously been investigated by Bera and coworkers [243], with the minimum-energy structure being the linear $C_{\infty v}$ species shown in Fig. A.1e**.** As shown in Table A.1, for a 3.97×3.97×3.97 $Å^3$ box we find 40, 84, and 101 stationary points for Kick, R-Kick and RASS, of which 26, 46 and 49 are unique structures, respectively (shown in Sections S2, S3 and S4 of SI, respectively). In our study, R-Kick and RASS are able to locate the global minimum 2 and 4 times respectively, while Kick fails to locate the global minimum. It is also interesting to compare the results of an unrestricted vs. restricted Kick search using box dimensions that favor the formation of (quasi-) linear candidate structures. The results for a 7.94×1.5×1.5 $Å^3$ box, where 7.94 Å corresponds to double the sum of the covalent radii of the constituent atoms, are presented in Table A.1**.** The R-Kick convergence rate almost doubled to 67% as compared to the previous cubic box while the performance of the Kick method remained approximately the same. The number of unique species obtained in the restricted search is substantially increased compared to both an unrestricted search at the same box size and the restricted search using a smaller, symmetric box. The global minimum is obtained a total of five times using the new box dimensions using R-Kick. All five of the lowest energy (quasi-) linear species reported by Bera et al. are located, i.e. SCNBO (linear, global min.), OCNBS (linear), NCSBO (bent at sulfur), NCOBS (bent at oxygen), and SNCBO (linear) using both R-Kick and RASS [243].

For the searches considered up to this point, fragmentation has not been an issue. Therefore, it remains unclear whether or not the connectivity criterion is effective at reducing fragmentation upon optimization. To explore this aspect, we carry out a search for C_2H_4 isomers using the Kick, R-Kick and RASS methods in a 4×4×4 $Å^3$ box. The molecules and fragments that

are found in the respective searches are shown in Fig. A.1f-i, and the search results are summarized in Table A.1. The Kick method converges to minima 70 times, of which 4 unique minima are obtained including two molecules and two fragments (see Section S2 of SI). The molecules found are ethylidene (CH_3CH) and ethylene (CH_2CH_2), while the fragments consist of H_2 paired with either vinylidene (CH_2C) or acetylene (CHCH). Of the 70 converged species, 11 are one of these two fragmented groups corresponding to a fragmentation rate of 15.7%. A search based on the R-Kick and RASS method increases the number of converged structures to 161 and 110 respectively but did not completely eliminate fragmentation (the unique structures found are the same as those found using the Kick method). In case of R-Kick and RASS, candidate structures are generated with C_2H_2 and H_2 connected to each other but on optimization they separate out into two separate molecules. The same four unique species are found for R-Kick and RASS. 11 and 14 of the 161 and 110 respectively converged species correspond to fragmented structures. Therefore, the connectivity criterion of the R-Kick and RASS method lowered fragmentation rate from 15.7 % to 6.8% and 12.7 %, respectively but did not completely eliminate it.

Applying additional system-specific filters to R-Kick can produce further gain in performance. In the case of C_2H_4, since fragmentation mainly leads to the formation of molecular H_2, the fragmentation rate can be reduced by rejecting any candidate structure that has a H-H bond. In addition, we implement a filter that each H atom in a candidate structure has a maximum of one bond, i.e. the valency of H atom is limited to one (the term “valency” here refers solely to the number of bonding partners in a candidate structure as determined by our geometric covalent radius definition of bonding, and not to any electronic property), based on the expectation that no bridging hydride species should result. With these two additional filters applied the convergence rate increases to 78% and fragmentation upon optimization is largely avoided. Based on these

results, these connectivity criteria are an effective means of reducing fragmentation. We note that it would be straightforward to implement such connectivity criteria in RASS, by building random structures in which atoms are constrained to have a predefined number, and types, of bonding partners. For example, besides limiting H atoms to only have one bonding partner, C atoms may be limited to have 4 or fewer bonding partners.

A.3.2. Statistics for candidate structure generation

To generate 250 structures with the R-Kick method, a large number of initial candidate structures are rejected due to not satisfying the additional filters (Table A.2). The Python code that implements the R-Kick method for generating these structures is given in the SI. For C_6, the generation of 250 structures requires the rejection of 17,464 initial candidate structures. Of the rejected candidates, 14,558 failed the minimum distance requirement, while a similar number of 14,077 failed the connectivity criterion. In total, the generation of 250 satisfactory candidate structures took ~10 seconds runtime (all codes were run on a single core of an 8-core Sandy Bridge Xeon processor clocked at 2.6 GHz). Compared to the original Kick method, the restricted approach increases the number of candidate structures that converge to stationary points from 62 to 144, corresponding to an efficiency gain of ~2.3 times. The number of structures that the code rejects is also a function of box size as shown in the case of BCNOS, where 2 different box sizes are used i.e. 3.97×3.97×3.97 $Å^3$ box and 7.94×1.50×1.50 $Å^3$ box. In the case of these two boxes, 12,012 and 157,731 structures are rejected respectively (see Table A.2).

Thus, a significant shortcoming of the R-Kick method is that the computational cost of filtering randomly generated candidate structures to enforce these requirements scales poorly with system size. This is because the probability that randomly generated coordinates will produce a

candidate structure where all atoms are connected to one another via a network of bonds, and where no pair of atoms exhibits unphysically short pairwise distances, becomes increasingly small as the size of a species increases. For example, Fig. A.2a shows the computational cost of generating 50 accepted candidate Si_6, Si_8, and Si_{10} species, where the time required for filtering is seen to scale exponentially with system size. Fig. A.2b shows that the rate on the semi-log scale at which the number of rejected structures increases with cluster size is similar to the rate of increase in the computational cost for generating 50 accepted candidate structures shown in Fig. A.2a. As a result, R-Kick method search is expected to be inefficient for systems with more than approximately 10-12 atoms.

Table A.2: Total number of structures generated, screened and rejected for the generation of 250 candidate structures and the number of structures filtered out by a specific criterion.

	C_6	Au_7	Si_8	BCNOS	C_2H_4
Total number of kicks generated	17,717	1,315,182	2,032,939	12,262 (157,981[a])	317,865 (1,566,044[b])
Total number of kicks rejected	17,464	1,314,932	2,032,689	12,012 (157,731[a])	317,615 (1,565,794[b])
Number of kicks failing d_{min} criterion	14,558	1,226,254	1,587,118	10,992 (156,372[a])	193,132 (950,494[b])
Number of kicks failing connectivity criterion	14,077	1,226,044	2,018,378	6,571 (94,233[a])	312,843 (1,541,008[b])
					41,4803[c]

[a] Structures of BCNOS generated in a 7.94×1.5×1.5 $Å^3$ box.
[b] Structures generated using an additional filter that rejects H-H bond and restricts the valency of H to 1.
[c] Structures failing the particular criterion of H valency equal to 1.

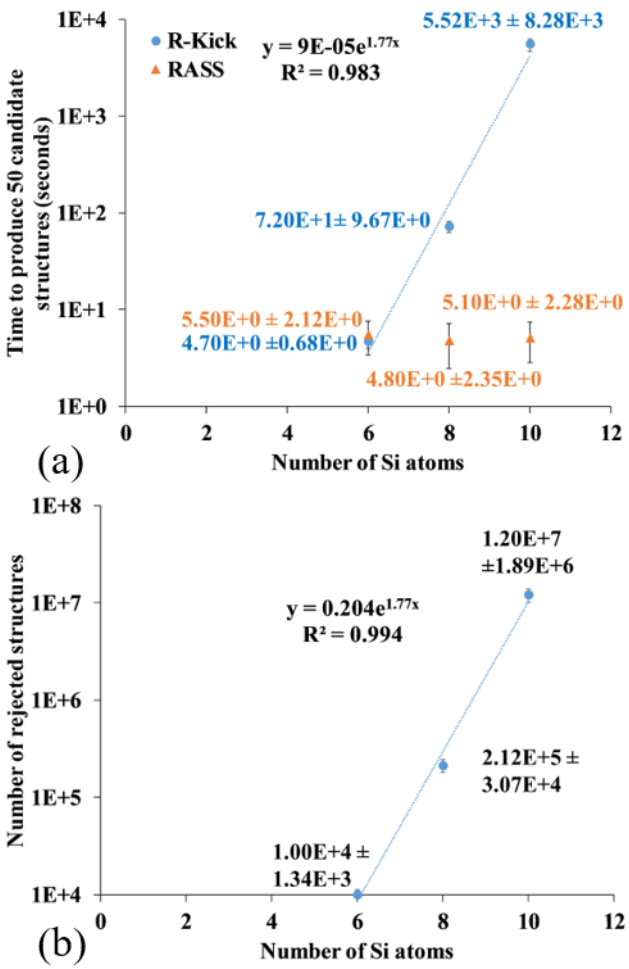

Figure A.2: Time required to generate 50 candidate structures for Si clusters of several sizes that pass both the d_{min} and the connectivity filters in R-Kick. The time required to create 50 accepted candidate structures of each size using RASS is included for comparison. The data labels give the time in seconds. (b) Number of structures rejected by R-Kick for the generation of 50 structures. The data labels give the average number of structures rejected over 10 parallel calculations for a given cluster size. The error bars in both plots is based on standard deviation of 10 separate calculations for a given cluster size. The equation represents the least-square fit.

Thus, beyond the size regime of 10-12 atoms, it is advantageous to replace the *kick-and-filter* operation of Kick-based methods with the *assembly* operation of RASS. To demonstrate the advantages of RASS for larger atomic configurations (> 12 atoms), a stochastic search over larger Si clusters ranging from 12 Si atoms to 20 Si atoms is carried out. Table A.3 indicates the performance of RASS in comparison to the original Kick method. For each case RASS is vastly superior to the Kick method and the time required for the generation of acceptable candidate structures is invariant with respect to the number of Si atoms (shown in Fig. A.3). For Si_{12}, RASS found 5 local minima that were below the global minimum reported by Bazterra et. al. [263] at the B3LYP/6-311++G** level of theory, with the lowest energy structure (shown in Fig. A.4) being 0.385 eV lower in energy. Similarly the lowest energy minima found for Si_{14} is 0.23 eV lower than the reported global minimum[263]. For Si_{16} and Si_{18} the lowest energy local minima found by RASS were 1.06 eV and 1.38 eV higher than the reported global minimum[264-265] (while the reported Si_{20} structure [266] does not have an online database to compare). We note that our aim here is to compare the convergence rates of Kick vs. RASS for larger systems, thus only 250 candidate structures were generated for each Si cluster species. In contrast a thorough stochastic search for low lying species, or a GA-based search for the global mininum where RASS was utilized as a random population generator, would involve many more candidate structures. Nevertheless, the present results clearly indicate that RASS is a far more efficient than the Kick method for cluster sizes larger than than ~12-15 atoms.

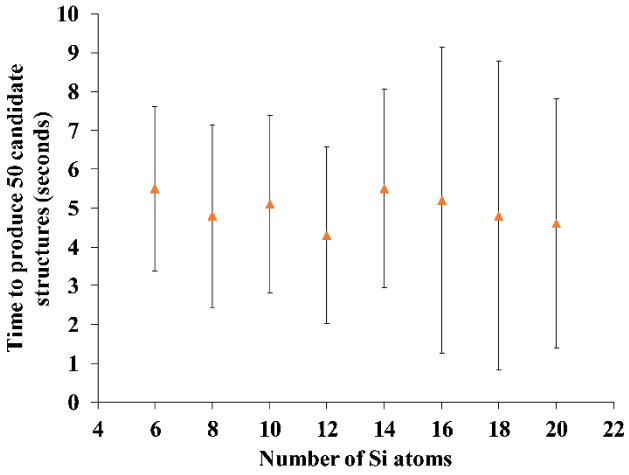

Figure A.3: Time required to generate 50 candidate structures for Si clusters of several sizes

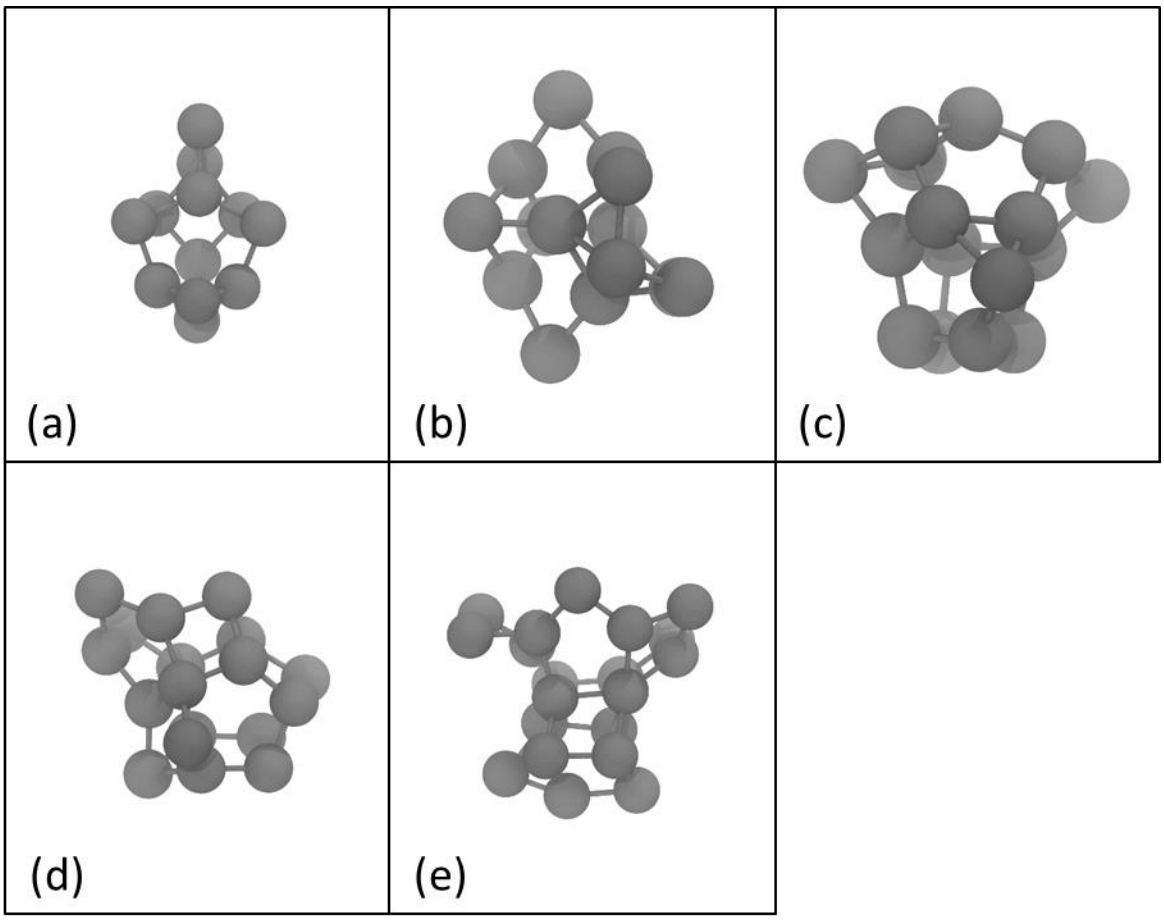

Figure A.4: DFT optimized (a) Si_{12}, (b) Si_{14}, (c) Si_{16}, (d) Si_{18} and (e) Si_{20} nanoclusters. These structures were optimized at the B3LYP/6-311++G** level of theory.

Table A.3: Comparison of original Kick method with RASS for Si clusters of 12 to 20 atoms by generating 250 candidate structures for each cluster species.

	Si_{12}	Si_{14}	Si_{16}	Si_{18}	Si_{20}
Number of candidate structures converged					
Kick	2	1	0	0	0
RASS	137	107	87	74	67
Convergence rate (in %)					
Kick	0.8	0.4	0	0	0
RASS	54.8	42.8	34.8	29.6	26.4
Number of unique structures					
Kick	1	0	0	0	0
RASS	132	102	86	74	67

A.4. Conclusions

The efficiency of random searches for the global minima of small molecules and clusters by the original Kick method can be substantially enhanced by filtering candidate structures by two criteria: 1) The distance between any pair of atoms must not be smaller than the anticipated minimum bond length between the two atoms; 2) Each atom must be connected to every other atom via a network of bonds. Both restrictions are readily definable in terms of covalent atomic radii (which have been tabulated for all elements in the periodic table in the literature), and therefore can be applied to any composition. Compared to the original Kick method, the implementation of these filters significantly enhances the convergence rate of candidate structures to stationary points, which generally increases both the number of unique minima obtained and the frequency with which the global minimum is located. The rate of fragmentation of candidate structure upon optimization is also reduced but fragmentation is not completely eliminated. We

have furthermore assessed the impact of enforcing the two criteria via filtering post random generation of structures (R-Kick), vs. enforcing the criteria during the random assembly of structures (RASS). While overall both methods lead to similar search results, the RASS method eliminates box-size-dependent biases characteristic of stochastic search methods and drastically reduces the computational cost of generating acceptable candidate structures as system size increases. For searches involving systems larger than ~15 atoms, the RASS algorithm presents a much more attractive option than Kick or R-Kick for generating an unbiased population of starting species for further optimization, whether using simple stochastic search or more sophisticated methods such as genetic algorithm.

Appendix B. Supplementary Information for Chapter 5

Table B1: Electron mobility within the bulk solids that have bands crossing the fermi level.

Bulk solid	μ_x (cm^2/[Vs])	μ_y (cm^2/[Vs])	μ_z (cm^2/[Vs])
u-$Li_{15}CoO_{16}$	39.7	58.1	55.6
u-$Li_{14}CoO_{16}$	36.8	37.5	34.9
u-$Li_{14}NaO_{16}$	46.5	82.6	35.6
u-$Li_{14}MgO_{16}$	44.6	44.6	78.7
u-$Li_{15}NiO_{16}$	188.6	95.1	65.9
u-$Li_{14}NiO_{16}$	67.5	65.2	98.5
c-$Li_{15}NiO_{16}$	61.0	61.0	90.4
u-$Li_{15}BaO_{16}$	34.6	20.3	39.5
c-$Li_{15}BaO_{16}$	38.9	38.9	57.6

Table B3:Gas phase complexation energies and Solvation free energies of ions in DMSO, calculate using scheme 1.

	$\Delta G^0_{g,bind}$	$\Delta G^*_{solv}(D^{m+})$
Li	-4.99	-6.05
Na	-3.83	-5.18
Mg	-16.56	-21.02
Co	-19.25	-23.41
Ni	-20.70	-24.94

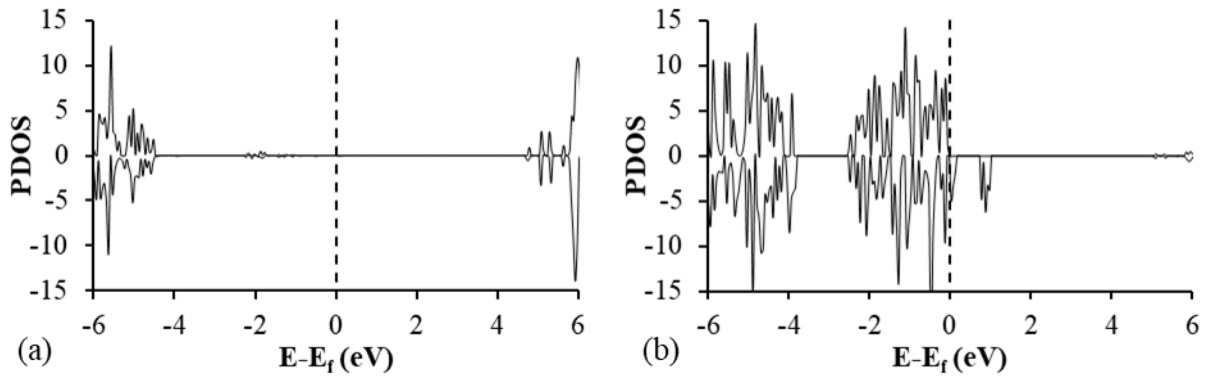

Figure B1: Partial density of states of all the O atoms in *c*-Li_2O_2 with a V_{Li}. The $2p_z$ orbitals of the O band which mainly attributes to the σ and σ∗ bands in the solid are shown in (a) while the π and π* formed from the O $2p_x$ and $2p_y$ are shown in (b)

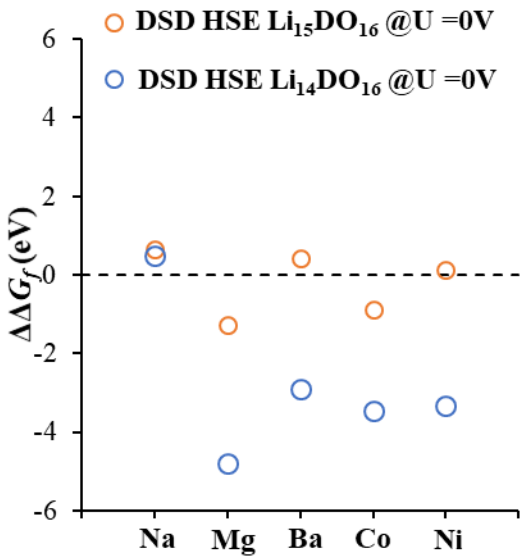

Figure B2: Difference in free energy of formation ($\Delta\Delta G_f$) for DSD $Li_{15}DO_{16}$ and $Li_{14}DO_{16}$ using HSE06. These structures are compared to *c*-Li_2O_2 and *c*-Li_2O_2 with a V_{Li}, respectively.

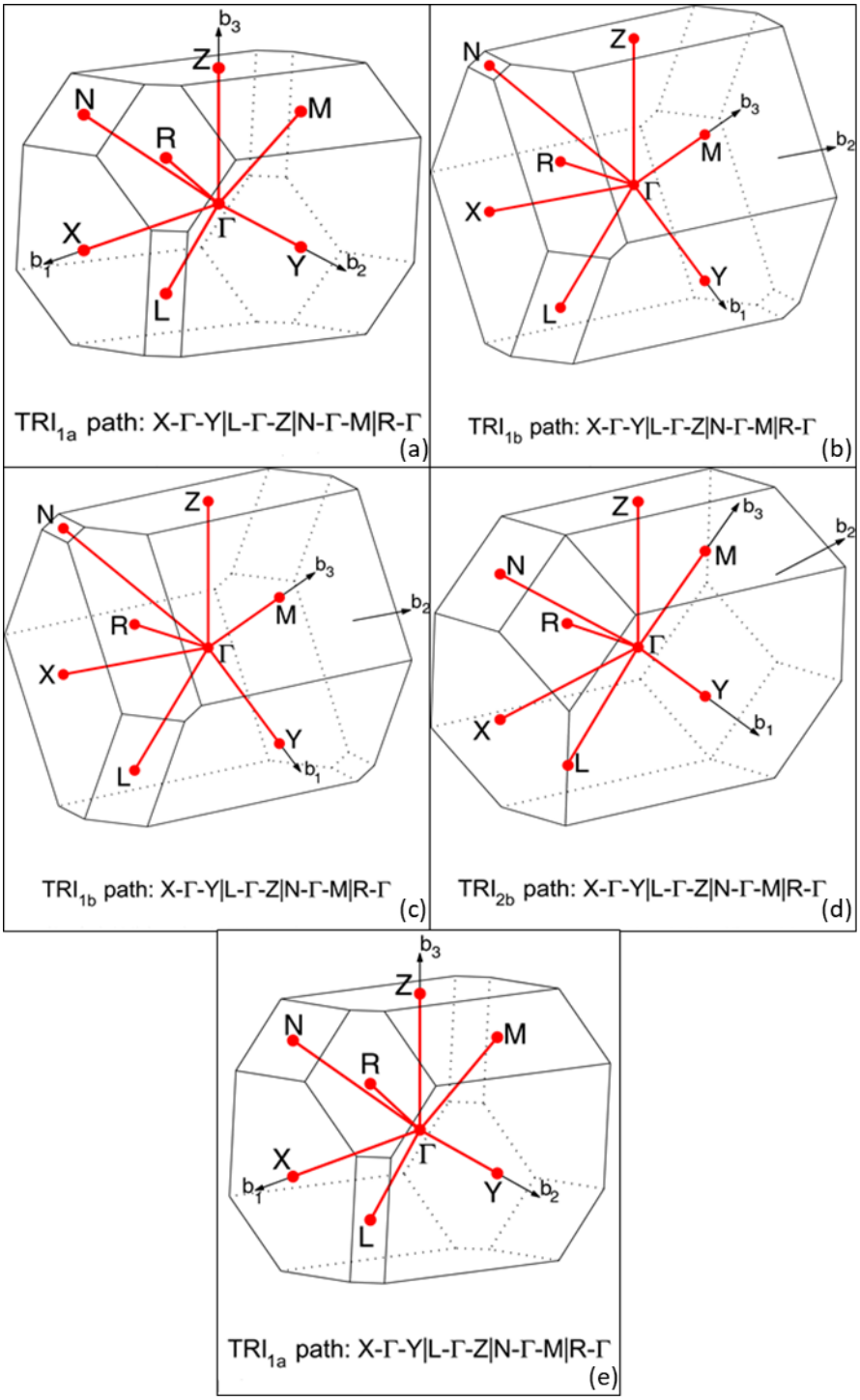

Figure B3: K vector path in reciprocal space along which the band structure is calculated for u-$Li_{15}O_{16}D_1$ structures where D is (a)Co, (b)Ba, (c)Na, (d) Mg and (e) Ni. The Kpaths were generated using the online tool aflow [267-268]

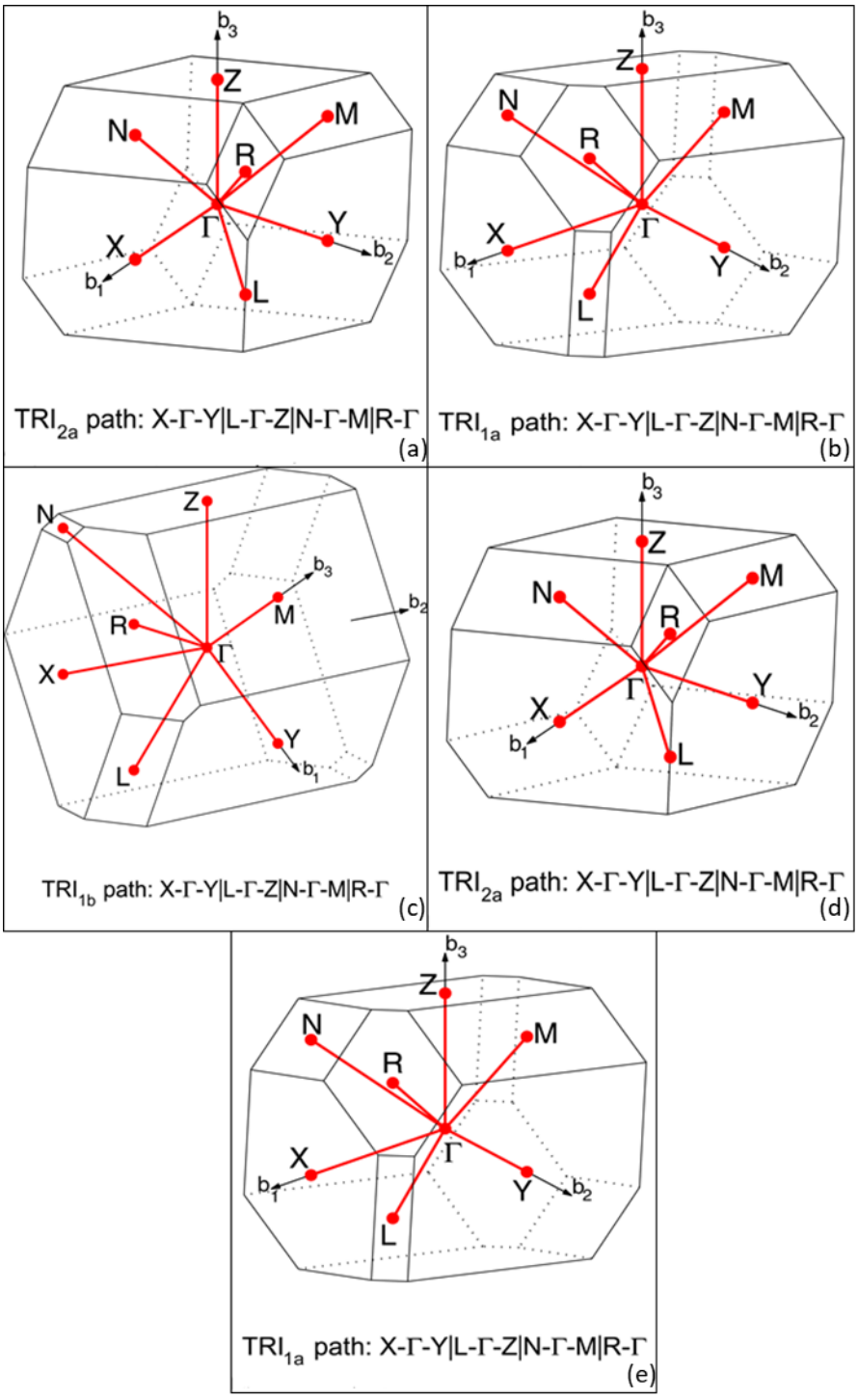

Figure B4: K vector path in reciprocal space along which the band structure is calculated for u-$Li_{14}O_{16}D_1$ structures where D is (a)Co, (b)Ba, (c)Na, (d) Mg and (e) Ni. The Kpaths were generated using the online tool aflow[267-268]

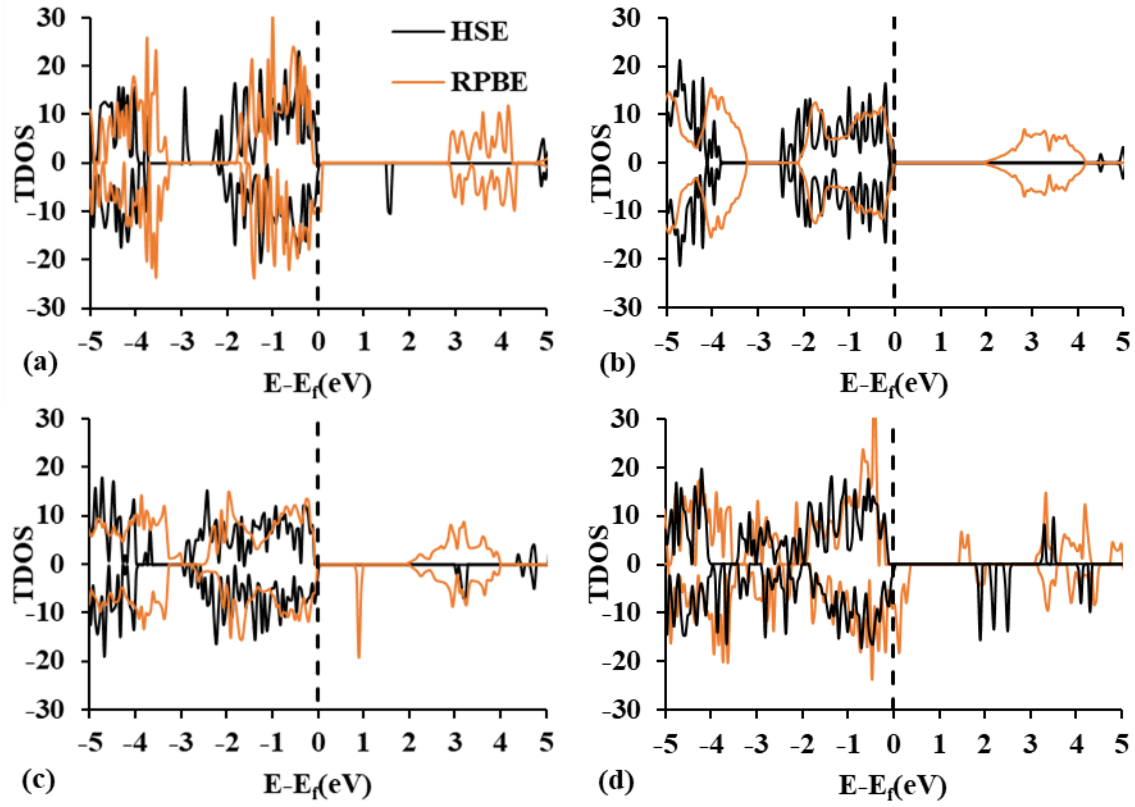

Figure B5: Calculated density of state for *u*-$Li_{15}O_{16}D_1$ structures where D is (a)Ba, (b)Na, (c) Mg and (d) Ni

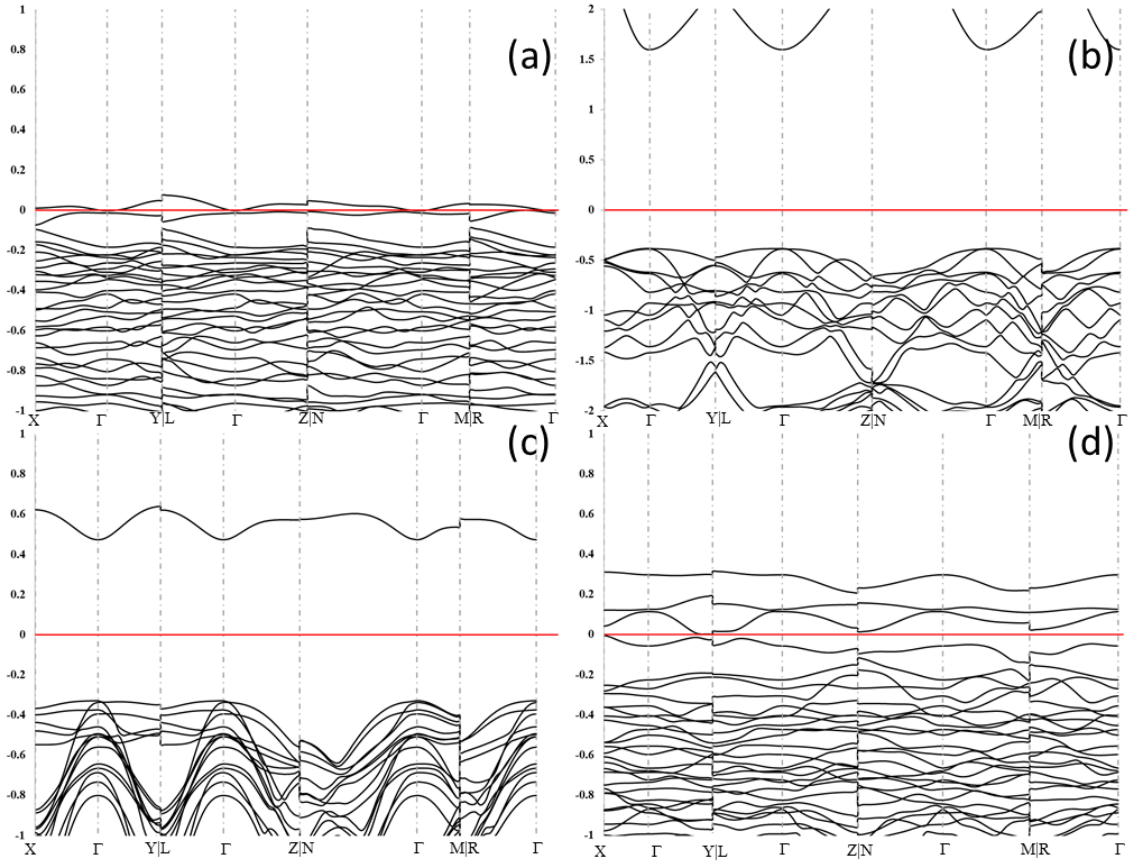

Figure B6: Calculated electronic band structure for u-$Li_{15}O_{16}D_1$ structures where D is (a)Ba, (b)Na, (c) Mg and (d) Ni

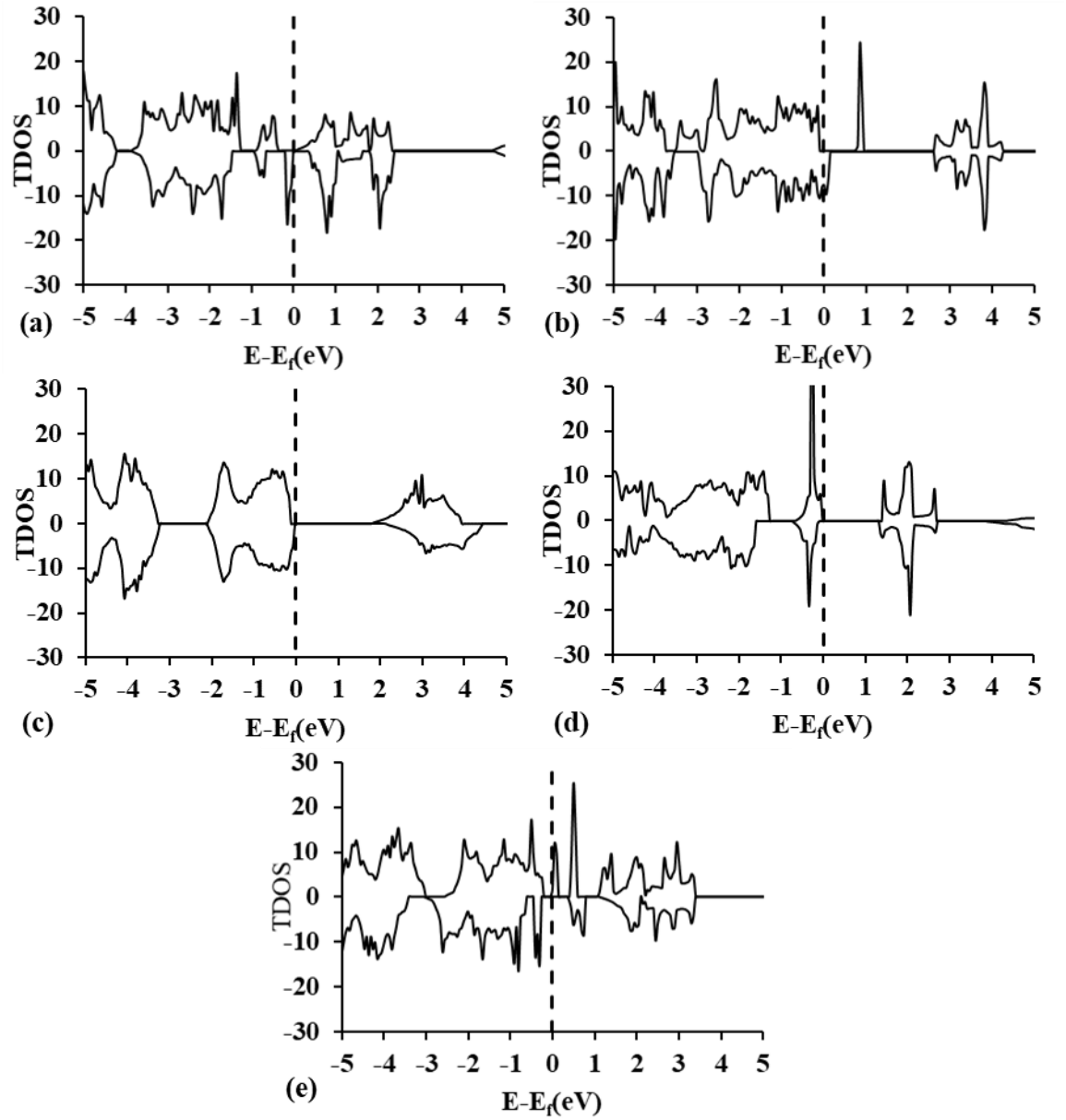

Figure B7: Calculated electronic density of state for substitutionally doped *c*-$Li_{15}O_{16}D_1$ structures where D is (a)Co, (b)Ba, (c)Na, (d) Mg and (e) Ni using RPBE functional only

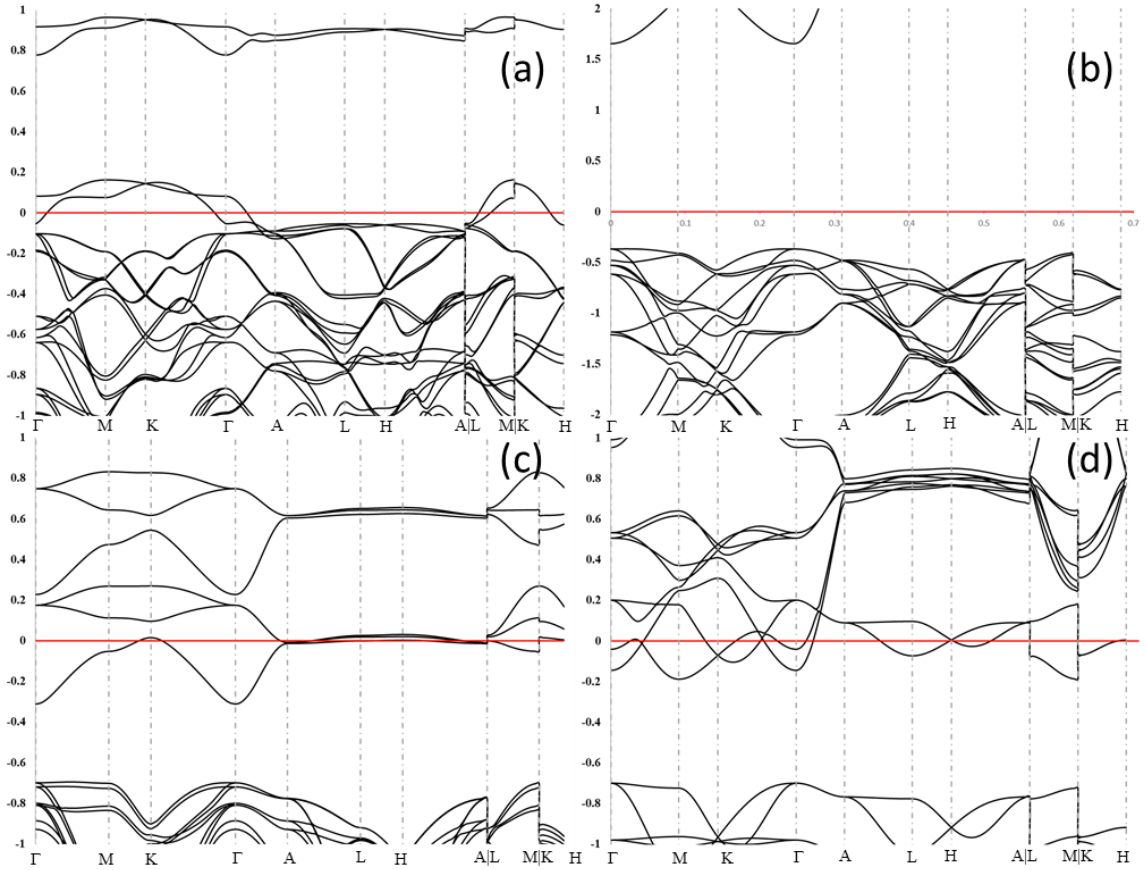

Figure B8: Calculated electronic band structure for substitutionally doped c-$Li_{15}O_{16}D_1$ structures where D is (a)Ba, (b)Na, (c) Mg and (d) Ni

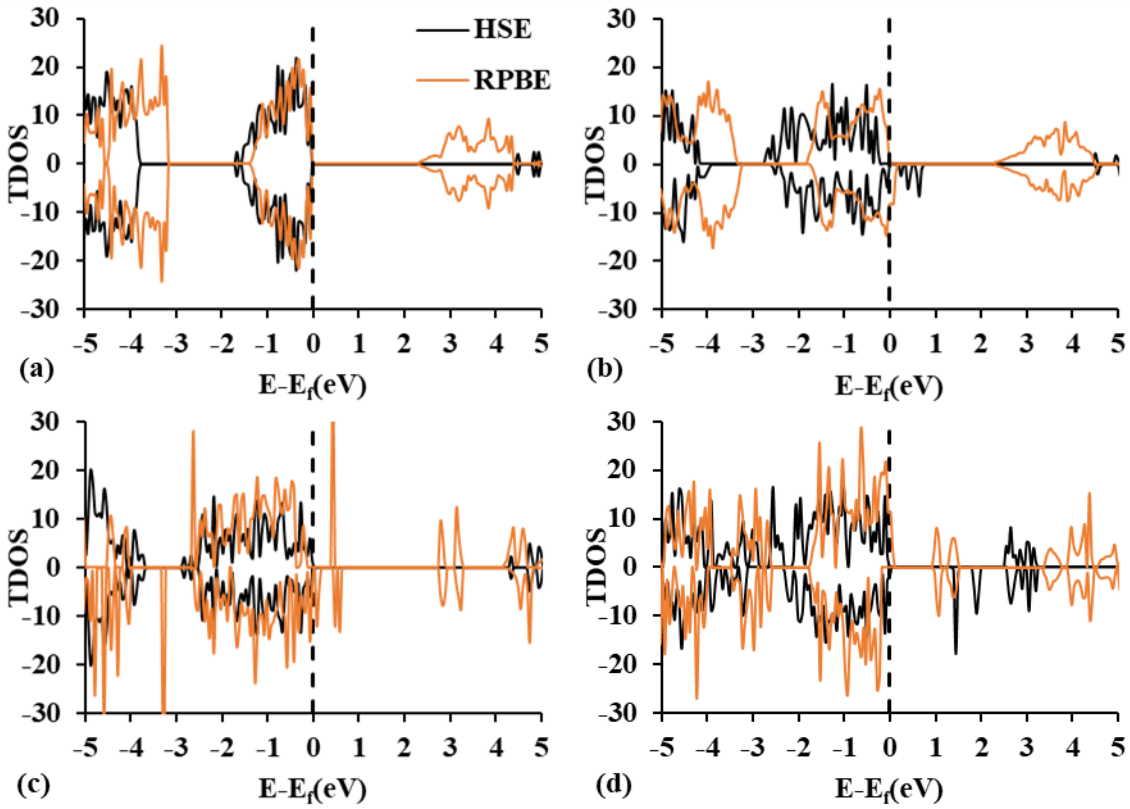

Figure B9: Calculated density of state for *u*-$Li_{14}O_{16}D_1$ structures where D is (a)Ba, (b)Na, (c) Mg and (d) Ni

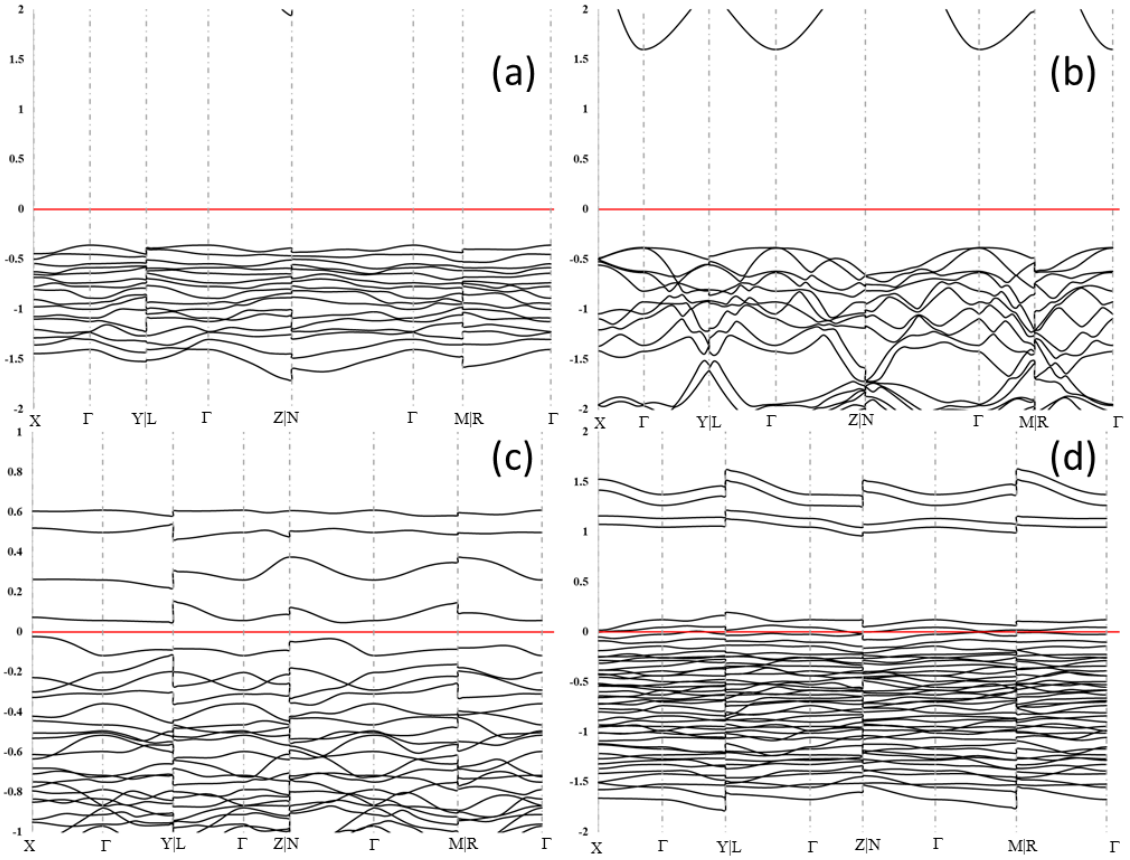

Figure B10: Calculated electronic band structure for u-$Li_{14}O_{16}D_1$ structures where D is (a)Ba, (b)Na, (c) Mg and (d) Ni

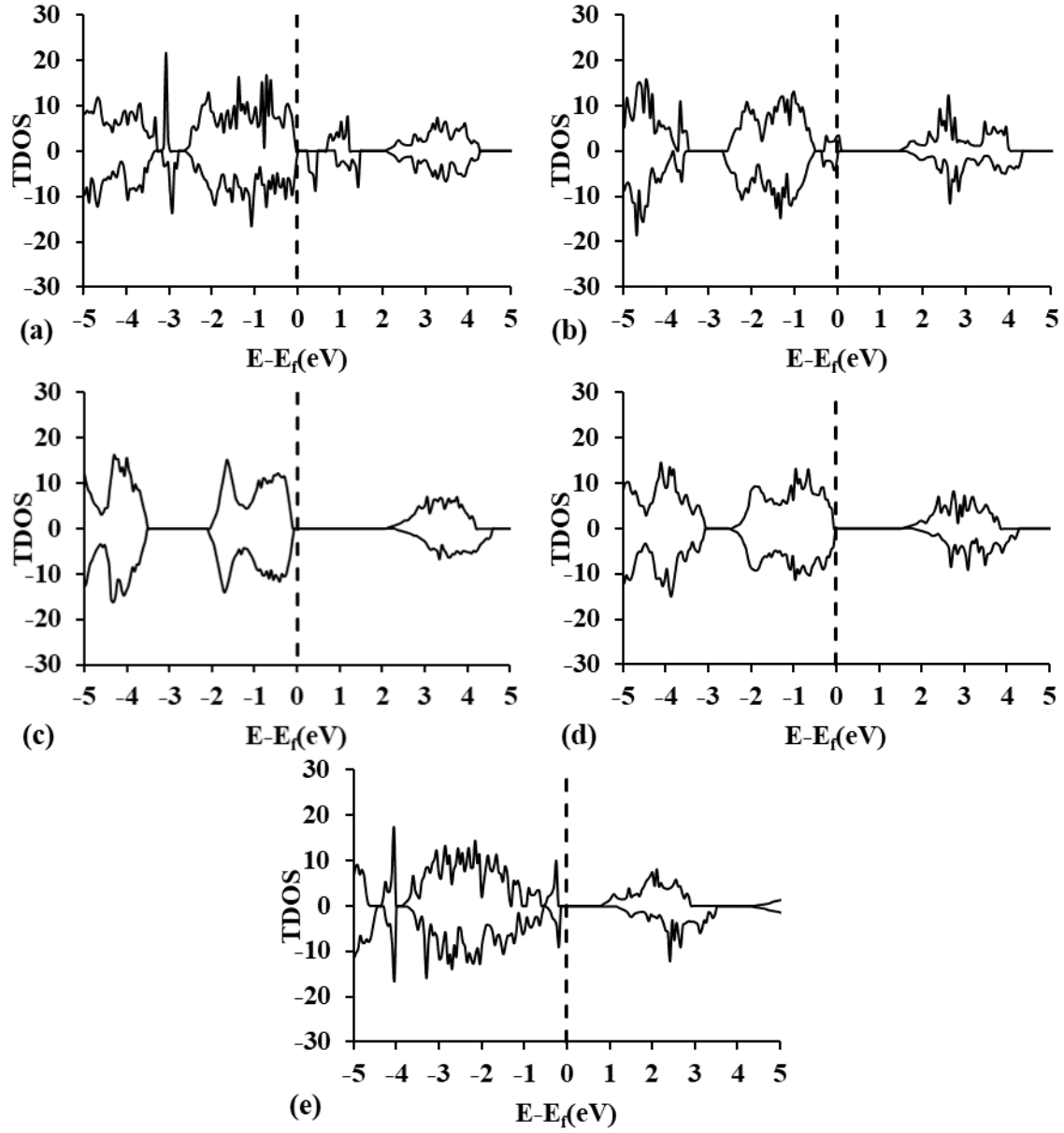

Figure B11: Calculated electronic density of state for substitutionally doped c-$Li_{14}O_{16}D_1$ structures where D is (a)Co, (b)Ba, (c)Na, (d) Mg and (e) Ni using RPBE functional.

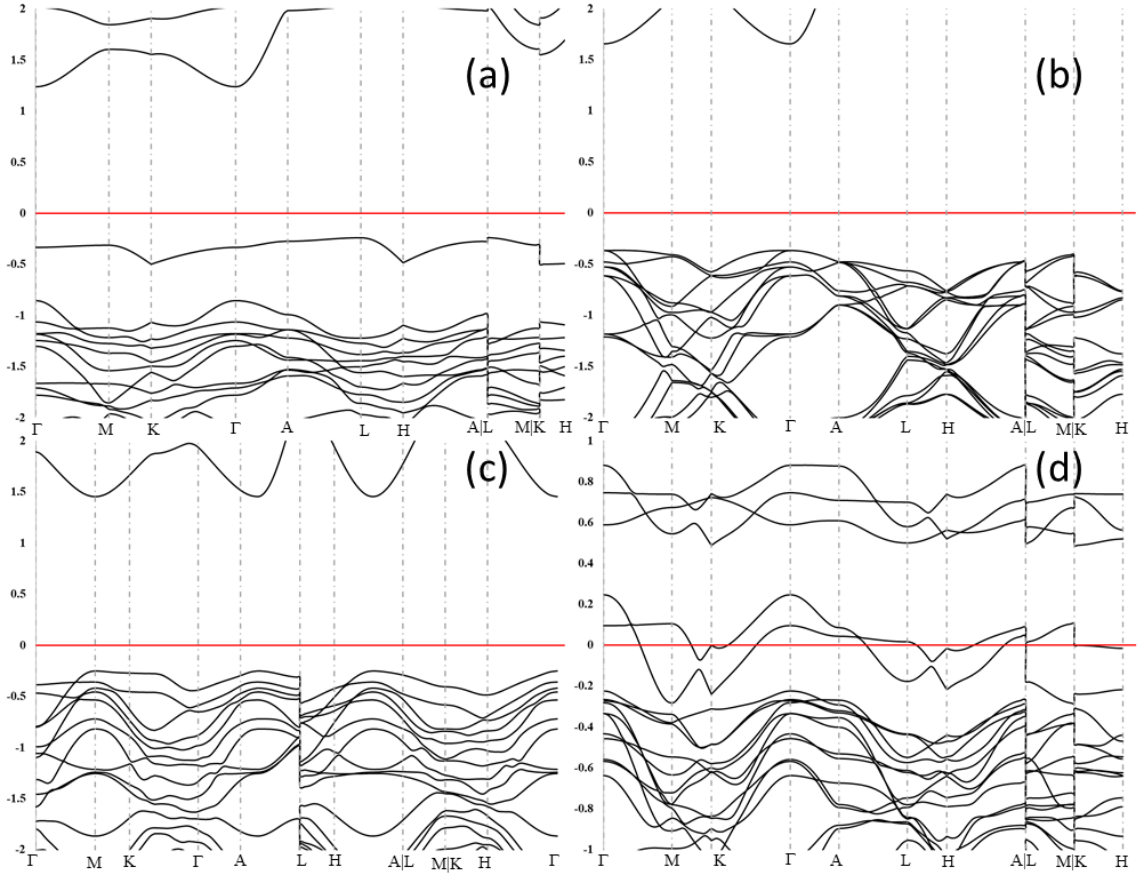

Figure B12: Calculated electronic band structure for substitutionally doped c-$Li_{14}O_{16}D_1$ structures where D is (a)Ba, (b)Na, (c) Mg and (d) Ni

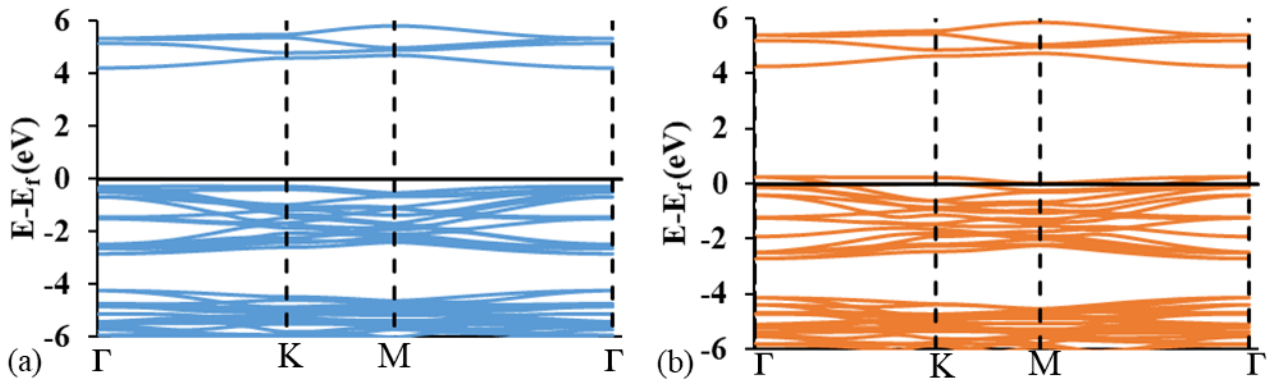

Figure B13: Spin decomposed band structure for *c*-$Li_{15}O_{16}$ (structure with 1 TP vacancy) the (a) spin up and (b) spin down states.

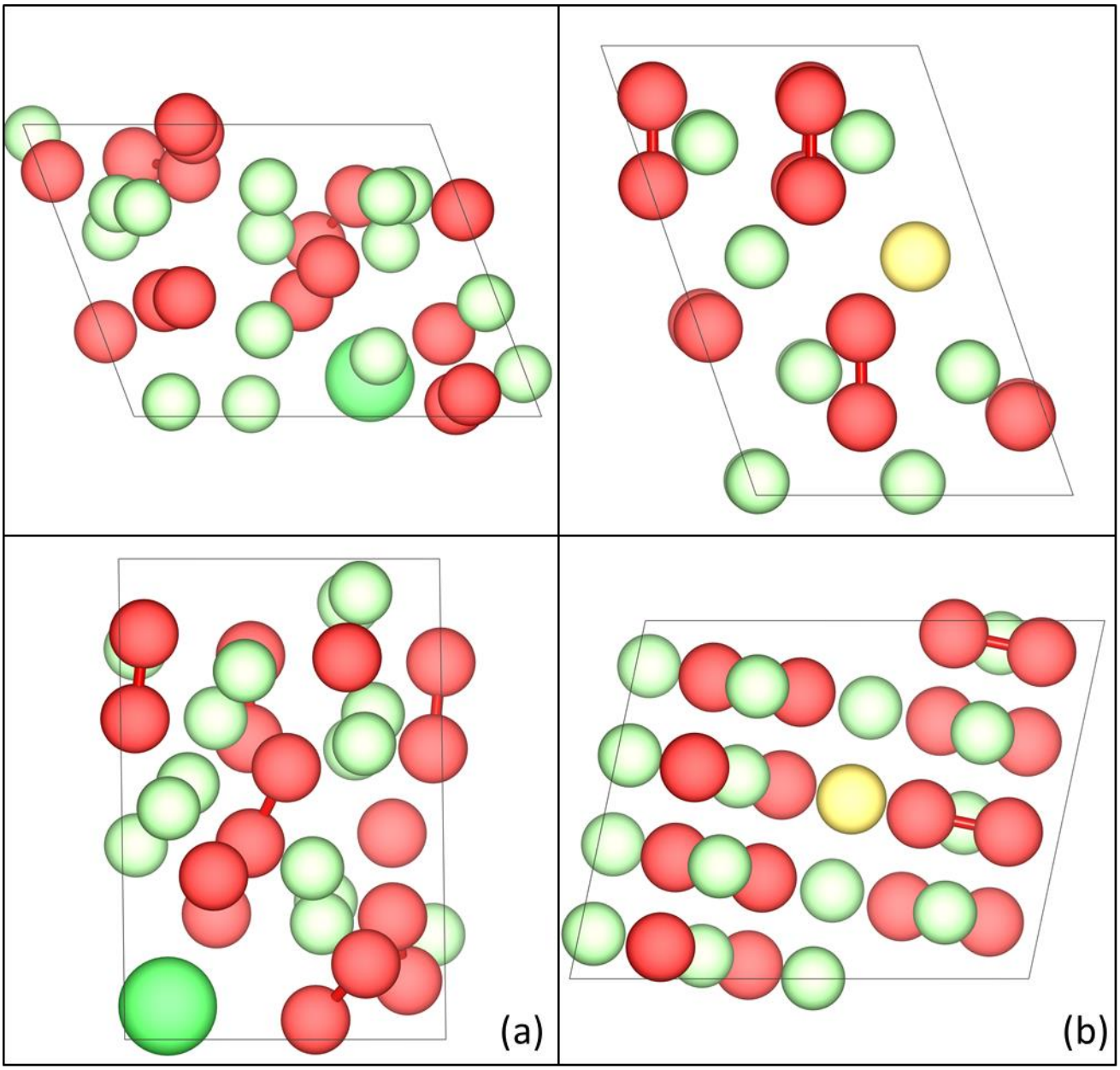
(a)
(b)

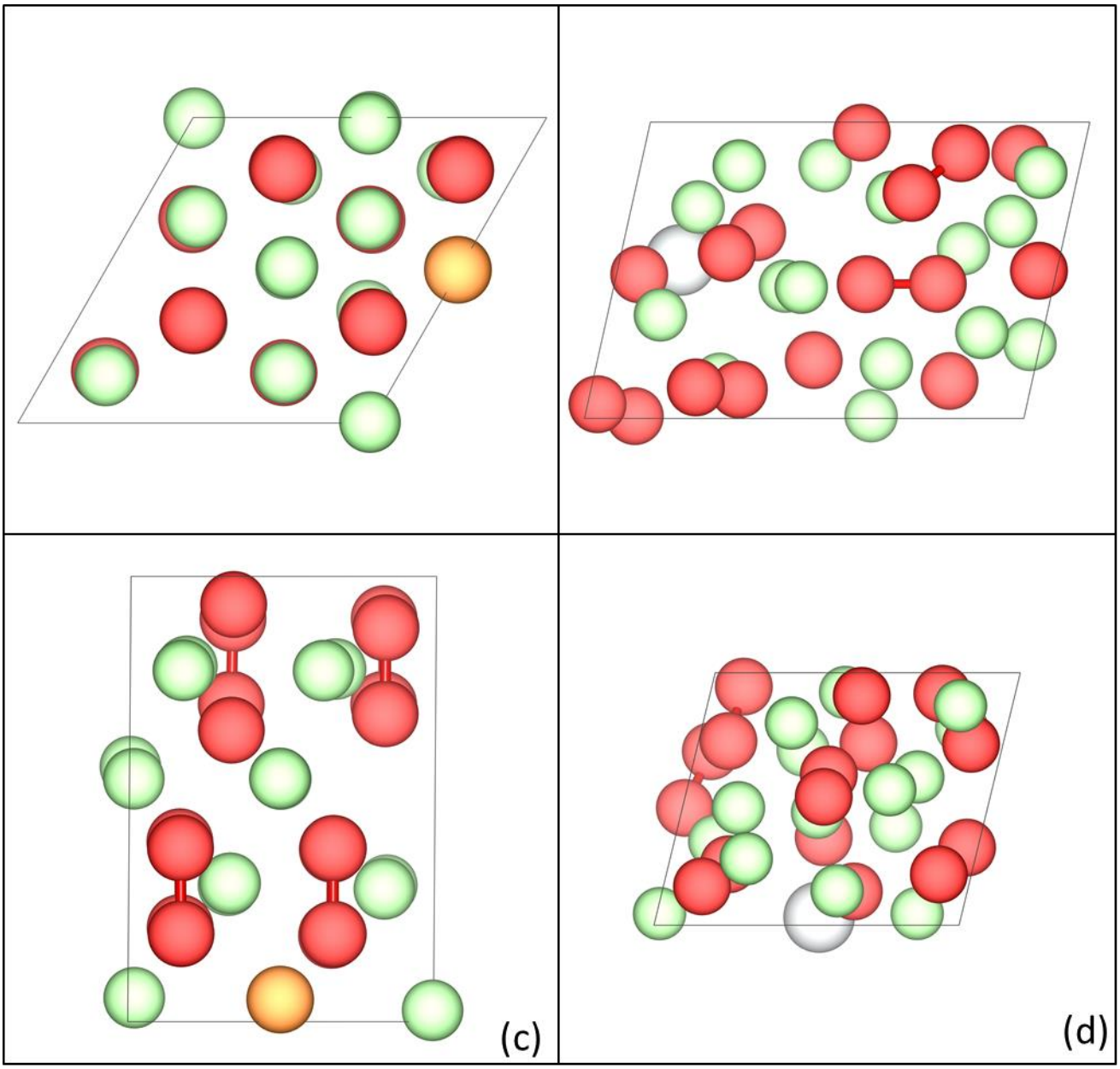

Figure B14: Schematic of u-$Li_{15}O_{16}D_1$ structure in the xy (top panel) and yz(bottom panel) where D is (a)Ba, (b)Na, (c) Mg and (d) Ni. Color code: Li= green, O= red, Ba= dark green, Na= pale yellow, Mg= orange and Ni= silver.

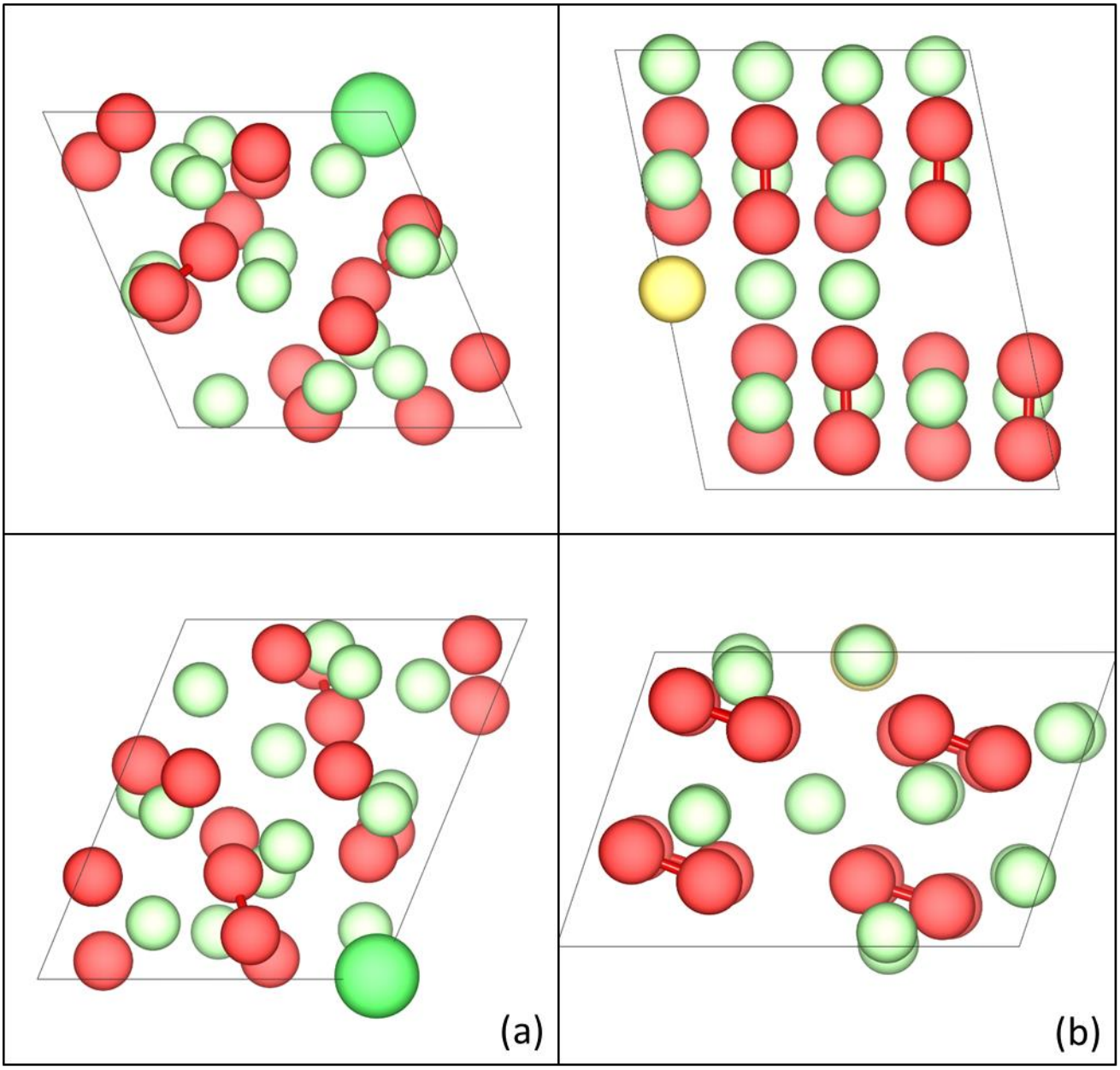
(a)
(b)

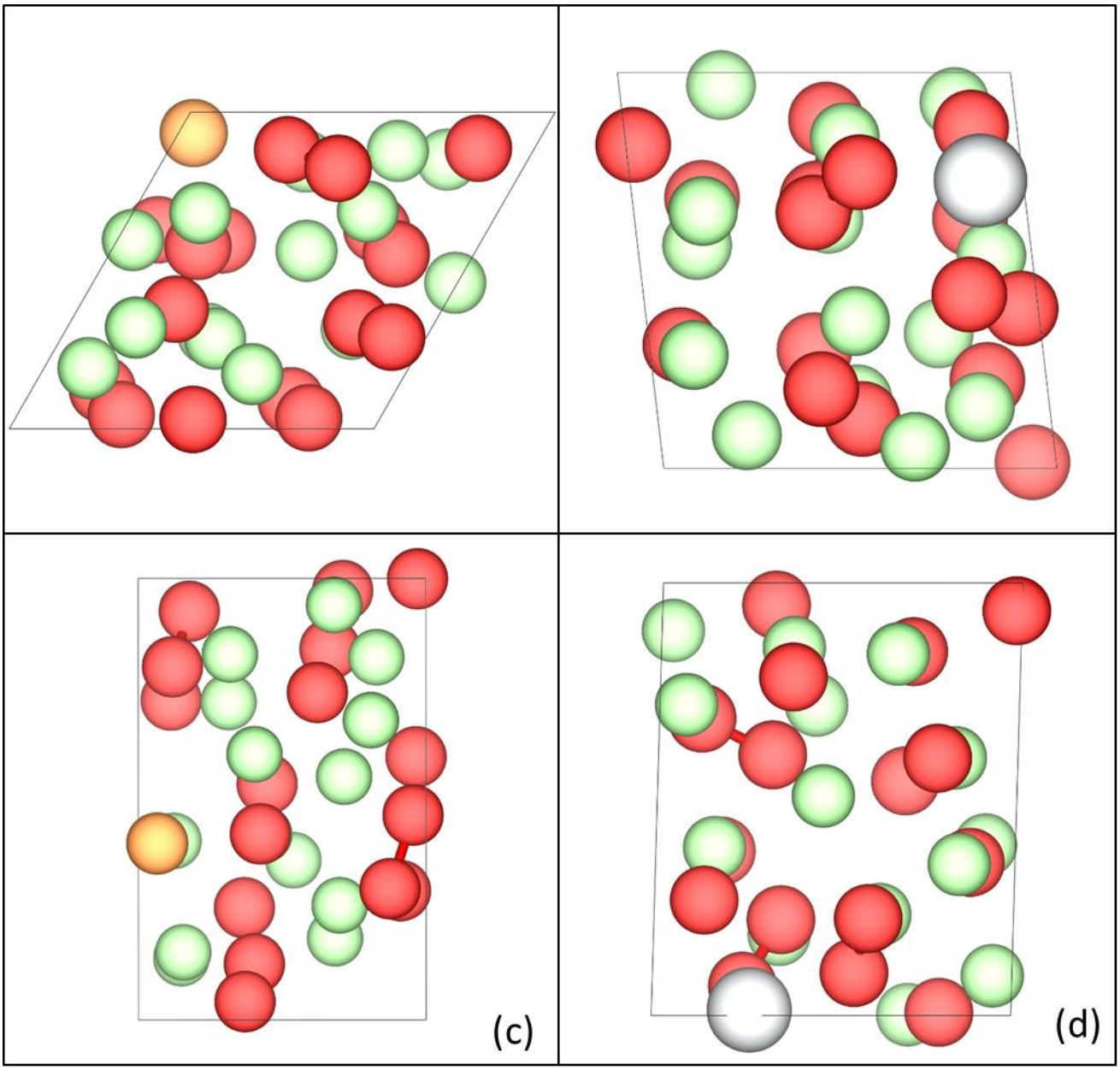

Figure B15: Schematic of u-$Li_{14}O_{16}D_1$ structure in the xy (top panel) and yz(bottom panel) where D is (a)Ba, (b)Na, (c) Mg and (d) Ni. Color code: Li= green, O= red, Ba= dark green, Na= pale yellow, Mg= orange and Ni= silver.

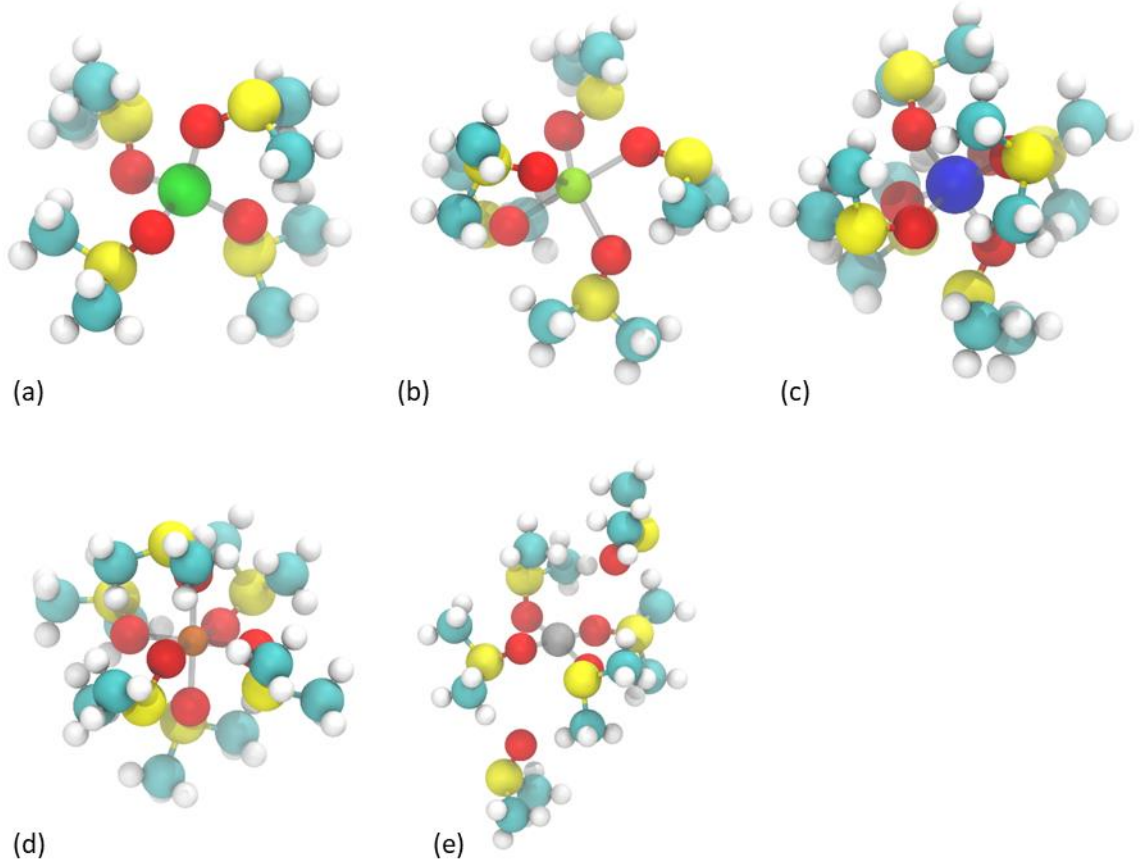

Figure B16: B3LYP/6-31G(d) optimized structure of (a) $Li^{+}(DMSO)_4$, (b) $Na^{+}(DMSO)_5$, (c) $Co^{+2}(DMSO)_6$, (d) $Mg^{+2}(DMSO)_6$ and (e)$Ni^{+2}(DMSO)_6$ in solution phase (implicit)

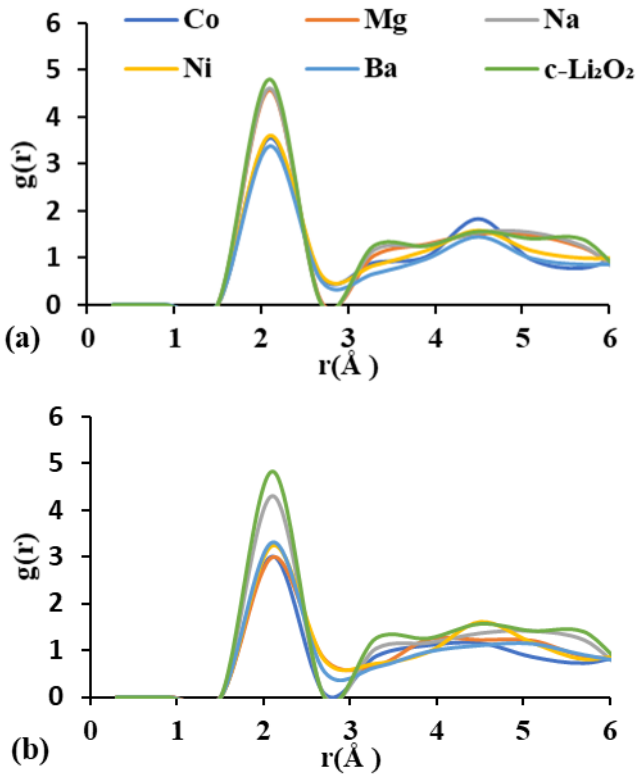

Figure B17: Radial distritbution function between Li atom and O atom $g(r)_{Li\text{-}O}$ for bulk solid of composition (a) *u*-$Li_{15}D_1O_{16}$ and (b)*u*-$Li_{14}D_1O_{16}$. Both figures also show the $g(r)_{Li\text{-}O}$ for *c*-Li_2O_2. The associated coordination number is shown in Table 1

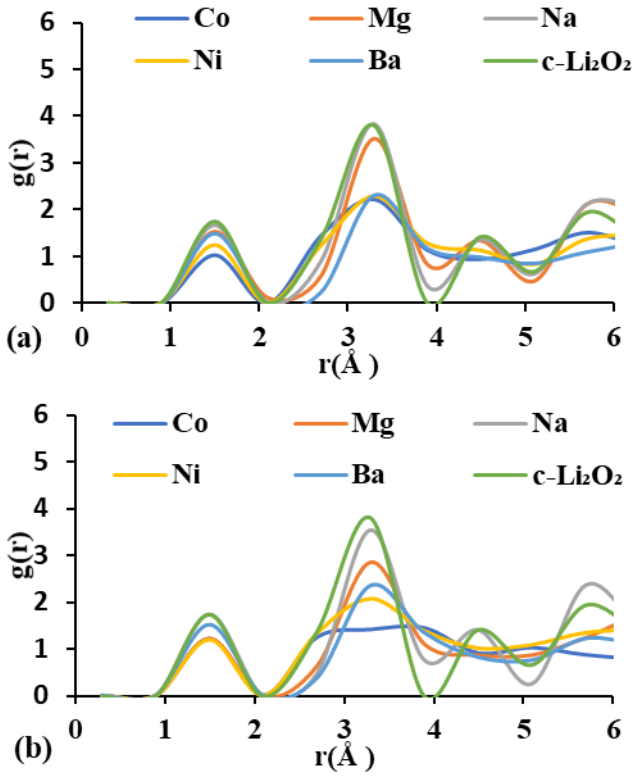

Figure B18: Radial distritbution function between O atom and O atom $g(r)_{O\text{-}O\ O}$ for bulk solid of composition (a) *u*-$Li_{15}D_1O_{16}$ and (b)*u*-$Li_{14}D_1O_{16}$. Both figures also show the $g(r)_{Li\text{-}O}$ for *c*-Li_2O_2. The associated coordination number for the first two peaks is shown in Table 1.

Configuration=*c*-$Li_{16}O_{16}$ (spin polarized)

1.00000000000000
6.2319033696757922 -0.0000000000580801 0.0000000000000000
-3.1159516805814622 5.3969866345265336 0.0000000000000000
0.0000000000000000 0.0000000000000000 7.6103200193658225
O Li
16 16
Direct
0.1666664999999981 0.3333335000000019 0.6511512885468633
0.1666664999999981 0.8333335000000019 0.6511512885468633
0.6666664999999981 0.3333335000000019 0.6511512885468633
0.6666664999999981 0.8333335000000019 0.6511512885468633
0.3333335000000019 0.1666664999999981 0.1511512885468633
0.3333335000000019 0.6666664999999981 0.1511512885468633
0.8333335000000019 0.1666664999999981 0.1511512885468633
0.8333335000000019 0.6666664999999981 0.1511512885468633
0.3333335000000019 0.1666664999999981 0.3488487114531367
0.3333335000000019 0.6666664999999981 0.3488487114531367
0.8333335000000019 0.1666664999999981 0.3488487114531367
0.8333335000000019 0.6666664999999981 0.3488487114531367
0.1666664999999981 0.3333335000000019 0.8488487114531367
0.1666664999999981 0.8333335000000019 0.8488487114531367
0.6666664999999981 0.3333335000000019 0.8488487114531367
0.6666664999999981 0.8333335000000019 0.8488487114531367
0.0000000000000000 0.0000000000000000 0.0000000000000000
0.0000000000000000 0.5000000000000000 0.0000000000000000
0.5000000000000000 0.0000000000000000 0.0000000000000000
0.5000000000000000 0.5000000000000000 0.0000000000000000
0.0000000000000000 0.0000000000000000 0.5000000000000000
0.0000000000000000 0.5000000000000000 0.5000000000000000
0.5000000000000000 0.0000000000000000 0.5000000000000000
0.5000000000000000 0.5000000000000000 0.5000000000000000
0.1666664999999981 0.3333335000000019 0.2500000000000000
0.1666664999999981 0.8333335000000019 0.2500000000000000
0.6666664999999981 0.3333335000000019 0.2500000000000000
0.6666664999999981 0.8333335000000019 0.2500000000000000
0.3333335000000019 0.1666664999999981 0.7500000000000000
0.3333335000000019 0.6666664999999981 0.7500000000000000
0.8333335000000019 0.1666664999999981 0.7500000000000000
0.8333335000000019 0.6666664999999981 0.7500000000000000

Configuration=*c*-$Li_{15}O_{16}$ (spin polarized)

1.00000000000000
6.3040979208035779 0.0000000000000000 0.0000000000000000
-3.1520489560451641 5.4595089498758584 0.0000000000000000
0.0000000000000000 0.0000000000000000 7.4435638209096036
O Li
16 15
Selective dynamics
Direct
0.1666664999999981 0.3333335000000019 0.6489384770167912 T T T
0.1739068568983726 0.8369536784491963 0.6536755230615943 T T T
0.6630463215508037 0.3260931431016273 0.6536755230615943 T T T
0.6630463215508037 0.8369536784491963 0.6536755230615943 T T T
0.3345026183658444 0.1654973816341556 0.1491430632073638 T T T
0.3345026183658444 0.6690047367316545 0.1491430632073638 T T T
0.8309952632683455 0.1654973816341556 0.1491430632073638 T T T
0.8333335000000019 0.6666664999999981 0.1493799424570259 T T T
0.3345026183658444 0.1654973816341556 0.3508569367926362 T T T
0.3345026183658444 0.6690047367316545 0.3508569367926362 T T T
0.8309952632683455 0.1654973816341556 0.3508569367926362 T T T
0.8333335000000019 0.6666664999999981 0.3506200575429740 T T T
0.1666664999999981 0.3333335000000019 0.8510615229832088 T T T
0.1739068568983726 0.8369536784491963 0.8463244769384057 T T T
0.6630463215508037 0.3260931431016273 0.8463244769384057 T T T
0.6630463215508037 0.8369536784491963 0.8463244769384057 T T T
0.9942464874774085 0.9884929749548245 0.9926693429623364 T T T
0.9942464874774085 0.5057535125225915 0.9926693429623364 T T T
0.5000000000000000 0.0000000000000000 0.0075842759167088 T T T
0.5115070250451755 0.5057535125225915 0.9926693429623364 T T T
0.9942464874774085 0.9884929749548245 0.5073306570376636 T T T
0.9942464874774085 0.5057535125225915 0.5073306570376636 T T T
0.5000000000000000 0.0000000000000000 0.4924157240832912 T T T
0.5115070250451755 0.5057535125225915 0.5073306570376636 T T T
0.1666664999999981 0.3333335000000019 0.2500000000000000 T T T
0.1660383709351340 0.8330194354675735 0.2500000000000000 T T T
0.6669805645324265 0.3339616290648660 0.2500000000000000 T T T
0.6669805645324265 0.8330194354675735 0.2500000000000000 T T T
0.3303261308970711 0.1696738691029361 0.7500000000000000 T T T
0.3303261308970711 0.6606517617941221 0.7500000000000000 T T T
0.8393482382058779 0.1696738691029361 0.7500000000000000 T T T

Configuration=*u*-$Li_{15}Co_1O_{16}$ (spin polarized)

1.00000000000000
6.5095446953337097 -0.4122213198961448 -0.3509800236893207
-2.5437986539763249 7.4685123175709354 1.0219987649510165
-2.7737964942825664 -3.0133878878917946 6.4806067208801101
O Li Co
16 15 1
Selective dynamics
Direct

0.7811650102632628	0.1110296782243705	0.5319140146230557	T	T	T
0.7276348112508615	0.3593999842448238	0.2924796464504436	T	T	T
0.4406190120500072	0.3144275524872945	0.5233335850526865	T	T	T
0.2928699886835097	0.4123352344659717	0.0829277704784590	T	T	T
0.2227631148926548	0.5383763084080566	0.7418729030043589	T	T	T
0.8918989013239981	0.4556019297778121	0.8906651500930665	T	T	T
0.9412986908964277	0.3966785294706082	0.2888990638473988	T	T	T
0.8870207542979195	0.0692830248910970	0.4267461910359078	T	T	T
0.0318816734977592	0.0296620973042418	0.0458660844982735	T	T	T
0.3323737632039541	0.0243213437470214	0.8307546880920604	T	T	T
0.5767753897483242	0.0291416142721571	0.8780238002236428	T	T	T
0.8074674215698642	0.7275062096378915	0.6173742242511122	T	T	T
0.5521703651813006	0.7101801983249475	0.5529343466451839	T	T	T
0.2187914265593036	0.8740612682731014	0.4292770563948977	T	T	T
0.3366432318393711	0.7737074679331650	0.0971061133516642	T	T	T
0.8530303049175895	0.8241888433039378	0.0089504227076857	T	T	T
0.3882019810561146	0.2201442805549125	0.0391790170359648	T	T	T
0.5000720497209160	0.4892008668322901	0.3790169435939715	T	T	T
0.7741981091519082	0.3699909198302727	0.5764487606461626	T	T	T
0.1692119702099179	0.3437280647135443	0.5153776447065527	T	T	T
0.9154928558562362	0.2618000389573591	0.0375207936787368	T	T	T
0.4524603703868535	0.1282452548031234	0.6553467075449977	T	T	T
0.2202545771096970	0.0728369823035944	0.3230655010735902	T	T	T
0.7624857025830505	0.9267328179257165	0.7830060672359650	T	T	T
0.0097872077847576	0.8886722395049161	0.5263125108098318	T	T	T
0.3128912811566849	0.7733954370836820	0.6400260720979086	T	T	T
0.6354798124827969	0.5631195441509360	0.7390922530267975	T	T	T
0.1062225638709512	0.8500486994485693	0.9085966002127288	T	T	T
0.6449768058317377	0.9062182556737466	0.0764523101710046	T	T	T
0.0157151642261744	0.6998747195743795	0.1715032206578027	T	T	T
0.4680165472366219	0.8528299864037445	0.3887374774237813	T	T	T
0.1974091411592649	0.5407596074726054	0.9499680593341863	T	T	T

Configuration=*u*-$Li_{14}Co_1O_{16}$ (spin polarized)
1.00000000000000
6.9946572561866045 0.9895097467630228 0.1795915861481595
-0.8714970426030557 7.0186076862174014 -0.5638788154521153
-0.2412604538618828 0.5075161857011923 6.7330269737202606
O Li Co
16 14 1
Selective dynamics
Direct
0.3749148895404204 0.2611107777412869 0.9953829213117729 T T T
0.3816116399597860 0.7456601287401696 0.9966812534335006 T T T
0.5850617421586932 0.2310482786980543 0.0000782840023277 T T T
0.5911333843306537 0.7734251683212392 0.0013902858727945 T T T
0.2046841408900590 0.9987784999895553 0.3890981894634464 T T T
0.2073027657009376 0.9978075088884424 0.6106772428462435 T T T
0.7233960929120684 0.0004191799005966 0.6160537578837335 T T T
0.7205230644933067 0.9981832699905127 0.3926985257874946 T T T
0.0275116172326975 0.4094695521248113 0.2403371911871730 T T T
0.0168394695618730 0.6051550375223584 0.7727222540665650 T T T
0.0201522874564972 0.3940394104432059 0.7654211973381564 T T T
0.0212166151590409 0.5976176359804626 0.2271881712587813 T T T
0.3849143525392051 0.2955142333359717 0.4961089305534969 T T T
0.3364161616545971 0.6587934454076532 0.4962074009046731 T T T
0.6328020802378092 0.5054220596668841 0.7054071101473198 T T T
0.6391641411591351 0.5033092185420998 0.2995195008925293 T T T
0.7548718930929184 0.7360862451254349 0.7622685313703315 T T T
0.7066958766092739 0.2446822584502897 0.2522663421992561 T T T
0.2686593509930830 0.7693154450752289 0.2572975900963428 T T T
0.2499507117690030 0.2366468875074972 0.7330185680130725 T T T
0.2647784079278424 0.2311983697692881 0.2585195250298398 T T T
0.2507822653895246 0.7613235033418988 0.7377142048546190 T T T
0.7534559134084944 0.2680569272340563 0.7619453290163065 T T T
0.7218562848491246 0.7526092825203108 0.2492885791641868 T T T
0.4771965396461866 0.0018715177398576 0.9691772311172855 T T T
0.9655965920584109 0.0003213597932543 0.5031420766459505 T T T
0.1529255469758084 0.4938332236650567 0.9843251949231373 T T T
0.1042055020350148 0.5070664453640958 0.5283234581854046 T T T
0.5403944351446697 0.5033626269419855 0.9959481122314529 T T T
0.4679375019233234 0.0270593532903192 0.5064253149180971 T T T
0.5080647331905652 0.4951461488880824 0.5014717252847163 T T T

Configuration=*u*-$Li_{15}Ba_1O_{16}$ (spin polarized)

1.00000000000000
7.5661661309714630 0.2907513927089545 -0.3209211391226753
-2.3778847184080978 5.3662651957916188 -0.2191901773482458
0.0306785821531162 0.2525830144448676 8.1246677350984857
Li O Ba
15 16 1
Selective dynamics
Direct
0.7842648823646762 0.5921576031167811 0.3588702478996041 T T T
0.4145484087124062 0.2858868591918351 0.6708553915728480 T T T
0.0066448100219612 0.9643648983785367 0.2134231123641598 T T T
0.1047125697284294 0.6290125026323693 0.2826383861954753 T T T
0.3002222728477957 0.0433999951004392 0.3995156524333897 T T T
0.9477082779744730 0.3811616533800328 0.7650299616738109 T T T
0.1563933929210602 0.7420791350286494 0.6048116123180423 T T T
0.4802007007972847 0.6061879199135144 0.2347864250935650 T T T
0.5604886658089900 0.8033403394977421 0.6814339628611233 T T T
0.8717206698788305 0.7690177466055875 0.6143393291344956 T T T
-0.0056265066078740 0.1496005845785267 0.4704844017656243 T T T
0.6598591714025873 0.2076334376089074 0.5238062692020083 T T T
0.1161935003070600 0.0346473502833732 0.8374917119129086 T T T
0.8208287719782371 0.7430955415184329 0.9274822861805599 T T T
0.2211110186460472 0.7146666686504124 0.9153190313529275 T T T
0.8430970264022221 0.2941787965784530 0.3527925718091036 T T T
0.3599015152622335 0.8364978617679629 0.2504546085236850 T T T
0.5090779709999805 0.3972550639529681 0.4100430284611960 T T T
0.2357155362451633 0.8894768235687471 0.1218355501676011 T T T
0.9961837959808271 0.2872908514742951 0.2464189902337644 T T T
0.6168951114358778 0.5165839022036591 0.5655790604137704 T T T
0.1917130379856619 0.4080483216235517 0.6347390293164735 T T T
0.4121081696812648 0.9697465033507228 0.6063834831094902 T T T
0.5890890561196536 0.5922814003191248 0.0285001870401709 T T T
0.9991524572315027 0.7002364913409393 0.7951333736324599 T T T
0.8591572751311202 0.0742426520165290 0.8509286099272463 T T T
0.7440443842541189 0.7309610462062807 0.1512753780503167 T T T
0.4039122579118820 -0.0021900474376355 0.7881498721905315 T T T
0.2349611147863858 0.4025431477923632 0.7964742530610871 T T T
0.8168110088469961 0.0576849657211146 0.6715275932706778 T T T
0.0288362673502153 0.8489489546362927 0.4285996092221982 T T T
0.6321094075928926 0.1458110293995314 0.0783510196098544 T T T

Configuration=*u*-$Li_{14}Ba_1O_{16}$ (spin polarized)

1.00000000000000
6.4535592251939313 1.9026323552052327 0.6116734218744037
-2.5563013880698806 1.9788261669244664 -6.3829868519175799
-1.3212485966636278 7.7282582896964636 0.0755014266738139
Li O Ba
14 16 1
Selective dynamics
Direct

0.3195025446368134	0.8101152230049888	0.5062759450340764	T	T	T
0.7086949393452426	0.1768934871127169	0.4651369854784216	T	T	T
0.9098866830170652	0.5696097932626895	0.8512699243361291	T	T	T
0.1181550048416777	0.4653226151027074	0.1338935442770742	T	T	T
0.7844689427824657	0.8168401027745907	0.4768534696820521	T	T	T
0.4740225471639367	0.5431215159627709	0.3038259894604133	T	T	T
0.4301389610444921	0.4540079680920079	0.9220837553345174	T	T	T
0.1576981701197999	0.0834234829122059	0.5186343016271531	T	T	T
0.4473453304262814	0.8999897571243762	0.1371890846506125	T	T	T
0.9613931836509686	0.5698881592346219	0.3692944320938468	T	T	T
0.4958847934271993	0.1286774258588758	0.8021285347278565	T	T	T
0.0762842463132093	0.4240858320197328	0.6408508754750916	T	T	T
0.6455931859738856	0.2770508383604373	0.1549139016323441	T	T	T
0.3628898073037133	0.7719004033811774	0.8161623158492913	T	T	T
0.4066466627252683	0.0409051368455113	0.5976256254226550	T	T	T
0.3148910745958270	0.5547862005415746	0.7225884861198819	T	T	T
0.4239826034932609	0.6556997256442908	0.0574936563101988	T	T	T
0.9457205071252731	0.6502198856019831	0.5761334997223909	T	T	T
0.5668479082585558	0.8209732010579079	0.3436934105826951	T	T	T
0.7081254253725014	0.4497282149598811	0.2963881750361104	T	T	T
0.6255953988357860	0.3236092144156827	0.9048982298018756	T	T	T
0.1343659647117558	0.3872107816398719	0.3979217565240530	T	T	T
0.8916807808078483	0.5654583498321093	0.1242999061392029	T	T	T
0.7304218766496293	0.0460375332417940	0.2858527974961697	T	T	T
0.9569979110044475	0.2031520342992275	0.5602157506569314	T	T	T
0.4138786610565233	0.1701173320977107	0.0481622015569651	T	T	T
0.1172498254416538	0.4334496060276539	0.8849792711167010	T	T	T
0.2222396900192241	0.9596272139319434	0.7624413448171382	T	T	T
0.0808117624588753	0.8464651684557647	0.4010935381907328	T	T	T
0.5858021246429814	0.8735174747843593	0.9258389425801928	T	T	T
0.9608224827537923	0.9874153224188005	0.0200713482671978	T	T	T

Configuration=*u*-$Li_{15}Na_1O_{16}$ (non spin polarized)

1.00000000000000
5.3588369256892481 -0.0544445925058265 -0.5948865470464305
-2.4913985651705461 7.7886109252524651 1.1093217728995730
0.6837940816282234 0.6038649077682811 6.1617323505503245
Li O Na
15 16 1
Selective dynamics
Direct
0.0138237889011675 0.0330112184404054 0.3754977784760646 T T T
0.2259378761043500 0.7832495530532292 0.9372995122624089 T T T
0.8028416633777605 0.2746410961718149 0.8158400074575032 T T T
0.0180957263712638 0.0292293778684465 0.8739783980380988 T T T
0.7615707518610905 0.5306046658468125 0.0009955680139211 T T T
0.2621008439268169 0.5307437650911893 0.2465434477386195 T T T
0.3045821596716583 0.2737555218878238 0.5657962209920755 T T T
0.7219642765397067 0.7869926606686873 0.1852935841355440 T T T
0.7226239513934507 0.7857763532444378 0.6866482750926010 T T T
0.2612140238196864 0.5306189493756066 0.7557621871413633 T T T
0.5073152155687929 0.0319558446626292 0.1260203841864357 T T T
0.2195301164842748 0.7873308204406527 0.4353669152104903 T T T
0.5105679981653644 0.0282274756609532 0.6248377462020633 T T T
0.8018562572141387 0.2754905370027831 0.3143616534591670 T T T
0.2982346903895649 0.2776414645648309 0.0641452364041466 T T T
0.5070245007434407 0.6794029396982856 0.9631334485024795 T T T
0.0300214747596105 0.3716161807192577 0.5410189767407391 T T T
0.4179751992879982 0.1759391944924725 0.3384005829342786 T T T
0.0125102012211561 0.6902109258062709 0.2019334675527161 T T T
0.4193991861035453 0.1750435781012780 0.8416648908539948 T T T
0.1065717826335107 0.8851284044596530 0.6624873932590845 T T T
0.0132465960643915 0.6894811209111482 0.7193150173272055 T T T
0.0170423916457478 0.3815323593149739 0.0386018120765725 T T T
0.9214862922489778 0.1846507690895599 0.0881957244807020 T T T
0.4943549979716739 0.6901878475209635 0.4603175150034965 T T T
0.6033445904385041 0.8859540075982064 0.4107244511055147 T T T
0.5114728598851002 0.3706614430977448 0.7999518216052118 T T T
0.5104780732154850 0.3715389214552030 0.2820349131190567 T T T
0.1052746916424063 0.8859010878980755 0.1592610000081688 T T T
0.6029813978060767 0.8762856083202288 0.9127174877448987 T T T
0.9216170695666194 0.1758346984455738 0.5899159015863521 T T T
0.7608973549766891 0.5303346090907944 0.5005366812890061 T T T

Configuration=*u*-$Li_{14}Na_1O_{16}$ (spin polarized)

1.00000000000000
6.2084612965897223 -0.1234471844440456 -0.1969648831982665
-1.2909421057660555 6.3598864894015490 5.2589275894230827
0.1120377092489602 -1.8708618636903112 5.1226535449576476
Li O Na
14 16 1
Selective dynamics
Direct
0.2841418363011660 0.4552690733973522 0.4844226122424015 T T T
0.6543380771916772 0.9451397851204124 0.7187514802374505 T T T
0.9517764337430377 0.2133440337200553 0.4411616633515860 T T T
0.0814291894105494 0.7026721198852720 0.5269540218625656 T T T
0.4762441449977236 0.2156209480465117 0.4483758128177847 T T T
0.8964346149589849 0.9621435785770841 0.2443515070562518 T T T
0.6006932976561866 0.6911452522927007 0.5177058888490312 T T T
0.1461077744306113 0.9622716767096674 0.7229201140026195 T T T
0.5297944970957158 0.4564296337369628 0.9849838570577796 T T T
0.7092953057404239 0.2075667059382477 0.9299890344877446 T T T
0.2121437935240118 0.1972625417073446 0.9696194218183166 T T T
0.3433247354824607 0.7154336987215678 -0.0007933670453332 T T T
0.8408891413086970 0.7050131606542978 0.0352406996918277 T T T
0.4061140643544585 0.9543573313327309 0.2474890203084196 T T T
0.9383769741318884 0.0975778871125963 0.8362847044216610 T T T
0.1866237677106231 0.1091008875246787 0.3389821323518877 T T T
0.6111642118787686 0.8044462052202993 0.1315273512187876 T T T
0.4708234889030780 0.2961891222865898 0.7404612210457278 T T T
0.1242283148595549 0.8166321113341537 0.1336319062414134 T T T
0.8681926446966985 0.8172184908722675 0.6372983303649293 T T T
0.3270727451855100 0.6092136508544993 0.7238408919033563 T T T
0.6816988673325205 0.0949616590870961 0.3268312055690567 T T T
0.7253037983073950 0.2875338238013213 0.2186853676598298 T T T
0.3691883324029570 0.8025803209397246 0.6302529785823587 T T T
0.8150048299239488 0.6248045144274593 0.7469003690110082 T T T
0.0846308416691260 0.6292843441123773 0.2348761424392717 T T T
0.4300743513271814 0.1069443776102589 0.8319449276614151 T T T
0.5553546505282835 0.6150589273816747 0.2238434070416489 T T T
0.2452255143904145 0.3023885663478478 0.2454179137630150 T T T
0.9939742071597293 0.2849373412145133 0.7342483951369456 T T T
0.0253675533966314 0.4563882300324486 0.9844469888492783 T T T

Configuration=*u*-$Li_{15}Mg_1O_{16}$ (spin polarized)

1.00000000000000
3.1241595636594761 -5.3981509068186453 -0.1945453090034200
3.1183654969995507 5.3865514059600716 0.1703673375636686
0.0987233233800355 -0.2935197361900735 7.8272241456257152
O Li Mg
16 15 1
Selective dynamics
Direct
0.8424964225454568 0.6704129272572091 0.1984085645894494 T T T
0.3372715862683642 0.1682921212636902 0.2111358194763668 T T T
0.8425579724910807 0.1719366560096784 0.1989195740055431 T T T
0.1643831366160771 0.3355940847391156 0.9032567618807279 T T T
0.6711422117252160 0.8355183445067121 0.8849708018834608 T T T
0.1645167362288021 0.8291976649698198 0.9033014210469577 T T T
0.3323293059006260 0.1656076020188893 0.4034736789448399 T T T
0.8377889884879055 0.1679384787934699 0.3903971185654115 T T T
0.8374165872087505 0.6682953440496573 0.3898647357725973 T T T
0.6692605028603351 0.8347864039874513 0.6925689544029673 T T T
0.1618474416199771 0.8305291503857846 0.7117874875004387 T T T
0.1617763535323738 0.3320640142742254 0.7117462483076916 T T T
0.6653575088760467 0.3327822834691209 0.6563178428755950 T T T
0.3315894558031942 0.6652180460676093 0.3877645896422560 T T T
0.6718863288181581 0.3358616719861971 0.9335976963038605 T T T
0.3292606229799735 0.6644525223656508 0.1954019553473416 T T T
0.1711255620385972 0.8438141598296378 0.3074387578980344 T T T
0.1714016475185998 0.3267478259383900 0.3071383337792838 T T T
0.6717501667793139 0.8355355735807560 0.2981318830375279 T T T
0.9892266108844383 0.4940110337102254 0.5475731342101956 T T T
0.5074305614490979 0.4964629785472992 0.5458792775868490 T T T
0.5075141958617656 0.0111053428541111 0.5465238184637631 T T T
0.3688725509179421 0.1845084440101995 0.7990171485215302 T T T
0.8074122165053689 0.1735205201782193 0.7891574840176867 T T T
0.8074935361274284 0.6340492349408489 0.7886030933553208 T T T
0.5079195014142348 0.4902222139908858 0.0510202359501296 T T T
0.5073114816540694 0.0174876364714946 0.0514361198049939 T T T
0.0042536457525458 0.0024566415559187 0.5685275659850783 T T T
0.6619721899150415 0.3303535105377847 0.3112379639436190 T T T
0.3429403935039398 0.6718386231852055 0.7907607207981145 T T T
0.9960383966976384 0.9978603734059227 0.0300891005367256 T T T
0.9957291810176412 0.4978835711188262 0.0492591115656932 T T T

Configuration=*u*-$Li_{14}Mg_1O_{16}$ (non spin polarized)

1.00000000000000
-3.3531864861296405 5.2880174689439263 0.0604732072602322
-6.2567336497248069 -0.2723599368195844 -0.0864033663495462
-0.1105039419620870 -0.1706004373974973 7.5223557682411339
O Li Mg
16 14 1
Selective dynamics
Direct
0.3386057673186286 0.8274089471810416 0.6470094117014544 T T T
0.8373230173923977 0.8312913280647319 0.6576022817890037 T T T
0.3283334817184425 0.3409744666983662 0.6495633450800055 T T T
0.8336032696694404 0.3422531117551149 0.6487704984683145 T T T
0.1712816848653253 0.6581969756146639 0.1591420070735659 T T T
0.6689624481569504 0.6599466496828256 0.1576489297054718 T T T
0.1647439933788736 0.1660363852349640 0.1417062703786237 T T T
0.6659537121548863 0.1664223368559012 0.1558999357382934 T T T
0.1773234877788155 0.6539090185552110 0.3584605243275778 T T T
0.6685883816651751 0.6553543812466875 0.3570622403826666 T T T
0.1663591024005220 0.1629284294952874 0.3423741159322842 T T T
0.6658851866544226 0.1672523528236164 0.3547067813836453 T T T
0.3370908665139893 0.8335165637680103 0.8461467057369472 T T T
0.8370989246080390 0.8326186547949005 0.8564350983250143 T T T
0.3277607877740746 0.3419271054039761 0.8473409553144784 T T T
0.8354155685579704 0.3420982436903535 0.8465368941473357 T T T
0.9722021061519447 0.0215823207491553 0.9785740783318758 T T T
0.5111255247553026 0.0190072308480131 0.9776951825335558 T T T
0.0019204627271795 0.5001458075248978 0.9980319494752325 T T T
0.5125937240590908 0.4800041574124997 0.9831176025631914 T T T
0.9850902355021532 0.0046871029813939 0.5190338003273064 T T T
0.5147468876939245 0.0040740729142344 0.5207710270147834 T T T
0.0013432865493043 0.5010439100349042 0.5059726587266571 T T T
0.3302350593554347 0.8390580066358813 0.2365768229616227 T T T
0.8366320242674770 0.8280068469398161 0.2497129369008367 T T T
0.3299706669871552 0.3225362269072381 0.2423594075999971 T T T
0.8437994019146107 0.3253382679825574 0.2422326388469048 T T T
0.1569040334581934 0.6722554205167083 0.7617597030098187 T T T
0.6775370617251026 0.6719048014050847 0.7610485032400460 T T T
0.1655144180467770 0.1726731634277836 0.7517578660010654 T T T
0.5072004261983882 0.4877147128541804 0.5114518269824324 T T T

Configuration=*u*-$Li_{15}Ni_1O_{16}$ (spin polarized)

1.00000000000000
8.9871312537671972 -0.3364535908715995 0.2647922085170479
1.4962552940646192 4.2890233558678341 4.3024468972128558
0.5774430053003198 -2.9521696349391346 4.5127471224377977
Li O Ni
15 16 1
Direct
0.9769260366066230 0.2515948616084260 0.2770982032755286
0.8736279179974969 0.6542234857161956 0.5365204239533596
0.1171683628276062 0.3382976938263113 0.6948992803456915
0.1557042677015692 0.7084903048710696 0.4060961367563317
0.4241325645946791 0.8414734820724886 0.0602668848075763
0.2883156743814409 0.1267362182878577 0.3313124090326698
0.5894499192743208 0.7453043191490164 0.5849307360662146
0.6296109822342056 0.0230655039269099 0.0208497619595451
0.3939779523885589 0.4566878948494360 0.4329958537256591
0.2262836064436050 0.8611939996481915 0.7530724348931549
0.8607832509088066 0.2899121322071274 0.7904523949279669
0.7753033679687344 0.5754217404542671 0.1340087850529985
0.4266654662143112 0.4449066603668207 0.9147361931152731
0.6487549184527253 0.1749837829549603 0.4709471182438781
0.9139529881818789 0.8335797554418554 0.8474805541179274
0.2421291963398756 0.5576203723443797 0.7205466776907867
0.2988300149789865 0.6350577964320934 0.1298504856885591
0.7376752616988164 0.4512412253081042 0.5028778661154583
0.6344122839319588 0.7518866317478838 0.9093129579060237
0.5741637792833159 0.4457382258571054 0.5981173330424714
0.0512482795461901 0.4913978857346873 0.3490305386018606
0.0295725544075999 0.0543937989543521 0.7062941222718998
0.8466044475704068 0.8917989542491301 0.1947540086736735
0.4892077235652230 0.9590954464181551 0.3195051222977378
0.3466659513200002 0.0887783866935268 0.7721085699074154
0.7226160084163160 0.8970199943936545 0.7152657947671465
0.4895555513409863 0.2014670584869196 0.2429583395036944
0.2487200160941151 0.1297708352361663 0.9754280067930977
0.8108125931663758 0.1150589193852625 0.1509872500033758
0.1084755451697588 0.0070407765753685 0.4596914804420573
0.9587853097980082 0.4993524649276805 0.9122199610346380
0.1368882071954552 0.5440483918745289 0.0303833149863372

Configuration=*u*-$Li_{14}Ni_1O_{16}$ (spin polarized)

1.00000000000000
6.2369750419085559 -0.0649261302242356 -0.1275170245842789
1.1073595730701680 6.4383157856194941 0.2898567629807568
1.8114912956269689 0.2591519437895213 7.1637105573825046
Li O Ni
14 16 1
Selective dynamics
Direct
0.8808727235795337 0.0716956994850550 0.6954508702732632 T T T
0.2584463481967381 0.0269739351268645 0.8892567744333267 T T T
0.5952744765464635 0.1355499369970648 0.3875972205287933 T T T
0.9108757066267988 0.4721863918356981 0.5019765184965967 T T T
0.6331506933965021 0.9476713026680368 0.0746859971862445 T T T
0.1588683907762639 0.3297182161299972 0.2046748912229273 T T T
0.1276633304059892 0.4771579550305265 0.7355956071293702 T T T
0.4826693232129299 0.3828038387047301 0.8441205904851462 T T T
0.5347469140029200 0.6405864019837406 0.2247934902227630 T T T
0.1097870903314618 0.7292616624696869 0.0124331153979103 T T T
0.8441283804647537 0.8319265873257191 0.3414632043631512 T T T
0.2135961295622925 0.9244135666144110 0.3933105641205607 T T T
0.7206219568160830 0.6557084234611608 0.8453997889117875 T T T
0.5281665426715313 0.8132090984282170 0.5866332698590896 T T T
0.4600409868517873 0.3179200994258493 0.5892071985987050 T T T
0.5061027088984480 0.1264076408792179 0.6660885440653541 T T T
0.8352552263259644 0.3716210810753002 0.7919890558463306 T T T
0.9192635938539713 0.1188971327645301 0.2788234196433851 T T T
0.5824972163590949 0.2512911540362572 0.0875418028843326 T T T
0.1848900981242611 0.2981434453197812 0.9500514320137379 T T T
0.3979070486612614 0.6972742222656264 0.8310426250038863 T T T
0.5265035302556872 0.8805475681065755 0.3369760551366777 T T T
0.0119885832992112 0.1858052359905387 0.4253371245888122 T T T
0.9355819073888608 0.0008023600406008 0.9461762791213082 T T T
0.9581833250264987 0.5825182659503051 0.2257341604977833 T T T
0.4551178437098504 0.3670620546689192 0.2141226618451701 T T T
0.0717346546727930 0.6937512287531703 0.5370387206681846 T T T
0.4262164312677009 0.7885816367145114 0.9982019891579498 T T T
0.8374019939458140 0.5465394616959675 0.0891333773064909 T T T
0.8383654314007789 0.7849672590086575 0.6072824982645005 T T T
0.8975684133678793 0.2675271370433110 0.0186671527265634 T T T

Appendix C: Copyright Information

C.1. Permission to Use Chapter 3 Text and Figures

Estimation of electric field effects on the adsorption of molecular superoxide species on Au based on density functional theory

S. H. Rawal, W. C. McKee and Y. Xu, *Phys. Chem. Chem. Phys.*, 2017, **19**, 32626
DOI: 10.1039/C7CP06242G

If you are not the author of this article and you wish to reproduce material from it in a third party non-RSC publication you must formally request permission using Copyright Clearance Center. Go to our Instructions for using Copyright Clearance Center page for details.

Authors contributing to RSC publications (journal articles, books or book chapters) do not need to formally request permission to reproduce material contained in this article provided that the correct acknowledgement is given with the reproduced material.

Reproduced material should be attributed as follows:

- For reproduction of material from NJC:
  Reproduced from Ref. XX with permission from the Centre National de la Recherche Scientifique (CNRS) and The Royal Society of Chemistry.
- For reproduction of material from PCCP:
  Reproduced from Ref. XX with permission from the PCCP Owner Societies.
- For reproduction of material from PPS:
  Reproduced from Ref. XX with permission from the European Society for Photobiology, the European Photochemistry Association, and The Royal Society of Chemistry.
- For reproduction of material from all other RSC journals and books:
  Reproduced from Ref. XX with permission from The Royal Society of Chemistry.

If the material has been adapted instead of reproduced from the original RSC publication "Reproduced from" can be substituted with "Adapted from".

In all cases the Ref. XX is the XXth reference in the list of references.

If you are the author of this article you do not need to formally request permission to reproduce figures, diagrams etc. contained in this article in third party publications or in a thesis or dissertation provided that the correct acknowledgement is given with the reproduced material.

Reproduced material should be attributed as follows:

- For reproduction of material from NJC:
  [Original citation] - Reproduced by permission of The Royal Society of Chemistry (RSC) on behalf of the Centre National de la Recherche Scientifique (CNRS) and the RSC
- For reproduction of material from PCCP:
  [Original citation] - Reproduced by permission of the PCCP Owner Societies
- For reproduction of material from PPS:
  [Original citation] - Reproduced by permission of The Royal Society of Chemistry (RSC) on behalf of the European Society for Photobiology, the European Photochemistry Association, and RSC
- For reproduction of material from all other RSC journals:
  [Original citation] - Reproduced by permission of The Royal Society of Chemistry

If you are the author of this article you still need to obtain permission to reproduce the whole article in a third party publication with the exception of reproduction of the whole article in a thesis or dissertation.

C.2.

C.2. Permission to Use Appendix A Text and Figures

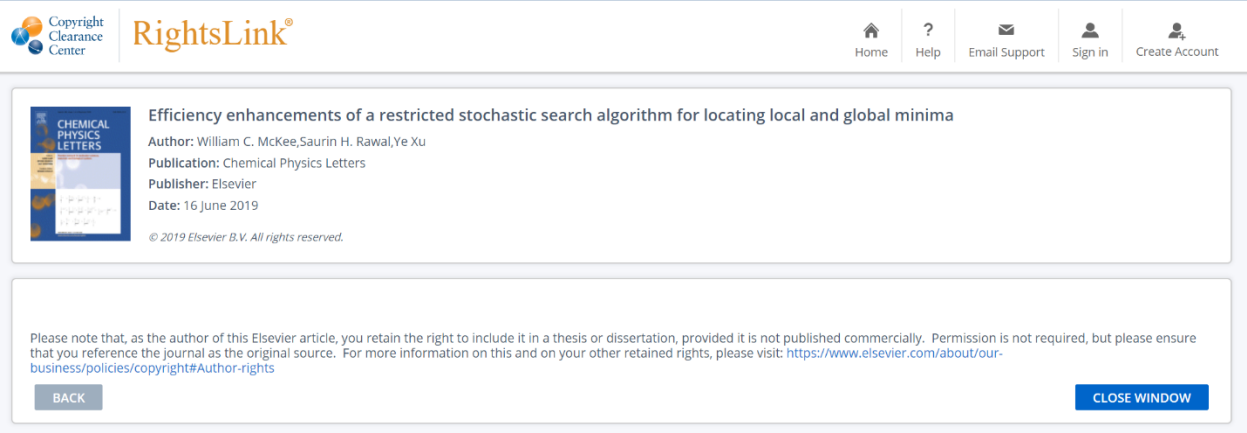

References

1. Lewis, N. S.; Nocera, D. G., Powering the planet: Chemical challenges in solar energy utilization. *Proceedings of the National Academy of Sciences* **2006,** *103* (43), 15729-15735.

2. Peng, Z. Q.; Freunberger, S. A.; Chen, Y. H.; Bruce, P. G., A Reversible and Higher-Rate Li-O_2 Battery. *Science* **2012,** *337* (6094), 563-566.

3. Bruce, P. G.; Freunberger, S. A.; Hardwick, L. J.; Tarascon, J. M., Li-O-2 and Li-S batteries with high energy storage. *Nature Materials* **2012,** *11* (1), 19-29.

4. Zhang, Y.; Zhang, X.; Wang, J.; McKee, W. C.; Xu, Y.; Peng, Z., Potential-Dependent Generation of O_2^- and LiO_2 and Their Critical Roles in O_2 Reduction to Li_2O_2 in Aprotic Li–O_2 Batteries. *J. Phys. Chem. C* **2016,** *120* (7), 3690-3698.

5. Bryantsev, V. S.; Blanco, M.; Faglioni, F., Stability of lithium superoxide LiO_2 in the gas phase: computational study of dimerization and disproportionation reactions. *J. Phys. Chem. A* **2010,** *114* (31), 8165-8169.

6. Xu, Y.; Shelton, W. A., Oxygen Reduction by Lithium on Model Carbon and Oxidized Carbon Structures. *J. Electrochem. Soc.* **2011,** *158* (10), A1177-A1184.

7. Xu, Y.; Shelton, W. A., O_2 reduction by lithium on Au(111) and Pt(111). *J. Chem. Phys.* **2010,** *133* (2), 024703.

8. Radin, M. D.; Siegel, D. J., Charge transport in lithium peroxide: relevance for rechargeable metal–air batteries. *Energy Environ. Sci.* **2013,** *6* (8), 2370-2379.

9. Mathiesen, N. R.; Yang, S.; García-Lastra, J. M.; Vegge, T.; Siegel, D. J., Charge Transport in Alkali-Metal Superoxides: A Systematic First-Principles Study. *Chem. Mater.* **2019,** *31* (21), 9156-9167.

10. Aetukuri, N. B.; McCloskey, B. D.; García, J. M.; Krupp, L. E.; Viswanathan, V.; Luntz, A. C., Solvating additives drive solution-mediated electrochemistry and enhance toroid growth in non-aqueous Li–O2 batteries. *Nat. Chem.* **2015,** *7* (1), 50-56.

11. Xia, C.; Fernandes, R.; Cho, F. H.; Sudhakar, N.; Buonacorsi, B.; Walker, S.; Xu, M.; Baugh, J.; Nazar, L. F., Direct evidence of solution-mediated superoxide transport and organic radical formation in sodium-oxygen batteries. *J. Am. Chem. Soc.* **2016,** *138* (35), 11219-11226.

12. McKee, W. C.; Rawal, S. H.; Xu, Y., Efficiency enhancements of a restricted stochastic search algorithm for locating local and global minima. *Chem. Phys. Lett.* **2019,** *725*, 1-7.

13. Hummelshøj, J. S.; Blomqvist, J.; Datta, S.; Vegge, T.; Rossmeisl, J.; Thygesen, K. S.; Luntz, A.; Jacobsen, K. W.; Nørskov, J. K., Communications: Elementary oxygen electrode reactions in the aprotic Li-air battery. *J. Chem. Phys.* **2010,** *132* (7), 071101.

14. Cota, L. G.; de la Mora, P., On the structure of lithium peroxide, Li2O2. *Acta Crystallogr. Sect. B: Struct. Sci.* **2005,** *61* (2), 133-136.

15. Adams, B. D.; Radtke, C.; Black, R.; Trudeau, M. L.; Zaghib, K.; Nazar, L. F., Current density dependence of peroxide formation in the Li–O 2 battery and its effect on charge. *Energy Environ. Sci.* **2013,** *6* (6), 1772-1778.

16. Lau, K. C.; Qiu, D.; Luo, X.; Greeley, J.; Curtiss, L. A.; Lu, J.; Amine, K., Theoretical exploration of various lithium peroxide crystal structures in a Li-air battery. *Energies* **2015,** *8* (1), 529-548.

17. Yang, G.; Wang, Y.; Ma, Y., A Stable, Magnetic, and Metallic Li3O4 Compound as a Discharge Product in a Li–Air Battery. . *J. Phys. Chem. Lett* **2014,** *5* (15), 2516-2521.

18. Yang, W.; Kim, D. Y.; Yang, L.; Li, N.; Tang, L.; Amine, K.; Mao, H. K., Oxygen-Rich Lithium Oxide Phases Formed at High Pressure for Potential Lithium–Air Battery Electrode. *Advanced Science* **2017**.

19. Radin, M. D.; Monroe, C. W.; Siegel, D. J., How dopants can enhance charge transport in Li2O2. *Chem. Mater.* **2015,** *27* (3), 839-847.

20. Timoshevskii, V.; Feng, Z.; Bevan, K. H.; Goodenough, J.; Zaghib, K., Improving Li2O2 conductivity via polaron preemption: An ab initio study of Si doping. *Appl. Phys. Lett.* **2013,** *103* (7), 073901.

21. Oganov, A. R.; Glass, C. W., Evolutionary crystal structure prediction as a tool in materials design. *J. Phys.: Condens. Matter* **2008,** *20* (6), 064210.

22. Oganov, A. R.; Ma, Y.; Lyakhov, A. O.; Valle, M.; Gatti, C., Evolutionary crystal structure prediction as a method for the discovery of minerals and materials. *Reviews in Mineralogy and Geochemistry* **2010,** *71* (1), 271-298.

23. Ballentine, L. E., *Quantum mechanics: a modern development*. World Scientific Publishing Company: 1998.

24. Hohenberg, P.; Kohn, W., Inhomogeneous electron gas. *Phys. Rev.* **1964,** *136* (3B), B864.

25. Kohn, W., Nobel Lecture: Electronic structure of matter—wave functions and density functionals. *Rev. Mod. Phys.* **1999,** *71* (5), 1253.

26. Lieb, E. H., Density functionals for Coulomb systems. In *Inequalities*, Springer: 2002; pp 269-303.

27. Levy, M., Electron densities in search of Hamiltonians. *Phys. Rev. A* **1982,** *26* (3), 1200.

28. Kohn, W.; Sham, L. J., Self-consistent equations including exchange and correlation effects. *Phys. Rev.* **1965,** *140* (4A), A1133.

29. Ceperley, D. M.; Alder, B., Ground state of the electron gas by a stochastic method. *Phys. Rev. Lett.* **1980,** *45* (7), 566.

30. Vosko, S. H.; Wilk, L.; Nusair, M., Accurate spin-dependent electron liquid correlation energies for local spin density calculations: a critical analysis. *Can. J. Phys.* **1980,** *58* (8), 1200-1211.

31. Perdew, J. P.; Zunger, A., Self-interaction correction to density-functional approximations for many-electron systems. *Phys. Rev. B* **1981,** *23* (10), 5048.

32. Wang, Y.; Perdew, J. P., Correlation hole of the spin-polarized electron gas, with exact small-wave-vector and high-density scaling. *Phys. Rev. B* **1991,** *44* (24), 13298.

33. Ernzerhof, M.; Scuseria, G. E., Assessment of the Perdew–Burke–Ernzerhof exchange-correlation functional. *The Journal of chemical physics* **1999,** *110* (11), 5029-5036.

34. Perdew, J. P.; Burke, K.; Ernzerhof, M., Generalized gradient approximation made simple. *Phys. Rev. Lett.* **1996,** *77* (18), 3865.

35. Hammer, B.; Hansen, L. B.; Nørskov, J. K., Improved adsorption energetics within density-functional theory using revised Perdew-Burke-Ernzerhof functionals. *Phys. Rev. B* **1999,** *59* (11), 7413.

36. Albers, R.; Christensen, N. E.; Svane, A., Hubbard-U band-structure methods. *J. Phys.: Condens. Matter* **2009,** *21* (34), 343201.

37. Nosé, S., A molecular dynamics method for simulations in the canonical ensemble. *Mol. Phys.* **1984,** *52* (2), 255-268.

38. Nosé, S., A unified formulation of the constant temperature molecular dynamics methods. *The Journal of chemical physics* **1984,** *81* (1), 511-519.

39. Hoover, W. G., Canonical dynamics: Equilibrium phase-space distributions. *Phys. Rev. A* **1985,** *31* (3), 1695.

40. Hoover, W. G., Constant-pressure equations of motion. *Phys. Rev. A* **1986,** *34* (3), 2499.

41. Thijssen, J., *Computational physics*. Cambridge university press: 2007.

42. Neugebauer, J.; Scheffler, M., Adsorbate-substrate and adsorbate-adsorbate interactions of Na and K adlayers on Al(111). *Phys. Rev. B* **1992,** *46* (24), 16067.

43. Makov, G.; Payne, M., Periodic boundary conditions in ab initio calculations. *Phys. Rev. B* **1995,** *51* (7), 4014.

44. Taylor, C. D.; Wasileski, S. A.; Filhol, J.-S.; Neurock, M., First principles reaction modeling of the electrochemical interface: Consideration and calculation of a tunable surface potential from atomic and electronic structure. *Phys. Rev. B* **2006,** *73* (16), 165402.

45. Rossmeisl, J.; Skúlason, E.; Björketun, M. E.; Tripkovic, V.; Nørskov, J. K., Modeling the electrified solid–liquid interface. *Chem. Phys. Lett.* **2008,** *466* (1), 68-71.

46. Peterson, A. A.; Abild-Pedersen, F.; Studt, F.; Rossmeisl, J.; Nørskov, J. K., How copper catalyzes the electroreduction of carbon dioxide into hydrocarbon fuels. *Energy Environ. Sci.* **2010,** *3* (9), 1311-1315.

47. Wellendorff, J.; Silbaugh, T. L.; Garcia-Pintos, D.; Nørskov, J. K.; Bligaard, T.; Studt, F.; Campbell, C. T., A benchmark database for adsorption bond energies to transition metal surfaces and comparison to selected DFT functionals. *Surf. Sci.* **2015,** *640*, 36-44.

48. Karlberg, G.; Rossmeisl, J.; Nørskov, J. K., Estimations of electric field effects on the oxygen reduction reaction based on the density functional theory. *Phys. Chem. Chem. Phys.* **2007,** *9* (37), 5158-5161.

49. Chen, L. D.; Urushihara, M.; Chan, K.; Nørskov, J. K., Electric Field Effects in Electrochemical CO_2 Reduction. *ACS Catal.* **2016,** *6* (10), 7133-7139.

50. Yeh, K.-Y.; Janik, M. J., CHAPTER 3 Density Functional Theory Methods for Electrocatalysis. In *Computational Catalysis*, The Royal Society of Chemistry: 2014; pp 116-156.

51. Frisch, M.; Trucks, G.; Schlegel, H.; Scuseria, G.; Robb, M.; Cheeseman, J.; Montgomery Jr, J.; Vrevon, T.; Kudin, K.; Burant, J., Gaussian 09, version A02. Wallingford, CT: Gaussian. Inc: 2009.

52. Becke, A. D., Becke's three parameter hybrid method using the LYP correlation functional. *J. Chem. Phys* **1993,** *98*, 5648-5652.

53. Hehre, W. J.; Ditchfield, R.; Pople, J. A., Self—consistent molecular orbital methods. XII. Further extensions of gaussian—type basis sets for use in molecular orbital studies of organic molecules. *J. Chem. Phys.* **1972,** *56* (5), 2257-2261.

54. Dill, J. D.; Pople, J. A., Self-consistent molecular orbital methods. XV. Extended Gaussian-type basis sets for lithium, beryllium, and boron. *J. Chem. Phys.* **1975,** *62* (7), 2921-2923.

55. Curtiss, L. A.; Redfern, P. C.; Raghavachari, K., Gaussian-4 theory. *J. Chem. Phys.* **2007,** *126* (8), 084108.

56. Miertuš, S.; Scrocco, E.; Tomasi, J., Electrostatic interaction of a solute with a continuum. A direct utilizaion of AB initio molecular potentials for the prevision of solvent effects. *Chem. Phys.* **1981,** *55* (1), 117-129.

57. Chase Jr, M. W.; Tables, N.-J. T., Data reported in NIST standard reference database 69, June 2005 release: NIST Chemistry WebBook. *J. Phys. Chem. Ref. Data, Monograph* **1998,** *9*, 1-1951.

58. Bryantsev, V. S., Calculation of solvation free energies of Li+ and O2− ions and neutral lithium–oxygen compounds in acetonitrile using mixed cluster/continuum models. *Theor. Chem. Acc.* **2012,** *131* (7), 1250.

59. Bryantsev, V. S.; Diallo, M. S.; Goddard Iii, W. A., Calculation of solvation free energies of charged solutes using mixed cluster/continuum models. *J. Phys. Chem. B* **2008,** *112* (32), 9709-9719.

60. Zuo, C.-S.; Wiest, O.; Wu, Y.-D., Parameterization and validation of solvation corrected atomic radii. *J. Phys. Chem. A* **2009,** *113* (43), 12028-12034.

61. Kelly, C. P.; Cramer, C. J.; Truhlar, D. G., Single-ion solvation free energies and the normal hydrogen electrode potential in methanol, acetonitrile, and dimethyl sulfoxide. *J. Phys. Chem. B* **2007,** *111* (2), 408-422.

62. Kelly, C. P.; Cramer, C. J.; Truhlar, D. G., Aqueous solvation free energies of ions and ion− water clusters based on an accurate value for the absolute aqueous solvation free energy of the proton. *J. Phys. Chem. B* **2006,** *110* (32), 16066-16081.

63. Kalidas, C.; Hefter, G.; Marcus, Y., Gibbs energies of transfer of cations from water to mixed aqueous organic solvents. *Chem. Rev.* **2000,** *100* (3), 819-852.

64. Marcus, Y., Gibbs energies of transfer of anions from water to mixed aqueous organic solvents. *Chem. Rev.* **2007,** *107* (9), 3880-3897.

65. Kwabi, D. G.; Bryantsev, V. S.; Batcho, T. P.; Itkis, D. M.; Thompson, C. V.; Shao-Horn, Y., Experimental and Computational Analysis of the Solvent-Dependent O2/Li+-O2− Redox Couple: Standard Potentials, Coupling Strength, and Implications for Lithium–Oxygen Batteries. *Angew. Chem. Int. Ed.* **2016,** *55* (9), 3129-3134.

66. Cheng, L.; Redfern, P.; Lau, K. C.; Assary, R. S.; Narayanan, B.; Curtiss, L. A., Computational Studies of Solubilities of LiO2 and Li2O2 in Aprotic Solvents. *J. Electrochem. Soc.* **2017,** *164* (11), E3696-E3701.

67. Palmer, D. S.; Llinàs, A.; Morao, I.; Day, G. M.; Goodman, J. M.; Glen, R. C.; Mitchell, J. B., Predicting intrinsic aqueous solubility by a thermodynamic cycle. *Molecular pharmaceutics* **2008,** *5* (2), 266-279.

68. Lee, C.; Yang, W.; Parr, R., Development of the Colle-Salvetti conelation energy formula into a functional of the electron density. *Phys. Rev, vol. B* **1988,** *37*, 785-789.

69. Zhao, Y.; Truhlar, D. G., A new local density functional for main-group thermochemistry, transition metal bonding, thermochemical kinetics, and noncovalent interactions. *J. Chem. Phys.* **2006,** *125* (19), 194101.

70. Zhao, Y.; Truhlar, D. G., Density functionals with broad applicability in chemistry. *Acc. Chem. Res.* **2008,** *41* (2), 157-167.

71. Ribeiro, R. F.; Marenich, A. V.; Cramer, C. J.; Truhlar, D. G., Use of solution-phase vibrational frequencies in continuum models for the free energy of solvation. *J. Phys. Chem. B* **2011,** *115* (49), 14556-14562.

72. Pratt, L. M.; Truhlar, D. G.; Cramer, C. J.; Kass, S. R.; Thompson, J. D.; Xidos, J. D., Aggregation of alkyllithiums in tetrahydrofuran. *J. Org. Chem.* **2007,** *72* (8), 2962-2966.

73. Westphal, E.; Pliego Jr, J. R., Absolute solvation free energy of Li+ and Na+ ions in dimethyl sulfoxide solution: A theoretical ab initio and cluster-continuum model study. *The Journal of chemical physics* **2005,** *123* (7), 074508.

74. Tsuchida, Y.; Matsumiya, M.; Tsunashima, K., Solvation structure for Fe (II), Co (II) and Ni (II) complexes in [P2225][NTf2] ionic liquids investigated by Raman spectroscopy and DFT calculation. *J. Mol. Liq.* **2018,** *269*, 8-13.

75. Tesmar, A.; Anusiewicz, I.; Chmurzyński, L., Bonding interactions in oxydiacetate and thiodiacetate cobalt (II) and nickel (II) complexes. *Struct. Chem.* **2017,** *28* (6), 1723-1730.

76. Okoshi, M.; Yamada, Y.; Yamada, A.; Nakai, H., Theoretical analysis on de-solvation of lithium, sodium, and magnesium cations to organic electrolyte solvents. *J. Electrochem. Soc.* **2013,** *160* (11), A2160-A2165.

77. Marcus, Y., Thermodynamics of solvation of ions. Part 5.—Gibbs free energy of hydration at 298.15 K. *J. Chem. Soc., Faraday Trans.* **1991,** *87* (18), 2995-2999.

78. Thakur, J.; Liu, L.; Neilson, D., Metal-insulator transition in a disordered two-dimensional electron gas including temperature effects. *Phys. Rev. B* **1999,** *59* (11), 7255.

79. Heyd, J.; Scuseria, G. E.; Ernzerhof, M., Hybrid functionals based on a screened Coulomb potential. *J. Chem. Phys.* **2003,** *118* (18), 8207-8215.

80. Paier, J.; Marsman, M.; Hummer, K.; Kresse, G.; Gerber, I. C.; Ángyán, J. G., Screened hybrid density functionals applied to solids. *J. Chem. Phys.* **2006,** *124* (15), 154709.

81. Kresse, G.; Furthmüller, J., Efficient iterative schemes for ab initio total-energy calculations using a plane-wave basis set. *Phys. Rev. B* **1996,** *54* (16), 11169.

82. Ma, S.; McKee, W. C.; Wang, J.; Guo, L.; Jansen, M.; Xu, Y.; Peng, Z., Mechanistic origin of low polarization in aprotic Na-O_2 batteries. *Phys. Chem. Chem. Phys.* **2017,** *19* (19), 12375-12383.

83. Kresse, G.; Joubert, D., From ultrasoft pseudopotentials to the projector augmented-wave method. *Phys. Rev. B* **1999,** *59* (3), 1758.

84. Ashcroft, N.; Mermin, N., *Solid State Physics (Saunders College, Philadelphia)* **1976**.

85. Föppl, H., Die kristallstrukturen der alkaliperoxyde. *Z. Anorg. Allg. Chem.* **1957,** *291* (1-4), 12-50.

86. Oganov, A. R.; Glass, C. W., Crystal structure prediction using ab initio evolutionary techniques: Principles and applications. *The Journal of chemical physics* **2006,** *124* (24), 244704.

87. Zhu, Q.; Oganov, A. R.; Lyakhov, A. O., Evolutionary metadynamics: a novel method to predict crystal structures. *CrystEngComm* **2012,** *14* (10), 3596-3601.

88. Adelhelm, P.; Hartmann, P.; Bender, C. L.; Busche, M.; Eufinger, C.; Janek, J., From lithium to sodium: cell chemistry of room temperature sodium–air and sodium–sulfur batteries. *Beilstein J. Nanotechnol.* **2015,** *6* (1), 1016-1055.

89. Christensen, J.; Albertus, P.; Sanchez-Carrera, R. S.; Lohmann, T.; Kozinsky, B.; Liedtke, R.; Ahmed, J.; Kojic, A., A Critical Review of Li/Air Batteries. *J. Electrochem. Soc.* **2012,** *159* (2), R1-R30.

90. Yadegari, H.; Sun, Q.; Sun, X., Sodium-Oxygen Batteries: A Comparative Review from Chemical and Electrochemical Fundamentals to Future Perspective. *Adv. Mater.* **2016,** *28* (33), 7065-7093.

91. Ren, X.; Wu, Y., A low-overpotential potassium–oxygen battery based on potassium superoxide. *J. Am. Chem. Soc.* **2013,** *135* (8), 2923-2926.

92. Armand, M.; Tarascon, J.-M., Building better batteries. *Nature* **2008,** *451* (7179), 652-657.

93. Whittingham, M. S., Materials challenges facing electrical energy storage. *MRS Bull.* **2008,** *33* (04), 411-419.

94. Dathar, G. K. P.; Shelton, W. A.; Xu, Y., Trends in the catalytic activity of transition metals for the oxygen reduction reaction by lithium. . *J. Phys. Chem. Lett* **2012,** *3* (7), 891-895.

95. Krishnamurthy, D.; Hansen, H. A.; Viswanathan, V., Universality in Nonaqueous Alkali Oxygen Reduction on Metal Surfaces: Implications for Li–O_2 and Na–O_2 Batteries. *ACS Energy Lett.* **2016,** *1* (1), 162-168.

96. Nørskov, J. K.; Rossmeisl, J.; Logadottir, A.; Lindqvist, L.; Kitchin, J. R.; Bligaard, T.; Jonsson, H., Origin of the overpotential for oxygen reduction at a fuel-cell cathode. *J. Phys. Chem. B* **2004,** *108* (46), 17886-17892.

97. Hyman, M. P.; Medlin, J. W., Theoretical study of the adsorption and dissociation of oxygen on Pt(111) in the presence of homogeneous electric fields. *J. Phys. Chem. B* **2005,** *109* (13), 6304-6310.

98. Montoya, J. H.; Shi, C.; Chan, K.; Nørskov, J. K., Theoretical insights into a CO dimerization mechanism in CO_2 electroreduction. . *J. Phys. Chem. Lett* **2015,** *6* (11), 2032-2037.

99. Johnson, L.; Li, C.; Liu, Z.; Chen, Y.; Freunberger, S. A.; Ashok, P. C.; Praveen, B. B.; Dholakia, K.; Tarascon, J.-M.; Bruce, P. G., The role of LiO2 solubility in O2 reduction in

aprotic solvents and its consequences for Li–O2 batteries. *Nat. Chem.* **2014,** *6* (12), 1091-1099.

100. Lu, J.; Lee, Y. J.; Luo, X.; Lau, K. C.; Asadi, M.; Wang, H.-H.; Brombosz, S.; Wen, J.; Zhai, D.; Chen, Z., A lithium–oxygen battery based on lithium superoxide. *Nature* **2016,** *529* (7586), 377-382.

101. Zhang, X.; Guo, L.; Gan, L.; Zhang, Y.; Wang, J.; Johnson, L. R.; Bruce, P. G.; Peng, Z., LiO2: Cryosynthesis and Chemical/Electrochemical Reactivities. *The Journal of Physical Chemistry Letters* **2017,** *8*, 2334-2338.

102. Xu, Y.; Mavrikakis, M., Adsorption and dissociation of O_2 on gold surfaces: Effect of steps and strain. *J. Phys. Chem. B* **2003,** *107* (35), 9298-9307.

103. Jiang, X.; Weaver, M. J., The role of interfacial potential in adsorbate bonding: electrode potential-dependent infrared spectra for saturated CO adlayers on Pt(110) and related electrochemical surfaces in varying solvent environments. *Surf. Sci.* **1992,** *275* (3), 237-252.

104. Roth, J. D.; Weaver, M. J., Role of double-layer cation on the potential-dependent stretching frequencies and binding geometries of carbon monoxide at platinum-nonaqueous interfaces. *Langmuir* **1992,** *8* (5), 1451-1458.

105. Jenkins, H.; Thakur, K., Reappraisal of thermochemical radii for complex ions. *J. Chem. Educ* **1979,** *56* (9), 576.

106. Ben-Amotz, D.; Herschbach, D. R., Estimation of effective diameters for molecular fluids. *J. Phys. Chem.* **1990,** *94* (3), 1038-1047.

107. Si, S. K.; Gewirth, A. A., Solvent organization above metal surfaces: Ordering of DMSO on Au. *J. Phys. Chem. B* **2000,** *104* (46), 10775-10782.

108. Peng, Z.; Chen, Y.; Bruce, P. G.; Xu, Y., Direct Detection of the Superoxide Anion as a Stable Intermediate in the Electroreduction of Oxygen in a Non-Aqueous Electrolyte Containing Phenol as a Proton Source. *Angew. Chem. Int. Ed.* **2015,** *54* (28), 8165-8168.

109. Rysselberghe, P. V., Remarks concerning the clausius-mossotti law. *J. Phys. Chem.* **1932,** *36* (4), 1152-1155.

110. Peng, Z.; Freunberger, S. A.; Hardwick, L. J.; Chen, Y.; Giordani, V.; Bardé, F.; Novák, P.; Graham, D.; Tarascon, J.-M.; Bruce, P. G., Oxygen Reactions in a Non-Aqueous Li^+ Electrolyte. *Angew. Chem. Int. Ed.* **2011,** *50* (28), 6351-6355.

111. Mavrikakis, M.; Stoltze, P.; Norskov, J. K., Making gold less noble. *Catal. Lett.* **2000,** *64* (2-4), 101-106.

112. Kim, J.; Samano, E.; Koel, B. E., Oxygen adsorption and oxidation reactions on Au(211) surfaces: exposures using O_2 at high pressures and ozone (O_3) in UHV. *Surf. Sci.* **2006,** *600* (19), 4622-4632.

113. Rossmeisl, J.; Qu, Z.-W.; Zhu, H.; Kroes, G.-J.; Nørskov, J. K., Electrolysis of water on oxide surfaces. *J. Electroanal. Chem.* **2007,** *607* (1), 83-89.

114. Daigle, A. D.; BelBruno, J. J., Density functional theory study of the adsorption of oxygen atoms on gold (111), (100) and (211) surfaces. *Surf. Sci.* **2011,** *605* (13-14), 1313-1319.

115. Pessoa, A. M.; Fajín, J. L.; Gomes, J. R.; Cordeiro, M. N. D., Cluster and periodic DFT calculations of adsorption of hydroxyl on the Au(hkl) surfaces. *J. Mol. Struct.:THEOCHEM* **2010,** *946* (1), 43-50.

116. Liu, Z.-P.; Hu, P.; Alavi, A., Catalytic role of gold in gold-based catalysts: a density functional theory study on the CO oxidation on gold. *J. Am. Chem. Soc.* **2002,** *124* (49), 14770-14779.

117. Torres, D.; Neyman, K. M.; Illas, F., Oxygen atoms on the (111) surface of coinage metals: On the chemical state of the adsorbate. *Chem. Phys. Lett.* **2006,** *429* (1), 86-90.

118. Baker, T. A.; Friend, C. M.; Kaxiras, E., Atomic oxygen adsorption on Au(111) surfaces with defects. *J. Phys. Chem. C* **2009,** *113* (8), 3232-3238.

119. Phatak, A. A.; Delgass, W. N.; Ribeiro, F. H.; Schneider, W. F., Density Functional Theory Comparison of Water Dissociation Steps on Cu, Au, Ni, Pd, and Pt. *J. Phys. Chem. C* **2009,** *113* (17), 7269-7276.

120. Santiago-Rodriguez, Y.; Herron, J. A.; Curet-Arana, M. C.; Mavrikakis, M., Atomic and molecular adsorption on Au(111). *Surf. Sci.* **2014,** *627*, 57-69.

121. Liu, S. X.; Ishimoto, T.; Koyama, M., First-Principles Calculation of OH^-/OH Adsorption on Gold Nanoparticles. *Int. J. Quantum Chem* **2015,** *115* (22), 1597-1605.

122. Arcelus, O.; Li, C.; Rojo, T. f.; Carrasco, J., Electronic Structure of Sodium Superoxide Bulk,(100) Surface, and Clusters Using Hybrid Density Functional: Relevance for Na–O2 Batteries. . *J. Phys. Chem. Lett* **2015,** *6* (11), 2027-2031.

123. Lau, K. C.; Curtiss, L. A.; Greeley, J., Density functional investigation of the thermodynamic stability of lithium oxide bulk crystalline structures as a function of oxygen pressure. *The Journal of Physical Chemistry C* **2011,** *115* (47), 23625-23633.

124. Lau, K. C.; Assary, R. S.; Redfern, P.; Greeley, J.; Curtiss, L. A., Electronic structure of lithium peroxide clusters and relevance to lithium–air batteries. *J. Phys. Chem. C* **2012,** *116* (45), 23890-23896.

125. McCloskey, B. D.; Scheffler, R.; Speidel, A.; Girishkumar, G.; Luntz, A. C., On the mechanism of nonaqueous Li–O2 electrochemistry on C and its kinetic overpotentials:

some implications for Li–air batteries. *The Journal of Physical Chemistry C* **2012,** *116* (45), 23897-23905.

126. Hummelshøj, J.; Luntz, A.; Nørskov, J., Theoretical evidence for low kinetic overpotentials in Li-O2 electrochemistry. *The Journal of chemical physics* **2013,** *138* (3), 034703.

127. Khetan, A.; Luntz, A.; Viswanathan, V., Trade-offs in capacity and rechargeability in nonaqueous Li–O2 batteries: solution-driven growth versus nucleophilic stability. . *J. Phys. Chem. Lett* **2015,** *6* (7), 1254-1259.

128. Black, R.; Adams, B.; Nazar, L., Non-Aqueous and Hybrid Li-O2 Batteries. *Advanced Energy Materials* **2012,** *2* (7), 801-815.

129. Fan, W.; Cui, Z.; Guo, X., Tracking formation and decomposition of abacus-ball-shaped lithium peroxides in Li–O2 cells. *The Journal of Physical Chemistry C* **2013,** *117* (6), 2623-2627.

130. Mitchell, R. R.; Gallant, B. M.; Shao-Horn, Y.; Thompson, C. V., Mechanisms of morphological evolution of Li2O2 particles during electrochemical growth. *The journal of physical chemistry letters* **2013,** *4* (7), 1060-1064.

131. Xu, J.-J.; Wang, Z.-L.; Xu, D.; Zhang, L.-L.; Zhang, X.-B., Tailoring deposition and morphology of discharge products towards high-rate and long-life lithium-oxygen batteries. *Nature communications* **2013,** *4*, 2438.

132. Zhai, D.; Wang, H.-H.; Yang, J.; Lau, K. C.; Li, K.; Amine, K.; Curtiss, L. A., Disproportionation in Li–O2 batteries based on a large surface area carbon cathode. *J. Am. Chem. Soc.* **2013,** *135* (41), 15364-15372.

133. Tatara, R.; Leverick, G. M.; Feng, S.; Wan, S.; Terada, S.; Dokko, K.; Watanabe, M.; Shao-Horn, Y., Tuning NaO2 Cube Sizes by Controlling Na+ and Solvent Activity in Na–O2 Batteries. *The Journal of Physical Chemistry C* **2018,** *122* (32), 18316-18328.

134. Sheng, c.; Yu, F.; Wu, Y.; Peng, Z.; Chen, Y., Disproportionation of sodium superoxide in Na-O2 batteries. *Angew. Chem.* **2018**.

135. Lutz, L.; Yin, W.; Grimaud, A.; Alves Dalla Corte, D.; Tang, M.; Johnson, L.; Azaceta, E.; Sarou-Kanian, V.; Naylor, A.; Hamad, S., High Capacity Na–O2 Batteries: Key Parameters for Solution-Mediated Discharge. *J. Phys. Chem. C* **2016,** *120* (36), 20068-20076.

136. Hartmann, P.; Bender, C. L.; Vračar, M.; Dürr, A. K.; Garsuch, A.; Janek, J.; Adelhelm, P., A rechargeable room-temperature sodium superoxide (NaO2) battery. *Nature materials* **2013,** *12* (3), 228-232.

137. Kim, J.; Park, H.; Lee, B.; Seong, W. M.; Lim, H.-D.; Bae, Y.; Kim, H.; Kim, W. K.; Ryu, K. H.; Kang, K., Dissolution and ionization of sodium superoxide in sodium–oxygen batteries. *Nature communications* **2016,** *7*.

138. Ortiz-Vitoriano, N.; Batcho, T. P.; Kwabi, D. G.; Han, B.; Pour, N.; Yao, K. P. C.; Thompson, C. V.; Shao-Horn, Y., Rate-dependent nucleation and growth of NaO2 in Na-O2 batteries. *J. Phys. Chem. Lett* **2015,** *6* (13), 2636-2643.

139. Trahan, M. J.; Gunasekara, I.; Mukerjee, S.; Plichta, E. J.; Hendrickson, M. A.; Abraham, K. M., Solvent-Coupled Catalysis of the Oxygen Electrode Reactions in Lithium-Air Batteries. *J. Electrochem. Soc.* **2014,** *161* (10), A1706-A1715.

140. Abraham, K. M., Electrolyte-Directed Reactions of the Oxygen Electrode in Lithium-Air Batteries. *J. Electrochem. Soc.* **2015,** *162* (2), A3021-A3031.

141. Gnanaraj, J.; Thompson, R. W.; DiCarlo, J.; Abraham, K., The role of carbonate solvents on lithium intercalation into graphite. *J. Electrochem. Soc.* **2007,** *154* (3), A185-A191.

142. Laoire, C. O.; Mukerjee, S.; Abraham, K. M.; Plichta, E. J.; Hendrickson, M. A., Influence of Nonaqueous Solvents on the Electrochemistry of Oxygen in the Rechargeable Lithium-Air Battery. *J. Phys. Chem. C* **2010,** *114* (19), 9178-9186.

143. Sharon, D.; Afri, M.; Noked, M.; Garsuch, A.; Frimer, A. A.; Aurbach, D., Oxidation of Dimethyl Sulfoxide Solutions by Electrochemical Reduction of Oxygen. . *J. Phys. Chem. Lett* **2013,** *4* (18), 3115-3119.

144. Kwabi, D. G.; Tułodziecki, M.; Pour, N.; Itkis, D. M.; Thompson, C. V.; Shao-Horn, Y., Controlling Solution-Mediated Reaction Mechanisms of Oxygen Reduction Using Potential and Solvent for Aprotic Lithium–Oxygen Batteries. . *J. Phys. Chem. Lett* **2016,** *7* (7), 1204-1212.

145. Lutz, L.; Alves Dalla Corte, D.; Tang, M.; Salager, E.; Deschamps, M.; Grimaud, A.; Johnson, L.; Bruce, P. G.; Tarascon, J.-M., Role of Electrolyte Anions in the Na–O2 Battery: Implications for NaO2 Solvation and the Stability of the Sodium Solid Electrolyte Interphase in Glyme Ethers. *Chem. Mater.* **2017,** *29* (14), 6066-6075.

146. Gutmann, V., Empirical parameters for donor and acceptor properties of solvents. *Electrochim. Acta* **1976,** *21* (9), 661-670.

147. Gutmann, V., Coordination chemistry of certain transition-metal ions. The role of the solvent. *Coord. Chem. Rev.* **1967,** *2* (2), 239-256.

148. Schmeisser, M.; Illner, P.; Puchta, R.; Zahl, A.; van Eldik, R., Gutmann donor and acceptor numbers for ionic liquids. *Chemistry-A European Journal* **2012,** *18* (35), 10969-10982.

149. Gritzner, G.; Danksagmüller, K.; Gutmann, V., Outer-sphere coordination effects on the redox behaviour of the Fe (CN) 63−/Fe (CN) 64− couple in non-aqueous solvents. *Journal of Electroanalytical Chemistry and Interfacial Electrochemistry* **1976,** *72* (2), 177-185.

150. Lodge, A. W.; Lacey, M. J.; Fitt, M.; Garcia-Araez, N.; Owen, J. R., Critical appraisal on the role of catalysts for the oxygen reduction reaction in lithium-oxygen batteries. *Electrochim. Acta* **2014,** *140*, 168-173.

151. Haynes, W. M., *CRC handbook of chemistry and physics*. CRC press: 2014.

152. Zakharchenko, T. K.; Kozmenkova, A. Y.; Itkis, D. M.; Goodilin, E. A., Lithium peroxide crystal clusters as a natural growth feature of discharge products in Li–O2 cells. *Beilstein J. Nanotechnol.* **2013,** *4*, 758.

153. Visco, S. J.; Nimon, V. Y.; Petrov, A.; Pridatko, K.; Goncharenko, N.; Nimon, E.; De Jonghe, L.; Volfkovich, Y. M.; Bograchev, D. A., Aqueous and nonaqueous lithium-air batteries enabled by water-stable lithium metal electrodes. *J. Solid State Electrochem.* **2014,** *18* (5), 1443-1456.

154. Zheng, D.; Lee, H.-S.; Yang, X.-Q.; Qu, D., Electrochemical oxidation of solid Li 2 O 2 in non-aqueous electrolyte using peroxide complexing additives for lithium–air batteries. *Electrochem. Commun.* **2013,** *28*, 17-19.

155. Xie, B.; Lee, H.; Li, H.; Yang, X.; McBreen, J.; Chen, L., New electrolytes using Li 2 O or Li 2 O 2 oxides and tris (pentafluorophenyl) borane as boron based anion receptor for lithium batteries. *Electrochem. Commun.* **2008,** *10* (8), 1195-1197.

156. Elliott, S. D.; Ahlrichs, R., An ab initio study of the monoxides and dioxides of sodium. *The Journal of chemical physics* **1998,** *109* (11), 4267-4280.

157. Tremblay, B.; Roy, P.; Manceron, L.; Pullumbi, P.; Bouteiller, Y.; Roy, D., Vibrational spectrum and structure of the K2O2 complex in solid argon: A far infrared and density functional theory study. *The Journal of chemical physics* **1995,** *103* (4), 1284-1291.

158. Seriani, N., Ab initio thermodynamics of lithium oxides: from bulk phases to nanoparticles. *Nanotechnology* **2009,** *20* (44), 445703.

159. In, N., Chemistry WebBook, NIST Standard Reference Database Number 69, June 2005 Release. *The date compiled by Huber KP*.

160. Kang, S.; Mo, Y.; Ong, S. P.; Ceder, G., Nanoscale stabilization of sodium oxides: implications for Na–O2 batteries. *Nano Lett.* **2014,** *14* (2), 1016-1020.

161. Hartmann, P.; Bender, C. L.; Sann, J.; Dürr, A. K.; Jansen, M.; Janek, J.; Adelhelm, P., A comprehensive study on the cell chemistry of the sodium superoxide (NaO 2) battery. *Phys. Chem. Chem. Phys.* **2013,** *15* (28), 11661-11672.

162. Bender, C. L.; Hartmann, P.; Vračar, M.; Adelhelm, P.; Janek, J., On the thermodynamics, the role of the carbon cathode, and the cycle life of the sodium superoxide (NaO2) battery. *Advanced Energy Materials* **2014,** *4* (12).

163. McCloskey, B. D.; Garcia, J. M.; Luntz, A. C., Chemical and electrochemical differences in nonaqueous Li–O2 and Na–O2 batteries. . *J. Phys. Chem. Lett* **2014,** *5* (7), 1230-1235.

164. Sun, Q.; Yang, Y.; Fu, Z.-W., Electrochemical properties of room temperature sodium–air batteries with non-aqueous electrolyte. *Electrochem. Commun.* **2012,** *16* (1), 22-25.

165. Kim, J.; Lim, H.-D.; Gwon, H.; Kang, K., Sodium–oxygen batteries with alkyl-carbonate and ether based electrolytes. *Phys. Chem. Chem. Phys.* **2013,** *15* (10), 3623-3629.

166. Liu, W.; Sun, Q.; Yang, Y.; Xie, J.-Y.; Fu, Z.-W., An enhanced electrochemical performance of a sodium–air battery with graphene nanosheets as air electrode catalysts. *Chem. Commun.* **2013,** *49* (19), 1951-1953.

167. Jian, Z.; Chen, Y.; Li, F.; Zhang, T.; Liu, C.; Zhou, H., High capacity Na–O 2 batteries with carbon nanotube paper as binder-free air cathode. *J. Power Sources* **2014,** *251*, 466-469.

168. Yadegari, H.; Li, Y.; Banis, M. N.; Li, X.; Wang, B.; Sun, Q.; Li, R.; Sham, T.-K.; Cui, X.; Sun, X., On rechargeability and reaction kinetics of sodium–air batteries. *Energy Environ. Sci.* **2014,** *7* (11), 3747-3757.

169. Bender, C. L.; Bartuli, W.; Schwab, M. G.; Adelhelm, P.; Janek, J., Toward Better Sodium–Oxygen batteries: A Study on the Performance of Engineered Oxygen Electrodes based on Carbon Nanotubes. *Energy Technology* **2015,** *3* (3), 242-248.

170. Das, U.; Lau, K. C.; Redfern, P. C.; Curtiss, L. A., Structure and stability of lithium superoxide clusters and relevance to Li–O2 batteries. . *J. Phys. Chem. Lett* **2014,** *5* (5), 813-819.

171. Luntz, A. C.; McCloskey, B. D., Nonaqueous Li–air batteries: a status report. *Chem. Rev.* **2014,** *114* (23), 11721-11750.

172. Luntz, A.; Viswanathan, V.; Voss, J.; Varley, J.; Nørskov, J.; Scheffler, R.; Speidel, A., Tunneling and polaron charge transport through Li2O2 in Li–O2 batteries. *The Journal of Physical Chemistry Letters* **2013,** *4* (20), 3494-3499.

173. Johnson, L.; Li, C.; Liu, Z.; Chen, Y.; Freunberger, S. A.; Ashok, P. C.; Praveen, B. B.; Dholakia, K.; Tarascon, J.-M.; Bruce, P. G., The role of LiO 2 solubility in O 2 reduction in aprotic solvents and its consequences for Li–O 2 batteries. *Nat. Chem.* **2014,** *6* (12), 1091.

174. McCloskey, B. D.; Scheffler, R.; Speidel, A.; Bethune, D. S.; Shelby, R. M.; Luntz, A., On the efficacy of electrocatalysis in nonaqueous Li–O2 batteries. *J. Am. Chem. Soc.* **2011,** *133* (45), 18038-18041.

175. Matsuda, S.; Uosaki, K.; Nakanishi, S., Improved charging performance of Li–O2 batteries by forming Ba-incorporated Li2O2 as the discharge product. *J. Power Sources* **2017,** *353*, 138-143.

176. Chen, Y.; Freunberger, S. A.; Peng, Z.; Fontaine, O.; Bruce, P. G., Charging a Li–O 2 battery using a redox mediator. *Nat. Chem.* **2013,** *5* (6), 489.

177. Zhang, W.; Shen, Y.; Sun, D.; Huang, Z.; Zhou, J.; Yan, H.; Huang, Y., Promoting Li2O2 oxidation via solvent-assisted redox shuttle process for low overpotential Li-O2 battery. *Nano Energy* **2016,** *30*, 43-51.

178. Liu, T.; Leskes, M.; Yu, W. J.; Moore, A. J.; Zhou, L. N.; Bayley, P. M.; Kim, G.; Grey, C. P., Cycling Li-O-2 batteries via LiOH formation and decomposition. *Science* **2015,** *350* (6260), 530-533.

179. Black, R.; Lee, J. H.; Adams, B.; Mims, C. A.; Nazar, L. F., The role of catalysts and peroxide oxidation in lithium–oxygen batteries. *Angew. Chem.* **2013,** *125* (1), 410-414.

180. Cui, Y.; Wen, Z.; Liu, Y., A free-standing-type design for cathodes of rechargeable Li–O 2 batteries. *Energy Environ. Sci.* **2011,** *4* (11), 4727-4734.

181. Amatucci, G.; Tarascon, J.; Klein, L., Cobalt dissolution in $LiCoO_2$-based non-aqueous rechargeable batteries. *Solid State Ionics* **1996,** *83* (1-2), 167-173.

182. Veith, G. M.; Nanda, J.; Delmau, L. H.; Dudney, N. J., Influence of lithium salts on the discharge chemistry of Li–air cells. *The journal of physical chemistry letters* **2012,** *3* (10), 1242-1247.

183. Matsuda, S.; Kubo, Y.; Uosaki, K.; Hashimoto, K.; Nakanishi, S., Improved energy capacity of aprotic Li–O2 batteries by forming Cl-incorporated Li2O2 as the discharge product. *J. Phys. Chem. C* **2016,** *120* (25), 13360-13365.

184. Hardwick, L. J.; Bruce, P. G., The pursuit of rechargeable non-aqueous lithium–oxygen battery cathodes. *Curr. Opin. Solid State Mater. Sci.* **2012,** *16* (4), 178-185.

185. Shao, Y.; Ding, F.; Xiao, J.; Zhang, J.; Xu, W.; Park, S.; Zhang, J. G.; Wang, Y.; Liu, J., Making Li-air batteries rechargeable: Material challenges. *Adv. Funct. Mater.* **2013,** *23* (8), 987-1004.

186. Matsuda, S.; Mori, S.; Hashimoto, K.; Nakanishi, S., Transition metal complexes with macrocyclic ligands serve as efficient electrocatalysts for aprotic oxygen evolution on Li2O2. *The Journal of Physical Chemistry C* **2014,** *118* (49), 28435-28439.

187. Garcia-Lastra, J.; Myrdal, J.; Christensen, R.; Thygesen, K.; Vegge, T., DFT+ U study of polaronic conduction in Li2O2 and Li2CO3: implications for Li–Air batteries. *The Journal of Physical Chemistry C* **2013,** *117* (11), 5568-5577.

188. Viswanathan, V.; Thygesen, K. S.; Hummelshøj, J.; Nørskov, J. K.; Girishkumar, G.; McCloskey, B.; Luntz, A., Electrical conductivity in Li2O2 and its role in determining capacity limitations in non-aqueous Li-O2 batteries. *J. Chem. Phys.* **2011,** *135* (21), 214704.

189. Zhao, Y.; Ban, C.; Kang, J.; Santhanagopalan, S.; Kim, G.-H.; Wei, S.-H.; Dillon, A. C., P-type doping of lithium peroxide with carbon sheets. *Appl. Phys. Lett.* **2012,** *101* (2), 023903.

190. Kang, J.; Jung, Y. S.; Wei, S.-H.; Dillon, A. C., Implications of the formation of small polarons in Li 2 O 2 for Li-air batteries. *Phys. Rev. B* **2012,** *85* (3), 035210.

191. Lyu, Z.; Wang, T.; Guo, R.; Zhou, Y.; Chen, J.; Wang, X.; Lin, M.; Tian, X.; Lai, M.; Peng, L., Promoting defective-Li 2 O 2 formation via Na doping for Li-O 2 batteries with low charge overpotentials. *Journal of Materials Chemistry A* **2019**.

192. Varley, J.; Viswanathan, V.; Nørskov, J.; Luntz, A., Lithium and oxygen vacancies and their role in Li 2 O 2 charge transport in Li–O 2 batteries. *Energy Environ. Sci.* **2014,** *7* (2), 720-727.

193. Ong, S. P.; Mo, Y.; Ceder, G., Low hole polaron migration barrier in lithium peroxide. *Phys. Rev. B* **2012,** *85* (8), 081105.

194. Weaver, J.; Frederikse, H., Crc handbook of chemistry and physics. *CRC Press, Boca Raton* **1977,** *76*, 12-156.

195. Ottakam Thotiyl, M. M.; Freunberger, S. A.; Peng, Z.; Chen, Y.; Liu, Z.; Bruce, P. G., A stable cathode for the aprotic Li-O2 battery. *Nature materials* **2013,** *12* (11), 1050-6.

196. Yang, J.; Zhai, D.; Wang, H.-H.; Lau, K. C.; Schlueter, J. A.; Du, P.; Myers, D. J.; Sun, Y.-K.; Curtiss, L. A.; Amine, K., Evidence for lithium superoxide-like species in the discharge product of a Li–O 2 battery. *Phys. Chem. Chem. Phys.* **2013,** *15* (11), 3764-3771.

197. Kang, S.; Mo, Y.; Ong, S. P.; Ceder, G., A facile mechanism for recharging Li2O2 in Li–O2 batteries. *Chem. Mater.* **2013,** *25* (16), 3328-3336.

198. Matsuda, S.; Mori, S.; Kubo, Y.; Uosaki, K.; Hashimoto, K.; Nakanishi, S., Cobalt phthalocyanine analogs as soluble catalysts that improve the charging performance of Li-O2 batteries. *Chem. Phys. Lett.* **2015,** *620*, 78-81.

199. Canali, C.; Jacoboni, C.; Nava, F.; Ottaviani, G.; Alberigi-Quaranta, A., Electron drift velocity in silicon. *Phys. Rev. B* **1975,** *12* (6), 2265.

200. Mo, Y.; Ong, S. P.; Ceder, G., First-principles study of the oxygen evolution reaction of lithium peroxide in the lithium-air battery. *Phys. Rev. B* **2011,** *84* (20), 205446.

201. Radin, M. D.; Tian, F.; Siegel, D. J., Electronic structure of Li 2 O 2 {0001} surfaces. *Journal of Materials Science* **2012,** *47* (21), 7564-7570.

202. Li, J.; Li, X.; Zhai, H.-J.; Wang, L.-S., Au20: a tetrahedral cluster. *Science* **2003,** *299* (5608), 864-867.

203. Ho, K.-M.; Shvartsburg, A. A.; Pan, B.; Lu, Z.-Y.; Wang, C.-Z.; Wacker, J. G.; Fye, J. L.; Jarrold, M. F., Structures of medium-sized silicon clusters. *Nature* **1998,** *392* (6676), 582.

204. Aguilera-Granja, F.; Balbás, L.; Vega, A., Study of the structural and electronic properties of Rh N and Ru N clusters (N< 20) within the density functional theory. *J. Phys. Chem. A* **2009,** *113* (48), 13483-13491.

205. Ivanov, A. S.; Boldyrev, A. I., Reliable predictions of unusual molecules. *Phys. Chem. Chem. Phys.* **2012,** *14* (46), 15943-15952.

206. Bandyopadhyay, D.; Sen, P., Density functional investigation of structure and stability of Ge n and Ge n Ni (n= 1− 20) clusters: Validity of the electron counting rule. *J. Phys. Chem. A* **2010,** *114* (4), 1835-1842.

207. Li, X.-P.; Lu, W.-C.; Zang, Q.-J.; Chen, G.-J.; Wang, C.; Ho, K., Structures and Stabilities of Pb n (n≤ 20) Clusters. *J. Phys. Chem. A* **2009,** *113* (22), 6217-6221.

208. Menon, M., Generalized tight-binding molecular dynamics scheme for heteroatomic systems: Application to Si m C n clusters. *J. Chem. Phys.* **2001,** *114* (18), 7731-7735.

209. Todorov, E.; Sevov, S. C., Synthesis, characterization, and bonding of heteroatomic clusters: Na13Cd20E7 (E= Pb, Sn), a further example of a structure containing empty icosahedra without an element of group 13. *Inorg. Chem.* **1997,** *36* (20), 4298-4302.

210. Gopakumar, G.; Lievens, P.; Nguyen, M. T., Interaction of diatomic germanium with lithium atoms: Electronic structure and stability. *J. Chem. Phys.* **2006,** *124* (21), 214312.

211. Wang, J.; Han, J.-G., A computational investigation of copper-doped germanium and germanium clusters by the density-functional theory. *J. Chem. Phys.* **2005,** *123* (24), 244303.

212. Hartke, B., Structural transitions in clusters. *Angew. Chem. Int. Ed.* **2002,** *41* (9), 1468-1487.

213. Üstünel, H.; Erkoç, Ş., Structural properties and stability of nanoclusters. *J. Comput. Theor. Nanosci.* **2007,** *4* (5), 928-956.

214. McKee, W. C.; Agarwal, J.; Schaefer III, H. F.; Schleyer, P. v. R., Covalent hypercoordination: can carbon bind five methyl ligands? *Angew. Chem. Int. Ed.* **2014,** *53* (30), 7875-7878.

215. Deaven, D. M.; Ho, K. M., Molecular Geometry Optimization with a Genetic Algorithm. *Phys. Rev. Lett.* **1995,** *75* (2), 288-291.

216. Ballone, P.; Andreoni, W.; Car, R.; Parrinello, M., Equilibrium Structures and Finite Temperature Properties of Silicon Microclusters from ab initio Molecular-Dynamics Calculations. *Phys. Rev. Lett.* **1988,** *60* (4), 271-274.

217. Wales, D. J.; Doye, J. P. K., Global Optimization by Basin-Hopping and the Lowest Energy Structures of Lennard-Jones Clusters Containing up to 110 Atoms. *J. Phys. Chem. A* **1997,** *101* (28), 5111-5116.

218. Goedeckter, S., Minima hopping: An efficient search method for the global minimum of the potential energy surface of complex molecular systems. *J. Chem. Phys.* **2004,** *120* (21), 9911-9917.

219. Pietrucci, F.; Andreoni, W., Graph Theory Meets Ab Initio Molecular Dynamics: Atomic Structures and Transformations at the Nanoscale. *Phys. Rev. Lett.* **2011,** *107* (8), 085504.

220. Grubmüller, H., Predicting slow structural transitions in macromolecular systems: Conformational flooding. *Physical Review E* **1995,** *52* (3), 2893-2906.

221. Zhai, H.; Ha, M.-A.; Alexandrova, A. N., AFFCK: Adaptive Force-Field-Assisted ab Initio Coalescence Kick Method for Global Minimum Search. *J. Chem. Theor. Comput.* **2015,** *11* (5), 2385-2393.

222. Call, S. T.; Zubarev, D. Y.; Boldyrev, A. I., Global minimum structure searches via particle swarm optimization. *J. Comput. Chem.* **2007,** *28* (7), 1177-1186.

223. Saunders, M., Stochastic search for isomers on a quantum mechanical surface. *J. Comput. Chem.* **2004,** *25* (5), 621-626.

224. Avaltroni, F.; Corminboeuf, C., Identifying clusters as low-lying mimina—efficiency of stochastic and genetic algorithms using inexpensive electronic structure levels. *J. Comput. Chem.* **2012,** *33* (5), 502-508.

225. Huang, W.; Sergeeva, A. P.; Zhai, H.-J.; Averkiev, B. B.; Wang, L.-S.; Boldyrev, A. I., A concentric planar doubly π-aromatic B19− cluster. *Nat Chem* **2010,** *2* (3), 202-206.

226. Islas, R.; Heine, T.; Ito, K.; Schleyer, P. v. R.; Merino, G., Boron Rings Enclosing Planar Hypercoordinate Group 14 Elements. *J. Am. Chem. Soc.* **2007,** *129* (47), 14767-14774.

227. Roy, D.; Corminboeuf, C.; Wannere, C. S.; King, R. B.; Schleyer, P. v. R., Planar Tetracoordinate Carbon Atoms Centered in Bare Four-membered Rings of Late Transition Metals. *Inorg. Chem.* **2006,** *45* (22), 8902-8906.

228. Olaya, A. J.; Ge, P.; Gonthier, J. F.; Pechy, P.; Corminboeuf, C.; Girault, H. H., Four-Electron Oxygen Reduction by Tetrathiafulvalene. *J. Am. Chem. Soc.* **2011,** *133* (31), 12115-12123.

229. Roy, D.; Navarro-Vazquez, A.; Schleyer, P. v. R., Modeling Dinitrogen Activation by Lithium: A Mechanistic Investigation of the Cleavage of N2 by Stepwise Insertion into Small Lithium Clusters. *J. Am. Chem. Soc.* **2009,** *131* (36), 13045-13053.

230. Pham, H. T.; Van Duong, L.; Pham, B. Q.; Nguyen, M. T., The 2D-to-3D geometry hopping in small boron clusters: The charge effect. *Chem. Phys. Lett.* **2013,** *577*, 32-37.

231. Heiles, S.; Logsdail, A. J.; Schäfer, R.; Johnston, R. L., Dopant-induced 2D–3D transition in small Au-containing clusters: DFT-global optimisation of 8-atom Au–Ag nanoalloys. *Nanoscale* **2012,** *4* (4), 1109-1115.

232. Alexandrova, A. N.; Boldyrev, A. I.; Fu, Y.-J.; Yang, X.; Wang, X.-B.; Wang, L.-S., Structure of the Na x Cl x+ 1−(x= 1–4) clusters via ab initio genetic algorithm and photoelectron spectroscopy. *J. Chem. Phys.* **2004,** *121* (12), 5709-5719.

233. Wheeler, S. E.; Schleyer, P. v. R.; Schaefer, H. F., SASS: A symmetry adapted stochastic search algorithm exploiting site symmetry. *J. Chem. Phys.* **2007,** *126* (10), 104104.

234. Addicoat, M. A.; Metha, G. F., Kick: Constraining a stochastic search procedure with molecular fragments. *J. Comput. Chem.* **2009,** *30* (1), 57-64.

235. Avaltroni, F.; Corminboeuf, C., Efficiency of random search procedures along the silicon cluster series: Sin (n= 5–10, 15, and 20). *J. Comput. Chem.* **2011,** *32* (9), 1869-1875.

236. Tai, T. B.; Nguyen, M. T., A Stochastic Search for the Structures of Small Germanium Clusters and Their Anions: Enhanced Stability by Spherical Aromaticity of the Ge10 and Ge122− Systems. *J. Chem. Theor. Comput.* **2011,** *7* (4), 1119-1130.

237. Pyykkö, P.; Atsumi, M., Molecular Single-Bond Covalent Radii for Elements 1–118. *Chem. Eur. J.* **2009,** *15* (1), 186-197.

238. Pyykkö, P.; Atsumi, M., Molecular Double-Bond Covalent Radii for Elements Li–E112. *Chem. Eur. J.* **2009,** *15* (46), 12770-12779.

239. Pyykkö, P.; Riedel, S.; Patzschke, M., Triple-Bond Covalent Radii. *Chem. Eur. J.* **2005,** *11* (12), 3511-3520.

240. Pyykkö, P., Additive Covalent Radii for Single-, Double-, and Triple-Bonded Molecules and Tetrahedrally Bonded Crystals: A Summary. *J. Phys. Chem. A* **2015,** *119* (11), 2326-2337.

241. Frisch, M. J.; Trucks, G. W.; Schlegel, H. B.; Scuseria, G. E.; Robb, M. A.; Cheeseman, J. R.; Scalmani, G.; Barone, V.; Mennucci, B.; Petersson, G. A.; Nakatsuji, H.; Caricato, M.; Li, X.; Hratchian, H. P.; Izmaylov, A. F.; Bloino, J.; Zheng, G.; Sonnenberg, J. L.; Hada, M.; Ehara, M.; Toyota, K.; Fukuda, R.; Hasegawa, J.; Ishida, M.; Nakajima, T.; Honda, Y.; Kitao, O.; Nakai, H.; Vreven, T.; Montgomery Jr., J. A.; Peralta, J. E.; Ogliaro, F.; Bearpark, M. J.; Heyd, J.; Brothers, E. N.; Kudin, K. N.; Staroverov, V. N.; Kobayashi, R.; Normand, J.; Raghavachari, K.; Rendell, A. P.; Burant, J. C.; Iyengar, S. S.; Tomasi, J.; Cossi, M.; Rega, N.; Millam, N. J.; Klene, M.; Knox, J. E.; Cross, J. B.; Bakken, V.; Adamo, C.; Jaramillo, J.; Gomperts, R.; Stratmann, R. E.; Yazyev, O.; Austin, A. J.; Cammi, R.; Pomelli, C.; Ochterski, J. W.; Martin, R. L.; Morokuma, K.; Zakrzewski, V. G.; Voth, G. A.; Salvador, P.; Dannenberg, J. J.; Dapprich, S.; Daniels, A. D.; Farkas, Ö.; Foresman, J. B.; Ortiz, J. V.; Cioslowski, J.; Fox, D. J. *Gaussian 09*, Gaussian, Inc.: Wallingford, CT, USA, 2009.

242. Ryu, S.; Lee, H. W.; Han, Y.-K., Performance of Density Functionals for the Calculation of Gold Clusters. *Bull. Korean Chem. Soc* **2011,** *32*, 2802-2804.

243. Bera, P. P.; Sattelmeyer, K. W.; Saunders, M.; Schaefer, H. F.; Schleyer, P. v. R., Mindless Chemistry. *J. Phys. Chem. A* **2006,** *110* (13), 4287-4290.

244. Libisch, F.; Cheng, J.; Carter, E. A., Electron-transfer-induced dissociation of H2 on gold nanoparticles: Excited-state potential energy surfaces via embedded correlated wavefunction theory. *Z. Phys. Chem.* **2013,** *227* (9-11), 1455-1466.

245. Raghavachari, K.; Whiteside, R. A.; Pople, J. A., Structures of small carbon clusters: Cyclic ground state of C6. *J. Chem. Phys.* **1986,** *85* (11), 6623-6628.

246. Hutter, J.; Lüthi, H. P., The molecular structure of C6: A theoretical investigation. *J. Chem. Phys.* **1994,** *101* (3), 2213-2216.

247. Grein, F.; Franz, J.; Hanrath, M.; Peyerimhoff, S. D., Theoretical studies on the electronic spectra of cyclic C6, in D3h and D6h symmetries. *Chem. Phys.* **2001,** *263* (1), 55-60.

248. Mantina, M.; Chamberlin, A. C.; Valero, R.; Cramer, C. J.; Truhlar, D. G., Consistent van der Waals Radii for the Whole Main Group. *J. Phys. Chem. A* **2009,** *113* (19), 5806-5812.

249. Lu, W.-C.; Wang, C.; Zhao, L.-Z.; Zhang, W.; Qin, W.; Ho, K., Appearance of bulk-like motifs in Si, Ge, and Al clusters. *Phys. Chem. Chem. Phys.* **2010,** *12* (30), 8551-8556.

250. Raghavachari, K.; Rohlfing, C. M., Bonding and stabilities of small silicon clusters: A theoretical study of Si7–Si10. *J. Chem. Phys.* **1988,** *89* (4), 2219-2234.

251. Rohlfing, C. M.; Raghavachari, K., A theoretical study of small silicon clusters using an effective core potential. *Chem. Phys. Lett.* **1990,** *167* (6), 559-565.

252. Zhu, X.; Zeng, X. C., Structures and stabilities of small silicon clusters: Ab initio molecular-orbital calculations of Si7–Si11. *J. Chem. Phys.* **2003,** *118* (8), 3558-3570.

253. Haertelt, M.; Lyon, J. T.; Claes, P.; Haeck, J. d.; Lievens, P.; Fielicke, A., Gas-phase structures of neutral silicon clusters. *J. Chem. Phys.* **2012,** *136* (6), 064301.

254. Haruta, M.; Kobayashi, T.; Sano, H.; Yamada, N., NOVEL GOLD CATALYSTS FOR THE OXIDATION OF CARBON MONOXIDE AT A TEMPERATURE FAR BELOW 0 C. *Chem. Lett.* **1987,** *16* (2), 405-408.

255. Valden, M.; Lai, X.; Goodman, D. W., Onset of catalytic activity of gold clusters on titania with the appearance of nonmetallic properties. *Science* **1998,** *281* (5383), 1647-1650.

256. Herzing, A. A.; Kiely, C. J.; Carley, A. F.; Landon, P.; Hutchings, G. J., Identification of Active Gold Nanoclusters on Iron Oxide Supports for CO Oxidation. *Science* **2008,** *321* (5894), 1331-1335.

257. Yoon, B.; Häkkinen, H.; Landman, U.; Wörz, A. S.; Antonietti, J.-M.; Abbet, S.; Judai, K.; Heiz, U., Charging Effects on Bonding and Catalyzed Oxidation of CO on Au_8 Clusters on MgO. *Science* **2005,** *307* (5708), 403-407.

258. McKee, W. C.; Patterson, M. C.; Huang, D.; Frick, J. R.; Kurtz, R. L.; Sprunger, P. T.; Liu, L.; Xu, Y., CO Adsorption on Au Nanoparticles Grown on Hexagonal Boron Nitride/Rh(111). *J. Phys. Chem. C* **2016,** *120* (20), 10909-10918.

259. Lee, H. M.; Ge, M.; Sahu, B. R.; Tarakeshwar, P.; Kim, K. S., Geometrical and Electronic Structures of Gold, Silver, and Gold−Silver Binary Clusters: Origins of Ductility of Gold and Gold−Silver Alloy Formation. *J. Phys. Chem. B* **2003,** *107* (37), 9994-10005.

260. Fa, W.; Luo, C.; Dong, J., Bulk fragment and tubelike structures of ${\mathrm{Au}}_{N}$ $(N=2\text{\ensuremath{-}}26)$. *Phys. Rev. B* **2005,** *72* (20), 205428.

261. Assadollahzadeh, B.; Schwerdtfeger, P., A systematic search for minimum structures of small gold clusters Aun (n=2–20) and their electronic properties. *J. Chem. Phys.* **2009,** *131* (6), 064306.

262. Gruene, P.; Rayner, D. M.; Redlich, B.; van der Meer, A. F. G.; Lyon, J. T.; Meijer, G.; Fielicke, A., Structures of Neutral Au_7, Au_{19}, and Au_{20}Clusters in the Gas Phase. *Science* **2008,** *321* (5889), 674-676.

263. Bazterra, V. E.; Oña, O.; Caputo, M. C.; Ferraro, M. B.; Fuentealba, P.; Facelli, J. C., Modified genetic algorithms to model cluster structures in medium-size silicon clusters. *Phys. Rev. A* **2004,** *69* (5), 053202.

264. Yoo, S., S. Yoo and XC Zeng, Angew. Chem., Int. Ed. 44, 1491 (2005). *Angew. Chem., Int. Ed.* **2005,** *44*, 1491.

265. Yoo, S., S. Yoo, XC Zeng, X. Zhu, and J. Bai, J. Am. Chem. Soc. 125, 13318 (2003). *J. Am. Chem. Soc.* **2003,** *125*, 13318.

266. Rata, I.; Shvartsburg, A. A.; Horoi, M.; Frauenheim, T.; Siu, K. M.; Jackson, K. A., Single-parent evolution algorithm and the optimization of Si clusters. *Phys. Rev. Lett.* **2000,** *85* (3), 546.

267. Setyawan, W.; Curtarolo, S., High-throughput electronic band structure calculations: Challenges and tools. *Computational materials science* **2010,** *49* (2), 299-312.

268. Curtarolo, S.; Setyawan, W.; Hart, G. L.; Jahnatek, M.; Chepulskii, R. V.; Taylor, R. H.; Wang, S.; Xue, J.; Yang, K.; Levy, O., AFLOW: an automatic framework for high-throughput materials discovery. *Computational Materials Science* **2012,** *58*, 218-226.

Vita

Saurin Hiren Rawal was born and raised in the city of Mumbai in Maharashtra, India. He completed his Bachelor's in Chemical Engineering from the University of Mumbai in 2012. He worked in the Indian Institute of Technology, Bombay as Junior Research Fellow from August 2012 to November 2012. In January 2013 he started his Master's degree in Chemical and Biochemical Engineering at Rutgers, The State University Of New Jersey under the guidance of Prof. Alexander V. Neimark. His thesis title was "Single File Diffusion". He graduated in May 2015 and join Louisiana State University in the same year to continue his doctoral degree under the guidance of Prof. Ye Xu. As a graduate student, he has authored three peer-reviewed journal articles and two more articles are in preparation. He has given 3 poster presentation and 3 conference presentations in various conferences. During his Ph.D. he did two research internships at Globalfoundries Inc and Proctor & Gamble company in the summer of 2018 and 2019 respectively. In addition to his love for research, he extremely passionate about endurance sports like running and biking along with science fiction novels and Japanese Manga. He anticipates receiving his doctoral degree in chemical engineering in the summer of 2020.